EPFL

Thèse n° 9644

Interfacial Engineering: The Key to Boost Perovskite Solar Cells Performance and Stability

Présentée le 14 décembre 2021

Faculté des sciences de base
Groupe SCI SB MN
Programme doctoral en chimie et génie chimique

pour l'obtention du grade de Docteur ès Sciences

par

Albertus Adrian SUTANTO

Acceptée sur proposition du jury

Prof. K. Sivula, président du jury
Prof. M. K. Nazeeruddin, directeur de thèse
Prof. M. Lira-Cantu, rapporteuse
Prof. E. Palomares, rapporteur
Prof. R. Buonsanti, rapporteuse

École polytechnique fédérale de Lausanne

2021

Acknowledgement

First, I would like to acknowledge my thesis director, Prof. Mohammad Khaja Nazeeruddin, for giving me the opportunity to do my PhD in the Group for Molecular Engineering of Functional Materials (GMF). It has been a great chance doing my research on a hot topic such as perovskite solar cells, which has exposed me to the multidisciplinary and multicultural working environment. Also, special thanks to Nazeer for giving me the freedom in carrying out my research as well as allowing me to develop my ideas, to learn from my mistakes, to solve various problems, to collaborate with many great scientists in the field, and to make a continuous improvement. All these experiences undeniably have shaped and developed myself both professionally and personally. Thank you for your support and advices!

Also, I would like to thank Prof. Kevin Sivula, Prof. Raffaella Buonsanti, Prof. Mónica Lira-Cantú, and Prof. Emilio Palomares for being the part of the jury and for dedicating their precious time to read and to evaluate my thesis.

I would like to convey my sincere gratitude to the past and present GMF members as well as the visitors for all the time we have spent together to collaborate, to have interesting discussions, and to do many activities outside the laboratory. Particularly, I would like to express my exceptional acknowledgement to Prof. Giulia Grancini for the collaboration and the guidance since the beginning of my PhD study. I really appreciate all of those lively and deep scientific discussion as well as your personal support during my PhD study. I have learned a lot of things from you, Giulia. I cannot thank you enough, grazie mille! I am also very grateful to Dr. Nikita Drigo, Cansu Igci, Dr. Valentin Queloz, Dr. Hiroyuki Kanda, and Dr. Inés García-Benito for all of their hard work and fruitful collaboration. This work would not be possible without your contribution. My gratitude also goes to Dr. Maria Cristina Momblona Rincón and Dr. Cristina Roldán-Carmona for all of the interesting discussion about work and also many other things. Thanks for the hikes, travels, lunches, dinners, and many other activities. I am grateful to my friend, Dr. Valentino Romano, for all the positive vibe and motivation during your stay at EPFL. Also, thank you for the Italian lesson that you gave. I would like to thank Mousa, Nadja, Alex, Ryosuke, Paek, Cho, Martina, Aron, Rui, and many-many other GMF members for creating a pleasant atmosphere in the group and making my stay enjoyable. I am also grateful to have amazing secretaries in our group, Géraldine Gfeller and Isabel Wild. Thank you for all of your help in assisting the administrative stuffs, sending the samples, and organizing various group activities.

I am very thankful to have wonderful collaborators from the other groups and institutions. Completion of this thesis would not be possible without all your efforts and advices. I am grateful to Rodrigo Szotak and Prof. Ana Flavia Nogueira from University of Campinas (Brazil) as well as Dr. Ahmad R. Kirmani and Lee J. Richter from National Institute of Standards and Technology (USA) for their hard work, particularly in the GIWAXS experiments, interpretation, and discussion. I would like also to thank my collaborators from Potsdam University (Germany): Dr. Pietro Caprioglio, Dr. Martin Stolterfoht, and Prof. Dieter Neher for the profound photophysical characterizations. I want to express my gratitude to Yvonne J. Hofstetter and Prof. Yana Vaynzof from Technical University of Dresden (Germany) for performing the UPS characterizations and analyses. I acknowledge Dr .Vellaichamy Joseph and Prof. Ming-Chou Chen from National Central University (Taiwan) for providing high quality hole-transporting materials. I am also thankful to Dr. Olga A. Syzgantseva from Lomonosov Moscow State University (Russia) for performing complex and exhaustive molecular simulation. I am grateful to Dr Pascal Schouwink and Dr. Mounir as well as the other EPFL staffs from both Valais and Lausanne campus for all the support

Finally, I would like to express my deep gratitude to my parents and family for their unconditional love, support, and encouragement. Without your support, I would not be able to pass all the difficult situation I encountered during my PhD study. I am also very grateful to my best friend, Victor Purnomo, for hearing all my problems and for becoming a great travel companion. I would like to thank my friend, Febri Baskoro and Lucia Dewi Santoso, for your support as well as all the interesting discussions we have together.

Thank you everyone!

Albertus Adrian Sutanto
Sion, July 2021

Abstract

Perovskite solar cells (PSCs) based on metal halide materials have become the rising star in the photovoltaic (PV) field since the first discovery in 2009. A remarkable advance in this technology has been demonstrated by reaching a certified power conversion efficiency (PCE) of over 25%, closing the gap with the well-established silicon-based PV. However, the instability under the operation condition hinders the commercialization of PSCs. In order to overcome this issue, interface engineering has been proposed as a solution not only to solve the stability issue but also to improve the PV performance. Thus, the works presented in this thesis are mainly focused on the interfacial design of PSCs and the investigation of the processes therein which could control the device lifetime as well as the PV performance.

A two-dimensional (2D)/three-dimensional (3D) interface has been demonstrated as an effective strategy to realize stable and efficient PSCs. Nevertheless, the fundamental understanding of the 2D/3D interface in determining the stability and performance of PSCs is still vague. Hence, I designed 2D/3D perovskite interfaces based on the thiophenealkylammonium halide cations as the building block for the 2D perovskite. The evolution of the 2D to quasi-2D perovskite phase was observed during the aging process. Only 2D/3D interface incorporating 2-thiopheneethylammonium iodide (2-TEAI) maintained the initial 2D phase. Further, in-situ grazing incidence wide-angle X-ray scattering (GIWAXS) experiments were performed to probe the structural evolution of the 2D/3D interface under thermal stress. This study confirmed that regardless of the 2D phase evolution, the 2D layer serves as a protecting layer for the 3D perovskite underneath.

Following up this work, three analogous 2-thiophenemethylammonium cations with different halides (2-TMAX, X: Cl, Br, I) were incorporated in the 2D/3D interface. 2-TMAI and 2-TMABr 2D/3D interfaces showed a transition to the *p-n* junction, while 2-TMACl 2D/3D exhibited a slight energetic mismatch. The favorable energy level alignment, especially in the case of 2-TMABr 2D/3D, is beneficial for hole extraction and electron blocking. Thus, eliminating the interfacial recombination by yielding zero interfacial loss and high open-circuit voltage with a PCE approaching 21%.

In addition, a Lewis base containing a phosphine oxide group, tris(5-((tetrahydro-2*H*-pyran-2-yl)oxy)pentyl)phosphine oxide (THPPO), has been employed at the interface. THPPO effectively passivated the undercoordinated Pb^{2+} defect by forming a coordinate bond, enhancing the photoluminescence (PL) intensity and carrier lifetime. Therefore, improved PCEs

of 13.31% and 20.70% were achieved in hole-transporting layer (HTL)-free and *n-i-p* structured PSCs, respectively.

Finally, new hole-transporting materials (HTMs) have been explored due to their important roles in preventing charge accumulation and recombination at the interface as well as in maintaining device stability. Carbazole and thiophene-based HTMs functionalized with triphenylamine groups were chosen due to their facile and low-cost synthesis. Car[2,3] and BT-4D demonstrated the best PV performance among the carbazole and thiophene series with maximum PCE of 19.23% and 19.34%, respectively. Remarkably, the BT-4D-based device exhibited excellent long-term stability by maintaining 98% of its initial PCE after 1186 h of continuous illumination.

Keywords

Photovoltaic, perovskite solar cells, interface, recombination, passivation, stability, 2D perovskite, 3D perovskite, Lewis base, hole-transporting materials.

Resumé

Les cellules solaires pérovskites (PSC) basées sur des matériaux d'halogénure métallique sont devenues l'étoile montante dans le domaine du photovoltaïque (PV) depuis leur première découverte en 2009. Une avancée remarquable de cette technologie a été démontrée en atteignant un rendement de conversion de puissance certifié (PCE) de plus de 25 %, comblant ainsi l'écart avec le PV au silicium bien établi. Cependant, l'instabilité dans les conditions de fonctionnement entrave la commercialisation des PSC. Afin de surmonter ce problème, l'ingénierie d'interface a été proposée comme une solution non seulement pour résoudre le problème de stabilité mais aussi pour améliorer la performance du PV. Ainsi, les travaux présentés dans cette thèse sont principalement axés sur la conception interfaciale des PSCs et l'étude des processus qui pourraient contrôler la durée de vie du dispositif ainsi que la performance du PV.

Une interface bidimensionnelle (2D)/tridimensionnelle (3D) a été démontrée comme une stratégie efficace pour réaliser des PSCs stables et efficaces. Néanmoins, la compréhension fondamentale de l'interface 2D/3D dans la détermination de la stabilité et de la performance des PSCs est encore vague. J'ai donc conçu des interfaces de pérovskite 2D/3D basées sur les cations d'halogénure de thiophènealkylammonium comme élément constitutif de la pérovskite 2D. L'évolution de la phase pérovskite 2D à quasi-2D a été observée pendant le processus de vieillissement. Seule l'interface 2D/3D incorporant l'iodure de 2-thiophèneéthylammonium (2-TEAI) a maintenu la phase 2D initiale. De plus, des expériences in situ de diffusion de rayons X à grand angle en incidence rasante (GIWAXS) ont été réalisées pour étudier l'évolution structurelle de l'interface 2D/3D sous contrainte thermique. Cette étude a confirmé qu'indépendamment de l'évolution de la phase 2D, la couche 2D sert de couche protectrice pour la pérovskite 3D sous-jacente.

Suite à ce travail, trois cations 2-thiophenemethylammonium analogues avec différents halogénures (2-TMAX, X : Cl, Br, I) ont été incorporés dans l'interface 2D/3D. Les interfaces 2D/3D 2-TMAI et 2-TMABr ont montré une transition vers la jonction p-n, tandis que l'interface 2D/3D 2-TMACl a montré un léger décalage énergétique. L'alignement favorable des niveaux d'énergie, en particulier dans le cas de 2-TMABr 2D/3D, est bénéfique pour l'extraction des trous et le blocage des électrons. Ainsi, la recombinaison interfaciale est éliminée, ce qui permet d'obtenir une perte interfaciale nulle et une tension en circuit ouvert élevée avec un PCE proche de 21 %.

De plus, une base de Lewis contenant un groupe oxyde de phosphine, l'oxyde de tris(5-((tétrahydro-2H-pyran-2-yl)oxy)pentyl)phosphine (THPPO), a été employée à l'interface. Le THPPO a efficacement passivé le défaut Pb^{2+} sous-coordonné en formant une liaison de coordination, améliorant l'intensité de la photoluminescence (PL) et la durée de vie des porteurs. Par conséquent, des PCE améliorés de 13,31 % et 20,70 % ont été obtenus dans les PSC sans couche de transport de trous (HTL) et à structure *n-i-p*, respectivement.

Enfin, de nouveaux matériaux de transport de trous (HTM) ont été explorés en raison de leur rôle important dans la prévention de l'accumulation et de la recombinaison des charges à l'interface ainsi que dans le maintien de la stabilité du dispositif. Les HTM à base de carbazole et de thiophène fonctionnalisés avec des groupes triphénylamine ont été choisis en raison de leur synthèse facile et peu coûteuse. Car[2,3] et BT-4D ont démontré la meilleure performance PV parmi les séries de carbazole et de thiophène avec un PCE maximum de 19,23% et 19,34%, respectivement. De manière remarquable, le dispositif à base de BT-4D a montré une excellente stabilité à long terme en conservant 98% de son PCE initial après 1186 h d'illumination continue.

Mots clés

Photovoltaïque, cellules solaires en pérovskite, interface, recombinaison, passivation, stabilité, pérovskite 2D, pérovskite 3D, base de Lewis, matériaux de transport de trous.

Symbols and Abbreviations

°C	degree Celcius
$<\tau>$	average lifetime
α	field dependence parameter
2-MP	2-mercaptopyridine
2-TEAI	2-thiopheneethylammonium iodide
2-TMABr	2-thiophenemethylammonium bromide
2-TMACl	2-thiophenemethylammonium chloride
2-TMAI	2-thiophenemethylammonium iodide
2D	two-dimensional
3-TMAI	3-thiophenemethylammonium iodide
3D	three-dimensional
5-AVAI	5-ammoniumvaleric acid iodide
5FBzAI	perfluorobenzylammonium iodide
Å	angstrom
AFM	atomic force microscopy
AL	active layer
ALD	atomic layer deposition
AM	air mass
AMP	(aminomethyl)piperidinium
AMPY	(aminomethyl)-pyridinium
APPI	atmospheric pressure photoionization
ASTM	American Society for Testing and Materials
AU	arbritary unit
AVA	ammonium valeric acid
BA	butylammonium
BABr	*n*-butylammonium bromide
BAI	butylammonium iodide
BDA	1,4-butanediamine
BIPV	building integrated photovoltaic
c-TiO_2	compact-TiO2

C_{60}	fullerene
CAI	cyclopropylammonium iodide
CB	conduction band
CBM	conduction band minimum
CIGS	cadmium indium gallium selenide
cm	centimeter
CV	cyclic voltammetry
D4TBP	D-4-*tert*-butylphenylalanine
DAI	dodecylammonium iodide
DCM	dichloromethane
DFT	density functional theory
DJ	Dion-Jacobson
DMF	dimethylformamide
DMSO	dimethyl sulfoxide
DPV	differential pulse voltammetry
E	electric field
E_b	electron binding energy
E_g	band gap
EPA	Environmental Protection Agency
EQE	external quantum efficiency
ESI	electrospray ionization
ETL	electron-transporting layer
ETM	electron-transporting material
EU	European Union
eV	electronvolt
EVA	poly(ethylene-co-vinyl acetate)
FA	formamidinium
FAI	formamidinium iodide
FEA	pentafluorophenylethylammonium
FF	fill factor
FPEAI	2-(4-fluorophenyl)ethyl ammonium iodide
fs	femtosecond
FS	forward scan
FTO	fluorine-doped tin oxide

GGA	generalized gradient approximation
GID	grazing incidence diffraction
GIWAXS	grazing incidence wide-angle X-ray scattering
GWh	gigawatt-hour
h	Planck constant
h	hour
HA	hexylammonium
HABr	*n*-hexylammonium bromide
HAD	1,6-hexamethylenediamine
HI	hysteresis index
HOMO	highest occupied molecular orbital
HRMS	high resolution mass spectrometry
HTAB	*n*-hexyltrimethylammonium bromide
HTL	hole-transporting layer
HTM	hole-transporting material
Hz	hertz
i-BA	isobutylammonium
I-V	current-voltage
$IC_{60}BA$	indene-C_{60} bisadduct
IDIC	indacenodithiophene end-capped with 1,1-dicyanomethylene-3-indanone
IEA	International Energy Agency
IEC	International Electrotechnical Commission
I_{in}	incident power
IP	ionization potential
IPA	isopropanol
IPCE	incident photon-to-electron conversion efficiency
IPFB	iodopentafluorobenzene
I_{ph}	photocurrent
ISOS	International Summit on Organic PV Stability
ITO	indium-doped tin oxide
J-V	current density-voltage
J_o	saturation current density
J_{ph}	photogenerated current density

J_{SC}	short-circuit current density
K	Kelvin
k_B	Boltzmann constant
KPFM	Kelvin-prove force microscopy
kV	kilovolt
L	liter
Li-TFSI	Li-bis(trifluoromethanesulphonyl) imide
LUMO	lowest unoccupied molecular orbital
M	molar
m	meter
MA	methylammonium
mA	milliampere
MABr	methylammonium bromide
MAI	methylammonium iodide
MALDI	matrix-assisted laser desorption/ionization
MD	molecular dynamics
meV	millielectronvolt
mg	milligram
MHz	megahertz
min	minutes
mM	millimolar
mmol	millimol
MOF	metal organic framework
mp-TiO_2	mesoporous-TiO2
MPP	maximum power point
MPPT	maximum power point tra king
MS	mass spectrometry
mV	millivolt
mW	milliwatt
n	number of the inorganic layer in 2D or quasi-2D perovskite
n-BA	*n*-butyl ammonium
n-BAI	*n*-butyl ammonium iodide
NC	nanocrystal
nF	nanofarad

nJ	nanojoule
nm	nanometer
NMA	naphtylmethylammonium
NMR	nuclear magnetic resonance
NS	nanosheet
ns	nanosecond
NW	nanowire
OABr	*n*-octylammonium bromide
OAI	octylammonium iodide
ODA	1,8- octanediamine
OFET	organic field effect transistor
OPV	organic photovoltaic
P3HT	poly(3-hexylthiophene)
PA	pentylammonium
PBE	Perdew-Burke-Ernzerhof
PCBM	phenyl-C_{61}-butyric acid methyl ester
PCE	power conversion efficiency
PDA	1,3-propane-diamine
PDMA	phenylenedimethanammonium
PEA	phenylethylammonium
PEAI	phenylethylammonium iodide
PeDA	1,5-pentamethylenediamine
PEDOT:PSS	poly(3,4-ethylenedioxythiophene) polystyrene sulfonate
PL	photoluminescence
PLQE	photoluminescence quantum efficiency
PLQY	photoluminescence quantum yield
PMA	phenylmethylammonium
P_{max}	maximum power
PMMA	poly(methyl methacrylate)
ppm	part per million
PS	polystyrene
ps	picosecond
PSC	perovskite solar cell
PTAA	poly[bis(4-phenyl)(2,4,6-trimethylphenyl)amine]

PV	photovoltaic
PVD	physical vapor deposition
PVDF-TrFE	polyvinylidene-trifluoroethylene
PVP	polyvinylpyrrolidone
PWh	petawatt-hour
q	elementary charge
QD	quantum dot
QFLS	quasi-Fermi level splitting
QTOF	quadrupole time-of-flight
q_{xy}	scattering observed in the plane of the substrate
q_z	scattering observed out-of-plane with respect to the substrate
r	radius
R	large organic cation
RH	relative humidity
RP	Ruddlesden-Popper
rpm	rotation per minute
RS	reverse scan
s	second
S	siemens
SBA	spiro bisacridine
SD	standard deviation
SEM	scanning electron microscopy
SFM	scanning force microscopy
spiro-OMeTAD	2,2,7,7-tetrakis(*N*,*N*-di-*p*-methoxyphenylamine)-9,9-spirobifluorene
STC	standard test condition
T	temperature
t	time
TA	transient absorption
tBP	4-tert-butylpyridine
Tc	crystallization temperature
TCO	transparent conducting oxide
T_d	decomposition temperature
t_G	Goldschmidt tolerance factor
TGA	thermogravimetric analysis

THF	tetrahydrofuran
THP	tetrahydropyran
THPPO	tris(5-((tetrahydro-2*H*-pyran-2-yl)oxy)pentyl)phosphine oxide
T_m	melting temperature
TMPP	tetraisopropyl methylenediphosphonate
TOPO	tri-*n*-octylphosphine oxide
TPA	tryphenylamone
TPPO	triphenylphosphineoxide
TrPL	transient photoluminescence
TWh	terrawatt-hour
U	surface potential
UPS	ultraviolet photoelectron spectroscopy
UV	ultraviolet
UV-vis	ultraviolet-visible
ν	frequency
V	Volt
v/v	volume per volume ratio
VB	valence band
VBM	valence band maximum
V_{OC}	open-circuit voltage
W	watt
w/v	weight per volume ratio
WBH	wide bandgap halide
WHO	World Health Organization
XPS	X-ray photoelectron spectroscopy
XRD	X-ray diffraction
XTOF	xerographic time-of-flight
θ	diffraction angle
λ	wavelength
μ	mobility
μ_o	mobility at zero field strength
µg	microgram
µL	microliter
µm	micrometer

μs	microsecond
Φ_{ph}	photon flux
$\Psi_{ph,\lambda}$	spectral photon flow incident on the solar cell

Contents

List of Figures

List of Tables

Chapter 1: Introduction

The ever-increasing energy consumption has become a critical issue in the society globally. The International Energy Agency (IEA) reported the total electrical energy consumption for 2018 reaching 24738.9 TWh with an expected continuous growth for the upcoming years.[1] Fossil-based fuels, such as coal, oil, and gas, are still dominating as the source of the electrical generation up to date.[2] However, the use of fossil-based fuels raises a lot of concerns in the society, mainly due to their negative impact to the environment, especially the generation of greenhouse gasses which contribute significantly on the climate change.[2] Consequently, there is an urgent need in implementing a carbon-neutral energy source as an alternative to the fossil-based fuels.

As one of the most environmentally friendly energy sources with an abundant availability on the planet, solar energy plays a very promising role for a clean energy conversion. The total global technical potential of solar energy is estimated to be 613 PWh per year.[3] This amount surpasses the current demand of the electrical energy, nevertheless, according to the data reported by IEA only 554382 GWh was utilized for electricity generation in 2018.[4] The tremendous availability of solar energy opens the possibility to solve energy crisis and provide a carbon-neutral energy. Photovoltaic (PV) technology or solar cell is one of the most promising candidates among the other technologies which allows a direct and clean conversion of sunlight to electricity.

PV technology itself is not a new technology, it has been existing around us for decades. Since the first PV cell based on silicon was demonstrated by Daryl M. Chapin, Calvin S. Fuller and Gerald L. Pearson back in 1954, scientists together with industries have been refining the technology extensively which enables us to harvest the energy from sun reliably and efficiently.[5] Nowadays, we can enjoy an efficient PV cell with the power conversion efficiency (PCE) of 26.7% for mono-crystalline (in heterojunction structure) and 22.3% for multi-crystalline silicon wafer-based technology which is over 4 times higher compared to 6% on the first discovery.[5, 6] So far, PV market has always been dominated by silicon wafer-based solar cell with a total production share of 95%.[7] Apart from the superior reliability and efficiency of silicon-based solar cell, it requires highly pure silicon crystals as a very slight presence of impurities will cause a deleterious effect on its performance.[8] Additionally, the fabrication of silicon solar cells involves an energy-intensive process.[8]

Many other PV technologies have emerged following the success of crystalline silicon solar cells. Thin-film solar cells, also commonly known as the second-generation PV, are

developed as alternatives to the crystalline silicon technology. These solar cells are fabricated from films that are much thinner than the wafers that constitute the crystalline silicon solar cells.[9] Thin-film PV technologies can be classified as III-V technology (e.g., GaAs, GaP, InP, InAs, and complex alloys from III-V materials), chalcogenide solar cells (e.g., cadmium indium gallium selenide (CIGS) and CdTe), and thin-film silicon solar cells. The thin-film solar cells were initially proposed as a solution for low-cost PV technology in comparison with the crystalline silicon solar cells. However, the recent decline of the crystalline silicon wafer's price makes the solar cells based on thin-films becoming less viable economically.[9]

The urge of developing PV technologies with low-cost materials drives a lot of efforts in finding new materials which are economically feasible. Organic materials as well as hybrid organic-inorganic materials have risen as the center of attention in PV technology recently because of their potential for realizing a low-cost PV. The solar cells technologies based on such materials are named as the third generation PV. In the earlier development stage of these PV technologies, organic solar cells and dye-sensitized solar cells were extensively investigated, however, less attention is given nowadays due to their low efficiency and also low stability. In 2009, hybrid organic-inorganic perovskite made its debut in the photovoltaic field. The first solar cell using the organic-inorganic perovskite material as the light absorber demonstrated a low power conversion efficiency of 3.8% due to the use of a liquid electrode which accelerated the perovskite degradation.[10] One of the major breakthroughs in the perovskite solar cells (PSCs) was achieved by replacing the liquid electrolyte using a solid-state organic hole-transporting material (HTM), namely 2,2,7,7-tetrakis(*N*,*N*-di-*p*-methoxyphenylamine)-9,9-spirobifluorene (spiro-OMeTAD).[11, 12] Nowadays, a maximum PCE exceeding 25% has been attained in a laboratory-scale device, making the PSCs technology is on par with the silicon-based solar cells which are currently the market leader in the photovoltaic industry.[6]

In addition to their high photovoltaic performance, organic-inorganic perovskites have demonstrated many advantages for photovoltaic applications in comparison with the other materials. First, PSCs can be fabricated by various deposition processes, such as solution process (e.g., spin-coating, spray-coating, slot-die coating, blade coating and inkjet printing) and sublimation process by physical vapor deposition (PVD).[13, 14] These versatilities in the PSCs fabrication processes open a promising route for large-scale industrial production. Second, the facile fabrication methods of perovskite will further enable the deposition of the perovskite thin-films on different types of substrates, such as on the flexible substrate for the utilization in wearable devices.[15, 16] Last, semitransparent perovskite thin-films can be produced in different colors by tuning their chemical composition while maintaining decent PCE values which allows

for possible application in the building integrated PV (BIPV), such as the installation for windows, roofs as well as building facades.[17-19]

1.1 Perovskite Materials

1.1.1 Three-dimensional (3D) Perovskite

Three-dimensional (3D) perovskite materials in general are written according to the chemical formula of ABX_3, where A and B are cations with different sizes, and X is an anion (Figure 1.1). More specifically for photovoltaic application, A is a small monovalent organic or inorganic cation (for instance, methylammonium (MA^+), formamidinium (FA^+), or Cs^+), B is a divalent metal cation, such as Pb^{2+} or Sn^{2+}, and X is a halide anion (for example Cl^-, Br^-, or I^-). The 3D perovskite structure forms a cubic crystal structure which consists of the corner-sharing $[BX_6]^{4-}$ octahedra as illustrated in Figure 1.1 . For this reason, the A cation should be small enough to fit in the perovskite lattice in order to maintain the cubic structure of the 3D perovskite.[20] The limit of the A cation size in the ABX_3 perovskite structure is expressed semi-empirically in the Goldschmidt tolerance factor (t_G) as follow:

$$t_G = \frac{(r_A + r_X)}{\sqrt{2}\,(r_B + r_X)} \tag{1.1}$$

where r is the ionic radius. The cubic structure is preserved when the t value is between 0.9–1.0, while a distorted perovskite structure is obtained when the t_G value is between 0.80–0.89.[21] This requirement narrows the A cation size into 2.6 Å.[20] Among the A-site cations used in the perovskite for photovoltaic application, perovskites based on FA, MA, and cesium (Cs) fall within the tolerance factor range as in $FAPbI_3$ (t_G ~ 1), $MAPbI_3$ (t_G ~ 0.9) and $CsPbI_3$ (t_G ~ 0.8), respectively.[22]

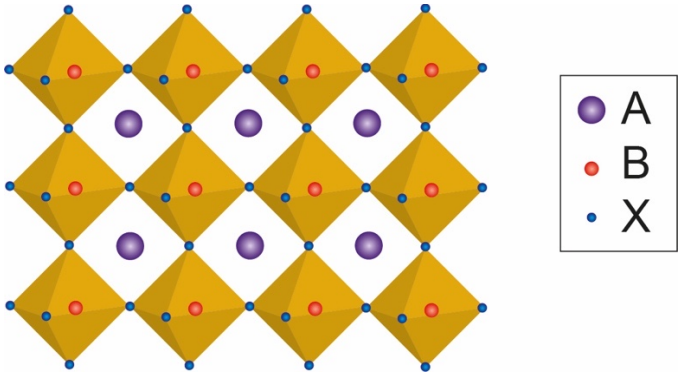

Figure 1.1 Schematic illustration of 3D perovskite structure.

3D perovskite materials have demonstrated excellent optical and electrical properties for their use in the PV devices. Some of the most remarkable properties of 3D perovskite include high extinction coefficients,[23] panchromatic absorption,[24, 25] long carrier diffusion length,[26, 27]

tunable band gap,[28, 29] and high carrier mobility.[30-32] High photovoltaic performance of PSCs can be achieved owing to those notable properties of 3D perovskites. Furthermore, 3D perovskites exhibit a high defect tolerance which allows a high open-circuit voltage (V_{OC}) despite being fabricated using a solution process.[33] However, one of the major bottlenecks in scaling-up and commercializing the PSCs based on the 3D perovskites is the poor stability of 3D perovskites under the operating condition. For instance, MA-based perovskite which has been the pioneer of highly efficient PSCs suffers from its high instability (i.e $MAPbX_3$ decomposes to gaseous methylamine and hydrogen iodide) and its degradation under heat or moisture.[34] On the other hand, $FAPbI_3$ exhibits a higher thermal stability in comparison with $MAPbI_3$, along with the lower band gap, and longer carrier lifetime. However, it forms a non-photoactive yellow δ-phase at room temperature instead of the desired photoactive black α-phase perovskite.[35, 36] Besides, $FAPbI_3$ perovskite demonstrates a poor stability towards humidity and solvents.[35, 36] Thus, many efforts have been explored in order to stabilize the performance of 3D perovskites, such as compositional engineering,[37, 38] interfacial engineering,[39-42] and device encapsulation using a moisture-resistant layer.[43-45]

1.1.2 Low-dimensional Perovskite

Low-dimensional perovskite, particularly two-dimensional (2D) perovskite is another class of perovskite material which is also known as a layered perovskite. It consists of a single or multiple inorganic layers separated by organic spacers and held together by Coulombic forces (Figure 1.2). To form 2D perovskite, a large organic cation (R) is required in the perovskite structure which will serve as the spacer between the inorganic layers.[20] Empirically, 2D perovskites have a general formula of $R_2A_{n-1}B_nX_{3n+1}$ where n denotes the number of the inorganic layer separated by R cations as the organic spacers. When n=1, a pure 2D perovskite phase (R_2BX_4) is obtained where a single inorganic layer is separated by the organic layer (Figure 1.2). On the other hand, a quasi-2D perovskite phase is assembled when there are multiple organic layers (n>1) spaced by the organic layers as shown in Figure 1.2.

The addition of the bulky R cation in the 2D perovskite structure enables the use of the cations which are previously restricted in the 3D perovskite due to the Goldschmidt tolerance factor limitation. Thus, a wide range selection of cations is now available for designing new 2D perovskite materials with the desired properties. Various cations, both aliphatic or aromatic ammonium salts, have been investigated for the 2D perovskite, such as *n*-butylammonium (*n*-BA^+), isobutylammonium (*i*-BA^+), hexylammonium (HA^+), ammonium valeric acid (AVA^+),

phenylmethylammonium (PMA^+), phenylethylammonium (PEA^+), and naphtylmethylammonium (NMA^+).[20]

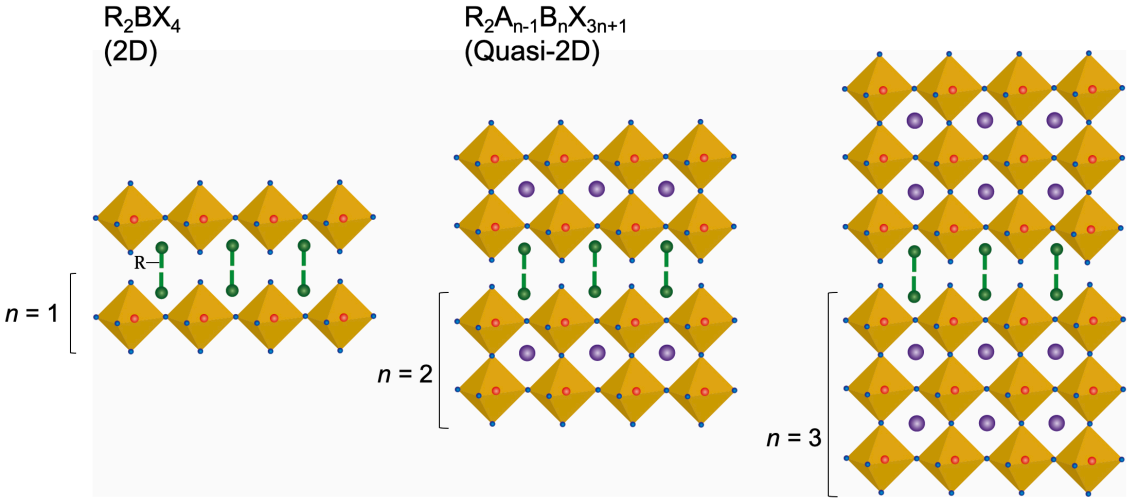

Figure 1.2 Schematic illustration of the low-dimensional perovskite structures.

The structures of 2D perovskite are further classified into Ruddlesden-Popper (RP) and Dion-Jacobson (DJ) phases. The RP perovskites are conceptually derived by cutting the 3D perovskite structure into slabs or inorganic layers with different thicknesses in <100> direction (Figure 1.3a).[46] Each inorganic layer is then sandwiched between bilayers of the bulky R cations. The inclusion of monovalent R cations forms RP perovskites, such as BA^+, pentylammonium (PA^+), HA^+ and PEA^+.[47-49] The RP phase has demonstrated a remarkable thickness (*n* number) control ability which is essential for tuning the optoelectronic properties of the 2D perovskite. So far, most of the 2D perovskites studied and reported in PSCs are based on the RP phase. Similar to RP phase, DJ phase is also obtained by cutting the 3D perovskite structure along with <100> direction and shares the same general formula of $R_2A_{n-1}B_nX_{3n+1}$. However, the inorganic slabs of the DJ phase stack exactly on top of each other as illustrated in Figure 1.3b. The use of divalent R cations will form DJ perovskites, such as 3- and 4-(aminomethyl)piperidinium (3- and 4-AMP^+), 3- and 4-(aminomethyl)-pyridinium (3- and 4-$AMPY^+$), 1,4-phenylenedimethanammonium ($PDMA^+$), 1,3-propane-diamine (PDA), 1,4-butanediamine (BDA), 1,5-pentamethylenediamine (PeDA), 1,6-hexamethylenediamine (HDA), and 1,8-octanediamine (ODA).[50] Recently, DJ perovskites have attracted more attention for photovoltaic applications due to the improved stability and higher conductivity because of the use of divalent cations.

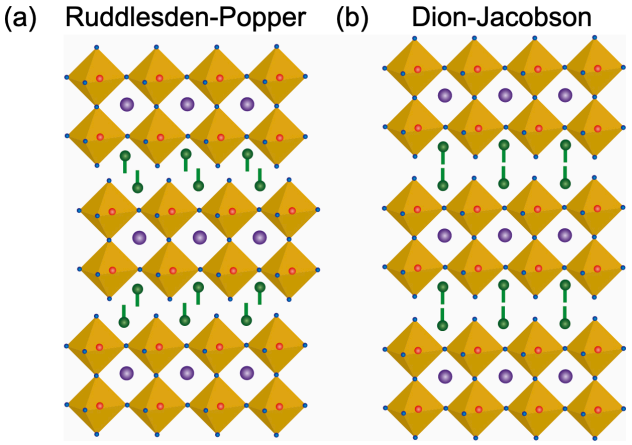

Figure 1.3 Schematic comparison between (a) Ruddlesden-Popper (RP) and (b) Dion-Jacobson (DJ) phase.

2D perovskites have some noticeable differences in the optoelectronic properties compared to the 3D counterpart. 2D perovskites exhibit narrower absorption range due to their large bandgap.[47, 51] The bandgap of 2D perovskites can be tuned by changing the number of inorganic layers (n). By the increasing n values, the bandgap of 2D perovskite will be reduced.[47, 51] Moreover, 2D perovskites show a large exciton binding energy, reaching hundreds of meV, which is caused by the mismatch of dielectric constant between the inorganic and organic layer.[47, 51-55] The exciton binding energy is decreased by increasing the number of inorganic layer (n). These flexible and tunable characteristics of 2D perovskite open the possibility to modify the optoelectronic properties for the device application. Additionally, 2D perovskites with $1 \leq n \leq 2$ show a quantum confinement effect owing to their strong excitonic behavior.[56, 57] This property further contributes to the high photoluminescence (PL) yield of 2D perovskites which might be suitable for light-emitting device application.[56, 57] However, the lower n number 2D perovskites ($1 \leq n \leq 2$) exhibit high exciton binding energy as well as high bandgap, making them less suitable for photovoltaic applications.[20]

The most distinctive property of 2D perovskites is their superior resistance to the moisture. In respect to the 3D perovskite, 2D perovskites have higher stability against moisture due to the hydrophobic nature of the bulky R cation in the crystal structure.[47, 58] Further, 2D perovskites exhibit a dense packing and highly-oriented arrangement which decreases the density of the grain boundary, hence preventing a direct contact between moisture and perovskite surface.[47, 58] The exceptional hydrophobicity of 2D perovskites is very beneficial for the device longevity in PSCs. For instance, $(PEA)_2(MA)_2Pb_3I_{10}$-based perovskite films (n=3) have demonstrated an excellent structural stability under the exposure of 52% relative humidity (RH) for 46 days.[49] However, a low PCE of 4.73% was achieved when it was incorporated in the solar

cells. Kanatzidis and co-workers have investigated quasi-2D perovskite materials based on $(BA)_2(MA)_2Pb_3I_{10}$ (n=3) which showed a remarkable moisture resistance by showing no sign of PbI2 formation as the product of the degraded perovskite after 2 months exposure under 40% RH. Nonetheless, the PSCs fabricated using $(BA)_2(MA)_2Pb_3I_{10}$ suffered from a poor PCE of 4.02%.[51] Some efforts, such as cation engineering and device engineering have been done to push the performance of the PSCs based on the low-dimensional perovskite. Improvements in the PV performance were indeed achieved by manipulating the number of inorganic layers and replacing the cation, for instance, BA with n=4 (PCE = 12.51%),[59] PEA with n=5 (PCE = 14.5%),[60] 2-thiophenemetylammonium with n=3 (PCE = 15.42%),[61] benzylammonium with n=9 (PCE = 17.4%),[62] and 3-bromobenzylammonium with $3 < n < 4$ (PCE = 18.2%).[63] Unfortunately, these values are still far below from the state-of-art 3D perovskite performance.

1.2 Perovskite Solar Cells

1.2.1 Working Principles of PSCs

The working mechanism of PSCs is basically driven by three main processes: (1) charge generation, (2) charge separation, and (3) charge transportation and collection. Figure 1.4 illustrates the working principle of PSCs.

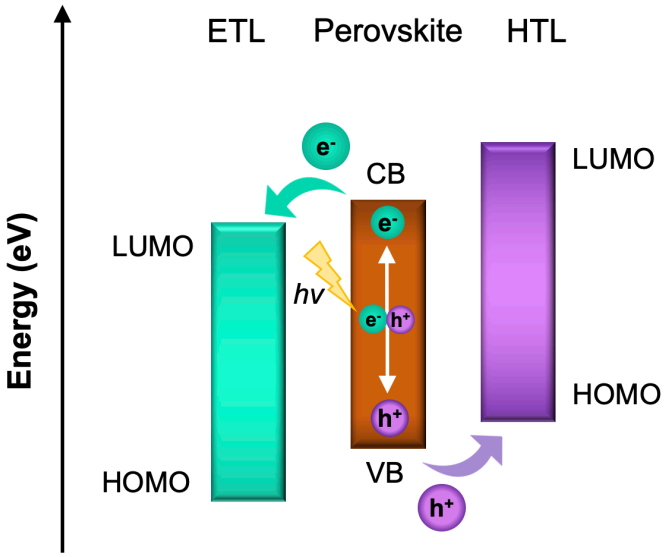

Figure 1.4 Schematic energy level diagram showing the working principles of PSCs.

1.2.1.1 Charge generation

In the first step, the charges are generated by the light harvester upon the exposure to light source. The light harvester must be able to absorb the incoming light in order to produce the photogenerated charges. Thus, the absorption coefficient of the perovskite materials as the light harvester plays an important role in this step. From the previous studies, perovskite materials have demonstrated a remarkable absorption coefficient.[23] In addition to the absorption coefficient, the band gap (E_g) of the perovskite is very essential for the charge generation process. E_g of the perovskite determines the energy of photons that can be absorbed since a semiconductor can only absorb photons with the energy equal to or higher than its E_g. Photons with the energy higher than E_g will further excite the electrons to the energy level higher than the conduction band (CB) of perovskite and these electrons will relax back to the CB quickly by releasing the excess energy in the form of heat. The range of the wavelength that can be absorbed by the perovskite is also attributed to the E_g.

In spite of charge generation process, there are recombination processes that occur in the light harvester which can further affect the solar cells performance.[9, 64] There are four main types of recombination processes commonly found in PSCs:

1. Radiative recombination

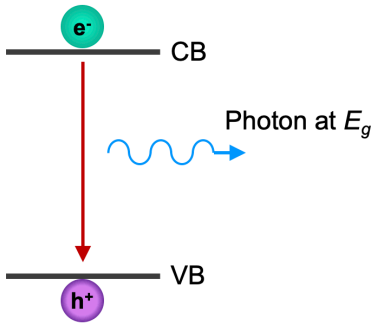

Figure 1.5 Schematic illustration of radiative recombination.

Radiative recombination process principally takes place in direct bandgap semiconductor. For this reason, radiative recombination is often mentioned as direct or band-to-band recombination. During the radiative recombination process, the excited electron in the CB will combine with the hole in the valence band (VB) as illustrated in Figure 1.5. As a result, the recombined hole and electron will release a photon with the energy equal to the bandgap of the semiconductor.[64] For a very high-quality direct bandgap semiconductor (for example GaAs), the radiative recombination of the carriers will determine the limit of the solar cell efficiency.[64] However, most of the solar cells are further limited by the non-radiative

recombination processes, such as defect or trap assisted recombination and Auger recombination (*vide infra*).

2. Defect or trap assisted recombination

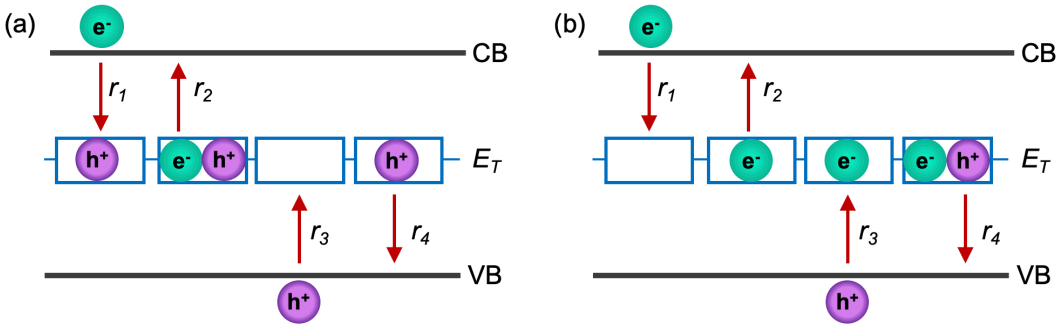

Figure 1.6 Schematic illustration of defect or trap assisted recombination for (a) donor type and (b) acceptor type trap.

Defect or trap assisted recombination is also called as the Shockley-Read-Hall (SRH) recombination, which is named after William B. Shockley, William T. Read, and Robert N. Hall who found the recombination theory back in 1952.[9] Defect assisted recombination is a non-radiative process in which the recombination of electrons and holes does not happen directly from bandgap to bandgap. This recombination is mainly caused by impurities or lattice defects in the semiconductor which leads to the formation of new recombination centers within the bandgap (E_T) which are often referred as trap states.[9]

Recombination centers or trap states could be differentiated into two types: donor type and acceptor type. Donor-type recombination center can trap a hole followed by electron capture from the CB, while acceptor-type recombination center can trap an electron followed by hole capture from the VB (Figure 1.6). These recombination centers result in non-radiative recombination and the excess energy is released as phonons (lattice vibration). Defect assisted recombination generally involves four step processes: r_1 is the electron capture from the CB, r_2 is the electron emission from the CB, r_3 is the hole capture from the VB, and r_4 is the hole emission from the VB.[9]

3. Auger recombination

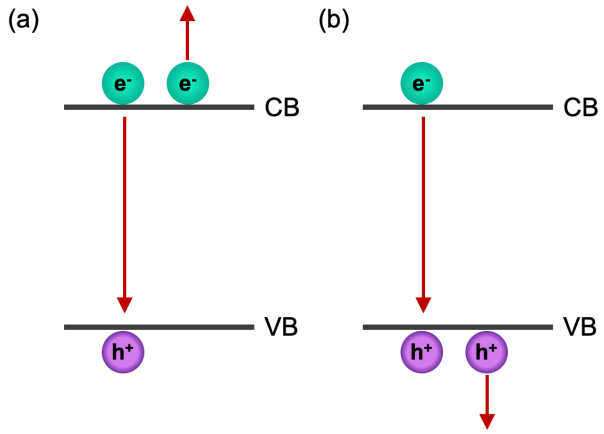

Figure 1.7 Schematic illustration of Auger recombination involving (a) two electrons and (b) two holes.

Auger recombination is a non-radiative process where the energy and momentum of the recombining hole and electron are transferred to another electron or hole.[9] Compared to the radiative and defect assisted recombination where two particles (an electron and a hole) participate in the process, Auger recombination involves three particles. If the third particle is an electron, it will be excited to the higher level of the CB followed by a relaxation process to the CB by transferring its energy in phonons and finally thermal energy (Figure 1.7a). Meanwhile, if the third particle is a hole, it will be excited to the lower level of VB followed by a rise back to the VB by transferring the energy in phonons (Figure 1.7b).[9] Auger recombination generally occurs in the semiconductor with indirect bandgap where the direct bandgap to bandgap recombination is very limited or not possible.[9] For semiconductors with indirect bandgap, Auger recombination is the dominant recombination process and it becomes the efficiency-limiting factor in high purity Si and Ge solar cells.[64]

4. Surface, interface, and grain boundary recombination

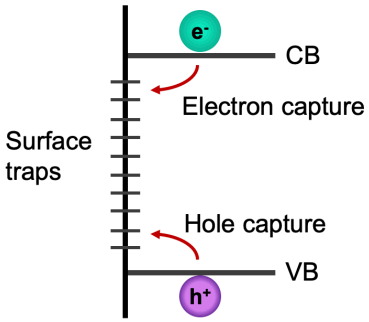

Figure 1.8 Schematic illustration of surface recombination.

The three recombination mechanisms discussed previously are classified as the bulk recombination processes which occur inside the bulk of the semiconductor. However, surface defect such as dangling bonds and absorbed impurity on the surface of the material could create a high density of trap states (Figure 1.8).[9, 64] Also, the interfaces between two different layer of semiconductors and the high-angle grain boundary in the polycrystalline materials could serve as the recombination centers.[64] These kinds of defects will induce the recombination similar to SRH process.

1.2.1.2 Charge separation

The photogenerated charges need to be separated into electrons (negative charges) and holes (positive charges) before they can be extracted and collected. The photogenerated charges can present in the form of excitons or free carriers depending on the permittivity of the materials. In order to generate free electron and holes that will contribute to the photocurrent, the photogenerated charges need to overcome the exciton binding energy (E_b). Low E_b values (lower than thermal energy at room temperature of 26 meV) are preferred in PV for an efficient charges dissociation to obtain free carriers. For instance, the studies on $MAPbI_3$ perovskite show that the E_b values of this class of material vary from 2 meV to 75 meV at room temperature.[65] The E_b values of $MAPbI_3$ is influenced by the grain size, where the single crystals $MAPbI_3$ exhibit the highest E_b values.[66]

1.2.1.3 Charge transportation and collection

After the photogenerated charges are separated into free carriers, electrons and holes will move within the semiconductor. In PSCs, charge selective contact are used to direct electrons and holes to the respective electrodes (anode and cathode). There are two types of charge selective contact which are commonly used in PSCs: electron-transporting layer (ETL) and hole-transporting layer (HTL). As the name suggests, ETL selectively transports the electrons and blocks the hole, while HTL selectively transports the hole and blocks the electron. In the device application, the perovskite layer is generally sandwiched between the ETL and the HTL.

The energy level alignment between the perovskite and charge selective contact is one of the most important parameters to ensure the charge transportation. For ETL, the lower occupied molecular orbital (LUMO) of the ETL must be deeper than the conduction band (CB) of perovskite to assure the electron extraction, while the higher occupied molecular orbital

(HOMO) of the ETL should be low enough so that the holes could not be transported to the ETL. For HTL, the HOMO of the HTL must be higher than the valence band (VB) of the perovskite to ensure the hole extraction, while the LUMO of the HTL should be high enough to block the electron transfer. The other important parameters for the ETL and HTL are the charge mobility and the conductivity of the materials. The electron or hole mobility is defined as how fast the electron or hole can be transported through the selective contact layer, while the conductivity of the materials is characterized as the product of the number of charges and the mobility. After the electron and holes are transported through the ETL and HTL, they are collected in the corresponding electrodes.

1.2.2 Device Architectures in PSCs

In the solar cells, perovskite layer is generally sandwiched between the charge selective contacts (ETL and HTL) and the electrodes. There are two main types of PSCs device architecture depending on how the ETL and HTL are in contact with the perovskite and electrode: normal (*n*-*i*-*p*) structure and inverted (*p*-*i*-*n*) structure. The schematic illustration of the PSCs architectures is displayed in Figure 1.9.

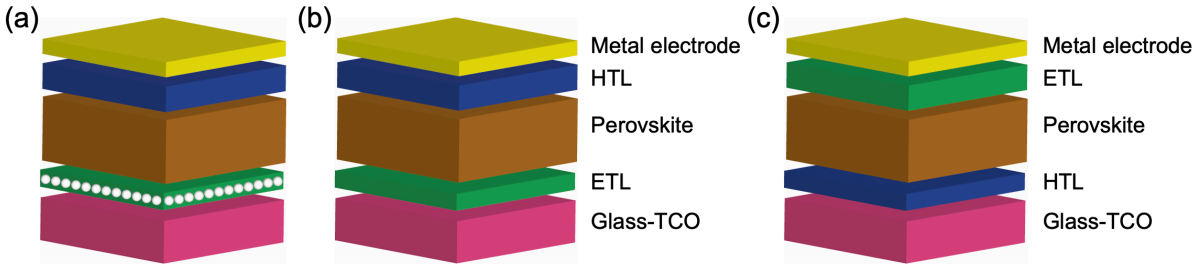

Figure 1.9 Schematic illustration of PSCs device architectures: (a) normal mesoscopic structure, (b) normal planar structure, and (c) inverted structure.

1.2.2.1 Normal (*n*-*i*-*p*) structure

In the normal structure, the perovskite is sandwiched between ETL and HTL in which the ETL is in contact with the front transparent conducting oxide (TCO) electrode, such as fluorine-doped tin oxide (FTO) or indium-doped tin oxide (ITO), and the HTL is in contact with the back-metal electrode, such as gold (Au) or silver (Ag). Since in the normal structure the light needs to propagate through the ETL first before reaching the perovskite layer, a transparent *n*-type semiconductor, such as TiO_2 and SnO_2, is commonly used as the ETL. Further, there are two different configurations of the normal structure: mesoscopic and planar configuration. Mesoscopic-configured PSCs employ a mesoscopic layer of nanoparticles, for

example TiO_2 nanoparticles, as a scaffold on the ETL side. The mesoscopic TiO_2 layer could improve the electron collection on the ETL and relieve the PSCs from the hysteresis effect.[67, 68] This mesoscopic structure is actually derived from the dye-sensitized solar cells (DSSCs) configuration. On the contrary, the mesoscopic layer is absent in the normal PSCs structure with planar configuration allowing a simpler device architecture.

1.2.2.2 Inverted (*p-i-n*) structure

In the inverted PSCs structure, the contact of the charge selective layer (ETL and HTL) with the electrodes are configured in the opposite way of the normal structure. The HTL is in contact with the front transparent conducting electrode, while the ETL is in contact with the back-metal electrode. A transparent *p*-type semiconductor, such as NiO_x, poly[bis(4-phenyl)(2,4,6-trimethylphenyl)amine] (PTAA), or poly(3,4-ethylenedioxythiophene) polystyrene sulfonate (PEDOT:PSS), is usually coated on top of the TCO to allow the light reach the perovskite layer without any major loss.[69] Inverted structure gives more flexibility in the device application since most of the charge selective layers used could be processed using low temperature which opens more diverse application of PSCs, for instance the development of PSCs on flexible substrates.

1.2.2.3 Other configurations

Apart from the widely used normal and inverted type PSCs, there are some other modified device structures based on these two conventional configurations. The modifications are commonly carried out in order to simplify the device architecture towards a cost-effective fabrication process. For instance, HTL-free PSCs has been demonstrated with the PCE of over 15% by passivating perovskite-gold electrode interface.[42] Similarly, ETL-free PSCs combined with interface engineering technique has been reported with the PCE of over 21%.[70] Another breakthrough in the engineering of the device structure is the use carbon-based materials to replace the costly metal back-electrode.[71] Despite the lower material cost, carbon-based material can be easily deposited through the solution processing methods, such as printing and doctor blading which further ease the fabrication process.[71]

1.2.3 PSCs Characterizations

1.2.3.1 Current density-voltage (*J-V*) characteristics

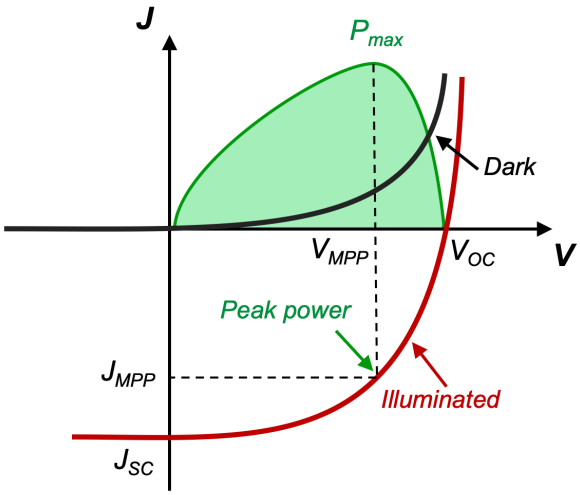

Figure 1.10 J-V characteristic of solar cells under dark and light illumination.

The photovoltaic parameters of PSCs are determined from the *J-V* characteristics of the device measured under illumination. To obtain reliable *J-V* characteristics, the solar cells measurement must be carried out under the standard test conditions (STC), which means the total irradiance of the light source should be calibrated to 1000 W/m^2. Additionally, the spectrum of the light source should match with the air mass (AM) 1.5 spectrum. The AM1.5 spectrum is defined as the spectrum of the solar irradiance when the surface facing the Sun is tilted at 37° to the horizontal plane.[9] Moreover, the temperature of the solar cells should be kept under the standard room temperature (25°C) during the measurement.[9]

The main parameters in the *J-V* characterization include the short-circuit current density (J_{SC}), the open circuit voltage (V_{OC}), the fill factor (*FF*), and the maximum power (P_{max}). The J_{SC} is described as the current density flowing through the external circuit when both electrodes are short circuited. A mask with a fixed aperture is normally used to determine the illuminated area so that an accurate J_{SC} value could be obtained under the STC. Next, the V_{OC} is defined as the voltage when there is no current flowing through the external circuit. Basically, V_{OC} indicates the maximum voltage that can be reached in the solar cells. The V_{OC} value depends on the photogenerated current density (J_{ph}) and the saturation current density (J_o) which can be derived from the following equation:

$$V_{OC} = \frac{k_B T}{q} \, ln\left(\frac{J_{ph}}{J_0}\right) \tag{1.2}$$

where k_B is the Boltzmann constant, T is the temperature, and q is the elementary charge.[9] J_{ph} commonly shows a small variation. However, the J_o value might vary by orders of magnitude since it is affected by the recombination process happening in the solar cells.

The FF is denoted as the ratio between the maximum power (P_{max}) generated by the solar cells and the product of V_{OC} and J_{SC} as expressed in the equation below:

$$FF = \frac{P_{max}}{V_{OC}\, J_{SC}} = \frac{V_{mpp}\, J_{mpp}}{V_{OC}\, J_{SC}} \tag{1.3}$$

where V_{mpp} and J_{mpp} indicate the voltage and current density at the maximum power point (MPP).[9] MPP is defined as the point on the *J-V* characteristics where the solar cells show the maximum power output. Finally, we can calculate the power conversion efficiency (PCE) of the solar cells based on the parameters mentioned above. PCE value is obtained from the ratio between the maximum power generated by the solar cells and the incident power (I_{in}):

$$PCE = \frac{P_{max}}{I_{in}} = \frac{V_{OC}\, J_{SC}\, FF}{I_{in}} \tag{1.4}$$

where under STC, I_{in} is the incident light with AM1.5 spectrum characteristic and irradiance of 1000 W/m².[9]

1.2.3.2 External Quantum Efficiency (EQE)

The external quantum efficiency (EQE) is the number of incident photons that are converted into hole-electron pairs in the light harvester and successfully collected on the electrodes. The EQE is usually expressed as a function of the wavelength (λ) and measured by illuminating the solar cells with monochromatic light with a specific wavelength of λ and recording the photocurrent (I_{ph}) response from the solar cells. Thus, the EQE value can be derived from the following equation:

$$EQE\ (\lambda) = \frac{I_{ph}(\lambda)}{q\ \Psi_{ph,\lambda}} \tag{1.5}$$

where q is the elementary charge and $\Psi_{ph,\lambda}$ is the spectral photon flow incident on the solar cells.[9] The photon flow value is obtained by measuring the EQE of a calibrated reference photo diode under the same light source. The EQE spectrum can be evaluated to understand the optical and electrical losses due to the parasitic absorption and recombination.

The EQE spectrum also could be used to calculate the J_{SC} of the solar cells provided the measurement is carried out under short circuit condition. Generally, the calculation of the J_{SC} value from EQE spectrum is carried out to verify the J_{SC} value obtained from the *J-V* measurement. The J_{SC} of the solar cells is calculated by integrating the EQE values in respect to

the photon flux (Φ_{ph}) of AM1.5 spectrum across all the corresponding wavelength as expressed in the following equation:[9]

$$J_{SC} = -q \int_{\lambda_1}^{\lambda_2} EQE(\lambda)\, \Phi_{ph,\lambda}^{AM1.5}\, d\lambda \qquad (1.6)$$

1.3 Limiting Factors in Perovskite Solar Cells

Although a high PCE comparable to the existing commercially available PV technology (such as Si-based PV) has been achieved in the PSCs, most of the highly performing PSCs only can be found in a laboratory scale. They are generally fabricated and tested under a strictly controlled environment, for instance in an inert atmosphere. This controlled environment undeniably differs from the actual operation condition, raising some critical issues related to the device durability, the environmental impact, and ultimately the commercialization process. The major limiting factors which can hinder the real-world application of PSCs include:

1.3.1 Toxicity

All of the highly efficient PSCs are fabricated using lead (Pb)-based perovskite materials as the light harvesting layer. The Pb content in the perovskite materials bring up serious toxicological and ecological issues as Pb itself is harmful for human health and environment. Pb poisoning could cause severe disease, such as anemia, hypertension, kidney damage, and neurological disorder. Further, Pb exposure in children and pregnant women could induce a serious intellectual retardation and behavioral problems.[72] The presence of more than 5 μg/dL of lead in the blood is categorized as lead poisoning.[73] The European Union (EU) has recently tighten the limit of the maximum Pb content in the drinking water to 5 μg/L.[74] The new regulation is half of the standard recommended by the World Health Organization (WHO), indicating that Pb toxicity is a very serious concern for the society. Additionally, lead iodide salt (PbI_2), the main chemical constituting the lead halide perovskite material, is highly soluble in water. Thus, increasing the risk of Pb leaching from the perovskite solar panel caused by the rainwater in case there is any leakage or breakage in the solar panel.

The dangerous contamination risk due to Pb poisoning urges the researcher to explore lead-free perovskite materials. Tin (Sn)-based perovskites are one of the most lead-free perovskite materials widely used in PSCs because of their similar properties to Pb-based perovskite and their potential in achieving high PV performance.[75] Different composition has been explored for Sn-based perovskite, for example, methylammonium tin iodide ($MASnI_3$), formamidinium tin iodide ($FASnI_3$), and cesium tin iodide ($CsSnI_3$). However, Sn-based

perovskites are generally very susceptible to the ambient air exposure, inducing the oxidation of Sn^{2+} to Sn^{4+}. Low dimensional perovskites have been introduced in order to suppress the degradation of Sn-based perovskites.[76] So far, the highest reported PCE for tin-based perovskite is 10.6%.[77] In fact, the precursor of Sn-based perovskite, SnI_2, is more toxic than PbI_2 due to increased acidification by the formation of HI.[78] However, the immediate decomposition of Sn^{2+} to Sn^{4+} which later converted to SnO_2 makes Sn-based perovskites less toxic than the Pb-based analogues.[75, 78] In addition, lead-free perovskites based on germanium (Ge),[79, 80] bismuth (Bi),[81, 82] indium (In),[83, 84] antimony (Sb),[85, 86] and silver (Ag)[87, 88] are tested for PSCs. Nonetheless, their PV performances are still inferior compared to the Sn-based PSCs.

Recently, a "safe-by-design" approach for developing legally and ethically responsible PSCs has been proposed to minimalize the Pb contamination risk. For instance, metal organic frameworks (MOFs) have become one of the viable options due to their capability in adsorbing Pb in the polluted water.[89, 90] Huckaba et al. reported the use of a porous MOF scaffold combined with a polymeric binding agent to sequester the lead from the aqueous solutions containing decomposed PSCs. The treated water was then exhibited a low lead contain below the lead threshold determined by environmental protection agency (EPA) for the drinking water.[89] Besides, Wu et al. incorporated a 2D conjugated thiol-containing MOF directly in the perovskite-metal electrode interface. The leaching test on the PSCs demonstrated that the MOF can adsorb over 80% of the leaked Pb by forming water-insoluble solids.[90] The encapsulation of PSCs using a self-healing polymer-based material has also been studied to reduce the lead leakage from the damaged perovskite solar module.[91] The combination of these "safe-by-design" approach should be integrated to make PSCs more environmentally safe and sustainable for the real-world application.

1.3.2 Stability

Long-term stability is a very important key to be considered parallel to the PCE in order to provide an economically feasible PV technology. To date, the benchmark of the solar modules' lifetime is mainly based on the silicon-based modules. The existing silicon-based solar modules have the average lifetime expectancy of 20-25 years. The industrial standards of stability testing procedure are currently based on the International Electrotechnical Commission (IEC) standards: IEC 61215. Some of the important tests according to IEC 61215 include outdoor exposure test, hot-spot endurance test, UV preconditioning, thermal cycling test, wet leakage current test, static mechanical load test, and hail test.[92] However, industrial testing procedure generally imposes a stricter standard than IEC 61215. For instance, to ensure a minimum 25 years

module lifetime of silicon-based solar panel, it needs to pass 500 thermal cycles in comparison with the 200 thermal cycles in IEC 61215.[92]

IEC 61215 standard has been adopted for testing the durability of PSCs under the operating condition.[20] Additionally, EIC 61646 standard for testing thin-film PVs has been implemented for PSCs. According to EIC 61646 standard, the testing should be carried out on the solar cells at 85°C under continuous 1-sun illumination. The solar cells must not exhibit more than 20% efficiency depletion over 1000 h to pass the test. This accelerated testing condition simulates 25 years equivalent of 1-sun illumination over 54,750 h with the assumption of 6 h of full sunlight intensity exposure every day.[20] Besides, modified stability testing standard for organic photovoltaic (OPV) based on International Summit on Organic PV Stability (ISOS) protocols has been recently proposed to standardize the stability measurement of PSCs.[93]

To fulfill the aforementioned stability testing procedures, it is noteworthy to understand the origin of PSCs instability. Primarily, the stability of PSCs is determined by both extrinsic and intrinsic factors. The extrinsic factors are mainly influenced by the environmental condition, such as the presence of moisture and oxygen. Encapsulation has been proposed as an immediate solution to overcome the instability due to the contact with the ambient air.[94] The intrinsic factors in PSCs stability are commonly related to the stability of the perovskite layer itself, the stability of the charge-transporting layers (ETL or HTL), the interface between the perovskite and the adjacent layer, and electrode degradation.[94] However, the intrinsic instability of one or more components in PSCs, such as the hygroscopicity, thermal instability, photo instability, and ion migration can induce an accelerated device degradation when it is further triggered by the extrinsic factors.[94, 95] The detailed discussion on the PSCs stability against various extrinsic and intrinsic factors is explained as follow.

1.3.2.1 Thermal Stability

PSCs should demonstrate an excellent thermal stability because the operating temperature of the solar cells in the field may reach over 85°C or even a very low temperature of -40°C, depending on the location.[96, 97] $MAPbI_3$ perovskite has been reported to decompose into gaseous methylamine (MA) and hydroiodic acid (HI), leaving only PbI_2 in the thin-film upon a heat stress at 85°C even under an inert N_2 atmosphere.[98] A further interaction with the moisture or ambient air will further accelerate the degradation process. The low thermal stability of $MAPbI_3$ makes this material less suitable for long-term operation at elevated temperature. Thus, in a quest for finding a more thermally stable perovskite materials, a less volatile cation is introduced in the perovskite structure to replace MA^+.

A heavier and bigger FA^+ cation was then incorporated in the perovskite structure as $FAPbI_3$. Eperon et al. reported that $FAPbI_3$ demonstrated an improved thermal stability compared to $MAPbI_3$, upon heating at 150°C in air for 1 h.[99] Further, $FAPbI_3$ exhibits a low bandgap of 1.47V, enabling a broader absorption range which is beneficial in enhancing the PV performance.[35] However, the photoactive black phase of α-$FAPbI_3$ is obtained at the temperature of 150–185°C and this black phase is not stable at room temperature.[36, 100] The α-$FAPbI_3$ phase will immediately change to the non-photoactive yellow phase of δ-$FAPbI_3$ at room temperature.[36, 100] Compositional engineering has been proposed as an effective solution to overcome the instability of α-$FAPbI_3$ at room temperature. The incorporation of multiple cations in the A site of perovskite structure have successfully improved the stability of α-$FAPbI_3$ phase at room temperature. Various combination of cations ranging from double cation (FA and MA),[101] triple cation (FA, MA, and Cs),[38] to quadruple cation (FA, MA, Cs, and Rb)[37] have been validated in improving not only the stability but also the PV performance of PSCs.

Furthermore, all inorganic perovskites, such as $CsPbI_3$ and $CsPbBr_3$, are reported to have a good thermal stability.[102, 103] However, similar to the $FAPbI_3$ counterpart, the photoactive black phase of those perovskites is only stable at high temperature. For instance, $CsPbI_3$ only exhibits the black phase (α-CsPbI3) at temperature of above 310°C while the yellow phase (γ-CsPbI3) is observed at room temperature.[104] Many different efforts have been made to stabilize the black phase of α-$CsPbI_3$ at room temperature, including solvent-additives engineering, alloying-element doping, and 2D nanocrystal engineering.[104]

1.3.2.2 Moisture Stability

The presence of moisture in the ambient air is undeniably one of the external factors that has the biggest implication on the PSCs' long-term stability. In principle, water can infiltrate to the perovskite lattice and disrupting the integrity of the perovskite structure.[105-107] The penetration of water molecules induces the formation of hydrated perovskite phases which will further dissolve the organic species, followed by the evaporation of the volatile species and finally decomposing the perovskite structure into PbI_2.[96] Various studies have been carried out to unveil the perovskite degradation mechanism due to moisture. So far, extensive investigations on the $MAPbI_3$ decomposition upon exposure to the moisture have been reported.

The decomposition of $MAPbI_3$ perovskite due to the moisture at the macroscopic level is simply indicated by the color change of the film from dark brown to yellow. Yang et al. investigated the moisture-induced degradation kinetics of the $MAPbI_3$ films by exposing them under the atmosphere with different relative humidity (RH) values.[106] A total decomposition

was observed when the film was kept under high RH atmosphere (80-100%) for 6 days. However, only a minimal degradation was noticed after several days of contact with the lower RH ambient air of 20%.[106] The UV-Visible (UV-Vis) absorption of the perovskite film were monitored using in situ experimental setup during the exposure under humidity. The absorption spectral features at higher-energy (< 500 nm) exhibited a continuous and fast decrease when the film was kept under the humid air.[106] The absorption onset at 760 nm which corresponded to the bandgap of the $MAPbI_3$ perovskite was steadily became less visible showing the similar spectral features of PbI_2.[106] Further, Yang et al. demonstrated that under high RH condition the perovskite evolved to the intermediate phase before it was fully decomposed to PbI_2 from grazing-incidence wide-angle x-ray scattering (GIWAXS) results.[106]

Leguy et al. performed a more detailed study on the formation of the intermediate phase during the degradation of $MAPbI_3$.[105] They proposed that $MAPbI_3$ turned into a colorless intermediate film which was found to be the monohydrate phase ($MAPbI_3.H_2O$) before finally leaving only PbI_2 behind.[105] This phase is reversible upon drying of the film. However, irreversible decomposition will occur upon the long exposure of the film in the significantly humid environment where the grains have been fully converted into monohydrate phase.[105] Despite the structural disintegration, the contact between moisture and $MAPbI_3$ perovskite film also causes morphological changes. Scanning force microscopy (SFM) and atomic force microscopy (AFM) analyses reveal the increase in the surface roughness and the decrease in the grain size.[105, 108] It is important to note that these morphological degradations are irreversible upon the drying of the film.

Additionally, moisture contamination affects the photophysical properties and the charge carrier dynamic of the perovskite film. Song et al. monitored the evolution of the perovskite films under nitrogen gas containing 80% RH of water vapor using photoluminescence (PL) study.[109] During initial contact with the moisture, water molecules form hydrogen bonds with the uncoordinated bonds on the perovskite surface and grain boundary of the $MAPbI_3$ film. Here, the water molecules act as passivating agent to the surface traps of the perovskite resulting in the improvement of both PL intensity and carrier lifetime. As the RH value increases, the water molecules build up on the surface creating a continuous layer. The water layer on the perovskite surface delocalizes the electron and increases the free electron density by 6 orders of magnitude (from ~10^{14} to ~10^{20} cm^{-3}) in period of 4 to 50 min. The large electron density on the surface then increases the non-radiative recombination rate and decreases the PL intensity. Further, the presence of the water on the surface also induces *n*-type doping which creates a donor energy level within the bandgap. Once the water vapor saturates

on the perovskite crystal surface, the monohydrate perovskite phase is formed. Due to its large bandgap of 3.1 eV, the monohydrate phase passivates the surface which results in the enhancement of PL intensity. While a certain amount of moisture is beneficial for the defect passivation, an excessive amount of water vapor gives negative impact to the perovskite stability. As the water penetrated into the bulk, the decomposition process begins. At this stage, $MAPbI_3$ becomes photo-inactive which is observed by the absence in the photogenerated carrier and complete loss in the PL intensity.

Although cation engineering can improve the thermal stability of the perovskite, it may behave differently under the moisture. For instance, $FAPbI_3$ have demonstrated a better thermal stability at high temperature compared to $MAPbI_3$ as discussed in the previous section. However, $FAPbI_3$ does not exhibit a better moisture stability than $MAPbI_3$. The presence of moisture will induce the destabilization of the black phase and accelerate the formation of the yellow δ-phase.[96] The incorporation of Cs in the $FAPbI_3$ perovskite have demonstrated the enhancement in the moisture stability. For instance, the incorporation of 10% Cs^+ in $FAPbI_3$ perovskite exhibited a stable black phase absorption spectra after 4h exposure to the 85% RH at room temperature.[110] Further, Wang et al. implemented mixed-cation and mixed-halide perovskite with the composition of $FA_{0.83}Cs_{0.17}Pb(I_{0.6}Br_{0.4})_3$ in the solar cells.[111] The devices showed an improved stability in PCE after 650h continuous 1-sun illumination even under the ambient condition, compared $MAPbI_3$ device which only survived for less than 100 h.[111] Despite the enhancement in the stability against moisture, multiple-cation perovskite, such as triple-cation perovskite (FA, MA, and Cs), shows an analogous degradation mechanism to $MAPbI_3$. The presence of hydrate water on the surface leads to a recrystallization process and formation of a more uniform perovskite with less impurities, resulting in the improvement of device performance.[112] On the other hand, the existence of bulk water will trigger the decomposition pathway.[112]

Furthermore, the presence of the moisture does not only deteriorate the perovskite layer, but also the hole-transporting layer (HTL). Most of the organic HTMs, such as spiro-OMeTAD, need to be doped in order to improve their hole transporting capability (hole mobility and conductivity).[113, 114] Li-bis(trifluoromethanesulphonyl) imide (Li-TFSI) is widely used as a dopant in HTM, however, it is hygroscopic in nature.[113] Upon the exposure to the moisture, the water molecules will interact with Li-TFSI resulting the formation of pinholes in the HTL which further degrade the photovoltaic performance of PSCs.[113-115]

1.3.2.3 Photo Stability

As mentioned in Section 1.2.2, titanium dioxide (TiO_2), either in a compact or mesoscopic form, is widely used as an ETL to achieve highly-efficient electron extraction in a normal (*n-i-p*) structure PSCs. However, TiO_2 is also well-known as a photocatalyst for the oxidation of water to produce OH radical as well as for the oxidation of other organic materials.[116] The photocatalytic activity of TiO_2 could induce the degradation of perovskite material under UV light exposure.[117] Ito et al. has reported a PCE deterioration of $MAPbI_3$-based PSC under a continuous light illumination for 12 h due to the TiO_2 photocatalytic activity.[117] The decomposition mainly took place at the TiO_2 and $MAPbI_3$ interface, where $MAPbI_3$ was degraded to gaseous MA (CH_3NH_2) and HI. Only PbI_2 remained in the device, causing a major PV performance degradation.[117]

Further, Leitjen et al. carried out a further investigation on the correlation of TiO_2 and device stability under UV-light illumination.[118] They proposed that there are many oxygen vacancies especially at the surface of TiO_2 which will act as deep electron-donating sites. These electrons could interact with the oxygen molecules from the atmosphere resulting in the oxygen adsorption to the vacancy sites. When the electron-hole pairs are generated in the presence of UV light, the electron at the oxygen adsorption sites will recombine with the hole in valence band by desorbing the oxygen. On the other hand, the electrons generated in the perovskite will go to the conduction band of TiO_2 or to the deeper surface trap. Then, the remaining free-electron in TiO_2 will recombine with the holes in spiro-OMeTAD side. Al_2O_3 nanoparticles were then used to replace TiO_2 resulting and improved long-term stability for 1000 h at 40°C.[118] Recently, the incorporation of bilayer ETLs by coating SnO_2 layer on top of compact TiO_2 layer have successfully demonstrated an enhanced long-term device stability under UV light illumination.[119]

In addition to the influence of UV light exposure, the photoinduced degradation of perovskite film have been studied under the white light illumination. The initial evidence of the $MAPbI_3$ decomposition under white light illumination in vacuum is marked by the color change of the film from black to gray.[120] $MAPbI_{3-x}Cl_x$ and $MAPbBr_{3-x}Cl_x$ also suffered from the similar photoinduced degradation process upon under white light illumination in an ultra-high vacuum condition.[121] The UV-vis absorption spectra revealed that the absorption onset at 760 nm was diminished, followed by a significant drop of absorbance between 400-600 nm upon exposure to the white light.[120-122] This effect becomes less noticeable when MA^+ is replaced with other cations, such as FA^+ or Cs^+.

Besides, the long-term exposure under white light could induce the rupture of the perovskite structure. Tang et al. have studied the effect of the illumination on the perovskite structure using in situ XRD.[120] PbI_2 and metallic Pb were observed on the $MAPbI_3$ films after a prolongated exposure of white light condition under high vacuum condition.[120] Moreover, Yang et al. also demonstrated the decomposition of perovskite into PbI_2 and metallic Pb using various mixed cations and mixed halides perovskites, such as $MAPb(I_{0.83}Br_{0.17})_3$, $FA_{0.83}MA_{0.17}Pb(I_{0.83}Br_{0.17})_3$, and $Cs_{0.1}(FA_{0.83}MA_{0.17})_{0.9}Pb(I_{0.83}Br_{0.17})_3$.[123] Additionally, under the operation condition, the sunlight exposure will gradually increase the device temperature which will induce a further thermal degradation of PSC as explained in section 1.3.2.1.

1.3.3 Cost

One of the most important factors in realizing a commercially feasible PSCs is the material costs. In spite of the low materials cost of the perovskite layer, the cost for the hole-transporting materials (HTMs) could be the major bottleneck for the production cost. First, the HTM used to generate highly efficient PSCs is generally based on spiro-OMeTAD or PTAA which is very expensive.[124-126] For instance, a high purity of spiro-OMeTAD is required to achieve a high PCE. However, the tedious purification processes are required to obtain a highly pure spiro-OMeTAD which has a major drawback: a high synthetic cost.[127-129] Thus, many alternative HTMs synthetized with low-cost starting materials and shorter synthetic steps are explored to find a low-cost yet efficient HTM. A further detailed discussion on the alternative HTMs will be continued in Chapter 6 of this thesis.

Additionally, the material used for the metal electrodes could contribute to the higher cost of PSCs. To deliver a highly efficient PCE, an expensive metal, gold, is commonly used as the metal electrode in PSCs due to its excellent electrical conductivity, appropriate work function, and superior long-term stability in comparison with the other metals.[130] There are some less expensive metals with high conductivity which can be used as an alternative of gold, such as silver (Ag),[110, 131] aluminum (Al),[132, 133] chromium (Cr),[134] and copper (Cu).[135] However, some of these materials have exhibited reduced stability compared to gold.[130] For instance, Ag and Al could interact with perovskite forming the metal halides.[118, 136-138] The formation of metal halides is accelerated at high temperature and applied electric field. These metal halides species, such as silver iodide, are resistive in nature, hindering the charge transfer from the adjacent layer. Moreover, the formation of the metal halides will induce an iodide deficiency in the perovskite layer.[96] Many attempts on replacing the metal electrode with carbon-based electrode

also have been done to achieve both low material cost and stable device performance.[71] PSCs employing the carbon-based electrode has demonstrated a promising PCE of 19.2%.[139]

1.3.4 Towards Shockley-Queisser Limit

Shockley-Queisser limit is defined as the maximum PCE could be attained by a single junction solar cell for a specific light illumination spectrum.[140] The calculation of the Shockley-Quisser limit was formulated for the first time on *p-n* junction solar cells by William Shockley and Hans-Joachim Queisser in 1951.[141] Several assumptions were made in order to define the maximum PCE of solar cells. First, the only recombination pathway existed on an ideal solar cell is the radiative recombination, determining the upper limit of the minority carrier lifetime.[142] Second, only the photons with the energy higher than the band gap of the semiconductor will be converted into electron-hole pairs with 100% quantum efficiency, while the photon with energy lower than the band gap will not be converted. The detailed band gap-dependent maximum PCE limit of a single junction solar cells under the standard AM1.5G illumination (ASTM G173-03) at 25°C is summarized in Figure 1.11.[140]

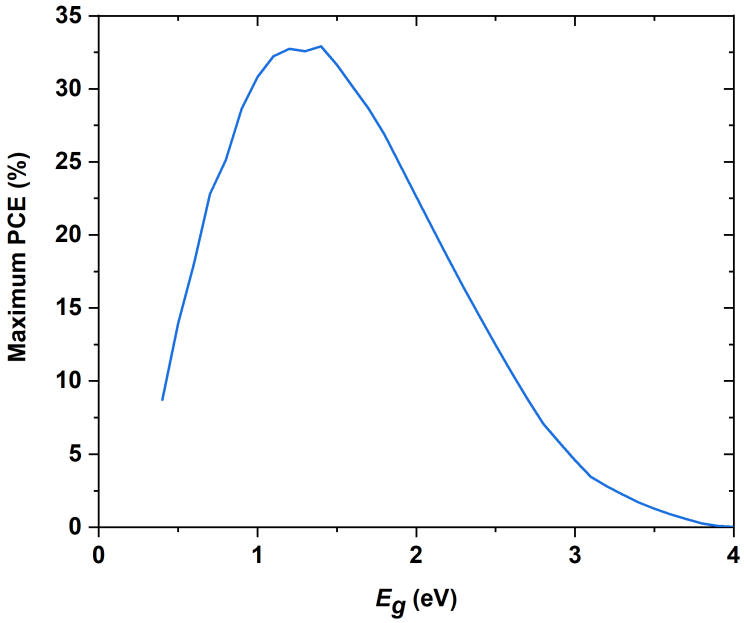

Figure 1.11 Shockley-Queisser limit of solar cells with different band gap operated under illumination of AM1.5G spectrum (ASTM G173-03) at 25°C. The figure is plotted based on the tabulated data from reference.[140]

Based on the data in Figure 1.11, perovskite materials, such as $FAPbI_3$ and $MAPbI_3$ with the band gap of ~1.4–1.5 eV,[143, 144] should be able to reach the maximum PCE of over 31% theoretically. Although PSCs have demonstrated a very high PCE of over 25% in the laboratory scale for the past decade, this value is still below the theoretical limits. Non-radiative recombination process caused by the defect or trap sites in the perovskite is one of the limiting factors in approaching the Shockley-Queisser limit. These defects present both in the bulk and at the interface of perovskites.[145] Many factors could induce the formation of the defect sites, such as impurities, point defects (e.g., vacancy and interstitial defects in the crystal lattice), and dangling bonds on the surface or grain boundary.[146-149]

Defect passivation has been proposed as a solution to suppress non-radiative recombination. Many attempts have been done to passivate the defect sites. For instance, interface passivation has recently become popular technique to improve the photovoltaic performance of PSCs.[149, 150] This interface passivation could be achieved by introducing an interlayer between perovskite and the adjacent layer, such as ETL or HTL.[149] Various materials have been explored for the interface passivation including small organic molecules, polymers, and graded perovskite interfaces.[149] A further discussion on the interface passivation will be presented on Chapter 2 of this thesis.

1.4 Motivation and strategy

PSCs have taken the research in the photovoltaic domain into the next level. A promising advance in PSCs' photovoltaics performance has been demonstrated for the last ten years. However, the limiting factors discussed in Section 1.3 are the main hindrance for the commercialization. Thus, it is essential to integrate the development of PSCs by taking those critical issues into account. By keeping this idea in mind, I focus the works in my thesis to address some of those issues, specifically interface and stability. First, the interface between perovskite and HTL are very crucial in determining the photovoltaic performance. The presence of the defects on the perovskite's surface results in the formation of the trap state, triggering non-radiative recombination process which is detrimental for the photovoltaic performance. Interfacial engineering by introducing an interlayer between perovskite and HTL has been seen as a viable strategy to passivate those defects. Interestingly, the material properties of that interlayer could be tuned in a such way that it acts as a barrier, protecting the perovskite layer underneath from the external factor (such as moisture) and improving the long-term device stability. Second, the stability issue also could be tackled by a smart molecular design of the HTM without compromising the photovoltaic performance.

In the next four chapters of this thesis, extensive and comprehensive investigation on the interface will be presented. Based on the literature search and analyses on various interfacial engineering techniques, I started my investigation on the hybrid multidimensional perovskite structure by incorporating a thin layer of 2D perovskite on top of 3D perovskite. The 2D/3D bilayer structure is chosen because of its ability in passivating the interface and enhancing the device longevity. Firstly, thiophene cations family as the building block for the 2D perovskite were studied by varying the alkyl length and position on the thiophene core. The effect of the 2D perovskite incorporation on the PV performance and the long term-stability under the storage in the ambient atmosphere were thoroughly investigated. Secondly, the stability investigation on the 2D/3D perovskite bilayer were performed using various in situ structural and optical characterizations. Thirdly, a comprehensive study on the surface passivation of 2D/3D perovskite was performed. Owing to the tunability properties of the 2D perovskite, I carefully evaluate the energetic landscape of 2D/3D perovskite interface by modifying the halides on the thiophene cations. Different degree of passivation effect could be achieved by simply tuning the energy level alignment between 2D/3D perovskite interface. Additionally, a passivation strategy using an organic molecule incorporating Lewis base by targeting a specific defect sites was explored.

After realizing the stability and performance improvement of PSCs by means of interfacial engineering, I am motivated to further explore the photovoltaic performance and stability aspect from another point of view. In this case, HTM used in PSCs also holds a crucial role in determining the device's long-term stability as well as in extracting the hole at the surface of perovskite, thus, preventing the nonradiative losses. So far, spiro-OMeTAD still serves as the state-of-art HTM for producing highly efficient PSCs. As explained in Section 1.3, the use of spiro-OMeTAD in PSCs limits the application of PSCs due to its instability and high-cost. Herein, I implement novel molecules based on the thiophene and carbazole molecules as HTMs in PSCs. Those molecules could be obtained with a simple synthetic steps and purification, resulting in a much lower cost compared to spiro-OMeTAD. The energy level alignment and hole-transporting properties are carefully tuned to enable the efficient hole transport. More importantly, the HTMs based on the thiophene and carbazole molecules have successfully demonstrate a superior long-term stability under continuous 1-sun illumination in comparison with spiro-OMeTAD as the benchmark, without sacrificing the PV performance. These results highlight the importance of the molecular design of HTMs in improving the stability of PSCs.

Chapter 2: Photovoltaic Performance and Stability Improvement of PSCs by Interface Engineering

2.1 The Importance of Interface Engineering in PSCs

Interface has always been the crucial factor in improving the performance of solar cells. Since the Si-based solar cells era, interface engineering has been implemented as one of the most important techniques in boosting the photovoltaic performance.[151] The concept of interface engineering also applies the same for PSCs. Moreover, PSCs are constructed of multilayer stacking, specifically there are minimum of 5 layers in the normal (*n-i-p*) configured device structure (see Chapter 1, Section 1.2.2.1). As a consequence, four major interfaces between each layer are formed within the device (i.e., transparent conducting oxide (TCO) electrode/ ETL/perovskite/HTL/metal electrode). Any imperfection on each layer's surface as well as on the contact between two layers could lead to the formation of defects acting as the non-radiative recombination center which is detrimental for the photovoltaic performance. Interface engineering has been considered as a viable solution to relieve the negative effect of the surface defect in PSCs by introducing a new interlayer between two surfaces.[149, 152] Moreover, when the interlayer is introduced on top of perovskite surface, it could provide the first encapsulation of the perovskite layer to the ambient atmosphere. Thus, the ideal interfacial layer is not only designed to mitigate the non-radiative recombination caused by the defect but also to enhance the device stability. In this thesis, the discussion about interface engineering will be limited to the perovskite/HTL interface in the *n-i-p* configured device structure. The roles of the interface engineering to improve the performance and stability of PSCs are further discussed in Section 2.1.1 and 2.1.2 of this chapter.

2.1.1 Photovoltaic Performance Improvement

Perovskite layer is commonly fabricated using solution process at low temperature, forming a polycrystalline perovskite film. As a result, various types of defects are generated in the perovskite layer. The common defects found in perovskite include vacancy (halide or Pb-site vacancy), interstitial (interstitial halide or Pb-site), antisite substitution of halide and Pb, dangling bonds, and grain boundary (Figure 2.1).[145, 149] These defects act as trap sites, inducing non-radiative recombination process which is harmful for PSCs' performance. For instance, the open-circuit voltage (V_{OC}) in the device is theoretically determined by the quasi-Fermi level splitting (QFLS) value of the perovskite absorber.[153] However, the recombination pathway in the

perovskite layer restrains the V_{OC} value of the PSCs below the radiative limit.[153] Despite the fact that perovskites have shown a high defect tolerance compared to the other light-harvesting materials, elimination of the defect by passivation technique is still critical for improving the device operation and performance.[150]

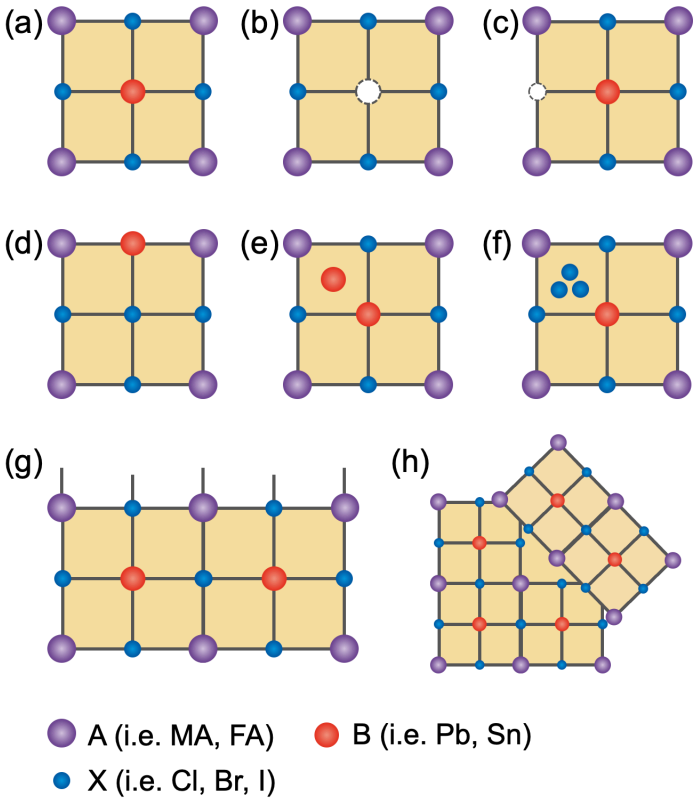

Figure 2.1 Schematic illustration of the possible defects in the perovskite lattice: (a) non-defective lattice, (b) B-site vacancy, (c) X-site vacancy, (d) B-X antisite substitution, (e) interstitial of A, (f) interstitial of X, (g) dangling bonds, (h) grain boundary.

Interface between perovskite and the adjacent layer has been considered as one part in the device which is most prone for the defect formation.[154] This stems true, especially for the perovskite layer deposited by the spin-coating process, because a discontinued crystal structure is formed at the surface.[149] Interface itself holds a very important role in the interfacial charges dynamics (such as charge separation, charge injection, charge collection, and charge recombination) following the charge generation process which happens in the perovskite layer.[152] In particular, for the *n-i-p* configured PSCs, the device is fabricated from bottom (glass-TCO side) to top (metal electrode side) which means the top surface of the perovskite will be in contact directly with the HTL after the perovskite layer deposition. The presence of the defects at the perovskite/HTL interface will directly influence the hole extraction process which could increase the series resistance in the device resulting in reduced J_{SC} and *FF* values.[149] Additionally,

the defects present at the interface are mostly deep-level defects which give larger contribution to the non-radiative recombination losses in comparison with the shallow-level defect in the bulk.[152] Thus, it is necessary to suppress the interfacial defects by engineering of the perovskite/HTL interface in order to boost the performance of PSC.

Passivation is the common term used in the solar cells for any technique used to eliminate non-radiative recombination centers by passivating the defect. Passivation technique actually has been implemented since the development of Si-based solar cells. In PSCs, passivation strategy by interface engineering also has been demonstrated as one of the effective methods to reduce the interfacial losses. Researchers have explored a diverse range of materials for the interface passivation, for example, excess PbI_2, organic ammonium salts, Lewis base, Lewis acid, organic molecules with improved hydrophobicity, wide bandgap materials, and low-dimensional perovskites.[149, 150, 152] Since different types of defects could present at the interface, each passivating agent should be carefully designed to target specific type of defect. A more detailed discussion on the various interface engineering techniques will be presented in Section 2.2.

2.1.2 Stability Improvement

The presence of defect at the interface is not only detrimental for the photovoltaic performance but it also has a negative impact on the stability of PSCs. The degradation process of the perovskite layer has been reported to be started from the grain boundary and interface.[152] Besides, the interaction between perovskite and the adjacent layer contributes to the device stability. Moreover, defects could trigger the unwanted kinetic process, such as ion or molecule migration, which is not desirable for the device longevity.[152] This process will induce the accumulation of ions or charges at the interface which is very disadvantageous for both photovoltaic performance and device stability of PSCs.[152] Hence, passivating those defects is an essential solution to enhance the device performance and stability.

On the other hand, extrinsic factor, such as moisture from the ambient air, also takes part in the degradation process of the perovskite layer. Recently, interface engineering has been also extensively used to provide a permeation barrier by depositing a thin hydrophobic layer on top of perovskite. However, these materials are generally resistive in nature, making the use of both passivation layer and moisture resistive layer less desirable to obtain high photovoltaic performance. Thus, the idea of creating an interfacial layer with the dual functions as permeation barrier and passivating agent has attracted a lot of interests in the field. The materials for interface passivation are then started to be developed to have additional

hydrophobic property in order to tackle both the defect and stability issues. Hydrophobic organic molecules and low-dimensional perovskite are among the best candidates to provide both functions.[149]

2.2 Interface Engineering Techniques

Various interface passivation strategies have been explored to target specific defects at the interface, such as grain boundaries, lattice vacancies, as well as dangling bonds on the perovskite's surface. Nowadays, the ultimate goal of the interface modification has been shifted not only for defect passivation purpose, but also for the stability improvement. Various interface engineering techniques for PSCs are summarized below.

2.2.1 Excess PbI_2

During the early stage of PSCs discovery, the existence of PbI_2 phase in the perovskite film is only considered as the byproduct of the decomposed film which has a negative impact on the PSCs.[155] In 2014, Wang and coworkers studied the carrier dynamics of the perovskite film with different content of PbI_2 using femtosecond transient absorption (fs-TA) technique.[156] They demonstrated the passivation effect of PbI_2 by observing that the film with more PbI_2 content exhibited slower relaxation rate than the one with less PbI_2 content. [156] The slower dynamics indicates the reduction of the trapped charges at the grain boundary of the perovskite due to PbI_2 passivation.[156] Further, Chen et al. evaluated the passivation characteristic of PbI_2 from the energetic point of view.[157] The ultraviolet photoelectron spectroscopy (UPS) reveals that the conduction band minimum (CBM) and valence band maximum (VBM) of PbI_2 are –3.45 and –5.75 eV, respectively, while the CBM and VBM for $CH_3NH_3PbI_3$ perovskite are –3.93 and –5.43 eV, respectively.[157] The larger bandgap of PbI_2 (2.3 eV) in comparison with $CH_3NH_3PbI_3$ (1.5 eV) provides an energy barrier by blocking the carrier transport in the trap states and routing it to the less defective channels present in the film.[157] Additionally, scanning electron microscopy technique (SEM) and scanning kelvin probe microscopy analyses show that PbI_2 is generally located at the grain edge, confirming its effectiveness in passivating the defects in the grain boundary.[157]

Many studies are then focused on the precise control of PbI_2 content in the perovskite film to optimize the passivation effect from PbI_2. Roldán-Carmona et al. used a non-stoichiometric ratio of PbI_2: $CH_3NH_3PbI_3$ in the perovskite precursor solution.[158] The final PbI_2 content in the thin-film is determined by incorporating excess concentration of PbI_2.[158] The presence of PbI_2 in the precursor solution improved the crystallinity of the perovskite film,

resulting in large and homogeneous grain formation.[158] Higher photoluminescence (PL) intensity and slower PL decay of the non-stoichiometric perovskite film indicate the reduction in the trap-assisted recombination due to the improvement of the perovskite grain.[158] The advantageous effect of PbI_2 incorporation to suppress the non-radiative recombination has been also reported in more complex mixed-cation and mixed-halide perovskite compositions, such as $MA_{0.17}FA_{0.83}Pb(I_{0.83}Br_{0.17})_3$ and $Cs_{0.05}(MA_{0.17}FA_{0.83})_{0.95}Pb(I_{0.83}Br_{0.17})_3$.[38, 159] Further, Jiang et al. controlled the excess PbI_2 content in the planar PSC using a sequential-deposition technique.[160] A high PCE of 21% and improvement in the device stability were obtained by incorporating a moderate amount of PbI_2 contents.[160] However, an excessive amount of PbI_2 in the perovskite film will degrade the device's PCE as well as stability due to the accumulation of the electron in the interface.[160] Additionally, double-side PbI_2 passivation on both front- and back-side of perovskite layer also has been demonstrated to further improve the device performance with a stabilized PCE of 22%.[161]

2.2.2 Alkylammonium halide

Alkylammonium halide salts are also popular materials used for surface passivation. This class of materials target both the anion and cation defects on the perovskite surface.[149] Additionally, alkylammonium halide salts create hydrogen or ionic bond with the defective sites, enhancing the passivation effect.[149] Despite the common usage in the perovskite precursor solution, short linear alkylammonium halides salts, such as methylammonium iodide (MAI) and methylammonium bromide (MABr), also could serve as passivating agents. For instance, Son et al. identified that the incorporation of excess MAI in the perovskite precursor formed a thin-layer around the grain boundary, reducing the hysteresis effect.[162] Further, Hawash and co-workers confirm the roles of a very thin MAI layer between perovskite and HTL in improving the energy level alignment which finally increases the PCE of PSCs.[163] The UPS and X-ray photoelectron spectroscopy (XPS) results reveal that MAI dissociates at the interface and the dissociated species tune the interfacial energy level, optimizing the energetic at the perovskite/HTL interface.[163] MAI also could be deposited on top of $FAPbI_3$ perovskite which improves the absorption at longer wavelength due to the formation of a thin-layer of $MAPbI_3$.[164] In addition, Zhang et al. demonstrated grain boundary passivation by a post-treatment of $FAPbI_3$ film using MABr due to MA^+ and Br^- exchange from MABr with FA^+ and I^- from $FAPbI_3$.[165] Although photovoltaic improvement is achieved by incorporating short linear alkylammonium halide salts, the modified perovskite layer is still vulnerable to the moisture degradation. Long chain or bulky ammonium halide salts with improved hydrophobicity are then proposed to

improve the stability. The use of large ammonium halide salts will induce the formation of low-dimensional (2D or quasi-2D) perovskite which will be explained further in Section 2.2.6.

2.2.3 Lewis acid and base

Lewis acids and bases are the other class of materials that could be used to passivate specific type of defects on the perovskite surface. Lewis acid is defined as a molecule or an ion that receives a pair of electrons, while Lewis base is described as a molecule or an ion that donates a pair of electrons.[149] Both Lewis acid and base could form a covalent bonds by sharing the electron pairs resulting in acid-base complex.[149] Therefore, Lewis acid is capable of passivating the defect sites containing lone pairs of electrons, such as halide anions (I^- and Pb-I antisite defect).[149, 150] Meanwhile, Lewis base passivation targets the electron-deficient defects, such as undercoordinated Pb^{2+}.[149, 150] The covalent bonds formed between Lewis acid/base and the defects will eliminate the traps sites originating from the undercoordinated ions, thus, reducing the non-radiative recombination centers and enhancing the photovoltaic performance of PSCs.

Abate et al. demonstrated the use of a Lewis acid, iodopentafluorobenzene (IPFB), for passivating the undercoordinated iodine anions on the perovskite surface.[166] They discovered that the presence of the iodine anions on the surface serves as hole traps which further induces the charges accumulation at the perovskite/HTL interfaces and leads to the faster non-radiative recombination.[166] IPFB passivates those defects by forming bonds from the undercoordinated halides anions as well as screening the electrostatic charge caused by the iodine anions.[166] As a result, a PCE improvement from 13% to 15% could be achieved.[166] Besides, fullerene (C_{60}) and its derivatives are also widely used as Lewis acid passivating agents in addition to their common application as ETLs due to the excellent electron transporting properties.[149, 167, 168] For instance, Shao and co-workers introduced a thin layer of phenyl-C_{61}-butyric acid methyl ester (PCBM) in the planar structured PSCs to passivate the defects caused by iodine anions.[169] The deposition of PCBM on top of perovskite layers effectively decreases the trap density by two orders of magnitude and suppresses the hysteresis effect.[169] Moreover, Liang et al. investigated three different fullerene derivatives: C_{60}, PCBM, and indene-C_{60} bisadduct ($IC_{60}BA$).[170] From this comparison, C_{60} showed the best interface passivation effect among the other fullerene derivatives.[170]

Lewis base passivating agents are generally characterized by the presence of atoms with lone pair electrons in the molecular structure, such as nitrogen,[171, 172] sulfur,[171, 173] oxygen,[174-177] and phosphorous.[176, 177] Noel et al. demonstrated for the first time the Lewis base passivation by

incorporating thiophene and pyridine on top of perovskite surface.[171] The sulfur and nitrogen atom in thiophene and pyridine, respectively, contain lone pair of electrons which could form coordinate covalent bond with the undercoordinated Pb^{2+} defects.[171] By treating the perovskite surface with thiophene and pyridine, the non-radiative recombination has been reduced significantly, indicated from the improvement on the carriers lifetime by approximately an order of magnitude.[171] Consequently, the PCEs were successfully improved from 13% to 15.3% and 16.5% for the PSCs incorporating thiophene and pyridine, respectively.[171] Further, Wen et al. developed a thiophene-based Lewis base, namely 3-hexylthiophene, which is not only boosting the device's PCE to 19.9%, but also significantly enhance the device stability by showing less than 20% degradation of its initial PCE upon 700 h of exposure in the ambient air.[178] In 2016, deQuilettes et al. reported the Lewis base containing phosphine oxide group, specifically tri-*n*-octylphosphine oxide (TOPO).[176] The perovskite thin-film coated with TOPO exhibited extended photoluminescence (PL) lifetime of 8.82 ± 0.03 μs as well as an outstanding PL quantum efficiency (PLQE) of 35 ± 1% owing to the Lewis base treatment.[176] The fluorescence imaging analysis reveals that the large PL improvement was located mostly at the grain boundaries.[176]

More complex Lewis base molecules are then developed to further optimize the passivation effect. Molecules with multiple functional groups are designed to benefit from the synergetic passivation effect compared to the one containing a single functional group. Lin et al. incorporated a thin layer of π-conjugated Lewis base, particularly indacenodithiophene end-capped with 1,1-dicyanomethylene-3-indanone (IDIC).[179] Both O and N atom from the carbonyl and cyano group of IDIC effectively passivate the undercoordinated Pb^{2+} of $MAPbI_3$ perovskite.[179] Further, Zhang et al. explored a bidentate molecule, 2-mercaptopyridine (2-MP), containing sulfhydryl and pyridine leading to the bidentate anchoring to the undercoordinated Pb^{2+} sites.[180] As a result, a strong bonding between 2-MP and the undercoordinated Pb^{2+} was obtained which also improved the moisture stability by preventing the water molecules to reach the perovskite surface due to the strong bidentate anchoring.[180] In addition, Yang et al. designed a new molecule, namely D-4-*tert*-butylphenylalanine (D4TBP), which contains three different functional groups: 4-tert-butylphenyl, amine, and carboxyl.[181] A significant passivation effect was observed by showing a small V_{OC} loss of 0.34 V in respect to the optical bandgap of the perovskite (1.57 eV).[181]

Another important breakthrough in the Lewis acid/base passivation technique is by designing a molecule containing both Lewis acid and base. The obtained zwitterion molecules have demonstrated a more synergetic passivation effect on both positively and negatively

charged defects.[149] Zheng and co-workers explored a series of choline-based molecules.[182] They discovered that L-α-phosphatidylcholine which had phosphate group ($–PO_4^-$) and quaternary ammonium group ($–N(CH_3)^{3+}$) exhibited an improved passivation effect due to the passivation of two different types of defect: undercoordinated Pb^{2+} and Pb-I antisite. Consequently, a V_{OC} loss of 0.39 V was obtained in the *p-i-n* configured PSCs.[182]

2.2.4 Hydrophobic organic layer

Perovskite degradation due to the contact with moisture has raised the concern to improve the hydrophobicity of the perovskite layer by mean of interface engineering in order to improve the stability of PSCs. The hydrophobic organic molecules have been considered as a solution to the stability issue by sandwiching them between perovskite and charge transporting layer. Functionalization of the hydrophobic organic molecules with certain functional groups, such as carbonyl and fluorine, could lead to the defect passivation in addition to the moisture resistance enhancement. Since these materials are generally insulating in nature, only a very thin layer must be applied in the device to avoid the obstruction of the charge transfer process.

The widely used hydrophobic materials for this purpose are based on long chain polymer structures, such as polyvinylpyrrolidone (PVP),[103] poly(methyl methacrylate) (PMMA),[183] and poly(ethylene-co-vinyl acetate) (EVA).[184] Li et al. introduced PVP as an interface passivation on top of $CsPbI_3$ perovskite.[103] The interaction between the perovskite surface and the lone pairs of electrons originating from oxygen and nitrogen of the acylamino group in PVP did not only reduce the nonradiative recombination indicated by the long diffusion length, but also stabilize the stability of $CsPbI_3$'s cubic phase.[103] The stability of the PSC passivated with PVP was also enhanced by retaining 75% of its initial efficiency after keeping the cells under ambient atmosphere with 45-55% RH for 500 h.[103] Further, Zuo et al. used a sequential deposition process by spin-coating PVP and MAI blend on top of PbI_2 film.[185] As a result, a pinhole-free $MAPbI_3$ film passivated with PVP mainly on the surface and grain boundary was obtained.[185] PSCs incorporating PVP exhibited high photovoltaic performance (PCE = 20.2% with V_{OC} = 1.16 V) as well as outstanding stability by retaining 85% of its initial efficiency after 2500 h under RH between 25 to 40%.[185]

Peng and co-workers demonstrated the use of PMMA film for defects passivation in PSCs.[183] They employed PMMA layers on both ETL/perovskite and perovskite/HTL interface. A high V_{OC} of 1.22V was successfully attained by using this strategy, indicating the reduction of the nonradiative recombination pathway which was also supported with the improvement of PL intensity.[183] The passivation effect originated from the carbonyl group present in PMMA,

triggering a Lewis base passivation with the undercoordinated Pb^{2+}.[183] It is worth nothing that an ultra-thin layer of PMMA was used to minimize the series resistance which could have impact on the device's *FF*.[183] Moreover, Huang et al. investigated another interfacial layer based on the EVA to provide a moisture barrier as well as to passivate the surface defects in the flexible *p-i-n* configured PSCs.[184] The increase in PL intensity and lifetime of EVA-treated perovskite film verified the defect passivation effect.[184] Additionally, the water contact angle tests revealed that perovskite film coated with EVA showed a higher contact angle than the control film indicating the improved hydrophobicity of the perovskite surface upon EVA deposition.[184] On the other hand, Wang et al. employed various insulating polymers including Teflon, polystyrene (PS), and polyvinylidene-trifluoroethylene copolymer (PVDF-TrFE).[186] They found that the charges are transported through the insulating polymer layer by a tunneling process.[186] Thus, the thickness of the insulating polymer layer is essential to be kept as thin as possible to ensure an efficient charge transfer.

2.2.5 Wide bandgap materials

Surface passivation technique using wide bandgap materials have been widely used in Si-based solar cells.[149] For instance, SiO_2, SiN, and amorphous silicon are employed as passivation layers in Si-based solar cells due to their wider bandgap in comparison with silicon.[149] Inspired from this technique, wide bandgap materials are also applied in PSCs for passivation purpose. In PSCs, wide bandgap passivating agents ranging from inorganic oxides, wide bandgap perovskites, quantum dots (QDs), nanocrystals (NC), nanowires (NW) to nanosheets (NSs) have been reported.[149, 152]

Koushik et al. used atomic layer deposition (ALD) method to deposit an ultra-thin wide bandgap inorganic oxide on top of perovskite layer, particularly Al_2O_3.[187] A 1 nm-thick Al_2O_3 layer was introduced in order to allow the hole transport through tunneling.[187] The PSCs passivated with Al_2O_3 layer exhibited enhanced photovoltaic performance (mainly the V_{OC}) and reduced hysteresis effect.[187] The introduction of Al_2O_3 layer in PSCs also provide an extra barrier to the moisture, leading to the significant improvement in the long-term stability by maintaining 70% of the initial PCE after 70 days exposure in the humid environment with RH of 40-70%, while the control device only retained 12% of its initial PCE.[187] Meanwhile, Bai and co-workers developed a new method by encapsulating the perovskite grains inside oligomeric silica matrix in a core-shell geometry.[188] Defects at the perovskite surface and grain boundaries were suppressed considerably in accordance with the improvement of PL lifetime and reduction of trap density.[188] Consequently, a high PCE of 21.5% was achieved for inverted PSCs structure

with an improved V_{OC} of 1.15 V.[188] The device treated with oligomeric silica demonstrated a very stable performance by retaining 80% of its initial efficiency after 5200 h of light exposure with UV irradiation.[188]

Perovskite material itself also could be utilized for the interface passivation. Thanks to its bandgap tunability,[28, 29] graded perovskite interface with wider bandgap than the main perovskite light-harvesting layer could be employed between the perovskite layer and HTM. There are four types of heterojunction that could be formed, depending on the energy alignment of between two layers.[189] Figure 2.2 shows the schematic illustration of the energy diagram of perovskite and the HTM layer. In type I heterointerface (Figure 2.2a), the valence band of the graded perovskite allows holes extraction to the HTM while blocking the electron transfer to the HTM, thus reducing nonradiative recombination.[149, 152] Meanwhile, type IV heterointerface (Figure 2.2d) effectively prevents the electron transfer from perovskite to HTM and allows holes to transport through the interface by tunneling.[152, 189] On the other hand, the energetic landscape of type II and III heterointerface (Figure 2.2b and c) result in the hole and electron recombination.[189]

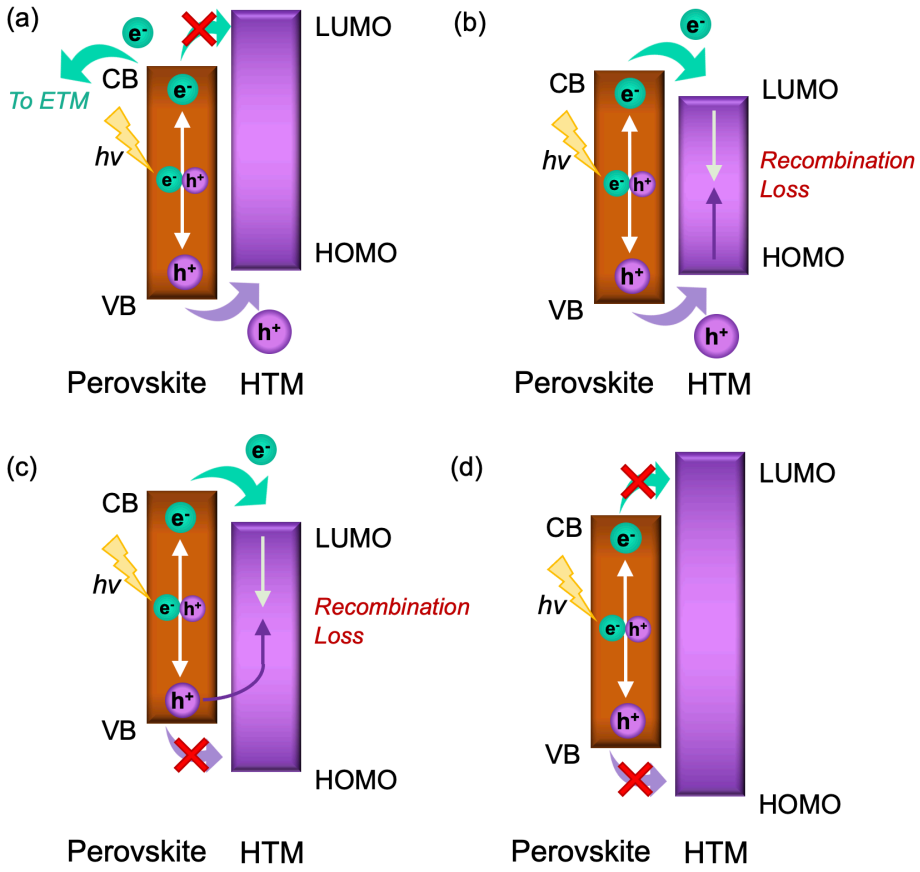

Figure 2.2 Schematic energy level diagram of possible heterointerface formed between perovskite and HTM: (a) type I, (b) type II, (c) type III, and (d) type IV.

Cho et al. introduced a thin layer of wide bandgap $FAPbBr_{3-x}I_x$ perovskite on top of the $(FAPbI_3)_{0.85}(MAPbBr_3)_{0.15}$ main perovskite layer.[190] The wide bandgap perovskite was grown in situ by reacting FABr with the excess PbI_2 on the surface of the main perovskite layer using solution process.[190] The formed wide bandgap perovskite layer effectively prevented the electron passage to the adjacent HTL leading to the reduction of the charge recombination at the interface.[190] Similarly, Ruan and co-workers grew a wide bandgap $MAPbBr_{3-x}I_x$ perovskite on top of $MAPbI_3$ layer.[191] In this case, they formed the wide bandgap layer by exposing the deposited $MAPbI_3$ film under MABr vapor.[191] Energetical barrier favoring electron blocking between the $MAPbI_3$ layer and the HTL was obtained using this method.[191] As a result, the electron lifetime was increased by 10 times compared to the control sample due to the less nonradiative recombination process.[191]

Multigraded perovskite heterojunction also could be realized by employing the perovskite NCs.[192] Li et al. designed $MAPbI_3$-based PSCs with $CsPbBr_xI_{3-x}$ graded perovskite interface.[192] They demonstrated a precise energy level alignment by finely tuning the VB and CB which was achieved by varying the Br:I ratio of the $CsPbBr_xI_{3-x}$ NCs (x=0, 0.3, 0.7, 1).[192] The 4-graded interfaces consisting $CsPbI_3/CsPbBr_{0.3}I_{2.7}/CsPbBr_{0.7}I_{2.3}$ were applied in the solar cells, enabling an efficient holes extraction while blocking the electrons backflow, resulting 40% of PCE improvement in HTL-free PSCs.[192] Further, Cha et al. introduced graded $MAPbBr_{3-x}I_x$ QDs layer on top of $MAPbI_3$ film.[193] To tune the energy level alignment, the perovskite QDs were synthesized using three different Br:I ratio with the composition of $MAPbBr_3$, $MAPbBr_{1.2}I_{1.8}$, and $MAPbBr_{0.9}I_{2.1}$.[193] They discovered that $MAPbBr_{0.9}I_{2.1}$ QDs interface exhibited a favorable VB alignment with $MAPbI_3$ leading to the best photovoltaic improvement.[193] Contrarily, $MAPbBr_3$ and $MAPbBr_{1.2}I_{1.8}$ QDs showed a poor performance due to the mismatch between the VB of the QDs films and $MAPbI_3$ film.[193]

In addition, perovskite NWs has been incorporated in PSCs to modify the electronic states of the perovskite surface. Zhang et al. synthesized $CsPbBr_3$ NWs with highly uniform shape and size.[194] Then, the $CsPbBr_3$ perovskite NWs colloidal suspension in chlorobenzene was dropped on top of the spin-coated $MAPbI_3$ solution.[194] Upon the annealing process, the dropped NWs slowly diffused into the $MAPbI_3$ films forming a gradient of $CsPbBr_3$ concentration across the thickness where the top of the film being $CsPbBr_3$ rich.[194] Moreover, $CsPbBr_3$ NWs formed interconnected network, resulting a uniform surface coverage.[194] Improved PL lifetime and higher surface potential across the surface showed by Kelvin-prove force microscopy (KPFM) revealed the defect passivation induced by this graded perovskite structure.[194] It is worth mentioning that $CsPbBr_3$ NCs with nanocubes morphology was also tested for comparison

purpose, however, the inhomogeneous distribution of the NCs was observed due to the aggregation of NCs upon dropping process on top of $MAPbI_3$ precursor.[194] On the other hand, Zhang et al. combined both perovskite NSs and QDs to construct graded perovskite interfaces.[195] All inorganic $CsPbBrI_2$ perovskite was fabricated in bulk-nanosheet-quantum dots configuration.[195] The graded interfaces composed of $CsPbBrI_2$ perovskite materials with different dimensionality (3D-2D-0D) promoted the hole extraction process with reduced nonradiative recombination losses, resulting in the high V_{OC} and *FF* of 1.19V and 80.5%, respectively.[195] Finally, an improvement of PCE from 10.38% to 12.39% was achieved in comparison with the control device fabricated without any graded interface.[195]

2.2.6 Low dimensional perovskite

Interface engineering using low dimensional perovskite has attracted a lot of attention in this field lately. Nowadays, most of the reported high-performance PSCs are implementing this technique in their devices. There are several important reasons that make this technique popular. First, the use of bulky or large organic cations could improve the stability against moisture due to the hydrophobicity.[47, 58] Second, the possibility of incorporating bulky organic cations relaxes the previous limitation imposed by the Goldschmidt tolerance factor, opening the vast library of various organic cations to be used for low dimensional perovskites (Figure 2.3).[20] Third, low dimensional perovskites are characterized by their wide bandgap.[47, 51] Thus, the defect passivation effect could be achieved by employing a graded 2D/3D perovskite structure, analogous to the passivation using wide bandgap materials as explained in Section 2.2.5.

In the 2D/3D perovskite stacking, 3D perovskite serves as the main light harvesting layer, while 2D perovskite is grown on top as a capping layer. As 2D perovskites exhibit lower conductivity and mobility due to their insulating nature in comparison to the 3D perovskite,[196, 197] it is important to deposit a thin layer of 2D on top of 3D perovskite in order to prevent the increased resistance in the charge transfer process. 2D/3D perovskite bilayer is commonly fabricated by in situ growth using a two-step deposition process.[198] In the first step, the 3D perovskite film is deposited on the prepared substrate followed by thermal annealing process. Then, the solution containing the bulky organic cation are spin-coated on top of the 3D perovskite film. The bulky organic cation is typically dissolved in isopropanol (IPA) or chloroform due to their low solubility to the 3D layer underneath.[198, 199] In situ formation of 2D perovskite is controlled by incorporating an excess PbI_2 content in the 3D perovskite layer which

will react with the large cation deposited in the second step. Finally, the 2D perovskite conversion is achieved by performing a thermal annealing process.

Ma et al. applied the two-step method to fabricate 2D/3D perovskite stacking.[200] A 3D perovskite $MAPbI_xCl_{3-x}$ film with the excess PbI_2 concentration (PbI_2 : MAI = 1.4 : 1.3) was deposited in the first step.[200] Then, cyclopropylammonium iodide (CAI) solution in IPA was introduced in the second step. After a thermal annealing of the film at 100°C for 20 min, CAI reacted with the excess PbI_2 on the surface forming 2D perovskite with the composition of CA_2PbI_4.[200] The conversion of excess PbI_2 phase and CAI to CA_2PbI_4 was confirmed by the disappearance of PbI_2 reflection in the XRD spectra when a higher concentration of CAI was introduced.[200] The PL spectra revealed that the incorporation of 2D layer improved the PL intensity, indicating the reduction in the nonradiative recombination.[200] Further, they found that the deposition of 10 mg/L CAI exhibited the best photovoltaic performance without causing any hindrance in the charge extraction.[200] The PSC employing $MAPbI_xCl_{3-x}/CA_2PbI_4$ demonstrated a PCE of 13% with an enhanced stability against moisture by maintaining 54% of its initial PCE after exposure under 63±5% humidity for 220 h.[200]

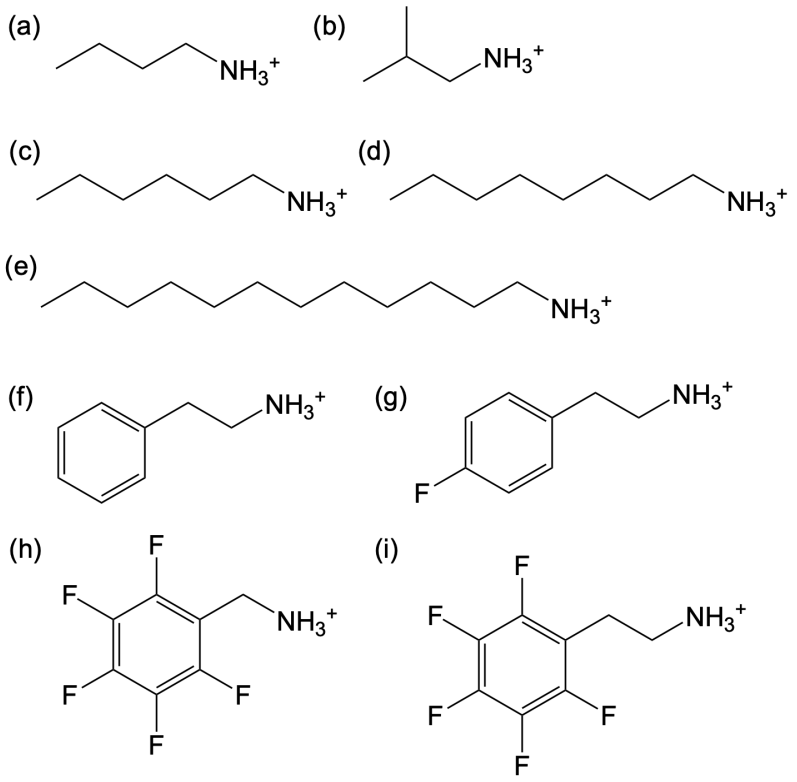

Figure 2.3 Several bulky organic cations used for 2D perovskites: (a) butylammonium, (b) isobutylammonium, (c) hexylammonium, (d) octylammonium, (e) dodecylammonium, (f) phenylethylammonium, (g) 2-(4-fluorophenyl)ethylammonium, (h) pentafluorobenzyl-ammonium, and (h) pentafluorophenylethylammonium.

Moreover, Yao et al. developed 2D/3D perovskite composite consisting of $MAPbI_3/(PEI)_2PbI_4$ (PEI = polyethylenimine).[201] An improved PCE of 15% with a minimal loss upon 14 days exposure to the air with 50% humidity was achieved by incorporating 2% of $(PEI)_2PbI_4$.[201] Similarly, 5-ammoniumvaleric acid iodide (5-AVAI) was employed to grow an ultrathin layer of $(5\text{-}AVA)_2PbI_4$ 2D perovskite on top of $(FAPbI_3)_{0.88}(CsPbBr_3)_{0.12}$ using two-step method.[202] The incorporation of 2D interlayer enhance the charge extraction efficiency at the interface due to the reduced recombination loss which was evidenced by the less hysteresis effect in the *J-V* curve.[202] Furthermore, the passivation effect was also indicated by the improvement of carrier lifetime, increasing the PCE from 13.72% (3D layer) to 16.75% (2D/3D bilayer).[202] The unencapsulated device demonstrated an exceptional long-term stability by conserving 98% of the initial PCE after 63 days exposure under the moisture (RH = 10%) in the dark.[202]

To further improve the photovoltaic performance, Cho et al. selectively grew $(PEA)_2PbI_4$ perovskite layer on top of $Cs_{0.1}FA_{0.74}MA_{0.13}PbI_{2.48}Br_{0.39}$ 3D perovskite by carefully controlling the ratio of excess PbI_2 and PEAI in the precursor solutions.[198] PEAI solution with concentration of 10 mg/mL was designed to match the excess PbI_2 content (PbI_2 : FAI = 1.05:1) in the 3D perovskite.[198] By dynamically spin-coating PEAI solution dissolved in IPA at the second step, an in situ reaction between PEAI and the excess PbI_2 on the surface occurred, forming a thin capping layer of $(PEA)_2PbI_4$ 2D perovskite. The XRD analysis showed that the excess PbI_2 was fully consumed after the annealing process indicating the successful conversion to $(PEA)_2PbI_4$ perovskite which was observed by the appearance of a new reflection at low angle (5.44°).[198] Additionally, the incorporation of 2D perovskite eliminated the presence δ-phase of the 3D perovskite.[198] The formation of a distinct 2D perovskite on top of 3D perovskite was supported by the appearance of an emission peak at 508 nm when the film was excited from the top side (2D perovskite side).[198] Further, the UPS analyses demonstrated that $(PEA)_2PbI_4$ perovskite formed a favorable energetic alignment with the 3D perovskite, where the VB allowed for an efficient hole transfer and the CB effectively blocked the electron backflow to the HTM layer.[198] As a result, the nonradiative recombination was significantly decreased in agreement with the lower recombination resistance derived from the impedance spectroscopy analysis.[198] The device fabricated using this 2D/3D perovskite stacking yielded a high V_{OC} and PCE of 1.15V and 20.75%, respectively.[198] Importantly, the 2D/3D device demonstrated a remarkable stability performance by retaining 85% of its initial PCE after keeping 800 h in continuous illumination at 50°C.[198]

Various linear alkylammonium cations with different alkyl length are also explored as the precursor of the 2D perovskite capping layer in the bilayer stacking. Gharibzadeh et al. reported $Cs_{0.17}FA_{0.83}Pb(I_{0.6}Br_{0.4})_3$ 3D perovskite treated with *n*-butylammonium bromide (BABr) on top resulting in the formation of a 45 nm-thick 2D perovskite layer.[203] Consequently, a very significant improvement in the carrier lifetime was observed after the deposition of the 2D perovskite layer, indicating the effective passivation effect by reducing the nonradiative recombination.[203] An exceptionally high V_{OC} of 1.31 V was obtained by incorporating BABr-based 2D perovskite.[203] This outstanding achievement in the V_{OC} approached more than 90% of the theoretical limit determined by Shockley-Queisser limit.[203] Meanwhile, Liu et al. incorporated isobutylammonium iodide (*i*-BAI) to grow a quasi 2D perovskite with the composition of $(i\text{-BA})_2FAPb_2I_7$ (n=2) on top of $FAPbI_3$ perovskite.[40] The slower PL decay of *i*-BAI post-treated film by more than one order magnitude suggested the diminution of the trap density in the interface.[40] Notably, the formation of $(i\text{-BA})_2FAPb_2I_7$ at the surface successfully suppressed the formation of the yellow phase of $FAPbI_3$ which further enhanced the long-term device stability under heat and continuous light exposure.[40]

Further, Yoo et al. compared three cations with different alkyl chains, such as BABr, *n*-hexylammonium bromide (HABr), and *n*-octylammonium bromide (OABr).[199] The post-treated $(FAPbI_3)_{0.92}(MAPbBr_3)_{0.08}$ 3D perovskite showed the PCE from 21.7% to 23.2%, 23.2%, and 23.1% when 2D perovskite incorporating BABr, HABr, and OABr were deposited on top, respectively.[199] The increase of the alkyl length from butyl to octyl improved the V_{OC} from 1.14 V to 1.17V.[199] These results were proportional with the PL lifetime indicating that the longer alkyl chain exhibited a better passivation effect at the interface and GBs.[199] Additionally, they proposed that chloroform could be used to dissolve the alkylammonium salts due to its lower solubility towards FAI in comparison with IPA, minimizing the dissolution of FAI on the 3D perovskite surface.[199] Remarkably, the optimized PSC showed the stabilized V_{OC} of 1.19V, resulting only 340 mV of V_{OC} loss.[199] The 2D/3D perovskite composite also demonstrated an excellent structural stability confirmed with XRD analysis by maintaining the perovskite phase after exposure to 90% RH for 8 days, while the 3D control film was completely degraded.[199] The operational stability was also tested by keeping the device under continuous illumination. The 2D/3D-based device retained 85% of the initial efficiency after 500h.[199]

In addition, a bulky organic cation with longer alkyl chain, such as dodecylammonium iodide (DAI) was examined.[42] Butylammonium iodide (BAI) and octylammonium iodide (OAI) were also compared to evaluate the trend between the three cations in the devices.[42] In general, the hydrophobicity and the electron blocking ability are improved with the increasing alkyl

length. Kim et al. demonstrated that the difference in the device performance between OAI and DAI was very small.[42] Although DAI-based 2D/3D PSCs showed the highest V_{OC} of 1.13V, the highest PCE was achieved by employing OAI due to the slightly higher J_{SC} and *FF*.[42] However, the 2D/3D PSCs employing DAI still exhibited the best long-time stability under both elevated temperature and humid environment.[42] Thus, it is important to choose the appropriate cations to obtain the best compromise between the device photovoltaic performance and stability.

More recently, bulky organic cations functionalized with fluorine atoms have received many attentions due to the improved hydrophobicity. Fluorine could easily form hydrogen bonds with water molecules due to its high electronegativity.[149] As a result, a protective layer against moisture is built on the interface when the molecule is deposited on top of perovskite layer.[149] To improve the hydrophobicity of PEAI, 2-(4-fluorophenyl)ethyl ammonium iodide (FPEAI) was designed as the 2D-forming cation.[204] $(FPEA)_2PbI_4$ 2D perovskite was grown in situ on top of Cs/FA/MA triple cation perovskite. The formed 2D/3D perovskite combination exhibited a reduced nonradiative recombination, achieving PCE of 20.54% when it was applied in the device.[204] As expected, the presence of fluorine atom in FPEAI was indeed boosting the long-term device stability in comparison with PEAI by retaining 99% of the device's original PCE after 864 h storage in dark condition with a controlled RH between 10-30%.[204]

Moreover, Paek et al. compared FPEAI with a more hydrophobic cation, namely perfluorobenzylammonium iodide (5FBzAI) which contain 5 fluorine atoms in the structure.[205] The presence of 5 fluorine atoms and a reduced length of 5FBzBAI compared to FPEAI enabled a strong interaction between the 2D and 3D perovskite via halogen bond, inducing a highly in-plane crystal orientation.[205] As a result, enhanced passivation effect was achieved by gaining 60 mV of V_{OC} which was two times larger than the V_{OC} improvement obtained by incorporating FPEAI.[205] The 5FBzAI-modified perovskite also showed higher hydrophobicity which was indicated by the higher water contact angle value.[205] Finally, the PSC employing 5FBzAI retained 86% of its initial PCE after 1100h exposure under continuous illumination outperforming the FPEAI-based device.[205]

A 2D perovskite capping layer employing pentafluorophenylethylammonium (FEA) cation was also investigated in the 2D/3D PSCs.[206] The perfluorinated benzene unit in FEA structure was expected to provide a highly hydrophobic interfacial layer on top of 3D perovskite. The 2D/3D PSCs employing FEA cation demonstrated an impressive stability by retaining 90% of the initial PCE in a humid environment (RH=40%) after 1000 h under continuous illumination without any encapsulation.[206] Besides, the presence of five fluorine atoms in the benzene ring improved the electronic properties in the 2D layer by facilitating the hole-

extraction process and preventing the ion migration at the perovskite/HTM interface.[206] Thereby, the interfacial nonradiative recombination was reduced to a great extent, resulting in a high PCE of 22%.[206]

On the other hand, Cho et al. introduced a self-assembled fluorinated cation as the building block of the low dimensional perovskite.[207] In this case, a highly fluorinated saturated molecules in the form of iodide salt, $(CF_3)_3CO(CH_2)_3NH_3I$ (A43), was designed in order to benefit from the improved hydrophobicity from the fluorine atoms as well as the tendency of this molecule to self-assemble forming a highly ordered structure.[207] The incorporation of A43 in the PSCs demonstrated an improved stability, especially by reducing the initial burn-in loss during the first 100 h of operation.[207] Further, a synergistic effect due to the interaction between interfacial layer and HTMs was explored. Jung et al. spin-coated a large organic cation, namely *n*-hexyltrimethylammonium bromide (HTAB) to form a thin layer of wide bandgap halide (WBH) perovskite on top of $(FAPbI_3)_{0.95}(MAPbBr_3)_{0.05}$ films.[208] A formation of low dimensional perovskite phase was confirmed by the appearance of a low angle reflection (5.4°) in the XRD spectrum.[208] The incorporation of the WBH layer did not only suppress the nonradiative recombination at the interface, but also promote the interdigitation of the alkyl chain of poly(3-hexylthiophene) (P3HT) with the analogous alkyl chain of HTAB via van der Waals interactions.[208] The self-assembled P3HT structure on top of WBH significantly improve the film morphology as well as the hole mobility by 4 orders of magnitude.[208] Therefore, a huge improvement of PCE from 15.8% to 22.8% was achieved primarily due to the increase in V_{OC} and *FF*.[208] The device exhibited a superior long-term stability against moisture by maintaining 80% of its initial PCE under 85% RH for 1008 h.[208]

Double-side passivation technique by employing a low dimensional perovskite both on the ETL/perovskite and perovskite/HTL interfaces was also tested in PSCs. Mahmud and co-workers introduced ultrathin BAI-based 2D perovskite layers (~20 nm) between both PMMA:PCBM/ perovskite and perovskite/spiro-OMeTAD interface.[209] PSCs fabricated with the double-side passivation exhibited a higher PL intensity in comparison with the devices employing only one-side passivation (at perovskite/spiro-OMeTAD interface).[209] The improvement in the PL intensity indicated the reduction of nonradiative recombination, which was reflected by the high V_{OC} value of 1.2V in the double-side passivated device with the maximum PCE of 22.77%.[209] The charges extraction efficiency was also enhanced despite the insulating nature of the 2D layer owing to the incomplete surface overage of the 2D perovskite, enabling the charge transfer through the uncovered area.[209] However, the PSCs with double-side showed a similar long-term stability as the control device due to the nonuniform coverage

of the 2D perovskite on the surface, allowing the moisture to penetrate to the 3D perovskite underneath.[209]

2.3 HTM Engineering

HTM engineering could not be separated in improving device stability and performance. Although some interfacial layer has been introduced between perovskite and HTM, the interface between HTM and the adjacent perovskite or the interlayer remains important. HTM itself has the main role to extract the holes from the perovskite interface. High hole-transporting properties are desired to efficiently extract and separate the holes from the electrons which further prevent the recombination at the interface. To gain an efficient hole extraction, ideally the following factors need to be considered in designing an HTM: (1) high hole mobility, (2) a matching energy level alignment with the adjacent layer, and (3) good film quality.

The hole mobility of the HTM could be enhanced by improving the planarity and the molecular packing as well as the implementation of donor-acceptor (D-A) and conjugation strategy.[210] The common alternative method to boost the hole transporting properties of HTM is by incorporating chemical additives or dopants, such as Li-bis(trifluoromethanesulphonyl) imide (Li-TFSI), tris(2-(1*H*-pyrazol-1-yl)-4-tert-butylpyridine)cobalt(III) (FK-209), and 4-*tert*-butylpyridine (tBP).[124] In addition, the energy level alignment between perovskite and HTM holds a very crucial role in determining the device performance. The HOMO level must be higher than the VB of perovskite to enable the efficient hole injection from perovskite to HTM. In general, it is also preferred to have a close difference between the HOMO of HTM and VB of perovskite in order to avoid a large voltage loss. It is also necessary for the HTM to have a higher LUMO value than the CB of perovskite in order to prevent the electron backflow.[124] Furthermore, HTM should form a good quality of film when it is deposited on top of perovskite layer, such as uniform coverage, absence of pinhole, and good contact with perovskite layer.[210] Thus, the solubility of the HTM becomes very important, especially if the deposition of the layer is carried out using solution process. Moreover, the use of strong polar and protic solvents is generally avoided to prevent the dissolution of the perovskite layer underneath.[124]

Other than having an excellent hole extraction efficiency, the HTM should be highly stable to ensure a satisfactory the device lifetime according to the PV standard. In the *n-i-p* structured PSCs, HTM layer provide the penultimate encapsulation (before the metal electrode) of the underlying perovskite layer. Therefore, HTM should exhibit thermal, light, chemical, and moisture stability.[210] The ideal HTM is generally designed with a high decomposition temperature in order to withstand the elevated operating temperature of PSCs in the real-world

application. Further, it should be able to maintain its physical and chemical integrity under a continuous sun irradiation, especially upon the UV light exposure.[124, 210] The HTM should also be chemically stable, which means the unwanted chemical interactions with the perovskite layer underneath must be prevented.[124] In addition, the resistance to the moisture is also one of the most important factors in determining the HTM stability. As discussed in the previous chapter, 3D perovskite materials exhibit a poor moisture stability. If the HTM used is hygroscopic in nature, it could attract moisture and induce the degradation of the perovskite layer underneath. Thus, an HTM should demonstrate an excellent moisture stability to prevent a further device degradation.

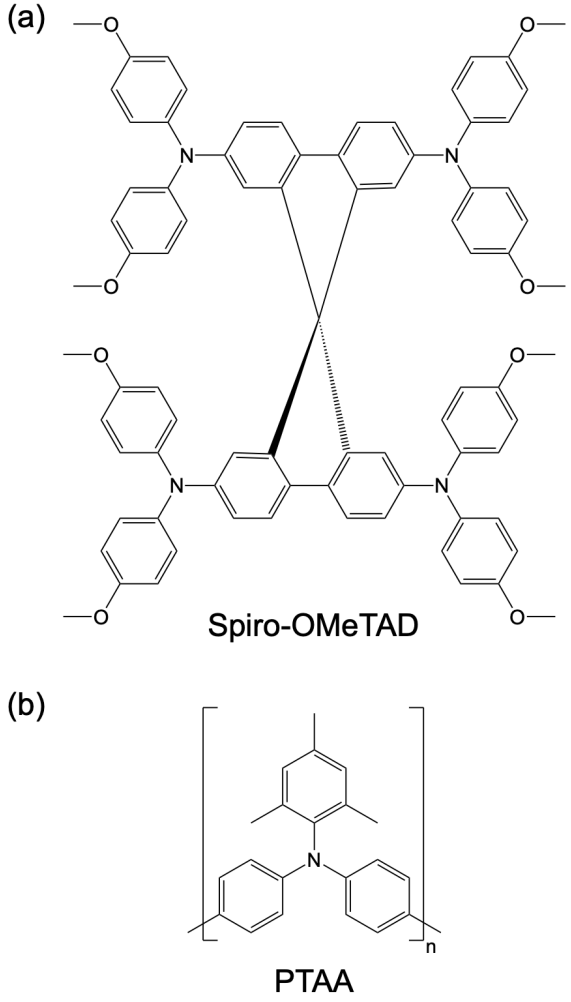

Figure 2.4 Molecular structure of (a) spiro-OMeTAD and (b) PTAA.

For the past decade, spiro-OMeTAD has been extensively used as the state-of-art HTM in the PSCs (Figure 2.4a). Most of the highly efficient PSCs reported in the literature are based on spiro-OMeTAD as the HTM.[211, 212] To fabricate high performance PSCs, a high-purity sublimation grade spiro-OMeTAD is necessary. Nevertheless, as mentioned in Section 1.3.3 of Chapter 1, the high quality spiro-OMeTAD requires exhaustive multiple steps synthesis and

purification process which results in the high cost of $92/g.[213] Additionally, the high hole-transporting property of spiro-OMeTAD only can be realized by chemically doping the precursor solution. Li-TFSI and Co-TFSI are commonly used to enhance the hole mobility as well as the conductivity of the spiro-OMeTAD film.[214, 215] Meanwhile, tBP is added to improve the film formation and to prevent Li-TFSI segregation.[216] However, researchers have investigated that the use of those dopants bring a negative impact to the long-term stability of the device. For instance, Li-TFSI and Co-TFSI are hygroscopic in nature which make the doped spiro-OMeTAD layer more hydrophilic, accelerating the degradation of the PSCs.[217, 218] Further, the migration of Li-TFSI damages the morphological integrity of the HTM indicated by the formation of pinholes.[115] Alternatively, a polymer-based HTM, namely poly[bis(4-phenyl)(2,4,6-trimethylphenyl)amine] (PTAA), has demonstrated high photovoltaic performance in PSCs (Figure 2.4b).[219] Besides, PTAA exhibited better thermal and long-term stability in comparison to spiro-OMeTAD.[220] However, the extremely high cost of PTAA reaching ~$2000/g makes it less feasible for the widespread application.[124]

Researchers then seek for alternative by developing dopant-free HTMs to exclude the dopants contribution in the device degradation. However, the performance of dopant-free HTM is still inferior compared to the one of spiro-OMeTAD.[221] Thus, the research on the doped-HTMs still keeps going due to their potential to compete with spiro-OMeTAD performance. Through a careful molecular engineering, researchers attempt to improve the long-term stability of the doped-HTM. Recently, Drigo et al. synthesized new molecules based on the spiro bisacridine (SBA).[222] When the SBA-based HTMs were applied in the solar cells, they were doped using the same condition as spiro-OMeTAD. Interestingly, all of the SBA-based compounds demonstrated better long-term stability than spiro-OMeTAD. MeSBA-DMPA exhibited a remarkable long-term stability by maintaining 88% of its initial efficiency after 1000 h of continuous illumination despite being doped. On the other hand, spiro-OMeTAD-based PSCs only could retain 64% of the initial PCE.[222] The main stability improvement of SBA-based HTMs could be observed from a slower decay during the initial burn-in period due to their favorable molecular packing in the bulk or at the interface, preventing the accelerated deterioration of the HTMs in the PSCs.[222]

Chapter 3: The Origin of the Stability Improvement in 2D/3D Perovskite Interfaces

Interface engineering by incorporating 2D/3D perovskite in a bilayer structure has been a popular strategy for realizing efficient perovskite solar cells (PSCs) with enhanced long-term stability. Nevertheless, the exact function of the 2D perovskite capping layer in preventing the degradation of the bulk 3D perovskite layer underneath still remains unclear. Herein, we investigated the evolution of the 2D/3D interface under various conditions by monitoring structural, photophysical, and photovoltaics characteristics. In the first section of this chapter, three thiophene-based bulky organic cations are introduced as the building block for the 2D perovskite layer. During the aging of the devices under dark condition in ambient atmosphere, we observed that 2D perovskites incorporating 2-thiophenemethylammonium iodide (2-TMAI) and 3-thiophenemethylammonium iodide (3-TMAI) transformed from lower to higher *n* number. On the other hand, 2D perovskite incorporating 2-thiopheneethylammonium iodide could maintain its initial 2D phase upon the aging. From this finding, we propose that the small cations in the 3D cage (i.e., MA^+) move towards the 2D layer, transforming the 2D layer to the higher *n* number (quasi-2D). If structurally stable, the 2D layer physically blocks the ion movement at the interface boosting the device stability. Further, in the second section of this chapter, we studied the thermal stability of 2D/3D perovskite interface by monitoring the structural evolution using in situ grazing incident wide angle X-ray scattering (GIWAXS). We discover that under thermal stress, the 2D crystalline structure undergoes a phase transformation into a quasi-2D phase while keeping the 3D bulk perovskite underneath intact. Moreover, the 3D bulk decomposition into lead iodide phase is prevented, emphasizing the fundamental role of 2D perovskite in realizing stable PSCs.

3.1 Dynamical evolution of the 2D/3D interface: a hidden driver behind perovskite solar cell instability

This section is based on the published work in J. Mater. Chem. A, 2020, 8, 2343-2348, DOI: 10.1039/C9TA12489F.[223] In this work I conceptualized the idea, designed the experiments, and performed the fabrication as well as the characterizations of perovskite thin films and solar cells. Dr. N. Drigo synthesized the thiophene-based cations. V.I.E. Queloz carried out the PL analyses. The GIWAXS experiments were performed in collaboration with Dr. A. Kirmani and Dr. L.J. Richter from NIST, USA.

3.1.1 Introduction

Within the last decade, perovskite solar cells (PSCs) have been receiving a great interest in the area of new generation photovoltaics, with power conversion efficiency (PCE) recently surpassing 25%.[224] Careful interface engineering between the perovskite active layer (AL) and the device interfaces, i.e., the electron or the hole transporting layers (ETL, HTL), is the key to device development and optimization. Various engineering strategies have been explored, including interface functionalization with bulky organic molecules,[208] inert polymeric layers,[186, 225, 226] inorganic interlayers,[227, 228] graphene or parent 2D materials,[229-231] Alternatively, layered perovskites, popularly referred as 2D,[47, 51] have been incorporated at the AL-ETL or -HTL interface, forming graded 2D/3D interfaces.[198, 200-202, 207, 232] Thanks to the superior robustness of the 2D compared to parent 3D perovskite, such 2D/3D architectures have attracted growing interest as a route to stable and efficient devices.[208] For instance, a combination of methylammonium (MA) lead iodide perovskite and aminovaleric acid-based 2D perovskite resulted in solar cells with greater than 1-year stability, demonstrating the robust nature of the combined systems.[39] The 2D perovskite has been shown to simultaneously function as a protective layer and surface defect passivant.[207, 233, 234] However, whether 2D is an essential ingredient for future PSCs technology or a popular transitory trend is an open question.[20, 46] To answer this point, it is imperative to understand how the 2D perovskite affects the quality of the 3D perovskite surface, and the processes therein, as well as the ultimate device behavior, performance and stability over time.

Here, we report the observation of a slow evolution of the performance of 2D/3D PSCs using a new family of thiophenealkylammonium-based organic cations as building blocks for the layered 2D perovskites and its impact on the device efficiency and stability. We reveal a double effect: first, unexpectedly, during aging for several months in dark and dry environment, the PSCs efficiency increases (from 15% to over 20% in the most striking case), mainly associated with an enhancement of the device open circuit voltage (V_{OC}). While this stems true also for the

control device, a significant boost is observed as derived from a slow structural rearrangement of the 2D/3D interface. We attribute this to the "soft" nature of the 2D perovskite overlayer that can act as an ion-scavenger. As a consequence of ion movement from the 3D towards the interface, small MA cations accumulate at the interface. As a getter, the 2D structure can incorporate the MA cations by self-modifying its pure layered structure into a quasi-2D (or mixed) phase.[51] This interface modification generally improves the device performance. On the other side, depending on the chemical nature of the 2D perovskite, a "more robust" 2D layer can prevent such structural change, physically blocking the ion movement. This leads to a dramatic increase in the device stability, retaining 90% of the initial value under continuous illumination over 1000 hours. The structural change in time has been monitored over a time window of months combining solar cell operation with thin film structural and optical characterization on aged samples and/or under different aging conditions (i.e., different thermal stress). Overall, results reveal that the conscious choice of proper 2D components can control the dynamical evolution of the 2D/3D interfaces and is a key element to control for the realization of efficient and stable devices.

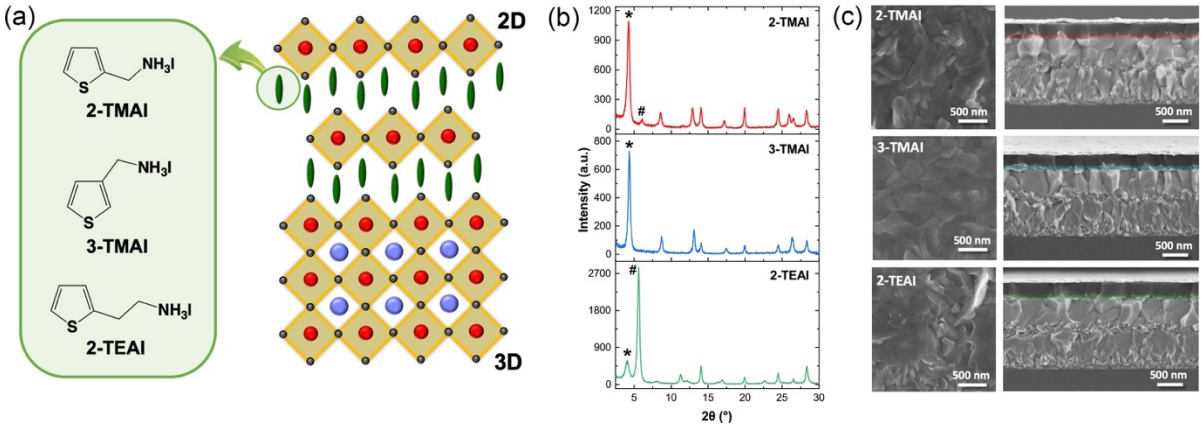

Figure 3.1.1 (a) Molecular structures of the cations (left) and sketch (right) of the derived 2D/3D interface. (b) X-ray diffraction (XRD) pattern at 2° incident angle of the 2D/3D film employing 2-TMAI, 3-TMAI and 2-TEAI cations in the 2D template. # and * denote diffraction peaks of 2D perovskite with n=1 and n=2, respectively. (c) Scanning electron microscopy images of the top view (left) of the perovskite films and cross-section (right) of the 2D/3D devices employing 2-TMAI, 3-TMAI and 2-TEAI cations in the 2D layer (highlighted with colored area).

3.1.2 Materials Characteristics

We synthesized a series of bulky thiophene-terminated cations as building blocks for layered 2D perovskite structure. Chemical formulae of the thiophenealkylammonium salts

namely 2-thiophenemethylammonium iodide (2-TMAI), 3-thiophenemethylammonium iodide (3-TMAI), and 2-thiopheneethylammonium iodide (2-TEAI) along with the derived 2D structure are shown in Figure 3.1.1a. Notably, they only differ on position and length of the alkyl chain connecting the thiophene core and the ammonium entity. The salts were prepared from the commercially available amines and HI (see Experimental Methods, Appendix A for details).

To create the 2D/3D thin films and devices, we dissolved the salts in isopropanol (IPA) and dynamically spin-coated them on top of a triple-cations $[(FAPbI_3)_{0.87}(MAPbBr_3)_{0.13}]_{0.92}$-$(CsPbI_3)_{0.08}$ based 3D perovskite film, where FA stands for formamidinium (see Experimental Methods, Appendix A for details). As a result, a thin layer of 2D perovskite is formed on top of the 3D bulk, as verified by low angle grazing incidence X-Ray Diffraction (XRD). Patterns are shown in Figure 3.1.1b. We note the presence of the peaks at 14°, and at 6° and 4° which correspond to (001) diffraction signals from the 3D perovskite, and, at lower angles, from (002) of the layered 2D perovskites, respectively. (The 2D crystal structures are either centro-symmetric or near centro-symmetric such that the (00l) diffraction, l odd, is forbidden or weak.) More in details, the peak at 6° relates to the formation of a pure 2D perovskite, which takes the formula of $R_2(MA)_{n-1}PbI_{3n+1}$ for n=1 (where n defines the number of the inorganic layers), while the peak at 4° relates to a mixed phase (or quasi-2D perovskite) where, in this case, n=2. Depending on the organic salts, slightly different 2D perovskites are formed: for 2-TMAI mostly n=2; for 3-TMAI only n=2; and for 2-TEAI mostly n=1 2D phase (see also XRD patterns of the pure 2D perovskite in Figure A.1.1 and Figure A.1.2, Appendix A). The 2D perovskite layer, ≈50 nm thick, covers the entire 3D surface, as shown in Figure 3.1.1c by top view and cross-sectional scanning electron microscopy (SEM) images. From the top surface image, we could observe that the 2D overlayer smooths out the surface, rendering it less defined in terms of grain boundaries and crystals borders with respect to the 3D surface (Figure A.1.3, Appendix A).

3.1.3 Device Characteristics

We implement these films as AL in standard (*n-i-p*) device structure solar cells. The optimized thiophenealkylammonium salts concentration implemented in the devices is 0.06M, resulting in ≈50 nm thick 2D layer on top of 3D layer (see Table A.1.1, Appendix A for details). The photovoltaic (PV) response of the thiophene-based 2D/3D cells are shown in Figure 3.1.2 and Table 3.1.1 (statistics in Table A.1.2 and Figure A.1.4, Appendix A). It is worth remarking that commonly device data shown in literature do not specify the aging status of the measured device, making the comparison among reported PCE rather difficult. This also hides important information on the slow dynamic behavior of the device interfaces that can alter the PSCs

performances.[235] Slow processes such as those related to ionic motion are still not yet fully understood[236-238] but pointed as common source of aging phenomena. To address this point, here we monitor the evolution of the devices PV performances by comparing fresh (measured 1 day after device fabrication) and aged devices over months (stored in dark and dry air environment with the humidity controlled below 10%).

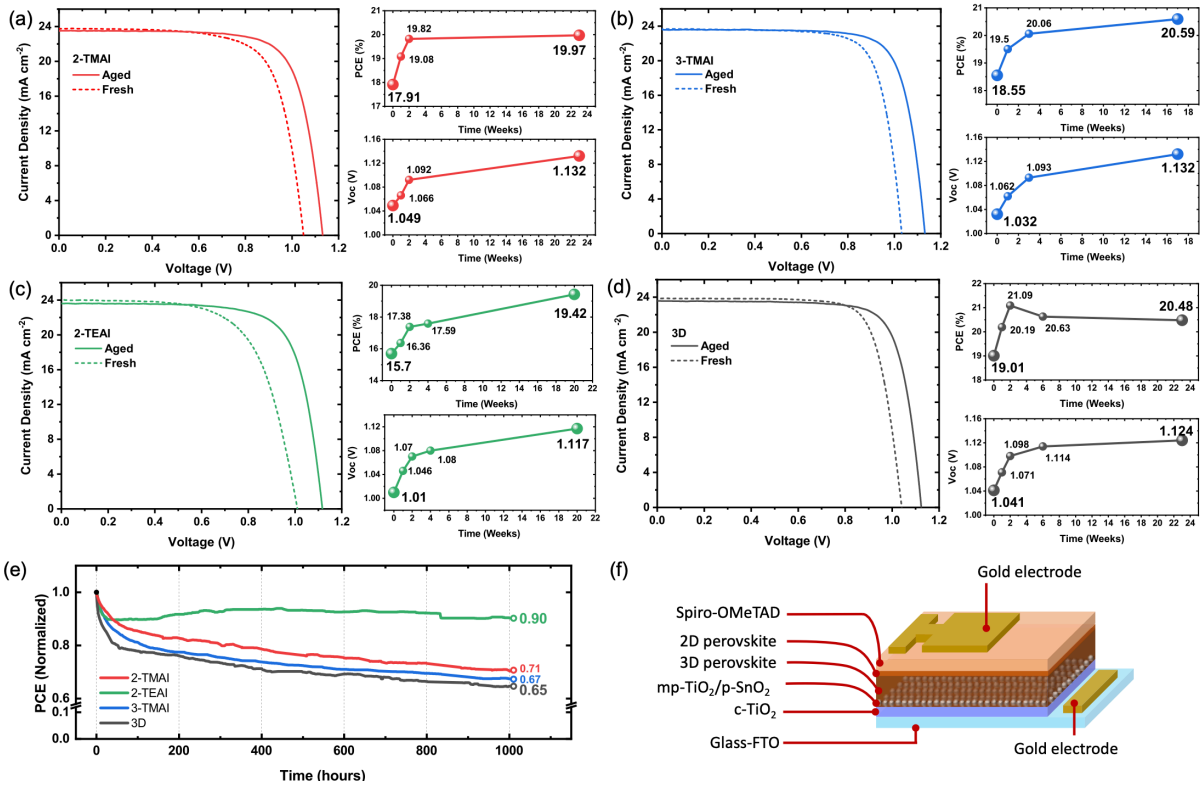

Figure 3.1.2 Photovoltaics characteristics of the 2D/3D PSCs employing (a) 2-TMAI, (b) 3-TMAI and (c) 2-TEAI, (d) 3D control. For each panel the current-voltage characteristics of fresh and aged devices are shown along with the time evolution of the power conversion efficiency (PCE) and open circuit voltage (V_{OC}) of the devices stored in the dark and dry environment (humidity <10%). (e) Stability test for freshly prepared devices under continuous 1 sun illumination for 1000 h in Ar atmosphere without any encapsulation. (f) Scheme of the device architecture.

Fresh device PCEs range from 15% to 19% depending on the 2D/3D system. For the control it reaches peak performances after 2 weeks resulting in 21.1% PCE, but decreasing afterwards (Figure 3.1.2d). On the other side, the 2D/3D systems all show a monotonic improvement in the PCE nearly saturating after 6 months. The aged samples all deliver around 20% PCE with an increase in the device *FF* and V_{OC}. The 3-TMAI device outperforms the 3D control after aging. Notably, the 2-TEAI 2D/3D systems shows the largest improvement of approx. 25% going from 15.70% to 19.42%. Hysteresis and IPCE spectra are reported in Figure

A.1.5 and Figure A.1.6 (Appendix A). This represents our first finding: the presence of the 2D layer improves the performances over time on month-base analysis. Notably, the highest performances of the devices (also the controller) are always reached after few days of storage in dark and in dry air. However, it is worth mentioning that the final V_{OC} is higher for the 2D/3D system employing 3-TMAI and 2-TMAI. In agreement with previous work on the 2D/3D interface,[239] this can be associated to a surface passivation effect of the 2D layer. To assess that, we investigated the device characteristics under different sunlight intensity, as shown in Figure A.1.7 and Figure A.1.8 (Appendix A) and we find the 2D layer has a beneficial effect on surface recombination. Studies of the device ideality factor, based on the intensity dependence of the V_{OC} (Figure A.1.7, Appendix A) and J_{SC} (Figure A.1.8, Appendix A) provide insight into the recombination kinetics in the device [240, 241]. Relative to the control, all 2D/3D devices exhibit indeed less monomolecular (trap-mediated) recombination which points toward a reduction of the surface trap density, responsible for the improve in the V_{OC} and *FF*. A second important observation relates to device stability where a distinct behavior is observed depending on the nature of the 2D cation. In general, the 2D/3D devices only slightly outperform the 3D reference when measured under continuous 1 sun illumination at full maximum power point for 1000 h in an inert atmosphere (Figure 3.1.2e) showing, after initial decay as commonly observed for 3D PSCs,[136] a similar degradation curve. Interestingly, the 2-TEAI based 2D/3D device behaves differently: the stability after the initial decay, as commented above, recovers and is kept at 90% of the initial PCE value with no sign of degradation for the 1000 h tested. This represents a net improvement with respect to the controller which decays to 65% of the initial value.

Table 3.1.1 Photovoltaic parameters of champion fresh and aged (for the time as indicated in Figure 2) of 2D/3D PSCs employing 2-TMAI, 3-TMAI, 2-TEAI, and 3D control.

Organic cations		V_{OC} (V)	J_{SC} (mA cm^{-2})	*FF*	PCE (%)
2-TMAI	Fresh	1.049	23.75	0.719	17.91
	Aged	1.132	23.50	0.751	**19.97**
3-TMAI	Fresh	1.032	23.67	0.760	18.55
	Aged	1.132	23.60	0.771	**20.59**
2-TEAI	Fresh	1.010	24.01	0.647	15.70
	Aged	1.117	23.60	0.737	**19.42**
3D	Fresh	1.041	23.87	0.765	19.01
	Aged	1.124	23.57	0.773	**20.48**

3.1.4 Stability Analyses and Degradation Mechanism

To rationalize our finding and elucidate the intimate mechanisms behind such long-term stability, we investigate the evolution in time of the 2D/3D structure by means of photoluminescence (PL) spectral analysis as a simple and immediate method to identify the emissive species, and related perovskite phase. PL measurements have been carried out over months, mimicking the same time window as for the device tests, as well as fresh but upon different thermal stress, see Figure 3.1.3.

Figure 3.1.3a–c shows the PL spectra from the front side (2D perovskite side) of the 2D/3D film exciting both the 2D and the 3D layer for the fresh and aged samples. A weak emission from the 3D perovskite at 770 nm is observed upon front side excitation. Contrarily, upon back side (3D perovskite side) excitation the emission from 3D perovskite is dominant, see Figure A.1.9, Appendix A. For fresh films, peaks at short wavelengths are observed, which manifest at: *1)* 520 nm and 570 nm for 2-TMAI; *2)* 570 nm only for 3-TMAI; *3)* 520 nm (dominant) and a shoulder at 550 nm for 2-TEAI. In agreement with XRD analysis, we can assign the 520 nm PL peak to the emission from n=1 2D perovskite, and the 570 nm peak to n=2 perovskite. This assignment also matches the emission from pure 2D thin films with n=1 or n=2 (see Figure A.1.10 and Figure A.1.11, Appendix A). This indicates the formation of distinct 2D perovskite phases depending on the nature of the organic cations. Upon aging, the emission spectra change: *1)* 520 nm peak (related to n=1 2D) vanishes, while the 570 nm peak grows in 2-TMAI; *2)* the 570 nm is unchanged, but a new broad peak at higher wavelength appears in 3-TMAI. This is related to the formation of a mixed 2D with a higher n value;[51] *3)* 2-TEAI based 2D/3D does not show any visible change. This indicates a structural rearrangement of the 2D/3D interface upon aging that holds true for all cases except for the 2-TEAI-2D/3D thin film. A stable n=1 2D phase upon aging is also observed for PEAI-based 2D/3D systems, confirming the general validity of our observation, see Figure A.1.12 and Figure A.1.13 (Appendix A). Such structural changes are also confirmed by Grazing Incidence Wide Angle X-ray Scattering (GIWAXS) analysis carried out on aged samples, as shown in Figure A.1.14 (Appendix A). This observation reveals a structural transformation of the 2D perovskite from a low n to a higher n quasi-2D/3D interface over time for all the cations except the 2-TEAI based 2D/3D.

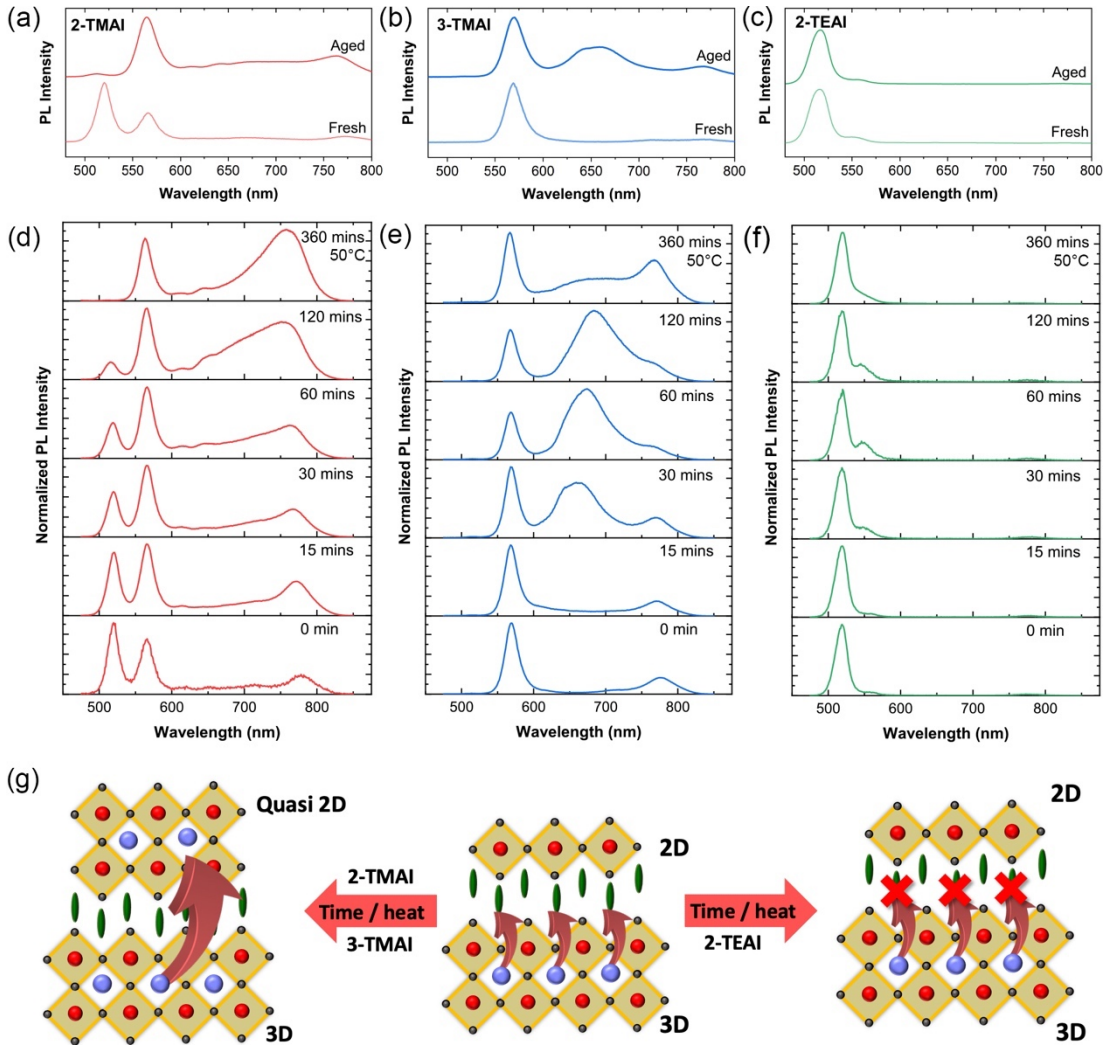

Figure 3.1.3 PL spectra upon excitation at 450 nm of fresh and 4 months aged 2D/3D perovskite films employing (a) 2-TMAI, (b) 3-TMAI, and (c) 2-TEAI 2D/3D systems; PL spectra upon thermal stress (heating the film at 50°C for the time as indicated in the legend) for (d) 2-TMAI, (e) 3-TMAI, and (f) 2-TEAI 2D/3D systems. (g) Cartoon illustrating the proposed interfacial mechanism.

To better elucidate the origin of this change, we simulate aging by stressing the thin films at 50°C from 0 to 360 minutes and we measure the evolution of the PL spectra over time (Figure 3.1.3d-f). A clear change in the emission peaks position and relative intensity is again observed for the 2-TMAI and 3-TMAI 2D/3D films, while only a minor modification happens for 2-TEAI films. More in detail, for 2-TMAI 2D/3D, the peak at 520 nm reduces in intensity in favor of the peak at 570 nm, vanishing completely after 360 min, while for 3-TMAI 2D/3D, the peak at 570 nm does not change. In both cases, a broad peak at higher wavelength grows. In contrast, for 2-TEAI the 520 nm peak is mostly unaltered (small shoulder at 550 nm appears) and no emission at longer wavelengths is observed. The broad red peak present in 2-TMAI and 3-TMAI

can be related to the formation of quasi-2D phase. This result matches with what is observed upon aging, pointing to a similar phenomenon behind such structural changes. It is worth mentioning that the aging does not degrade the 3D bulk underneath, since the absorption spectra of the films do not change (Figure A.1.15, Appendix A) and also the XRD patterns of aged and thermally stressed films show no change in the 3D structures (Figure A.1.16 and Figure A.1.17, Appendix A).

The preceding observations can be explained by the following mechanism as shown in Figure 3.1.3g. The 2D perovskite, in case of 2-TMAI and 3-TMAI, functions as a dynamical "sponge" that can embed small ions (such as MA or FA) migrating from the 3D bulk underneath immobilizing them into the new quasi-2D structure. This does not happen for the 2-TEAI 2D/3D that only physically blocks the ion at the interface, preserving the initial purity of the 2D phase (n=1). We can thus infer that the presence of a structurally robust 2D layer (such as in the case of the 2-TEAI) is paramount to control device stability, demonstrating that the purity of the layered 2D structure and its robustness against ion movement and infiltration has crucial impact on the long-term device stability. We can speculate that this intimately relates to the different packing motif of the organic cations dictated by the length of the side alkyl chain which imparts the robustness of the 2D structure.

3.1.5 Conclusion

We revealed that 2D/3D interfaces are dynamical in nature, acting as ion-scavengers and self-transforming, upon aging or thermal stress, into quasi-2D graded interfaces. In general, the deposition of 2D layer with various thiophene alkylammonium iodide cations protect the 3D layer from the degradation in the ambient air. This can improve the device performance upon dark aging, but does not lead to stable device operation under illumination. Proper engineering of the 2D/3D system, by judicious choice of the organic cation can lead to structurally stable and robust 2D overlayers (with n=1) that have a decisive role in improving device stability under illumination. A careful molecular design of large organic cation which can maintain the quasi-2D graded interface (n=2) over dark aging and thermal stress is very important to deliver both stable and efficient PSCs. These observations pave the way for new for the development of an intelligent molecular engineering approach to guide smart device design and application of stable 2D/3D interfaces even beyond PVs.

3.2 In situ analysis reveals the role of 2D perovskite in preventing thermal-induced degradation in 2D/3D perovskite interfaces

This section is based on the published work in Nano Lett., 2020, 20, 3992-3998., DOI: 10.1021/acs.nanolett.0c01271.[242] *In this work I conceptualized the idea, designed the experiments, and performed the fabrication as well as the characterizations of perovskite thin films and solar cells. Dr. N. Drigo synthesized the thiophene-based cations. In situ GIWAXS and TrPL experiments were done in collaboration with R. Szostak, Dr. J.C. Germino, and Prof. A.F. Nogueira from University of Campinas, Brazil.*

3.2.1 Introduction

Critical device stability is currently the well-known issue for market uptake.[98, 107, 136, 243-246] Behind the most recent advances, engineering multi-dimensional perovskite interfaces has been revealed as an interesting approach to improve hybrid perovskites devices lifetime mainly due to the improved humidity resistance of the 2D layer.[20, 47, 49, 51, 52, 59, 61, 200, 247-249] Examples span from large aminovaleric acid-based cations,[39] to widely used phenylethylammonium,[198] butylammonium iodide, octylammonium iodide, and dodecylammonium iodide (DAI) iodide 2D,[42] to fluorous based cations[207, 232] synthetized *ad hoc* to improve robustness against water and, more recently, thiophene-based cations.[223] In most cases, 2D perovskites simultaneously act as a surface defect passivant layer, and retard charge recombination at the interface with a positive effect on device open circuit voltage.[42, 198, 199, 207, 208, 223, 232, 250-252] On top, as mentioned above, 2D perovskites show high humidity resilience due to their increased chemical stability and hydrophobicity, which slows down device degradation.[253-256] However, so far, little is known on the role of 2D perovskite upon thermal stress, which is also a recognize cause of perovskite device degradation. This calls for a deep understanding of the interface behavior upon heating, crucial to assess device stability.[93] Here we address this need by an in-depth investigation of the 2D/3D film properties during thermal stress, monitoring the structural evolution of the interface, and their related optoelectronic and dynamical properties as well as full device behavior.

We performed combined in situ grazing incidence wide angle X-ray scattering (GIWAXS) with steady state and time resolved photoluminescence (PL) measurements on two study cases of 2D/3D perovskite systems, used in the most common highly efficient device configuration.[198, 223] They consist of a bulky thiophene- or phenyl-terminated cations in the form of 2-thiophenemethylammonium iodide (2-TMAI) or phenylethylammonium (PEAI) forming (2-TMAI)$_2$PbI$_4$ and PEA$_2$PbI$_4$ 2D perovskites, respectively which overlayer the bulk 3D perovskite

(see Figure 3.2.1a). The structural evolution of the interface is monitored upon exposing the sample to a thermal cycle, simulating the working conditions under real device operation. We reveal that a slow dynamical variation of the 2D/3D interface manifests, leading to a structural modification of the 2D perovskite structure. In concomitance, the 3D perovskite bulk if protected by the 2D layer is unperturbed while, in absence of the 2D layers, it shows visible sign of structural degradation. We thus identified a key role of the 2D capping layer in blocking the thermal degradation of the 3D perovskite bulk maintaining its structural integrity and retarding thermally-induced degradation in perovskite solar cells.

3.2.2 Device Characteristics

To create the 2-TMAI- (or PEAI-) 2D/3D thin films and devices, we dissolved the organic salts in isopropanol (IPA) and dynamically spin-coated them on the top of a triple-cations $[(FAPbI_3)_{0.87}(MAPbBr_3)_{0.13}]_{0.92}(CsPbI_3)_{0.08}$ based 3D perovskite film, where MA stands for methylammonium, FA stands for formamidinium (see experimental methods in Appendix A for details). As a result, a thin layer of 2D perovskite (~60 nm) is formed on top of the 3D bulk as shown by the scanning electron microscope (SEM) image in Figure 3.2.1a (right). While the main focus being the study of the interface structural modification, we also fabricated 2-TMAI 2D/3D and PEAI 2D/3D solar cells and we tested them upon the same thermal cycle as used for the in situ measurements. Statistics on device current-voltage characteristics and photovoltaic parameters are reported in Figure 3.2.1b-e and Table 3.2.1, respectively. It is interesting to notice that upon thermal stress the device characteristic is not that dramatically affected showing no massive effect of the thermal stress on the device efficiency. A small decrease is only observed for the device fill factor, which however does not dramatically reduce the overall device performances. Table 3.2.1 reports the device parameters comparing the fresh and the "heated" devices. This contrasts with common knowledge for 3D perovskite solar cells, showing a demonstrated reduction in device performances upon heating (see Table A.2.1, Appendix A).[257]

Table 3.2.1 Photovoltaic parameters of 2D/3D perovskite solar cells employing PEAI and 2-TMAI as the bulky cations (considering a statistic of 32 devices).

Treatment	V_{OC} (V)	J_{SC} (mA cm^{-2})	*FF*	PCE (%)
PEAI 2D/3D				
Control	1.10 ± 0.01	23.4 ± 0.2	0.74 ± 0.02	19.1 ± 0.5
Heated 50°C – 100 mins.	1.09 ± 0.01	23.2 ± 0.2	0.74 ± 0.01	18.6 ± 0.6
2-TMAI 2D/3D				
Control	1.10 ± 0.02	23.2 ± 0.2	0.74 ± 0.02	18.9 ± 0.3
Heated 50°C – 100 mins.	1.10 ± 0.01	23.1 ± 0.1	0.73 ± 0.01	18.4 ± 0.2

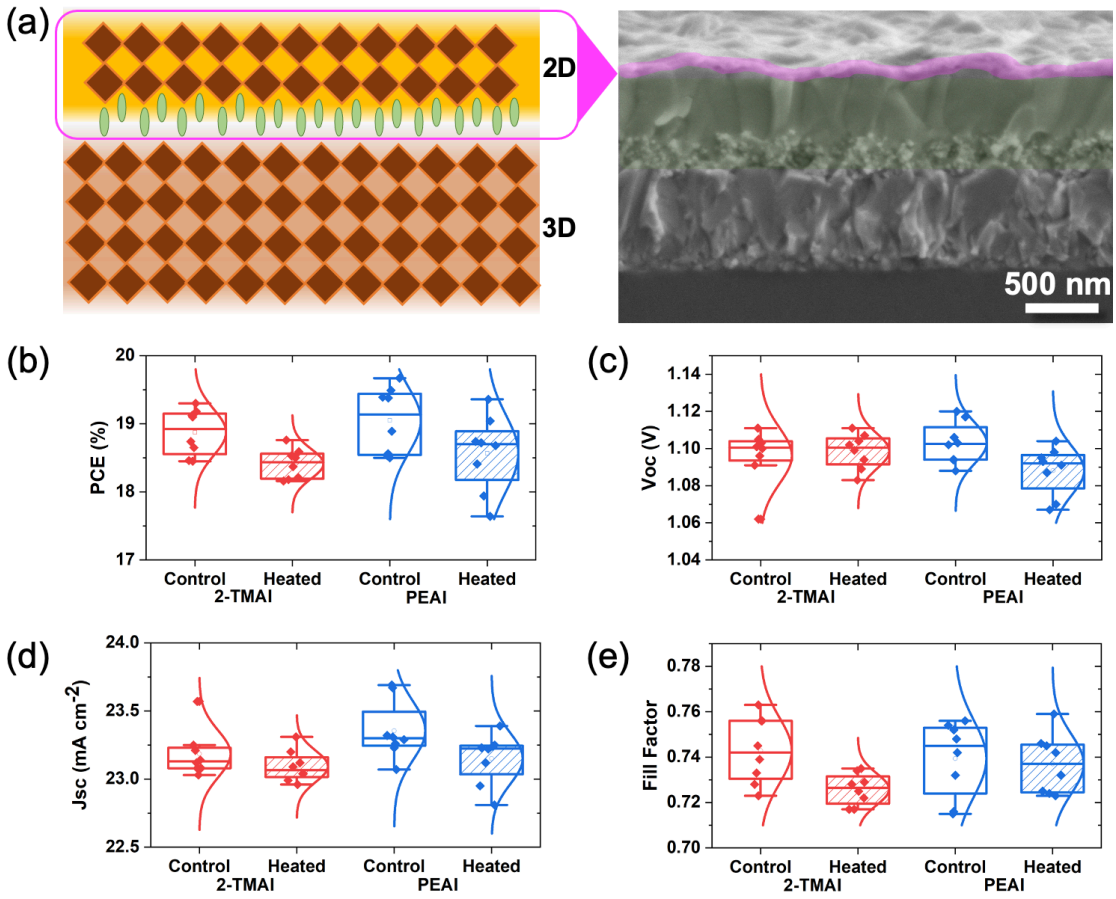

Figure 3.2.1 (a) Cartoon of the 2D/3D interface (left) and the corresponding cross-sectional SEM image of the 2-TMAI 2D/3D interface. (b), (c), (d), (e) Statistics of the device photovoltaic properties (PCE, V_{OC}, J_{SC}, *FF*) by comparing the fresh device and the thermally aged devices heated according to the thermal cycle shown in Figure 3.2.2.

3.2.3 Structural evolution under thermal stress

To get deeper insights on the 2D/3D interface role under thermal stress and its structural stability, we carried out in situ GIWAXS (measurements performed at the Brazilian Synchrotron National Laboratory (LNLS) in the XRD2 beam line, see Appendix A.2 for additional data) during a temperature cycle as schematically shown in Figure 3.2.2a. In particular, the experiment is performed under thermal annealing conditions and inert atmosphere (N_2), adopting this thermal cycle: first we raised the temperature up to 100°C after the deposition of the large organic cations, kept it constant for 6 minutes, decreased down to 50°C and kept for 160 minutes (see top chart in Figure 3.2.2b, c).

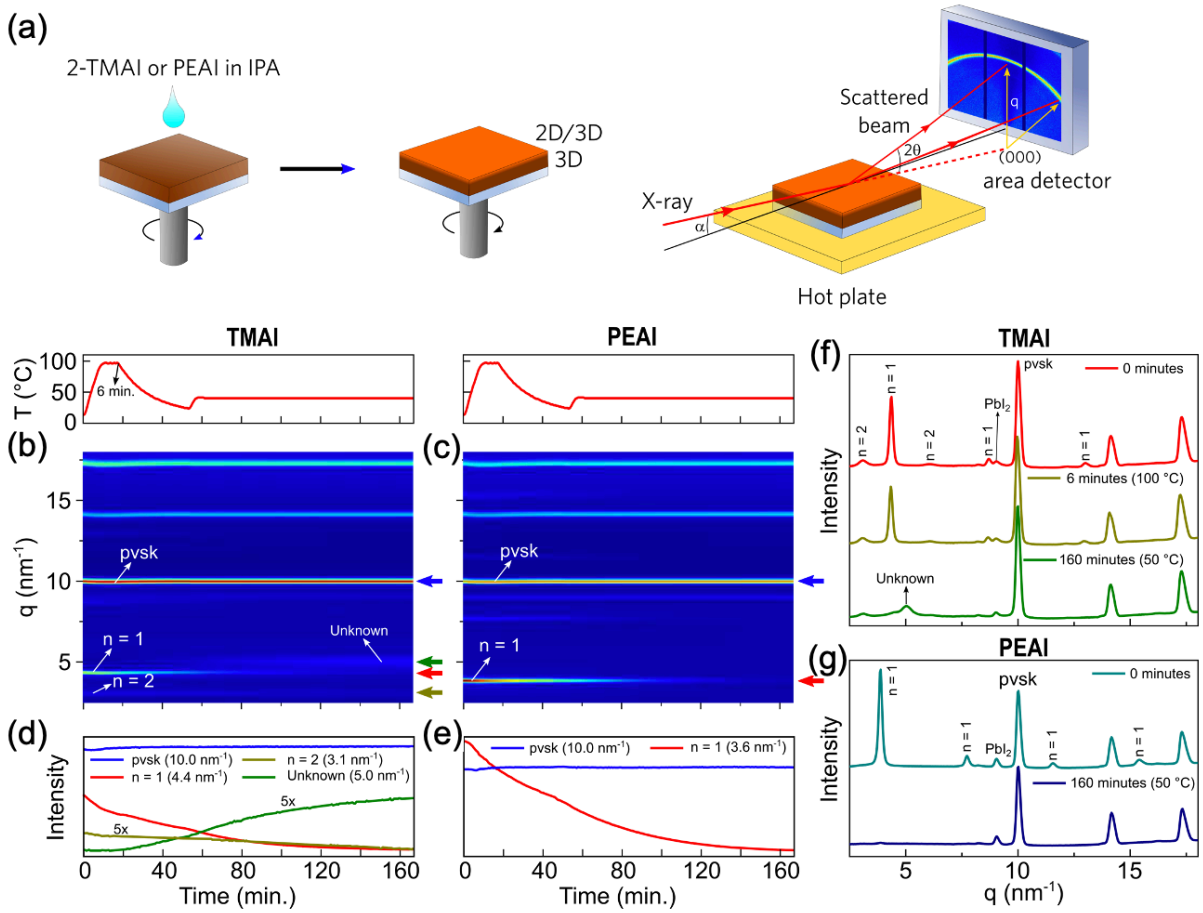

Figure 3.2.2 (a) Cartoon drawing illustrating the deposition of 2D perovskite on top of 3D perovskite and the schematic drawing of in situ GIWAXS measurement, (b), (c) In situ GIWAXS diffraction maps as a function of time and temperature for 2-TMAI and PEAI modified perovskite (pvsk) films, respectively. (d), (e) Respective intensity of the main peaks as a function of time. (f), (g) Respective X-ray diffraction patterns at different times.

Upon the spin coating of the 2D cation on top of the 3D, just after dropping the solution and in the beginning of the thermal annealing (Figure 3.2.2f, 0 minutes), we clearly observed the immediate appearance of new peaks at low q values of 4.4 nm^{-1} and 3.1 nm^{-1} for 2-TMAI. These features correspond to first order peaks of 2D perovskite layers.[223] They refer to a different structure of the 2D perovskite forming isolated single (n= 1) inorganic layers spaced by the large cation, giving the diffraction at 4.4 nm^{-1}, and to a mixed phase (commonly known in literature as quasi-2D or mixed 2D) where more than one inorganic layers (in this case is well defined with n= 2) are held together and intercalated by the large cation, giving the diffraction at 3.1 nm^{-1}, respectively. For the PEAI 2D based interface, a single n= 1 2D phase is formed, leading to the formation of pure PEA_2PbI_4 2D layer, confirmed by first order peak at q = 3.6 nm^{-1}.

In both cases, with thermal aging, the intensity of the n= 1 peak decreases (Figure 3.2.2d, e) and vanishes in the time window investigated for 160 minutes (Figure 3.2.2, g). This reveals a dynamical change of the 2D perovskite layer structure under thermal stress which loses its n=1 crystalline phase. In the case of 2-TMAI 2D/3D, also the intensity of the n= 2 peak decreases (Figure 3.2.2d, f), however, in this case, a new peak emerges in concomitance to the reduction of 2D peaks. This happens after 20 minutes, manifested as a new broader peak at q value of 5.0 nm^{-1} (Figure 3.2.2b, green curve), which keeps increasing during the thermal aging at 50°C and reaches a plateau. This peak it is not related to a 2D phase, as for the comparison of the pure n=1 and n=2 2-TMAI-based 2D perovskites (see Figure A.2.1, Appendix A). Moreover, it is neither related to any quasi-2D perovskite with $n > 2$ structure, suggesting that a mixed intermediate structure is formed at the interface. The more detailed procedure to calculate the peaks and their calculated values with $n > 2$ can be found in the Appendix A and in the Table A.2.4, respectively.

On the other hand, in the case of PEAI 2D/3D no further evolution is observed upon thermal aging. Figure 3.2.2 also reports the diffraction signal related to the 3D perovskite structure. It is remarkable to notice that the mutation only alters the 2D superficial layer, while the 3D perovskite underneath remains unaltered and stable (Figure 3.2.2d,e). Repeating the same measurements for the bulk 3D perovskite, the behavior is strikingly different: in this case, see Figure A.2.2 (Appendix A), the 3D peak reduces by 15% in magnitude, revealing a clear material degradation upon heating, in agreement with common knowledge. On the contrary, when the 2D overlayer is present (Figure 3.2.2d, e), 2-TMAI and PEAI, no reduction was observed. This provides compelling evidence of the fundamental role of the 2D perovskite in enhancing the robustness of the 2D/3D system, with a special action on improving the thermal stability of the 3D perovskite underneath.

3.2.4 Photophysical evolution under thermal stress

To confirm and better elucidate the structural changes in the 2D layer, we monitor the PL spectral evolution, as a sensitive probe of the material band gap and variation thereof, indicative of any possible structural change (i.e., n variation), following a similar thermal cycle, as shown in Figure 3.2.3.

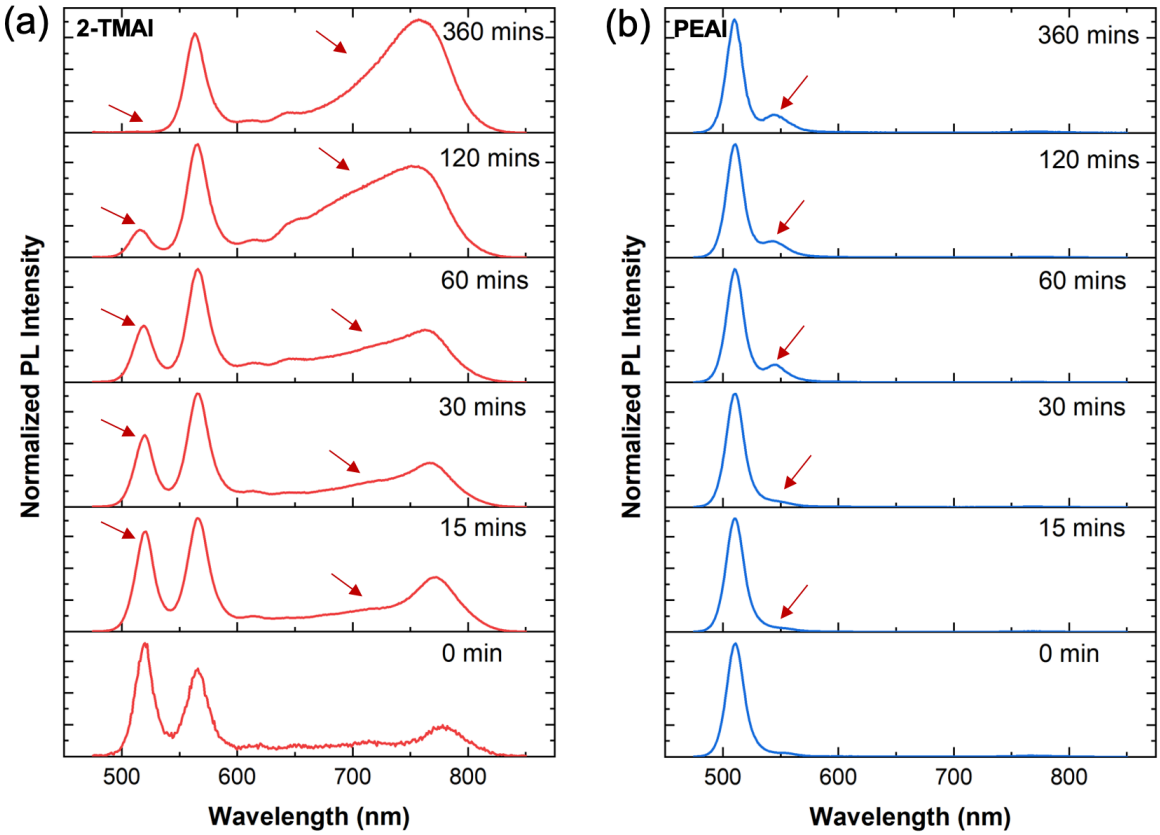

Figure 3.2.3 PL spectra of (a) 2-TMAI 2D/3D and (b) PEAI 2D/3D perovskite thin films upon thermal aging at 50°C and excitation at 450 nm from the front (in other words, from the 2D side).

As the PL spectra were recorded from the front side (2D perovskite side) of 2D/3D film, they mainly show the emission from the 2D perovskite top layers. The PL measurements were carried out after thermal annealing at 100° C and without heating at 50°C (time 0 for PL characterization). At time 0, the 2-TMAI 2D/3D film PL spectrum shows two emission bands centered at 519 nm and 567 nm, while the PEAI 2D/3D film shows only one band at 510 nm and a small shoulder at 555 nm. According to literature, these bands correspond to the emission from n=1 and n=2 phases of 2D perovskites, respectively,[223, 258] in excellent agreement with the GIWAXS results. From the normalized PL spectra reported in Figure 3.2.3 it is also evident that for the 2-TMAI 2D based interface a broader emission in the 700-800 nm spectral range gradually appears during the annealing process. This suggests the formation of a mixed disordered phase,[259, 260] in agreement with the GIWAXS data. On the other hand, for PEAI 2D/3D, the variation of the shape of PL spectra is less dominant, while the absolute intensity (reported in Figure A.2.3a, Appendix A) of the n=1 PL peak abruptly diminishes, in agreement with the GIWAXS data. This suggests that PEAI-based 2D is structurally more robust and less prone to form a quasi-2D (n>1) phase under this condition.[52, 261] Similar behavior of the intensity

is observed for the 2-TMAI 2D based interface, showing a decrease of the *n*=1 PL peak and a concomitant increase of the broader emission at longer wavelength side (Figure A.2.3b, Appendix A). These measurements prove a dynamical variation of the 2D-surface perovskite bandgap. To gain a deeper understanding on the mechanism behind such dynamical structural/band gap evolution, we also measured the PL spectra of the 2D/3D perovskite films upon aging the film for a long-time window of seven weeks without any heating. The films were stored in a dark and dry environment (RH <20%) at room temperature and the PL spectra periodically recorded over time. Interestingly, we observe an analogous modulation of the emission features for both 2-TMAI 2D/3D and PEAI 2D/3D over slow dark aging as shown in Figure A.2.4 (Appendix A). This phenomenon indicates that a similar transformative process happens even at room temperature, over several-weeks time window, while being accelerated under thermal stress. We can rationalize our results considering an intrinsic dynamical evolution of the 2D/3D perovskite interface upon aging which manifest as: i) de-structuration of the 2D perovskite overlayer; ii) formation of an additional mixed phase at the interface; all combined with iii) improved resilience to degradation of the 3D perovskite bulk underneath independently from the 2D cation used.

Finally, it is worth pointing the attention to the fact that device performances with the 2D overlayer do not dramatically reduce upon heating, despite the interface structural rearrangement. This is due to the role of the 2D perovskite which preserves the 3D bulk nature and function. To better analyze the interfacial processes, we implemented time-resolved PL (TrPL), with the idea to monitor the charge carrier dynamics in the 3D bulk upon the thermal cycle. The thermal aging for TrPL measurement was performed under the same condition as in steady state PL measurement. Results are reported in Figure 3.2.4 for the 2D/3D interface (blue and red) compared with the controller samples without the 2D layer. It is worth noticing that, upon thermal aging, the PL signal of the bare 3D film shows an enhancement of the lifetime with a marked long living tail. This happens at time 0, but is even more evident after 15 minutes of annealing, and it continues to increase up to 360 minutes of thermal aging (Figure A.2.5, Appendix A). This stem true also for the 2D/3D interface, where the increase in the lifetime is even more evident. We can attribute the longer living signal to a beneficial effect of the restructuring of the interface, leading to surface passivation effect and retarded surface charge carrier recombination.[239, 259]

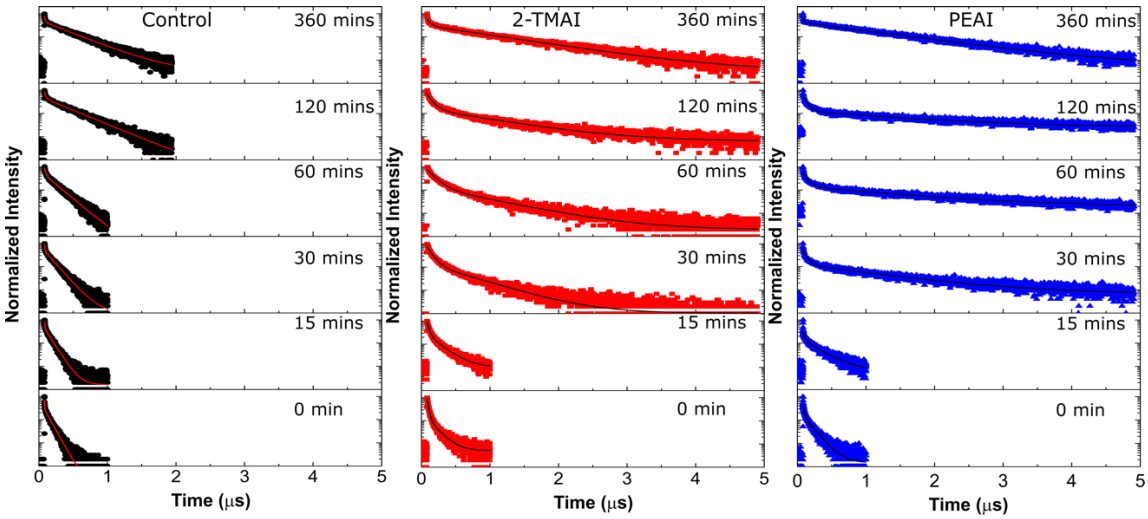

Figure 3.2.4 TrPL decays (λ_{exc} = 440 nm; F = 9.7 nJ cm^{-2}; λ_{PL} at the maximum of the 3D at 780 nm emission at 50°C in the samples) of the 2D/3D modified perovskites: 3D control (black); 2-TMAI (red); and PEAI (blue). The fits of the decays are also shown.

3.2.5 Conclusion

In conclusion, the in situ structural and optical analysis on 2D/3D perovskites interfaces and devices give a compelling proof of an intrinsic dynamical structural variation of the 2D perovskite layer after thermal stress which i) protects the 3D perovskite from degradation regardless of the 2D perovskite phases evolution upon heating; ii) does not perturb the dynamical processes at the interface and iii) is beneficial to keep the device performances unaltered under thermal stress. Our results have highlighted the key role of the 2D surface functionalization in retarding perovskite degradation upon thermal stress, providing a clear direction on how to gain on perovskite device longevity.

3.3 Conclusion

In this chapter, we have investigated in depth the role of the 2D perovskite on top of 3D perovskite in improving PSCs stability. In general, the 2D perovskite protects the 3D bulk perovskite underneath, leading to a stable device performance upon exposure to ambient atmosphere, continuous light illumination, and heat. This study reveals that the degradation mechanism of the 2D perovskite is highly dependent on the large organic cation used. When the 2D perovskite structure is not robust enough, the 2D phase will transform to the quasi-2D phase with a larger *n* number upon the aging in the dark. Interestingly, when the 2D perovskite is structurally robust, there is no phase transformation observed, leading a significant improvement in the long-term device stability. In addition, we discover that the 2D/3D interface

with the quasi-2D perovskite (i.e., n= 2) exhibits a higher photovoltaic performance than the one incorporating a pure 2D perovskite phase (n= 1). Nonetheless, the quasi-2D perovskite is prone to the phase transformation over the aging period. Thus, finding a large organic cation which could form a structurally stable quasi-2D perovskite is important for attaining both efficient and stable PSCs.

Further, the dynamic structural evolution of the 2D/3D perovskite interface have been also observed upon the thermal aging. However, the 2D perovskite layer effectively prevents the thermal degradation of the 3D perovskite regardless the structural transformation observed. Despite the dynamical structural variation of the 2D/3D perovskite interface, the charge dynamics are not significantly affected after heating. As a result, the incorporation of 2D/3D perovskite also improves the durability of the device upon the heat exposure. These findings provide a critical understanding on how the engineering of 2D/3D perovskite interface could increases the PSCs lifetime.

Chapter 4: 2D/3D Perovskite Engineering Eliminates Interfacial Recombination Losses in Hybrid Perovskite Solar Cells

Interface engineering and design is paramount in the optimization of multilayer device stack. This stems true for multi-dimensional (2D/3D) perovskite solar cells, where high efficiency can be combined with promising device durability. However, the ultimate complex function of 2D/3D device interface remains vague. Here, we provide the exact knowledge on the interface energetics and we demonstrate that the 2D/3D perovskite interface forms a *p-n* junction able of reducing the electron density at the hole transport layer interface and ultimately suppressing interfacial recombination. As a consequence, we demonstrate photovoltaic devices with enhanced fill factor (*FF*) and open-circuit voltage (V_{OC}) of 1.19V which approaches the potential internal Quasi-Fermi Level Splitting (QFLS) voltage of the perovskite absorber, nullifying the interfacial losses. We thus identify the essential parameters and energetic alignment scenario required for 2D/3D perovskite systems in order to surpass the current limitations of hybrid perovskite solar cell performances.

This chapter is based on the published work in Chem, 2021, 7, 1903-1916, DOI: 10.1016/j.chempr.2021.04.002.[262] *In this work I conceptualized the idea, designed the experiments, and performed the fabrication as well as the characterizations of perovskite thin films and solar cells. Dr. N. Drigo synthesized the thiophene-based cations. V.I.E. Queloz carried out the steady state PL measurements. The PLQY experiment, QFLS calculation, and drift diffusion simulation were performed in collaboration with Dr. P. Caprioglio and Dr. M. Stolterfoht from University of Postdam, Germany. The UPS depth profiling measurements were carried out in collaboration with Y.J. Hofstetter and Prof. Y. Vaynzof from Technical University of Dresden, Germany.*

4.1 Introduction

Understanding and exploiting interfacial physics is the key in perovskite solar cell engineering and optimization.[263, 264] That is especially true when interface losses play a dominant role and complex interface functionalization is essential to minimize them. In the field of hybrid perovskite engineering, much attention has been lately focused on multi-dimensional perovskite interfaces consisting of a wider band gap layered (namely, two dimensional-2D) perovskite deposited between the bulk 3D perovskite and the hole transporting layer (HTL) in a standard mesoporous configuration.[39, 42, 198, 199, 207, 223, 232] Such configuration is currently among the most effective strategies to enhance both the efficiency and stability of perovskite solar cells.[39, 206, 208, 250, 265, 266]

It is generally considered that the 2D perovskite acts as both an efficient mean to passivate the surface traps (leading to reduced defect recombination) and an electron blocking layer due to its wider band gap.[150, 209, 212, 239, 267, 268] However, despite these empirical observations, the energetic alignment at the interface and the relative function of the 2D/3D interface is only qualitatively depicted with only a partial understanding of these aspects. This lack of knowledge prevents the advancement of device efficiencies towards the theoretical Shockley-Queisser predictions beyond the common trial and error approach.[269] More specifically, the exact role of the interface band structure and energetics and their effect on the processes and loss mechanisms remains largely unexplored, mainly due to the lack of direct experimental evidences.

In this work we target the interface energetics of optimized 2D/3D perovskite systems by measuring the vertical energy level landscape by an innovative UPS depth profiling technique. The analysis reveals intriguing variations of the interfacial energetics which depend on the chemical nature of 2D overlayer. Specifically, we explore a series of thiophene based cations that form the 2D perovskite layer, which differ slightly in their chemical structure, and which when integrated in a 2D/3D based perovskite solar cell, deliver approximately 21% power conversion efficiency (PCE) and open-circuit voltage (V_{OC}) approaching 1.2 V. The photovoltaic performance is intimately linked to 2D/3D interfacial band bending and a natural formation of a *p-n* junction in optimal devices.

By calculating the quasi-Fermi level splitting (QFLS) from photoluminescence quantum yield (PLQY) for the neat material and the complete device, we identify that the optimal energetic alignment and reduced electron density at the interface serve as the reasons for such a significant reduction in the non-radiative interfacial recombination losses. This allows us to reach radiative efficiencies of 2% in completed devices which is far above average.[264] Importantly,

the recombination mechanisms proposed is corroborated by drift-diffusion simulation. The optimized 2D/3D interface shows zero interfacial voltage losses, reaching the QFLS-potential of the neat perovskite absorber and thus nullifying the energy losses at the interfaces. As such, we rationalized the mechanisms and the effect of 2D/3D interfaces on the effective reduction of the interfacial energy losses, providing a clear path for pushing perovskite solar cells performances closer to their theoretical limits.[264]

In particular, we elucidate the fundamental principles of how the creation of 2D/3D heterojunctions and the energy alignment at the hole-selective interface allow us to overcome the decisive interfacial recombination losses of minority carriers at the interface to spiro-OMeTAD interface. This is achieved with a 2-thiophenemethylammonium bromide (2-TMABr) based 2D perovskite layer which forms an apparent *p-n* junction with the perovskite, thereby blocking the minority carriers from reaching the spiro-OMeTAD layer. Notably, in this system, the main voltage loss is only due to non-radiative recombination in the perovskite absorber layer, while interface recombination is essentially absent. This finding bares important implications for further perovskite design as several perovskites now achieve radiative efficiencies that are very close to the radiative limits.[101, 176, 264, 270, 271] Hence, our approach to effectively suppress the interfacial recombination may hold the key to create near ideal perovskite cells in the near future if applied to perovskite layers with very high PLQYs.

4.2 Thin-films and devices characteristics

The 2D/3D interfaces investigated here are based on a novel set of bulky thiophene-terminated cations, namely 2-thiophenemethylammonium iodide (2-TMAI),[223, 242] 2-thiophenemethylammonium bromide (2-TMABr), and 2-thiophenemethylammonium chloride (2-TMACl) that serve as a building block for the formation of the 2D perovskite layer on top of 3D bulk layer (Figure 4.1a). The 3D perovskite layer is based on a triple-cation composition $[(FAPbI_3)_{0.87}(MAPbBr_3)_{0.13}]_{0.92}(CsPbI_3)_{0.08}$ with a bandgap of 1.610 eV. The chemical structures of the thiophene-methylammonium salts are shown in Figure 4.1b. The three different 2-thiophenemethylammonium halides (2-TMAX, where X: Cl, Br, I) were prepared from the commercially available amines and the corresponding acids (see experimental methods). The salts were then diluted in isopropanol (IPA) and dynamically spin-coated on top of the triple-cation based 3D perovskite film. 2D perovskites are selectively grown by controlling the excess PbI_2 composition (PbI_2:FAI = 1.05:1) in the 3D perovskite which reacts with the thiophene ammonium halide cations to form the 2D layer.[198, 223, 242]

Figure 4.1b shows also the X-ray diffraction (XRD) patterns of the 2D/3D films collected at a low diffraction angle. When the 2-TMAX is used to coat the 3D layer, intense reflexes at 4.3° and 8.6° appear at the XRD diffractograms, consistent with the key characteristic peaks of 2D perovskites (n=2).[223, 242] In case of 2-TMAI, an additional reflection at 6.1° was observed which corresponds to the n=1 phase of 2D perovskite.[223] The XRD pattern of 3D perovskite layer as the control are reported on Figure B.1 (Appendix B). Cross-sectional scanning electron microscopy (SEM) images shown in Figure 4.1c show that the 500 nm thick 3D perovskite layer is continuously coated by a 2D overlayer with a thickness of approximately 50-60 nm. The top surface images reveal that the formation of the 2D layers results in smoother surfaces, with less defined grain boundaries and crystals borders. This is particularly evident for the cases of 2-TMAI and 2-TMABr, while for the case of 2-TMACl a distribution of distinct phases with larger and more elongated grains is visible.

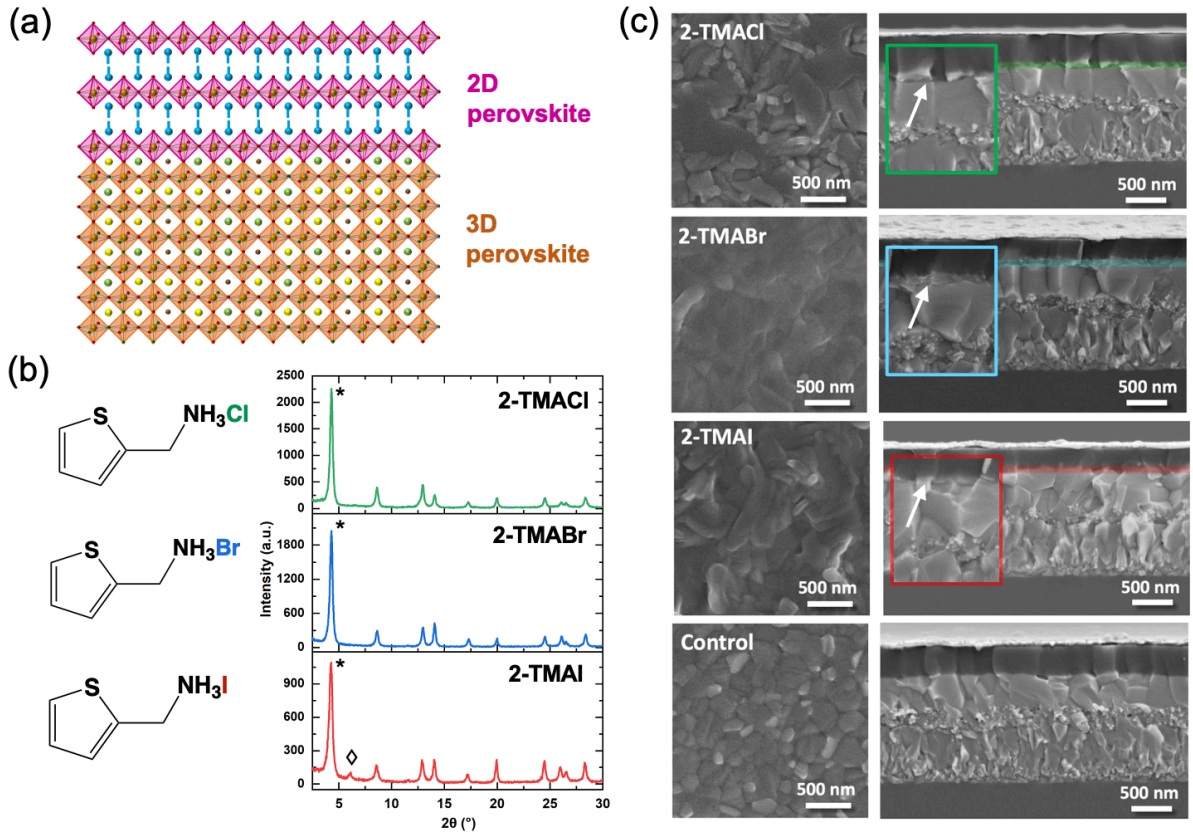

Figure 4.1 Structural and morphological characterization of 2D/3D perovskite films. (a) Schematic illustration of the 2D/3D perovskite interface. (b) Molecular structure (left) and X-ray diffraction (XRD) pattern at 2° incident angle of the 2D/3D film employing 2-TMAI, 2-TMABr, and 2-TMACl respectively (◊ and * denote 2D perovskite phase with n=1 and n=2, respectively). (c) Top view (left) and cross-section (right) micrographs of the 3D only device as

control and the 2D/3D perovskite solar cells (PSCs) employing 2-TMAI, 2-TMABr, and 2-TMACl. Insets show the magnified cross-section micrographs on the 2D/3D interface.

The absorption spectra of the 2D/3D thin films are reported in Figure B.2 (Appendix B), while Figure B.3 (Appendix B) shows the PL spectra upon excitation from the front side of the film. Notably, in all cases, a clear peak at lower wavelength region is observed, confirming to the formation of a distinct 2D perovskite overlayer. 2-TMAI-based 2D/3D exhibits PL emission peak at 520 and 570 nm which corresponds to *n*=1 and *n*=2 phase of 2D perovskite, respectively. On the other hand, 2-TMABr and 2-TMACl-based 2D/3D only show an emission peak at low wavelength region (~545 nm) which is associated to *n*=2 phase. More in details, in agreement with what we recently reported,[223] the 2-TMAI-based 2D/3D shows a slightly reduced band gap with respect to the 2-TMABr and 2-TMACl, as revealed by the photoluminescence peak emission shift (of around 0.1eV) in Figure B.3 (Appendix B).

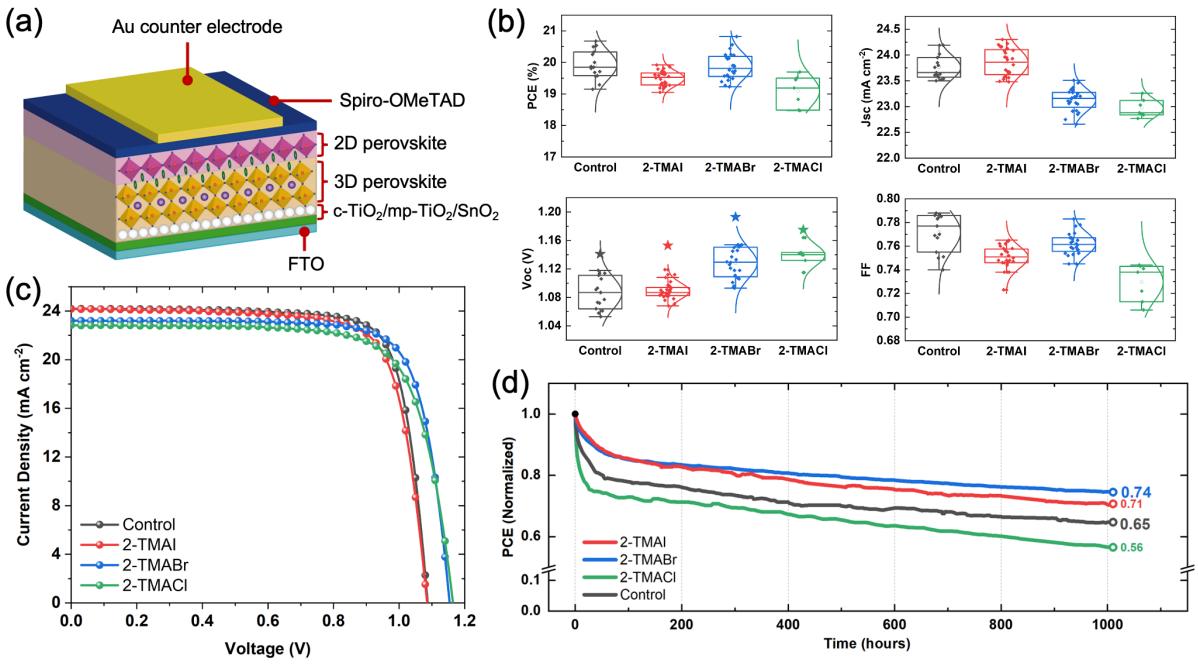

Figure 4.2 Photovoltaic performances of 2D/3D PSCs. (a) Schematic device structure of the 2D/3D PSCs. (b) Statistics of the photovoltaics parameters of 3D PSCs as a control and 2D/3D PSCs based on 2-TMAI, 2-TMABr, 2-TMACl on over 70 devices. Note that the stars symbols in the V_{OC} subpanel represent the V_{OC} measured without using a mask. (c) *J-V* curves of the champion cells of 3D and 2D/3D PSCs employing 2-TMAI, 2-TMABr, and 2-TMACl. (d) Stability test under continuous 1 sun illumination for 1000 h in inert gas (Ar) atmosphere without any encapsulation. The stability data of 2-TMAI 2D/3D and control device were collected from the same experimental batch from Chapter 3.1 for a fair comparison.

The photovoltaic (PV) response of the 2-TMAX based 2D/3D perovskite solar cells are shown in Figure 4.2 with the PV parameters for champion devices summarized in Table 4.1 (Appendix B). The statistics of the photovoltaics parameters are compiled in Table B.1, while the hysteresis measurements are reported in Figure B.4 and Table B.2 (Appendix B). With respect to the control, a clear increase in the V_{OC} is observed with the 2D perovskite layer, higher for 2-TMABr and 2-TMACl. It is important to note that the device V_{OC} reported here is underestimated due to the use of a small mask (0.16 cm^2) on a large pixel (0.54 cm^2). The reduction in V_{OC} values due to the mask effect could be calculated by the equation $\Delta V_{OC} = kT/q \ln(A_{aperture}/A_{device})$ where kT/q is the thermal voltage, $A_{aperture}$ is the mask aperture, and A_{device} is the pixel area.[272] Considering that the dark current of the pixel is not affected by the mask, this implies a ~3.4-fold overestimation of the dark saturation current (J_o), which is equivalent to a voltage loss of 31 mV. By measuring without mask, the real maximum device voltage (shown by stars in Figure 4.1b) for the reference cell is 1.141 V, while for 2-TMAI, 2-TMABr and 2-TMACl, they are 1.153 V, 1.193V and 1.175V, respectively (see also Figure B.5, Appendix B), among the highest values reported so far for *n-i-p* devices with a mesoporous structure.

Table 4.1 Photovoltaic parameters of the champion PSCs based on 3D perovskite and 2D/3D perovskite hybrids employing 2-TMAI, 2-TMABr and 2-TMACl tested under AM 1.5G illumination (100 mW cm^{-2}).

	V_{OC} (V)	J_{SC} (mA cm^{-2})	*FF*	PCE (%)
2-TMAI/3D	1.09	24.2	0.76	19.9
2-TMABr/3D	1.15	23.2	0.78	20.8
2-TMACl/3D	1.16	22.8	0.74	19.7
Control	1.09	24.2	0.79	20.7

Importantly, the 2-TMABr shows a remarkable increase in V_{OC}, without compromising the fill factor (*FF*) which remains comparable to the control device, resulting in an overall increase in the device efficiency. On the other side, 2-TMACl shows a reduction of the *FF*. The highest PV performance is therefore achieved with 2-TMABr-based 2D devices delivering a power conversion efficiency (PCE) of 20.82%. We note that in this series of 2D perovskites, a slight decrease in the short-circuit current (J_{SC}) is observed. The J_{SC} values obtained from the *J-V* measurements are in agreement with the calculated J_{SC} from the external quantum efficiency (EQE) spectra (Figure B.6, Appendix B). This decrease might be related to the limitation in the charge transport induced by the presence of the bulky organic moieties. The long-term stability of the devices was monitored under continuous illumination of 1-sun intensity for 1000 hours in

an argon atmosphere and is shown in Figure 4.2d. While the performance of the standard 3D device is reduced to 65% of its initial PCE, the 2D-functionalized solar cells show a reduced loss in the PCE with the 2-TMABr/3D devices displaying the best stability retaining 75% of the initial PCE after 1000 hours. This confirms that the 2D surface functionalization has a crucial impact on the device lifetime with best performances reached with the 2-TMABr based 2D perovskite. 2D/3D perovskite devices are demonstrated to be highly sensitive to the nature of the organic cation which impact on the device V_{OC} and *FF*.

4.3 Energetical landscape of the 2D/3D interfaces

To elucidate the link between material properties and device performances, it is necessary to directly probe the energetic alignment of the 2D/3D interfaces. Traditional methodology based on UPS measurements is only capable of probing the top 1-2 nm of the surface and will not provide insights regarding the buried 2D/3D interface. Recently, we developed a method termed ultra-violet photoemission spectroscopy (UPS) depth profiling technique, which allows probing the energetic landscape at the bulk of materials and across buried interfaces.[273] The principle of the technique is shown in Figure 4.3a and is based on the essentially damage-free etching enabled by Argon gas-cluster ion beams (1) in combination with UPS measurements (2) after each etching step. While this method has been previously applied solely to organic systems and organic/inorganic systems,[274-276] this is the first example of its application for the study of perovskite materials. Using this method, we are able to accurately measure the progression of the vacuum level and valence band positions as a function of film depth as depicted in the illustration in Figure 4.3b, providing for the first time an in situ measurement of the interfacial energy levels alignment in a 2D/3D system (Figure 4.3c). The position of the conduction band is then estimated by adding the corresponding optical gap.

The UPS measurements reveal that the ionization potential (IP) of the 2D and 3D perovskites are all very similar (in the range 6.2-6.6 eV). This is in agreement with previous studies on BA_2PbI_4 (IP=6.5 eV) and BA_2PbBr_4 (IP=5.8eV),[277] the IP values of which were found to be in good agreement with those of the corresponding 3D perovskites.[278, 279] The similarity of the IPs is also in agreement with the results of Zhang et al., that observe a change in IP of only 0.1 eV between the 3D and the 2D perovskites they investigated.[277] The matching IPs explain why 2D perovskites can serve as capping layers for 3D perovskites in the *n-i-p* architecture in which they can permit the extraction of holes, whilst blocking electrons due to their higher lying conduction band.

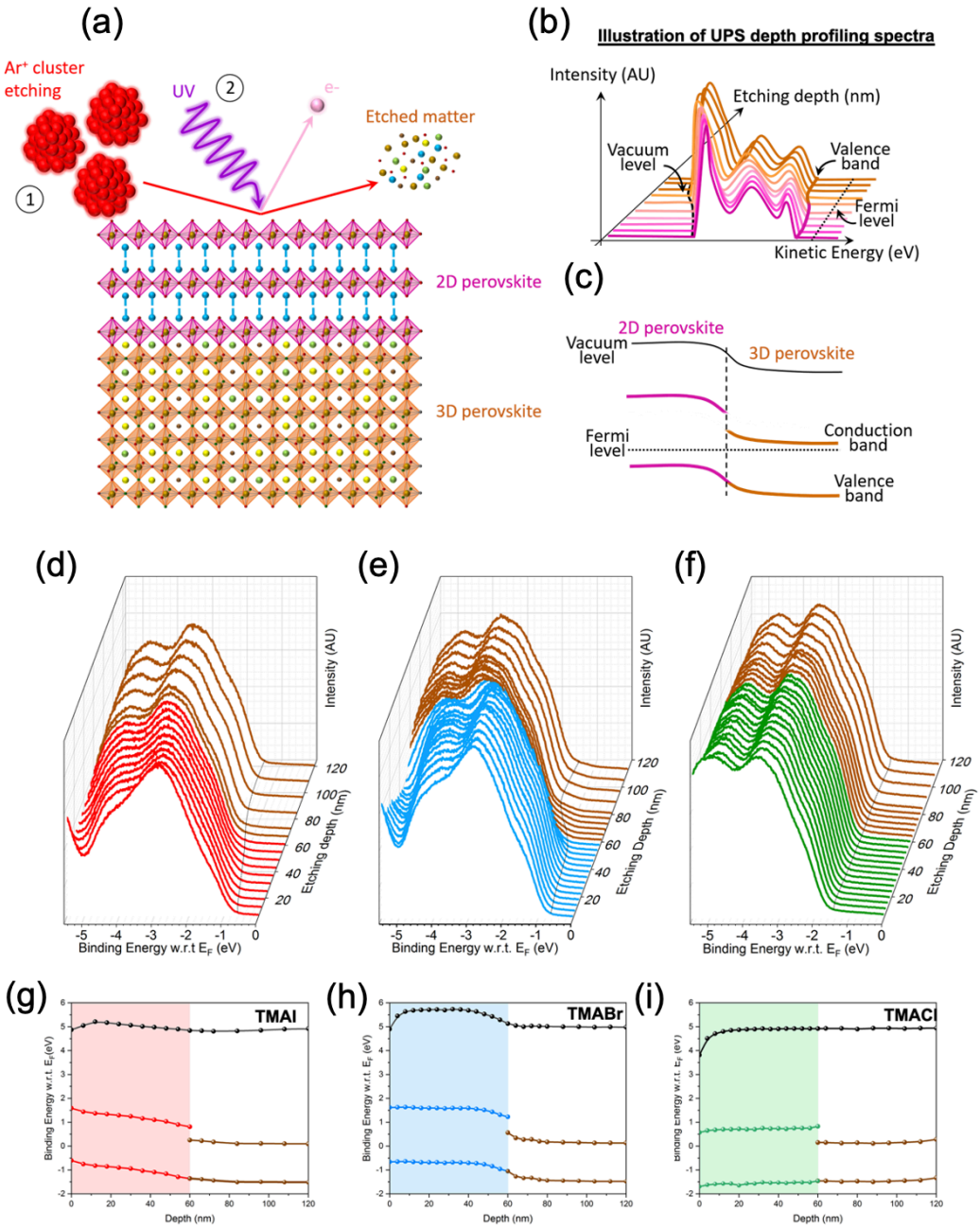

Figure 4.3 UPS depth measurement of 2D/3D perovskite interface. (a) Schematic representation of the UPS depth profiling technique which combines (1) etching by Ar ion clusters with (2) UPS measurements. (b) Illustration of the evolution of the UPS spectra as a function of depth. (c) The corresponding energy level diagram extracted from (b). (d-i) Measured UPS spectra and corresponding energetic level diagrams of 2-TMAI (d,g), 2-TMABr (e,h), and 2-TMACl (f,i) with the 3D perovskite layer. Note: dashed line in UPS spectra is a guide to the eye.

While the ionization potentials of the materials are similar, UPS depth profiling of the three sets of 2D/3D samples reveals significant differences in their interfacial energetic alignment. Examining the band structure, it is clear that exchanging the halide on the bulky cations has important consequences for the evolution of the valence band levels: i) 2-TMABr and 2-TMAI show a shift in valence band compared to the 3D perovskite, indicating an effective energy level alignment to promote hole extraction, while 2-TMACl exhibited an opposite trend, with a slight uphill energy barrier (over the entire 2D layer). This results in the first two cases in the formation of a *p-n* junction which promotes charge extraction. Notably, this is consistent with the low FF observed in the 2-TMACl 2D/3D devices. ii) All the 2D/3D interfaces exhibit excellent electron blocking properties, with the energetic barrier being enhanced from 0.55 eV for 2-TMAI to 0.63 eV and 0.68 eV for 2-TMABr and 2-TMACl, respectively. The improvement in electron blocking suggests a more efficient reduction of minority carriers at the HTL interface of the device, in good agreement with corresponding enhancement in the open-circuit voltage observed from the photovoltaic results.

Notably, in all cases, the 3D perovskite is *n*-type, in agreement with the PbI_2 excess used in this case (see reference measurement on a 3D film in Figure B.7, Appendix B).[279] Surprisingly, while the 2D layer formed by the 2-TMACl cation follows a similar character to that of the 3D perovskite, 2-TMABr and 2-TMAI denote a clear transition toward a *p*-type material. Such a transition is responsible for the formation of a *p-n* junction at the interface offering the possibility to improve the charge extraction and reduce interface recombination. This is particularly evident for the 2-TMABr case as well as for the 2-TMAI case, while it is less manifested at the 2-TMACl based interface, possibly due to a less homogeneous 2D surface layer (see SEM top view in Figure 4.1c). As such, this proves that band bending happens at optimized 2D/3D perovskite interface, contributing in improving the device performance, as reported for other PV technologies.[280] Similar formation of a *p-n* junction also occurs for other cations such as 2-thiopheneethylammonium iodide (2-TEAI) and 3-thiophenemethylammonium iodide (3-TMAI) (Figure B.8, Appendix B) which also show high photovoltaic performance as reported in Chapter 3.1.[223]

These results are also supported by numerical drift-diffusion device simulations, based on a well-established model,[153, 281-285] which compare the effect of the additional 2D layer and the different energetic alignment scenarios based on the experimental results obtained for the reference 3D sample, 2-TMABr and 2-TMACl (Figure B.9a-c, Appendix B). The effect of the enhanced electron blocking at the 2D/3D interface is evident when comparing the carrier densities in the proximity of the HTL interface (Figure B.9d-f, Appendix B, dashed red circle).

In the case of 2D/3D systems, the electron density at that interface is significantly reduced when compared to the reference 3D case. In excellent agreement with the experimental *J-V* results, when incorporating the 2-TMABr layer into the device structure, the simulated V_{OC} increases from ~1.14V to ~1.19V (Figure B.9g, Appendix B). This increase can be attributed to the strong reduction of the electron density in the 2D in the proximity to the HTL which effectively limits the interfacial recombination losses (see Figure 4.3h).[286] Overall, in case of the 2-TMABr cation, the band bending reduces the electron accumulation at the interface with the HTL, thereby reducing charge recombination while effectively driving holes to the HTM without inducing FF losses. Together these processes provide an effective mean to eliminate the severe non-radiative recombination loss at the HTM/perovskite interface.

4.4 Photophysical characteristics

To further corroborate these findings and to understand the physical processes governing these 2D/3D interfaces triggering the improvement in device V_{OC}, we measured the PL spectra as shown in Figure B.10a-b and we calculated the photoluminescence quantum yield (PLQY, Figure B.10c, Appendix B). The PLQY values were then used to derive the quasi-Fermi level splitting (QFLS) in neat materials and complete solar cell devices as shown in Figure 4.4. This analysis allowed us to assess the relative contribution of bulk and interfacial recombination losses, but also the impact of the interfacial energy alignment.[153, 264, 287] We note that the neat materials exhibit PLQYs over 1% (see Figure B.10a,c, Appendix B), which is quite typical for mixed perovskites. The results also highlight that the addition of a 2D layer improves the QFLS of the neat perovskite absorber (triangle in Figure 4.4a) indicating a trap passivating behavior and/or a reduction of minority charges at the defect-dense perovskite surface in the presence of the 2D layer.[264] More importantly, however, the PLQY of the 2-TMABr device approaches 2% which is far above average (see Figure B.10b,c, Appendix B).[283] The deviation from the Shockley-Queisser radiative limit V_{OC} is due to mainly two factors. The first one is the non-radiative recombination in the perovskite absorber. As observed from the PLQY of the neat materials, the QFLS is already limited to roughly 1.25 eV, indicating a certain degree of recombination limiting the potential V_{OC}. The second limiting factor is interface recombination between the perovskite and the transport layers. Usually, the latter is strongly limiting the V_{OC} of Pb-based perovskite cells. Notably, in our 2D/3D system, since the QFLS of the neat materials matches with good degree to the V_{OC} of the complete device, the main voltage loss is only due to non-radiative recombination in the perovskite absorber layer, while interface recombination is essentially absent.

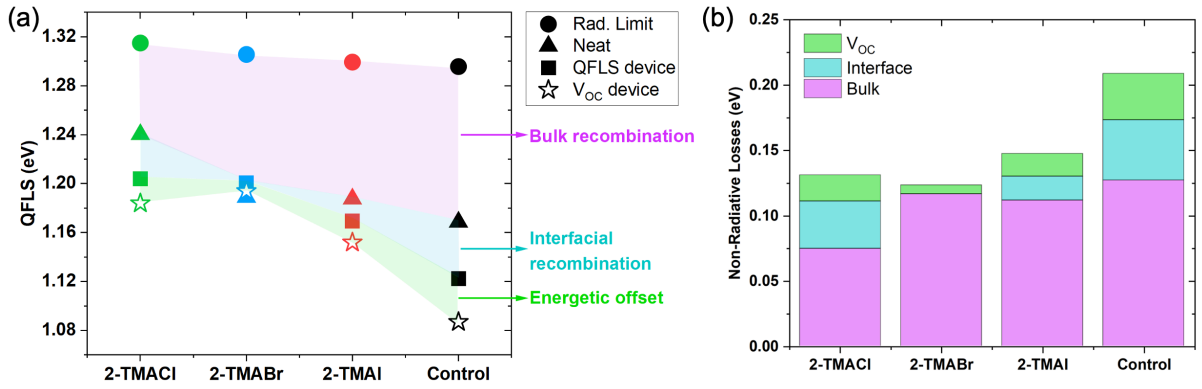

Figure 4.4 Calculated QFLS and calculated energy losses due to non-radiative recombination. (a) QFLS calculated from the PLQY for the neat material and the full device for the different samples investigated in the study. Moreover, the Shockley-Queisser radiative limit and the experimental V_{OC} are plotted for each sample. (b) Different type of energy losses calculated from (a) in order to compare the contribution of the different recombination processes for each system.

Figure 4.4 further shows that the trend in the non-radiative recombination losses in the devices as determined from the PLQY (squares in Figure 4.4a) follows the trend observed in the *J-V* measurements. Interestingly, when the QFLS of the device is compared to the QFLS of the neat material, we found that all devices that employ the 2D layer display smaller energy losses due to less interfacial recombination losses compared to the reference cell. This confirms a key conclusion from the UPS measurements and the numerical simulations, which is that the 2D layer effectively reduces the density of minority carriers at the HTL interface. Importantly, the device based on 2-TMABr as cation exhibits an equal QFLS in the neat material and in the complete device, which is also approximately equal to the device V_{OC} (stars in Figure 4.4a). This highlights the presence of a lossless perovskite/HTL interface and that the 2-TMABr 2D/3D layer enables to reach the QFLS-potential of the neat perovskite layer.[264] These results are in accordance to the UPS depth profiling and simulations data. However, in the case of the reference device and to a lesser extend in the devices with the other 2D layers, the internal QFLS is considerably higher than the external V_{OC}. As recently discussed, this effect can be explained by an internal bending of the hole quasi Fermi level, which impacts primarily the device V_{OC} rather QFLS in the perovskite layer and suggesting an energy misalignment between the perovskite and the transport layer which represents an additional interfacial recombination loss that is not captured by measuring the PL emission from the cell.[153, 283] Considering that the internal QFLS is significantly higher than the external V_{OC} in the reference device an energy misalignment between the perovskite and the spiro-OMeTAD is suggested. Hence, the

application of 2D layers might further reduce the detrimental effect of an energetic misalignment between the perovskite and the spiro-OMeTAD layer as it effectively blocks the minority carriers from reaching the spiro-OMeTAD layer. In fact, we found that 2-TMABr and the formation of the *p-n* junction, is most effective at suppressing all interfacial recombination losses where the V_{OC} is only limited by the radiative efficiency of the neat material.

4.5 Conclusion

We demonstrate, by combining a comprehensive analysis on device performances, device and interface QFLS and interface energetics, that even subtle changes in the composition of the 2D perovskite can lead to differences of the energetic alignment at the 2D/3D interface, with a direct impact on charge density distribution, interfacial recombination and ultimately device performance. Our work provides the first demonstration of an optimized 2-TMABr based 2D/3D perovskite solar cells with zero interfacial voltage losses, reaching the QFLS-potential of the neat perovskite absorber and thus nullifying the energy losses at the interfaces. UPS depth profiling is demonstrated to be a valuable method allowing the direct probe of the interfacial alignment and band bending. Overall, this knowledge is essential to drive interfacial chemistry and functionalization to guide a smart device optimization. Combining chemical manipulation of the 2D perovskite and deep understanding of the 2D/3D interface energetics and recombination processes, our results provide clear evidence that 2D/3D interface engineering with optimal energetics allows to nullify the non-radiative interfacial recombination of electron and holes, demonstrating a breakthrough in the path to further enhance perovskite solar cell performance.

Chapter 5: Lewis Base Surface Passivation Using a Phosphine Oxide Derivative

Interfacial engineering of perovskites using a Lewis base molecule has become a viable strategy for reducing the density of surface defects. As discussed in the Section 2.2.3 of Chapter 2, the lone pair of electrons present in the Lewis base could form a coordinate bond with the defect sites, such as under undercoordinated Pb^{2+} which results in the defect passivation. In this chapter, we designed a new Lewis base containing phosphine oxide group, namely tris(5-((tetrahydro-2*H*-pyran-2-yl)oxy)pentyl)phosphine oxide (THPPO), and introduced it in the perovskite solar cells (PSCs). The PL, XPS, NMR, and GIWAXS experiments reveal that the P=O terminal group of THPPO effectively targets the undercoordinated Pb^{2+} sites at the perovskite surface. Further, the UPS analyses suggest that energetical alignment of the passivated perovskite layer is favorable for the hole extraction. Consequently, improvement of PCEs from 19.87% to 20.70 % and from 5.84% to 13.31% are achieved in *n-i-p* PSCs and hole transporting layer (HTL)-free PSCs, respectively.

This chapter is based on the published work in ACS Appl. Energy Mater., 2021, 4, 2, 1259–1268, DOI: 10.1021/acsaem.0c02472.[288] *In this work I contributed equally with C. Igci where we conceptualized the idea and designed the experiments. Specifically, I performed the fabrication as well as the characterizations of perovskite thin films and solar cells. C. Igci synthesized the passivation molecule and characterized it. V.I.E. Queloz and Dr. H. Kanda carried out the steady state and transient PL measurements. Dr. M. Mensi contributed to the XPS measurements and analysis. The GIWAXS and UPS measurements were performed in collaboration with Dr. N. Shibayama from University of Tokyo Japan.*

5.1 Introduction

Perovskite solar cells (PSCs) have rapidly advanced and recently achieved over 25% power conversion efficiency (PCE) since the first report with a PCE of 3.8% in 2009.[10, 289] Nevertheless, defects have been the center of attention in the device engineering as their presence in PSCs detrimentally influence the photophysical and photoelectrical properties of films and devices. Defects can induce the formation of trap states in the perovskite and at the interface with the adjacent layer, which can cause undesirable nonradiative recombination.[41, 162, 285, 290-294] For instance, undercoordinated Pb^{2+} sites negatively affect charge carrier dynamics leading to the loss of charge carriers, thereby degrading photovoltaic performance.[295-297] Therefore, it is necessary to design and develop defect passivation strategies to improve device performance.

To date, various defect passivation strategies in PSCs have been reported by using inorganic,[298-300] organic molecules,[301-304] and polymers,[295, 305, 306] also through additive engineering,[307, 308] grain-boundary engineering,[309] and multidimensional engineering,[42, 208, 223, 310] which can result in reduced nonradiative charge recombination, efficient charge collection, and thereby improving device performance.[42, 208, 223, 295, 298-310] Lewis base molecules have been demonstrated as efficient passivating agents by targeting the undercoordinated Pb^{2+}, resulting in the improvement of carrier dynamics and device performance.[171, 176, 177, 179, 181, 311, 312] Among the Lewis bases, molecules including phosphine oxide such as tri-*n*-octylphosphine oxide (TOPO),[176, 313-316] triphenylphosphineoxide (TPPO),[177] and tetraisopropyl methylenediphosphonate (TMPP) [177] have been regarded as promising passivation agents due to their electron-donating ability.

In this study, we synthesized a new Lewis base organic molecule containing a phosphine oxide group, ((tetrahydro-2*H*-pyran-2-yl)oxy)pentyl)phosphine oxide (THPPO), as a passivating agent on top of a perovskite layer (Figure 5.1a). The P=O group of THPPO passivates the perovskite surface by forming a chemical bond with the undercoordinated Pb^{2+}. The perovskite film treated with THPPO showed reduced nonradiative carrier recombination and improved photovoltaics performance when it was applied in the device. We incorporated THPPO in two different types of devices: one is a device with a *n-i-p* configuration (Figure 5.1b) and the other is a hole-transporting layer (HTL)-free device for the development of simplified and cost-effective PSCs. The introduction of THPPO led to an improvement in the PCE from 19.87% to 20.70% of the *n-i-p* devices and 5.84% to 13.31% of the HTL-free devices.

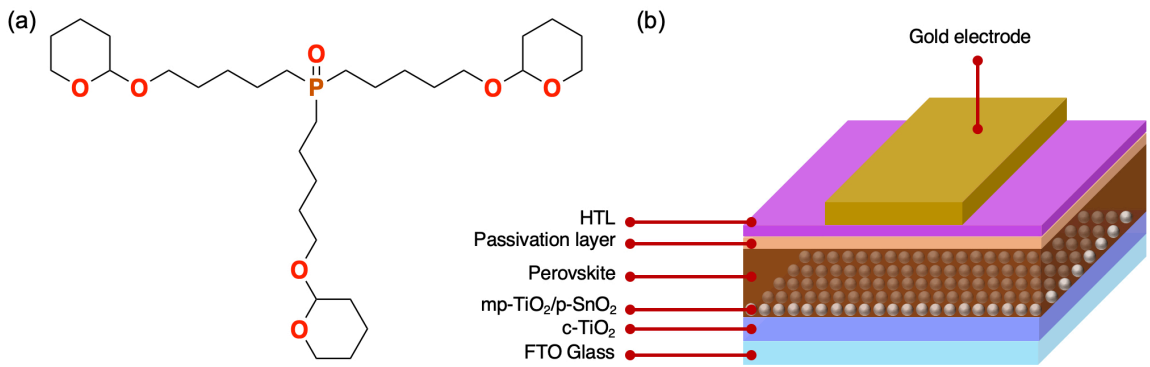

Figure 5.1 (a) Molecular structure of THPPO and (b) device structure of *n-i-p* PSCs employing fluorine-doped tin oxide (FTO), compact TiO_2 (c-TiO_2), mesoporous TiO_2 (mp-TiO_2), SnO_2, perovskite, THPPO as a passivation layer, HTL, and gold electrode.

5.2 Molecular Design and Synthesis

In the molecular design of THPPO, the phosphine oxide group that provides a Lewis base was chosen as an active passivation agent for the perovskites. It was functionalized with a five-carbon alkyl substituent chain to make it soluble in common organic solvents. The tetrahydropyranyl ether unit was combined with the ether group as effective anchors at the interface between perovskite and HTL.[317] The general synthetic scheme and the detailed synthetic procedure of THPPO are presented in Scheme C.1 and Appendix C. The synthesis of THPPO began with a carboxylic acid reduction reaction of commercially available 5-bromopentanoic acid by borane-tetrahydrofuran complex to the corresponding primary alcohol.[318] The obtained 5-bromopentan-1-ol was then attached to tetrahydropyran (THP) group in the presence of *p*-toluenesulfonic acid in dichloromethane to attain tetrahydropyranyl ether functional group.[319] As a last step, 2-((5-bromopentyl)oxy)tetrahydro-2*H*-pyran with magnesium formed a Grignard reagent, which reacted with phosphorous trichloride to furnish an alkyl-phosphine intermediate product. Then, the intermediate product was oxidized with hydrogen peroxide in dichloromethane with high yield to obtain the novel passivation molecule THPPO.[320, 321] Purification of the final compound was performed by column chromatography without the need for high-pressure vacuum distillation. The synthesized product chemical structure was verified by ^{1}H, ^{13}C, and ^{31}P nuclear magnetic resonance (NMR) spectroscopy and mass spectroscopy (Figure C.1 and Figure C.2, Appendix C). THPPO is soluble in common organic solvents such as tetrahydrofuran (THF), chloroform, toluene, and chlorobenzene, typically used for the deposition of a passivation layer in the PSCs.

5.3 Thin-films Characteristics

We deposited the THPPO solution dissolved in chlorobenzene with various concentrations (0.005, 0.010, 0.020, and 0.030 M) on top of a triple-cation-based perovskite layer $[(FAPbI_3)_{0.87}(MAPbBr_3)_{0.13}]_{0.92}(CsPbI_3)_{0.08}$. Figure 5.2a shows the steady-state photoluminescence (PL) spectra of the control and THPPO-treated perovskite thin films. The films were excited with 550 nm light from the top side of the film. The emission spectra of all of the films show a peak at 767 nm regardless of the concentration of THPPO while the PL intensity was improved by increasing the concentration of THPPO. The absorption spectra of the films did not show any new absorption peak and a noticeable shift of the band edge at 780 nm (Figure C.3, Appendix C). The improvement of the PL intensity can be attributed to the passivation effect of THPPO, which can lead to a reduction of the density of trap states in the perovskite with enhanced radiative recombination. Meanwhile, the unchanged position of the PL emission peak and the absorption onset implies that the deposition of THPPO did not degrade or modify the crystal structure of the underlying perovskite. To gain a better understanding of the carrier dynamics of the films, we performed time-resolved PL (TrPL) measurements of the films upon excitation at 480 nm (Figure 5.2b). The TrPL decay curves were fitted to a biexponential decay function (Table C.1, Appendix C). All the THPPO-treated perovskite thin films exhibited significantly prolonged PL lifetimes for the fast and slow components of the PL decay (t_1 and t_2, respectively). For example, the film with 0.030 M THPPO had t_1= 19.0 ns and t_2= 192.3 ns while the control film had t_1=12.6 ns and t_2 = 96.4 ns indicating that THPPO can effectively reduce the density of traps on the surface of the perovskites by passivation.

X-ray diffraction (XRD) of the perovskite films showed the typical pattern of the triple-cation and mixed-halide perovskites.[38] The deposition of THPPO did not cause an additional formation of a new pattern indicating that it did not alter the crystalline structure of the perovskites (Figure 5.2c). As we used an excessive amount of PbI_2 in the perovskite, the pristine film accordingly showed a noticeable peak at 12.7° that can be assigned to the residual PbI_2. However, the peak intensity was reduced by the deposition of THPPO. As PbI_2 is a well-known Lewis acid, the reduction of the PbI_2 peak intensity of the THPPO-treated films can be explained by the formation of the PbI_2·THPPO adduct (Figure 5.2c).[322] [323]

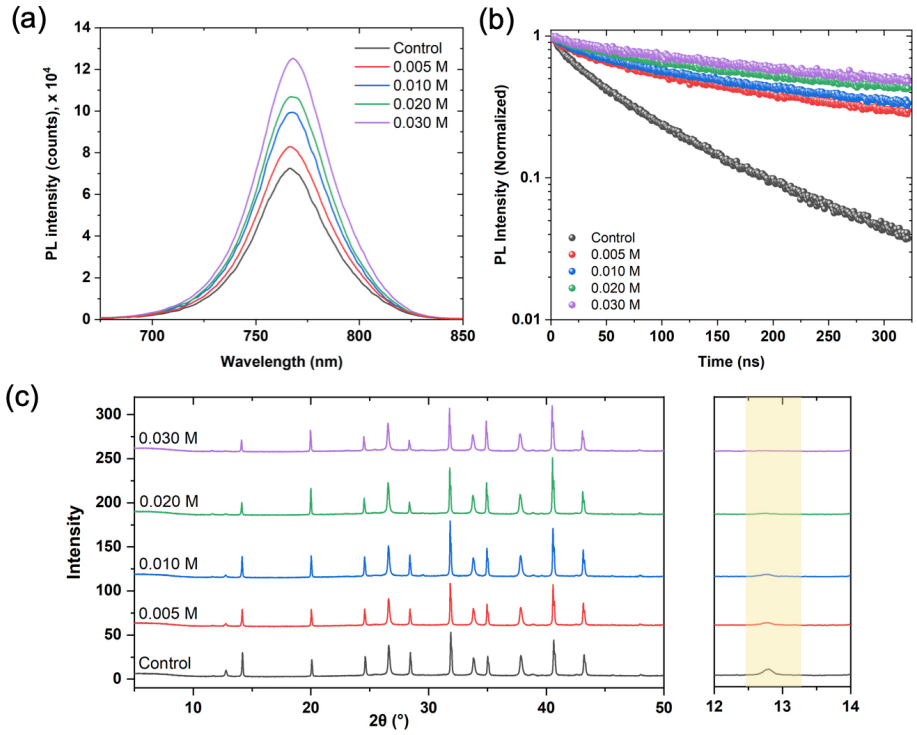

Figure 5.2 (a) Steady-state PL spectra (λ_{exc}= 550 nm), (b) time-resolved PL spectra (λ_{exc}= 480 nm), and (c) XRD patterns of control perovskite film and passivated films with various concentrations of THPPO.

The surface morphology of the perovskite films treated with various concentrations of THPPO was observed by scanning electron microscopy (SEM) images (Figure 5.3a). The pristine film showed sparsely distributed bright grains, which can be attributed to the residual PbI_2. Upon the deposition of 0.005 M THPPO, the density of the bright grains decreased, and the color became darker as PbI_2 was transformed into the PbI_2·THPPO adduct, which is consistent with the result of XRD.[322] The use of 0.010 M THPPO decreased the effective area of perovskite grains while increasing its occupation between the grains. Therefore, the surface contact area between the perovskite grains and THPPO was significantly increased, possibly leading to more effective passivation. However, a further increase in the concentration of THPPO resulted in thicker and nonhomogeneous coverage on top of the perovskite grains showing a stronger contrast. The cross-sectional SEM images showed well-deposited electron transporting layers (compact TiO_2/mesoporous TiO_2/SnO_2) and perovskite layer (~500 nm) and top Au electrode. However, the THPPO layer was not easily recognized due to its very low thickness (Figure C.4, Appendix C).

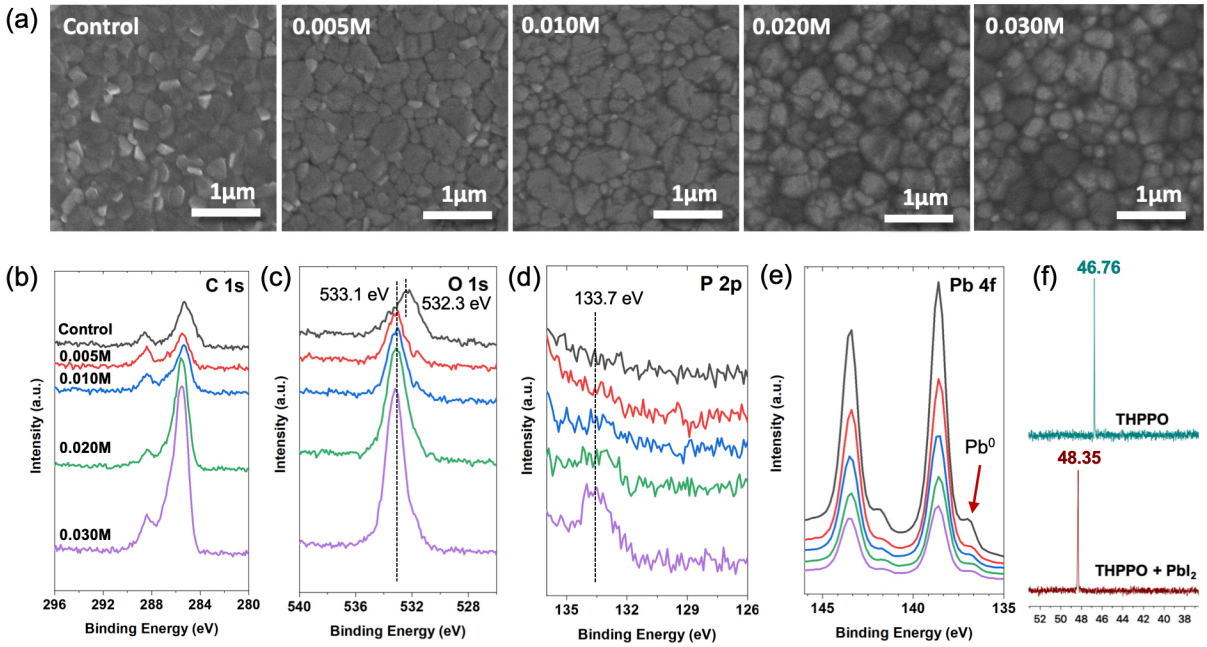

Figure 5.3 (a) SEM images: surface morphology of control perovskite film and films with various concentrations of THPPO. Core-level XPS spectra of (b) C 1s, (c) O 1s, (d) P 2p, and (e) Pb 4f of control perovskite film and films with various concentrations of THPPO. (f) ^{31}P NMR spectra of 0.01 mmol THPPO and THPPO mixed with 0.01 mmol PbI_2 in dimethyl sulfoxide (DMSO)-d_6.

The presence of THPPO on the perovskite surface was characterized by X-ray photoelectron spectroscopy (XPS). The C 1s spectrum of the control film exhibited two main peaks at 285.5 and 288.4 eV, which can be attributed to the C-C bond and the C=O bond, respectively (Figure 5.3b).[41] The increase in the THPPO concentration resulted in a significant increase in the peak intensity of the C-C bond because the deposited THPPO has an increasing number of C-C bonds of three pentyl chains with tetrahydropyran ether. The peak of the C=O bond at 288.4 eV may have originated from the contamination of the perovskite upon exposure to the ambient air during the sample transfer for the measurement.[324] The peak at 532.3 eV of the control film in the O 1s spectra, can be also attributed to the O=C bond formed by the surface oxidation (Figure 5.3c).[325, 326] The deposition of THPPO caused an appearance of an additional peak at 533.1 eV that arose from tetrahydropyran and ether of THPPO showing a significant increase in the intensity with the increase in the concentration of THPPO.[327] In the P 2p spectra, we confirmed a peak that originated from the P=O bond of THPPO at 133.7 eV (Figure 5.3d).[328, 329]

The Pb 4f spectra verified the passivation effect of THPPO (Figure 5.3e). The pristine film showed four prominent peaks at 136.9, 138.6, 141.8, and 143.4 eV. Pb $4f_{7/2}$ and Pb $4f_{5/2}$ peaks at 138.6 and 143.4 eV, respectively, can be attributed to lead halide bonds, while Pb $4f_{7/2}$ and Pb

$4f_{5/2}$ peaks at 136.9 and 141.8 eV, respectively, can be attributed to Pb^0. It is worth noting that the Pb^0 peak can arise out of the undercoordinated Pb^{2+}, which can act as a nonradiative recombination center, leading to the degradation of the device performance.[330, 331] Upon the deposition of THPPO, the apparent decrease in the intensity of Pb^0 was observed and confirmed by the quantitative analysis of Pb^0 (Table C.2, Appendix C). The reduction in the Pb^0 ratio can be explained by the coordination between the undercoordinated Pb^{2+} and the lone pair of electrons from the Lewis base of THPPO, which resulted in defect passivation. [171, 332, 333]

To further elucidate the interaction between THPPO and the undercoordinated Pb^{2+} on the perovskite surface, we performed ^{31}P NMR spectroscopy (Figure 5.3f). The measurement was carried out using 0.01 mmol THPPO dissolved in 0.5 mL of DMSO-d_6 followed by the addition of 0.01 mmol PbI_2. As the dissociation of PbI_2 in the solution can yield the undercoordinated Pb^{2+}, we can investigate the underlying mechanism of the passivation by examining its interaction with THPPO. While the phosphorous peak of pristine THPPO was at 46.76 ppm, the addition of PbI_2 shifted the peak to 48.35 ppm. The downfield shift indicates that the electron density of the phosphorous nucleus decreases as the P=O functional group as a Lewis base donates electrons to Pb^{2+}, triggering the passivation effect.[176, 177, 311]

To investigate the molecular stacking state of THPPO, we carried out grazing-incident wide-angle X-ray scattering (GIWAXS) analysis. The control film had a Debye-Scherrer ring at q_z = 1.0 $Å^{-1}$ which can be attributed to the (100) crystal planes of the cubic phase of the perovskite (Figure 5.4a). Upon the deposition of THPPO on top of the perovskite layer, new peaks appeared at q_z = 0.40 and 0.79 $Å^{-1}$, which resulted from the out-of-plane orientation of THPPO on the perovskite layer (Figure 5.4b). Azimuthally integrated intensity profile of the film with THPPO also clearly showed the prominent peak at 0.40 $Å^{-1}$ having a lattice spacing of 15.9Å that corresponds to the size of THPPO simulated by a molecular mechanics force field (Figure 5.4c and Figure C.5, Appendix C). The peak at 0.79 $Å^{-1}$ can be ascribed to the second diffraction peak of THPPO. We examined the angular dependence of the diffraction peak at 0.40 $Å^{-1}$ to obtain a detailed insight into the molecular stacking state of THPPO (Figure 5.4d). The intensity of the peak became prominently high at the low incident angle range below 20° indicating a vertically well-aligned THPPO, so-called 'edge-on' stacking. Therefore, the P=O group can effectively interact with the undercoordinated Pb^{2+} of the perovskite octahedral that can lead to the formation of the Lewis adduct, which agrees well with the result of the ^{31}P NMR analysis.

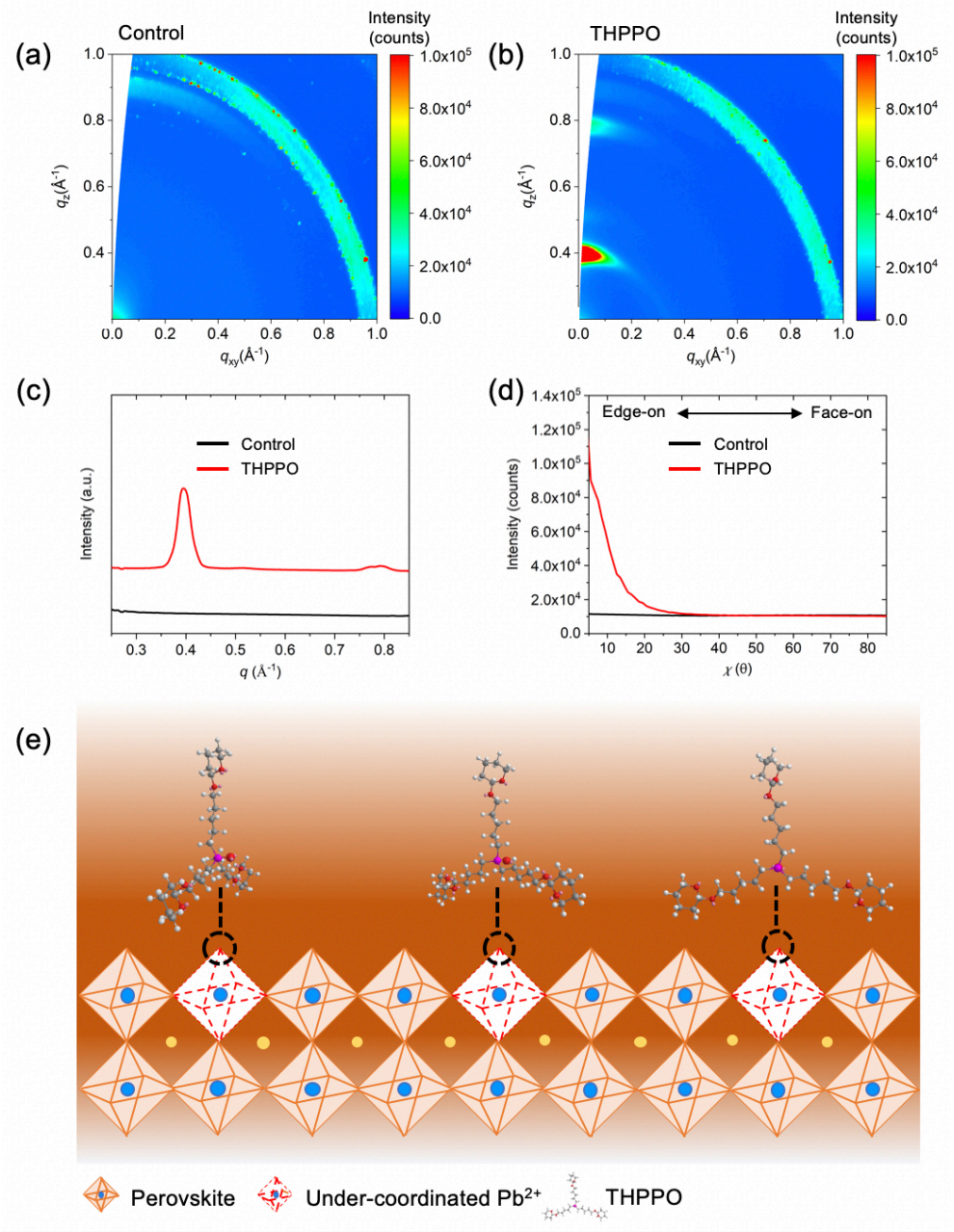

Figure 5.4 GIWAXS patterns of (a) control perovskite film and (b) THPPO-treated perovskite film. (c) Azimuthally integrated intensity profile obtained from GIWAXS patterns. (d) Angular dependence of the peak intensity at 0.40 Å^{-1}. (e) Cartoon illustration of the proposed passivation mechanism. The concentration of THPPO is 0.030 M.

We performed ultraviolet photoelectron spectroscopy (UPS) to examine the energy-level alignment of perovskites upon the surface modification using THPPO (Figure 5.5 and Figure C.6, Appendix C). The control film exhibited a valence band (VB) energy of 5.70 eV and the energies gradually increased to -5.60 eV, -5.59 eV, and -5.58 eV according to the deposition of 0.005, 0.010, and 0.020 M of THPPO on top of the perovskite film, respectively. The positive shift in the VB edge by the THPPO treatment resulted in a favorable energetic alignment

between perovskite and spiro-OMeTAD or gold electrode, which can facilitate hole transfer between the layers.

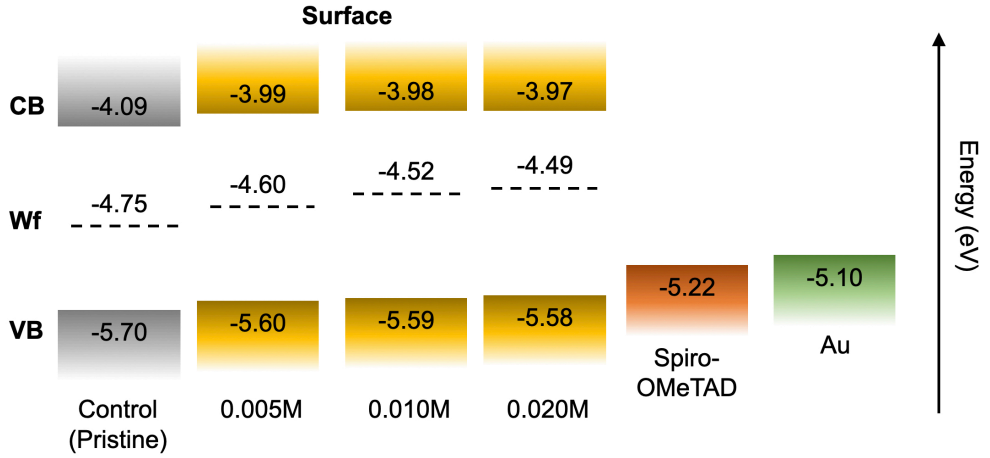

Figure 5.5 Energy-level diagram showing the valence band (VB), work function, and conduction band (CB) of the control and THPPO-passivated perovskite films.

5.4 Devices Characteristics

We employed THPPO as a passivating agent in PSCs without HTL (fluorine-doped tin oxide (FTO)/compact TiO_2 (c-TiO_2)/mesoporous TiO_2 (mp-TiO_2)/SnO_2/perovskite/THPPO/Au). Various concentrations of THPPO from 0.005 to 0.030 M were applied to find an optimal condition of THPPO treatment in PSCs. All of the THPPO-passivated devices showed improved photovoltaic performance compared to the control device (Figure 5.6a and Table C.3, Appendix C). The best-performing device was achieved upon the deposition of 0.010 M THPPO having open-circuit voltage (V_{OC}) of 0.866 V, short-circuit current density (J_{SC}) of 23.32 mA cm^{-2}, and fill factor (FF) of 0.689, resulting in a PCE of 13.31%. We also measured the external quantum efficiency (EQE) of the device (Figure C.7, Appendix C). We statistically confirmed that the improvement of PCE by the THPPO treatment mainly resulted from the enhancement in V_{OC} (Figure 5.6b and Table C.4, Appendix C). The average V_{OC} of the control device was 0.64 V and increased to 0.84 V with the use of 0.010 M of THPPO and it saturated with a further increase in the concentration of THPPO (Figure 5.6c). The improvement in V_{OC} can be ascribed to the reduced nonradiative recombination owing to the defect passivation effect of THPPO that we confirmed by the PL analyses.[292] The average J_{SC} and *FF* of the devices also improved by applying 0.010 M of THPPO from 22.3 mA cm^{-2} to 23.1 mA cm^{-2} and from 0.31 to 0.62, respectively. The improvements can be explained by the reduced density of trap states owing to the passivation effect of THPPO. In addition, the favorable energetic band alignment between THPPO and Au

can lead to the facilitation of charge transfer. However, a further increase in the THPPO concentration degraded both J_{SC} and *FF* because of the insulating nature of THPPO.[315] It can hinder the efficient charge transfer by increasing the series resistance at the interface (Figure C.8 and Table C.4, Appendix C). We also fabricated the device to compare THPPO and trioctylphosphine oxide (TOPO), one of the most widely used phosphine oxide based passivation agent.[176, 313, 314] The device employing 0.010 M TOPO resulted in a lower photovoltaic performance with a PCE of 9.36% compared to that of the device using 0.010 M THPPO (Figure C.9, Appendix C).

Using the optimized THPPO treatment of 0.010 M, we developed PSCs including spiro-OMeTAD as an HTL (FTO/c-TiO_2/mp-TiO_2/SnO_2/perovskite/THPPO/spiro-OMeTAD/Au). Prior to the device fabrication, we performed ^{31}P NMR spectroscopy to confirm the well-formed THPPO on top of the perovskite despite the deposition of spiro-OMeTAD, which also used chlorobenzene as a solvent (Figure C.10, Appendix C). While the control device exhibited V_{OC} of 1.064 V, J_{SC} of 23.76 mA cm^{-2}, FF of 0.786, and PCE of 19.87%, the device with the THPPO passivation layer showed V_{OC} of 1.108 V, J_{SC} of 24.08 mA cm^{-2}, FF of 0.776, and PCE of 20.70%. (Figure 5.6d and Table C.5, Appendix C). We measured the EQE spectrum of the device with passivation (Figure C.11, Appendix C). Also, we evaluated the *J-V* hysteresis of the THPPO-passivated device and the control device by measuring them under reverse and forward bias scans. The control device showed PCE of 19.85 % and 17.70 % under reverse and forward bias scans (Figure C.12, Appendix C), respectively, resulting in a hysteresis index (HI) of 0.11 defined as [($PCE_{reverse}$–$PCE_{forward}$)/$PCE_{reverse}$]. Meanwhile, the THPPO-passivated device showed more stable *J-V* hysteresis behavior having HI of 0.06 resulted from the PCEs of 20.67 % and 19.43 % under reverse and forward bias scans, respectively (Figure C.12 Appendix C). The improvement of the *J-V* characteristics can be attributed to the passivation effect and the favorable band alignment for charge extraction.

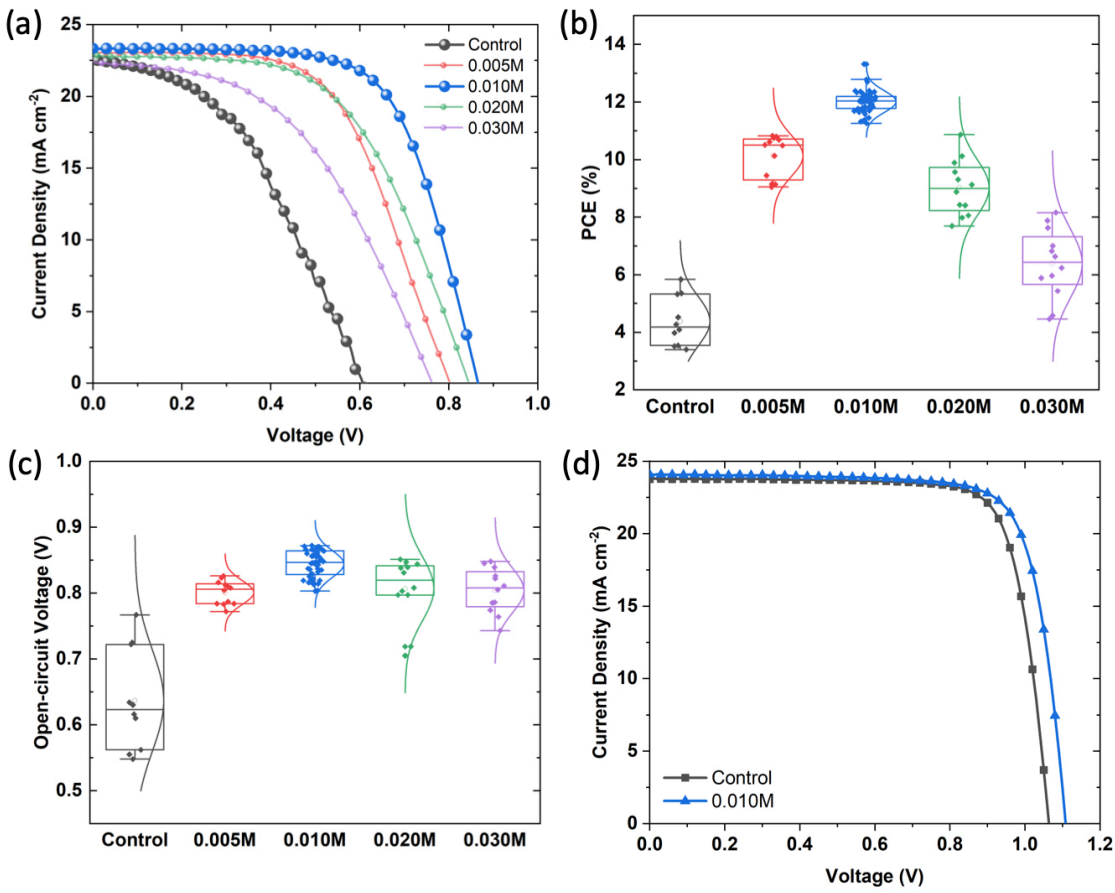

Figure 5.6 Photovoltaic characteristics of control and THPPO-passivated perovskite solar cells. (a) Current density-voltage (*J-V*) curves, statistics of (b) PCE and (c) V_{OC} of 96 HTL-free devices. (d) *J-V* curves of *n-i-p* devices using spiro-OMeTAD as an HTL.

Lastly, we performed the stability measurement of the HTL-free devices by storing the devices under dark with the relative humidity kept below 10 % (Figure C.13, Appendix C). A significant improvement in the stability was observed for the THPPO-passivated device that retained 96 % of its maximum efficiency after 360 h however, the control device only retained 62 % of its maximum efficiency for the same time window. The improvement in the device stability might be correlated with the THPPO's high decomposition temperature (T_d) of 251 °C obtained from the thermogravimetric analysis (Figure C.14, Appendix C).

5.5 Conclusion

We successfully synthesized a new molecule, THPPO, based on phosphine oxide derivative and demonstrated its application as a passivating agent in PSCs. We observed significant improvements in the PL characteristics of the perovskite films by introducing THPPO. It was attributed to the defect passivation effect of THPPO, which reduced the undesirable nonradiative recombination at the interface. Various analyses such as XPS, XRD,

and ^{13}P NMR spectroscopy verified the defect passivation effect in which a chemical interaction occurs between undercoordinated Pb^{2+} and P=O functional group of THPPO. It can lead to the formation of the Lewis adduct based on the well-aligned THPPO on top of the perovskite layer. Consequently, the PCE of the HTL-free device increased from 5.84 to 13.31% and that of the device with spiro-OMeTAD as an HTL increased from 19.87% to 20.70%. We believe this study provides insights into an important approach to design a new passivating molecule that can improve the performance of the PSCs but also sheds light on the understanding of defect passivation mechanism.

Chapter 6: Engineering of Hole-transporting Materials for Low-cost and Stable Solar Cells

Engineering of hole-transporting materials (HTMs) is one of the keys in achieving stable and low-cost perovskite solar cells (PSCs). Despite the high efficiency generated using 2,2,7,7-tetrakis(*N*,*N*-di-*p*-methoxyphenylamine)-9,9-spirobifluorene (spiro-OMeTAD), the so-called state-of-art HTM is mainly disadvantaged by its low stability and high synthetic cost. Thus, we designed new HTMs based on the carbazole and thiophene molecules as the building blocks for the stable and low-cost HTMs. In the first part of this chapter, two isomeric carbazole molecules functionalized with four triphenylamine (TPA) groups at different position have been investigated as HTMs in PSCs. The impact of triarylamine substitution on the isomeric structural linkage of carbazole on the optical, thermal, electrochemical, and photovoltaic properties has been extensively studied by combining experimental and simulation methods. The results have revealed that the carbazole-based HTM with TPA substitution at 1,3,6,8 positions (**Car[1,3]**) yields a better photovoltaic performance of 19.23% and long-term stability (by retaining >80% of its initial efficiency after 1000 h light exposure) compared to the one with TPA substitution at 2,3,6,7 positions (**Car[2,3]**). The planar molecular structure of **Car[1,3]** allows a dense packing of the molecules, leading to the improved hole-transporting capability. Thanks to the rigid structure of carbazole core, these carbazole-based HTMs demonstrate high thermal decomposition temperatures (> 420 °C) which could enhance the devices' long-term stability.

In the second part of this chapter, we have applied TPA-substituted thiophene-based HTMs with varying number of thiophene in the center as HTMs in PSCs: bithiophene (**BT-4D**), terthiophene (**TT-4D**) and quarterthiophene (**QT-4D**). The optoelectronic, electrochemical, and thermal properties of the compounds have been investigated systematically. The *n-i-p* configured perovskite solar cells (PSCs) fabricated with BT-4D as HTM shows the maximum power conversion efficiency (PCE) of 19.34% due to its better hole-extracting properties and film formation compared to **TT-4D** and **QT-4D**, which exhibit PCE of 17% and 16%, respectively. Importantly, PSC employing **BT-4D** demonstrates exceptional stability by retaining 98% of its initial PCE after 1186 h of continuous one sun illumination. The remarkable long-term stability and facile synthetic procedure of BT-4D shows a great promise for efficient, stable, and low-cost HTMs for PSCs for commercial applications.

6.1 Isomeric carbazole-based hole-transporting materials: Role of linkage position on the photovoltaic performance of perovskite solar cells

This section is based on the published work in Chem. Mater., 2021, 33, 9, 3286–3296, DOI: 10.1021/acs.chemmater.1c00335.[334] In this work I contributed equally with Dr. V. Joseph (National Central University, Taiwan) where we conceptualized the idea and designed the experiments. Specifically, I performed the fabrication as well as the characterizations of perovskite thin films and solar cells. Dr. V. Joseph synthesized the carbazole-based HTMs. We collaborated with Dr. O.A. Syzgantseva and M. Syzgantseva (Lomonosov Moscow State University, Russia) to perform the theoretical computation. The xerographic time-of-flight (XTOF) measurement were carried out in collaboration with Dr. V. Jankauskas (Vilnius University, Lithuania) and Dr. K. Rakstys (Kaunas University of Technology, Lithuania).

6.1.1 Introduction

In a typical *n-i-p* configured PSC, a hole transporting material (HTM) is sandwiched between the perovskite light absorber and the metallic electrode. The essential role of HTMs is to extract and promote positive charge (hole) transport from the photoactive perovskite layer to the metal electrode. They prevent the electron-hole recombination process at the interface and block the passage of electrons to the metal anode by suitably aligned HOMO-LUMO energy levels with the valence and conduction band of adjacent perovskite layers.[11, 126, 335, 336] For realizing high power conversion efficiency in PSCs, we need to have both an HTM and an electron transporting material (ETM) for efficient charge separation and transportation. Low-cost and highly stable ETMs such as TiO_2 and SnO_2 have been broadly explored with desirable electron-transporting characteristics for PSC applications.[337, 338] On the other hand, 2,2'7,7'-tetrakis(*N,N'*-di-*p*-methoxyphenylamine)-9,9'-spirobifluorene (spiro-OMeTAD) is extensively used as a hallmark HTM to achieve a high PCE in PSC.[339-341] However, complicated processes associated with the synthesis and purification of spiro-OMeTAD influence the overall cost of the PSC device. Further, a highly pure sublimed quality of spiro-OMeTAD restricts its large-scale applications. Thus, the quest for developing cost-effective HTMs possessing excellent hole-transporting properties is widely accelerated.[342-346]

In principle, a well-aligned HOMO level of an HTM with the valence band of perovskites is required in order to promote an efficient hole injection from the perovskite to the HTM.[11, 126, 335, 336] Additionally, HTMs should have excellent thermal and photochemical stability under operating conditions. So far, inorganic,[347] polymeric[348] and small molecular organic molecules[124] are employed as HTMs in PSCs. Small molecular HTMs are of interest owing to their precise molecular weight, high purity, facile synthesis and reliable batch-to-batch reproducibility. Generally, polyaromatic hydrocarbons such as naphthalene,[349] anthracene,[350] fluorene,[351, 352]

pyrene,[353, 354] carbazole,[355-357] anthanthrone,[358] quinacridone,[359] fused thiophenes,[360] etc. are exploited as potential scaffolds for HTMs.

Carbazole is a versatile platform and is extensively used for optoelectronic applications due to its excellent hole-transporting properties and thermal stability. Furthermore, carbazole-based materials possessing triarylamine functional groups are widely studied as HTM in PSC. For example, Yin et al. reported tetra-substituted carbazole (1,3,6,8) with triarylamine having the PCE of 18.32% in solution-processed planar PSCs.[361] Similarly, Chen et al. investigated carbazole-based HTM with diphenylamine substitution at the 1,3,6,8 positions, which showed PCE of 17.8%.[362] Many other research groups studied carbazole-triarylamine/diarylamine connected via phenyl, biphenyl, triphenylamine, and dibenzofuran core as HTMs for PSC.[363-366] In addition, isomeric carbazole-triarylamine based HTMs have been reported to result in different photovoltaic performances by altering the substitution position at the carbazole core.[367-369] For instance, Li et al. demonstrated that 2,7-difunctionalized carbazole exhibit superior PCE than the corresponding 3,6-difunctionalized carbazole.[369] However, tetra-substituted isomeric carbazoles as HTMs are scarcely investigated in the literature.

To probe the structure-function relationships between isomeric carbazole-based HTMs and charge transporting nature, we developed two structural isomers of *N*-butylcarbazole derivatives by varying the functional position of the carbazole core. We presumed that structural isomerism in carbazole derivatives could be beneficial to manipulate the hole transporting nature. Herein, we report the synthesis and characterization of two carbazole isomers functionalized with triphenylamine (TPA) groups and their application as HTMs in perovskite solar cells. Interestingly, the PSC device comprising **Car[2,3]** as the hole transporting material exhibited a high power conversion efficiency of 19.23%. The low-lying HOMO and higher hole-mobility of **Car[2,3]** contributed to a higher open-circuit voltage (V_{oc}) and high short-circuit current J_{sc}, respectively, and thereby resulted in an improved power conversion efficiency over the **Car[1,3]** analogue. The effect of the linking topology of carbazole with triarylamine on optical and electrochemical properties is elaborated. Furthermore, the molecular dynamic computational study shows that TPA substitution on the 2,3,6,7 positions of **Car[2,3]** increases the molecule's planarity and facilitates a better HTM-perovskite interaction, resulting in improvement of photovoltaic properties. Besides, the enhanced long-term stability shows the robustness of **Car[2,3]** compared to spiro-OMeTAD as the benchmark. Further, we have calculated the cost of **Car[2,3]** and found to be is ~$27/g (Table D.1.1, Appendix D), while the benchmark spiro-OMeTAD involving multistep synthesis is $92/g.[213] Thus, our results demonstrate a viable and cost-effective HTM to achieve longer stability.

6.1.2 Synthesis of the Carbazole-based HTMs

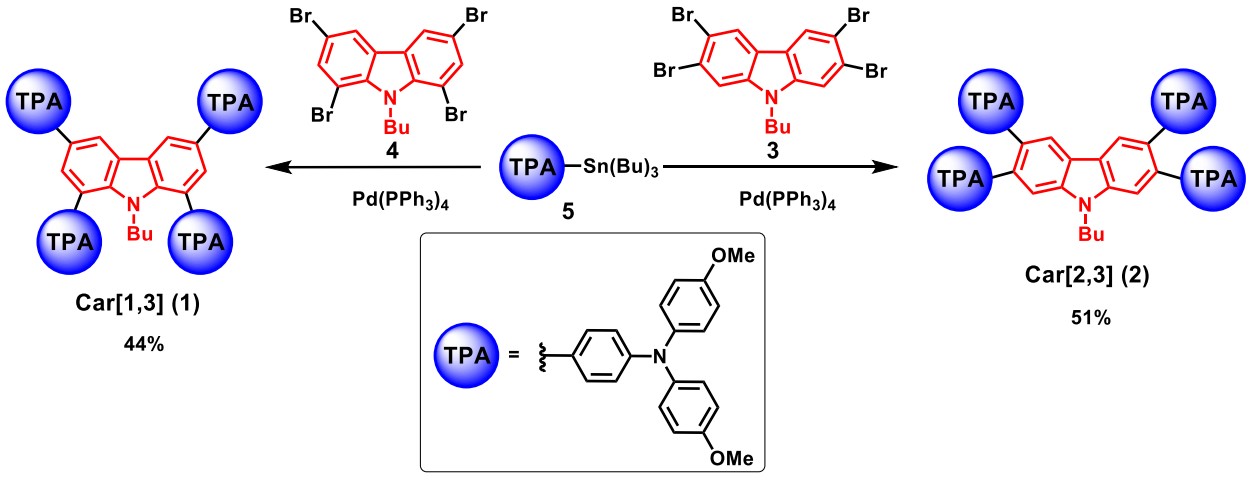

Scheme 6.1.1 Synthetic route for the target compounds **Car[1,3]** and **Car[2,3]**.

The synthetic route for the target molecules is presented in Scheme 6.1.1 The intermediates 1,3,6,8-tetrabromo-9-butyl-9*H*-carbazole (**4**) and 2,3,6,7-tetrabromo-9-butyl-9*H*-carbazole (**3**) were synthesized by following the literature procedures.[370, 371] The palladium-catalyzed Stille cross-coupling reactions of 4-methoxy-*N*-(4-methoxyphenyl)-*N*-(4-(tributylstannyl)phenyl)-aniline (**5**) with the respective bromo intermediates (**3** & **4**) under nitrogen atmosphere yielded the target molecules. The obtained compounds are pale-yellow in color. All the compounds are found to be soluble in common organic solvents which would make them facile for solution processed device fabrication. ^{1}H NMR, ^{13}C NMR spectroscopy and HRMS analysis (Figure D.1.1–Figure D.1.6, Appendix D) thoroughly characterized all the combinations, and the results were found to be matched with the proposed molecular structure.

6.1.3 Optical, Electrochemical, and Thermal Characteristics

To gain more insight into the effects that the isomerism of the TPA unit has on the structural, optical and electrochemical properties of the carbazole-based HTM derivatives, various physical characterizations were performed. The absorption spectra of the compounds recorded in *o*-dichlorobenzene are displayed in Figure 6.1.1 and the relevant data are compiled in Table 6.1.1. The absorption maximum of the compounds appears at 340 nm for **Car[1,3]** and 356 nm for **Car[2,3]**. The bathochromic shift of 16 nm observed for **Car[2,3]** arises from the linear conjugation along the 2,7-position of carbazole.[372]

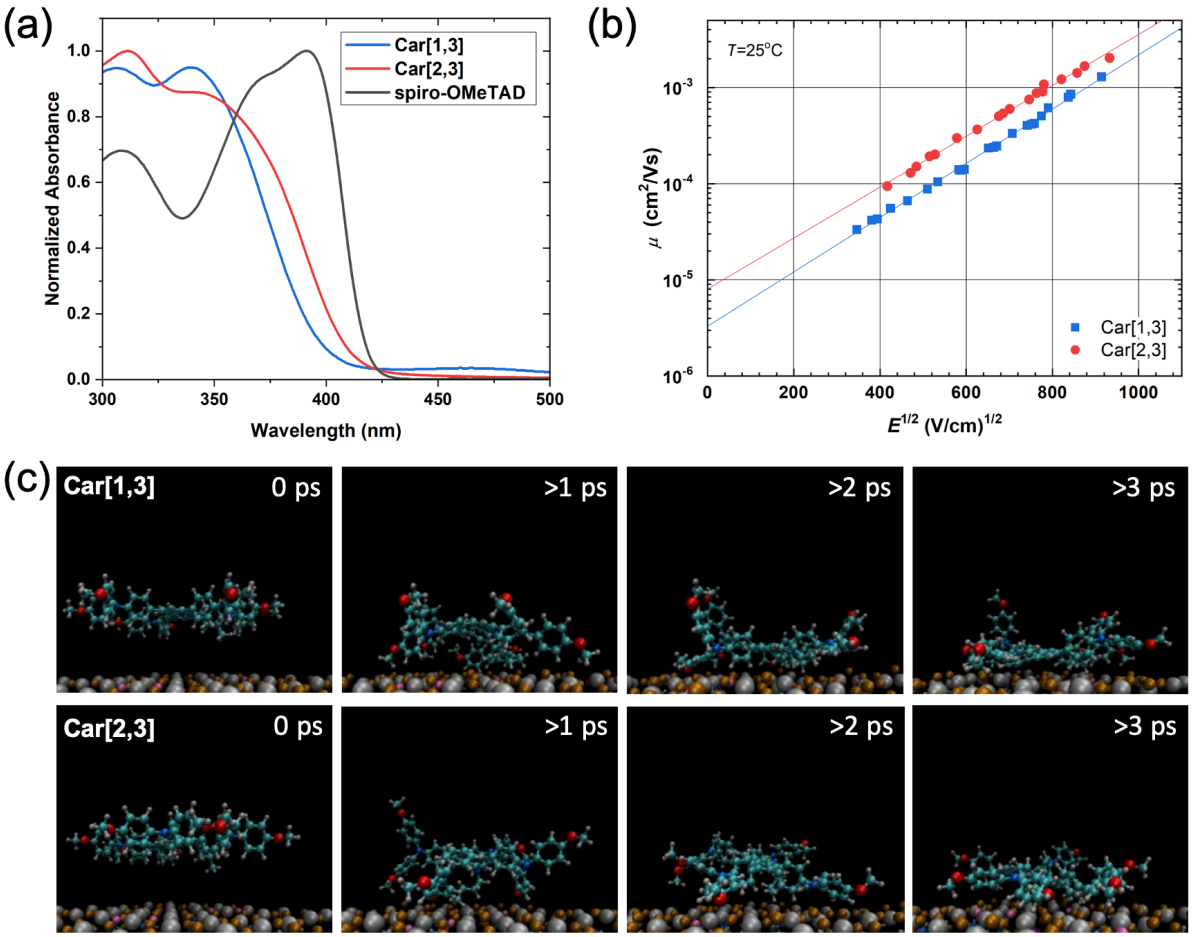

Figure 6.1.1 (a) Absorption of spectra of the compounds recorded in *o*-dichlorobenzene. (b) Hole drift mobility field dependencies for **Car[1,3]** and **Car[2,3]**. (c) Adsorption of **Car[1,3]** (top) and **Car[2,3]** (bottom) HTMs on the top of the perovskite surface in the course of molecular dynamics simulations. C, O, N, H, Pb, I, Br, and Cs are represented by cyan, red, blue, while, gray, brown, mauve and violet spheres, respectively.

A differential pulse voltammogram of the compounds recorded in *o*-dichlorobenzene solution with Bu_4NPF_6 as a supporting electrolyte is displayed in Figure D.1.7 (Appendix D). The oxidation potential was calibrated using ferrocene as an internal standard. The lower oxidation potential of **Car[1,3]** arises from the augmentation of donor strength along 1,3,6,8 positions of carbazole when compared to the isomer **Car[2,3]** connected via 2,3,6,7 positions of carbazole. The HOMO energy level of the compounds vs NHE is calculated by adding 4.44 eV to the oxidation potential. The calculated HOMO energy level was well aligned with the perovskite valence band energy which endorses an effective extraction and transportation of the hole from the perovskite active layer to the metal electrode (anode). The optical band gap of the compounds is derived from the onset of the absorption spectra. The LUMO values are obtained

by the addition of the HOMO and band gap values. The estimated HOMO/LUMO values of the compounds are -5.22/-2.20 eV for **Car[1,3]** and -5.29/-2.31 eV for **Car[2,3]**.

Table 6.1.1 Thermal, optical and electrochemical properties of **Car[1,3]** and **Car[2,3]**.

HTM	T_d [°C][a]	T_m [°C][b]	λ_{abs} (soln)[c] [nm]	HOMO [eV]		LUMO [eV][f]		ΔE_g [eV][g]	λ_{onset} (soln)[c] [nm]	μ_0 [$cm^2 V^{-1} s^{-1}$][h]
				DFT[d]	DPV[e]	DFT	DPV			
Car[1,3]	426	213	340	-4.35	-5.22	-0.71	-2.20	3.02	410	3.2×10^{-6}
Car[2,3]	422	185	356	-4.40	-5.29	-0.91	-2.31	2.98	416	8.0×10^{-6}

[a]Decomposition temperature corresponding to 5% weight loss determined from TGA; [b]Melting temperature; [c]Absorption spectra measured in *o*-dichlorobenezene; [d]Calculated from density functional theory; [e]Determined from DPV in *o*-dichlorobenzene at 25 °C with reference to Fc/Fc^+ internal standard (at +0.64 V); [f]HOMO = -(4.44+0.64+E_{ox}) against NHE; [f]LUMO = HOMO + ΔE_g; [g]$\Delta E_g = 1240/\lambda_{onset}$; [h]Mobility values at zero field strength.

The compounds' thermal properties were studied by thermogravimetric analysis (TGA) recorded under a nitrogen atmosphere at the heating rate of 10 °C/min. From TGA, it is observed that both the compounds exhibited a high thermal decomposition temperature of greater than 420 °C corresponding to a 5% weight loss (Figure D.1.8, Appendix D). The high thermal stability is attributed to rigid carbazole and TPA units present in the molecule. Thus, the devices fabricated with these materials are expected to exhibit excellent thermal stability.

To understand the compounds' electronic properties, density functional theory (DFT) calculations were performed at the B3LYP/6-31* level of the Gaussian 03W software. The computed absorption wavelength, oscillator strength and their orbital contribution are listed in Table D.1.2 (Appendix D). The longer wavelength of the computed absorption maximum was in line with the trend of experimental results. The HOMO concentrated on the one/two triarylamine unit for both compounds, while the LUMO is localized on the carbazole core and phenyl group attached to it (Figure D.1.9, Appendix D). This indicates the migration charge from the peripheral triarylamine to the central carbazole unit. The computed HOMO/LUMO values of the compounds are -4.35/-0.71 eV for **Car[1,3]**, and -4.40/-0.91 eV for **Car[2,3]**. Further, the trend of the calculated HOMO/LUMO energy levels of the compounds is consistent with that of the experimental results.

In addition, we performed xerographic time-of-flight (XTOF) measurement on the carbazole-based HTMs in order to investigate the hole-transporting properties of the synthesized molecules. The compounds hole mobility values at zero field strength are summarized in Table 6.1.1, while the hole drift mobility field dependencies of the compounds

are reported in Figure 6.1.1b. Both **Car[1,3]** and **Car[2,3]** yield the hole mobility values in the same order of magnitude, while **Car[2,3]** has a higher hole mobility value of 8.0 × 10^{-6} cm^2 V^{-1} s^{-1} in comparison to the one of **Car[1,3]** (3.2 ×10^{-6} cm^2 V^{-1} s^{-1}).

To figure out the difference between **Car[1,3]** and **Car[2,3]** HTMs upon interaction with perovskite, we modeled the adsorption of both HTMs on top of perovskite surface using the first principle of molecular dynamics (MD) simulations. The HTM molecules were allowed to freely relax and interact with the perovskite surface at the temperature of 300 K during the simulation. We observed that **Car[2,3]** adopts a more planar configuration on the perovskite surface, as compared to **Car[1,3]**, for which larger out-of-plane displacements of TPA branches are observed (Figure 6.1.1c). Thus, a planar configuration of **Car[2,3]** results in a larger number of noncovalent interactions with the perovskite surface in contrast to **Car[1,3]**. The large number of noncovalent interactions between the perovskite surface and **Car[2,3]** could promote a better hole-injection from perovskite to the HTM layer. Besides, the planar conformation of **Car[2,3]** is more favorable for a dense stacking of HTM molecules, while the distorted conformation of **Car[1,3]** with out-of-plane TPA configurations is unfavorable for the dense packing of HTM molecules. These results are in agreement with the higher hole mobility of **Car[2,3]** as shown in Figure 6.1.1b and Table 6.1.1.

6.1.4 Devices Characteristics

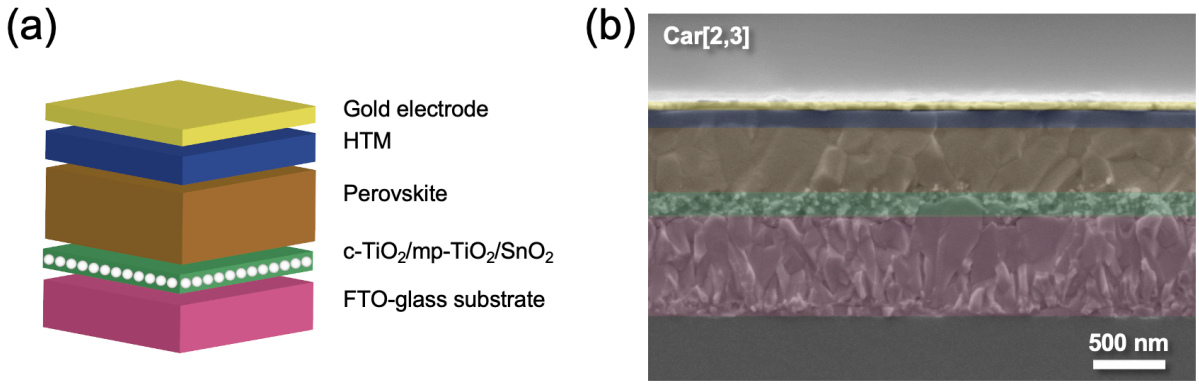

Figure 6.1.2 (a) Schematic illustration of the device configuration. (b) Cross-section scanning electron microscope (SEM) image of PSC incorporating **Car[2,3]** as the HTM. The color code of each layer is consistent to the cartoon illustration in (a).

We fabricated PSCs using the carbazole HTMs into *n-i-p* device configuration. The device structure is illustrated schematically in Figure 6.1.2a consisting of the following layers: a fluorine-doped tin oxide (FTO)-coated glass substrate, compact TiO_2 (c-TiO_2), mesoporous TiO_2 (mp-TiO_2), SnO_2, perovskite, an HTM, and a gold electrode. The device using spiro-

OMeTAD as the HTM was also fabricated following the same device architecture for the comparison. A triple cation-based perovskite layer with the composition of $[(FAPbI_3)_{0.87}(MAPbBr_3)_{0.13}]_{0.92}(CsPbI_3)_{0.08}$ was used in this study. All the HTMs were doped with 4-*tert*-butylpyridine (tBP), Li-bis(trifuoromethanesulphonyl) imide (Li-TFSI), and tris(2-(1*H*-pyrazol-1-yl)-4-*tert*-butylpyridine)cobalt(III) (FK-209). We investigated the morphology of the HTMs using scanning electron microscopy (SEM) analysis. Figure 6.1.2b shows the complete PSC's cross-section SEM image incorporating **Car[2,3]** as the HTM. The cross-section analysis confirms the formation of a ~150 nm-thick of **Car[2,3]** as well as **Car[1,3]** (Figure D.1.10a, Appendix D) on top of perovskite layer. Meanwhile, a ~250 nm-thick HTM was observed in the PSC incorporating spiro-OMeTAD (Figure D.1.10b, Appendix D). The cross-section morphology also reveals that all the HTMs were well deposited on top of the perovskite without any formation of a morphological defect, such as pinhole and nonuniform deposition (Figure 6.1.2b and Figure D.1.10). In order to understand better the surface morphology of the deposited HTMs, we performed top-view SEM imaging as shown in Figure D.1.11. The top-view SEM images of **Car[1,3]**, **Car[2,3]**, and spiro-OMeTAD exhibited a uniform coverage of HTMs on top of the perovskite layer.

Table 6.1.2 Photovoltaic parameters of the champion PSCs incorporating **Car[1,3]**, **Car[2,3]**, and spiro-OMeTAD as HTMs.

HTM	V_{oc} **(V)**	J_{sc} **(mA cm^{-2})**	***FF***	**PCE (%)**
Car [1,3]	1.031	22.87	0.687	16.20
Car [2,3]	1.076	22.90	0.780	19.23
Spiro-OMeTAD	1.108	23.03	0.791	20.20

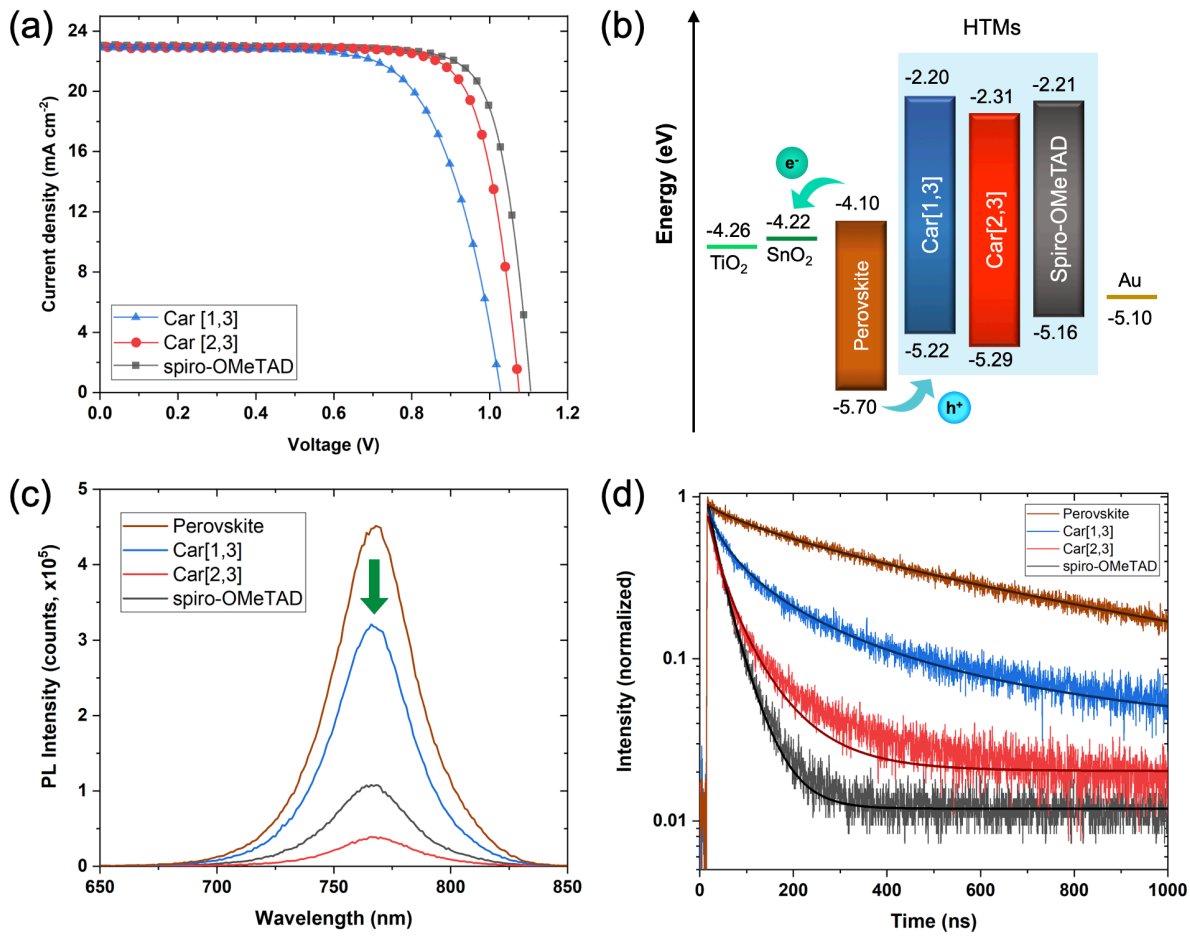

Figure 6.1.3 (a) *J-V* curves of PSCs employing **Car[1,3]**, **Car[2,3]** and spiro-OMeTAD as HTMs. (b) Schematic energy level diagram of the carbazole-based HTMs. The energy level values of TiO_2, SnO_2, perovskite, and the gold electrode are included for comparison.[119, 373] (c) Steady-state photoluminescence (PL) spectra upon excitation at 625 nm. The perovskite and HTM layers are prepared on top of the glass substrate. (d) Transient PL (TrPL) spectra of perovskite thin-films with **Car[1,3]**, **Car[2,3]** and spiro-OMeTAD deposited on top upon excitation at 635 nm.

The photovoltaic characteristics of the best performing PSCs employing **Car[1,3]** and **Car[2,3]** as HTMs are summarized in Table 6.1.2 and the corresponding current density-voltage (*J-V*) curves are plotted in Figure 6.1.3a. We also investigated the photovoltaic characteristics of PSCs based on spiro-OMeTAD as a benchmark (Table 6.1.2 and Figure 6.1.3a). The incorporation of **Car[1,3]** and **Car[2,3]** results in the maximum PCEs of 16.20% and 19.23%, respectively. We achieved comparable short-circuit current density (J_{SC}) values of the devices based on the carbazole HTMs, which is also confirmed statistically in Table D.1.3 and Figure D.1.12 (Appendix D). The observed J_{SC} values are in agreement with the hole-mobility values reported in Table 6.1.1. The J_{SC} trend is also consistent with the incident photon to electron conversion efficiency (IPCE) spectra presented in Figure D.1.13 (Appendix D, within 5% of the error range).

Interestingly, the final PCE values of the carbazole-based PSCs are significantly influenced by the open-circuit voltage (V_{OC}) and fill factor (*FF*). The PSCs incorporating **Car[1,3]** as the HTM suffer from the lower V_{OC} and *FF* values than **Car[2,3]**. The lower V_{OC} value of the **Car[1,3]**-based device could originate from the slightly higher HOMO level of **Car[1,3]** in respect to the valence band of perovskite (Figure 6.1.3b). Meanwhile, the HOMO level of **Car[2,3]** aligns better with the valence band of the perovskite, ensuring a more efficient hole injection from the perovskite to the HTM.[373] **Car[1,3]**'s poor FF value could be due to its lower conductivity which causes a higher resistivity from the HTM layer (*vide infra*).[374] It is also worth mentioning that the photovoltaic performance of **Car[2,3]**-based PSCs is comparable with the one of spiro-OMeTAD as the control device. Moreover, the PSC based on **Car[2,3]** demonstrates a similar hysteresis behavior with spiro-OMeTAD (Figure D.1.14), indicating a comparable hole extraction capability that could reduce the ion accumulation on the perovskite-HTL interface.[375]

To investigate the trend of the photovoltaic parameters obtained in the devices, we carried out the lateral conductivity measurement of **Car[1,3]**, **Car[2,3]** and spiro-OMeTAD. The lateral conductivity was measured by using a two-contact electrical conductivity setup with organic field effect transistor (OFET) substrates. All substrates having interdigitating gold electrodes with a channel length of 2.5 μm were prepared by spin coating under the same conditions and dopant concentration as in the fabrication of the devices. Current-voltage (*I-V*) scans between –10 and +10 V were recorded, and the conductivity of the different molecules was calculated using Ohm's law. The conductivity shows a similar trend to the hole mobility, where doped **Car[2,3]** has a higher lateral thin-film conductivity (7.22×10^{-5} S cm^{-1}) than that of **Car[1,3]** (3.79×10^{-5}) (Table D.1.4 and Figure D.1.15, Appendix D). The higher conductivity value of **Car[2,3]** is also in agreement with a more favorable molecular stacking of **Car[2,3]** in comparison with **Car[1,3]** from the computational experiment (see Figure 6.1.1c), resulting in higher J_{SC} and FF when it is applied in the solar cells. The conductivity of doped spiro-OMeTAD was determined to be $\sigma = 9.65 \times 10^{-4}$ S cm^{-1}, which is comparable to the values reported in the literature.[376] Although the conductivity values of **Car[1,3]** and **Car[2,3]** are lower than those of spiro-OMeTAD, the conductivity of the layer is high enough for efficient charge transport.

To further understand the hole extraction efficiency, we investigated the steady-state photoluminescence (PL) properties of the perovskite thin-films with the HTM deposited on top. The PL of a bare perovskite film deposited on top of the glass substrate was also measured as a reference. The PL spectra of the bare perovskite film and HTM-coated perovskite films were measured upon a 625 nm excitation wavelength and presented in Figure 6.1.3c. The bare perovskite film shows an emission peak at 767 nm which is in agreement with the emission peak

of a typical $[(FAPbI_3)_{0.87}(MAPbBr_3)_{0.13}]_{0.92}(CsPbI_3)_{0.08}$ perovskite film.[223] We observe a slight blue shift on the emission peaks upon the deposition of HTM on top of the bare perovskite layer. This blue shift could be due to the optical properties of the perovskite-HTM interface and the chemical interaction of the HTM and perovskite surface.[377] Upon the deposition of HTM on top of the perovskite layer, we notice that the PL intensities are quenched. The percentage of PL quenching with respect to the bare perovskite layer as the reference is reported in Table D.1.5 (Appendix D). Interestingly, **Car[2,3]** shows a significantly larger PL quenching value of 91.5% in comparison to **Car[1,3]** (32.1%). The larger PL quenching value of the HTM-coated perovskite layer with respect to the bare perovskite layer demonstrates a more efficient hole extraction process at perovskite-HTM interface.[27, 377] These results indicate that **Car[2,3]** has a better hole extracting efficiency compared to **Car[1,3]**, which is in agreement with their hole-mobility and lateral conductivity values (Table 6.1.1 and Table D.1.4). It is also worth mentioning that **Car[2,3]** exhibits a larger PL quenching than the one of spiro-OMeTAD (76.7%) confirming a comparable hole-extracting capability of **Car[2,3]**.

Furthermore, we performed the transient PL (TrPL) measurement to gain a deeper understanding in the carrier dynamics of perovskite thin-films incorporating **Car[1,3]**, **Car[2,3]**, and spiro-OMeTAD as HTMs. A bare perovskite layer coated on a glass substrate were measured as a reference. The TrPL spectra are measured upon 635 nm excitation wavelength and plotted in Figure 6.1.3d. The TrPL spectra were then fitted according to the stretched exponential decay function (see Appendix D for details).[26, 99, 378] The fitting parameters are summarized in Table D.1.6 (Appendix D). The average lifetime, $<\tau>$, value is decreased upon deposition of HTMs on top of the perovskite layer with respect to the bare perovskite layer ($<\tau>$= 559.94 ns). Among the carbazole-based HTMs, **Car[2,3]** exhibits a shorter average lifetime of 26.96 ns than **Car[1,3]** ($<\tau>$= 74.00 ns). The faster decay and the larger PL quenching values of **Car[2,3]** indicate that **Car[2,3]** has a more efficient hole injection from the perovskite layer to the HTM layer.[377] It is also worth mentioning that **Car[2,3]** demonstrates a comparable average lifetime value of spiro-OMeTAD ($<\tau>$= 26.05 ns) suggesting a comparable hole-extraction efficiency between **Car[2,3]** and spiro-OMeTAD.

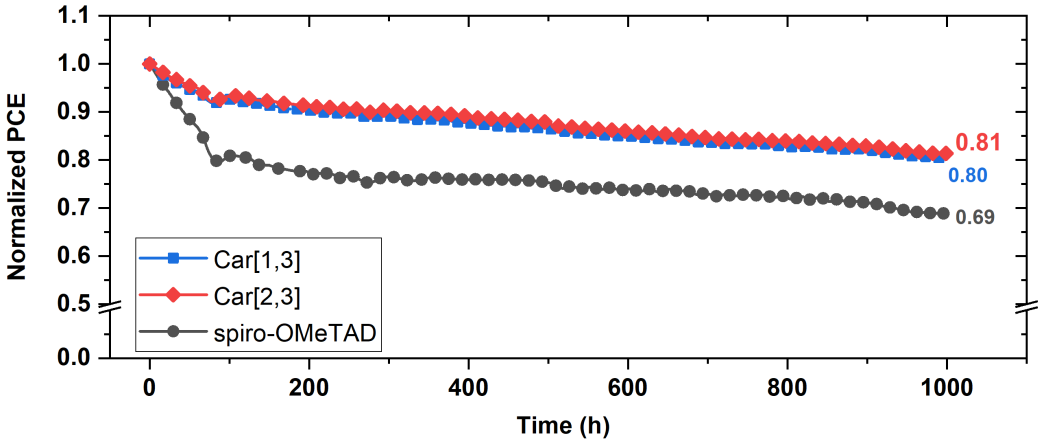

Figure 6.1.4 Long-term stability test of the unencapsulated PSCs based on **Car[1,3]**, **Car[2,3]** and spiro-OMeTAD as HTMs. The test was performed under continuous 1-sun illumination for 1000 h in a N_2 atmosphere.

We studied the PSCs stability employing **Car[1,3]**, **Car[2,3]**, and spiro-OMeTAD as HTMs. The stability test was carried out on the unencapsulated devices under continuous 1-sun exposure generated by a light-emitting diode (LED) source in a N_2 atmosphere. The performance of the devices was tracked under the maximum power point (MPP) condition. The long-term stability behavior of the devices is reported in Figure 6.1.4. Both **Car[1,3]** and **Car[2,3]** exhibit a similar degradation mechanism: a faster degradation during the first 80 h followed by a slower decay until 1000 h, retaining ≥80% of their initial PCEs. Contrarily, the device employing spiro-OMeTAD shows a much faster decay during the first 80 h, resulting in keeping only 69% of its initial efficiency after 1000 h of light exposure. These results reveal that the devices' long-term stabilities were enhanced by employing **Car[1,3]** and **Car[2,3]** as HTMs, outperforming the spiro-OMeTAD as the state of the art HTM compared under the same condition.[379] Additionally, we performed the stability test of the unencapsulated cells incorporating **Car[2,3]** and spiro-OMeTAD by keeping the PSCs under an ambient atmosphere (relative humidity <15%) in the dark. The device based on **Car[2,3]** demonstrates a better stability compared to spiro-OMeTAD after 19 days (Figure D.1.16), Appendix D. The improved long-term stability of the carbazole-based HTMs is also in good agreement with the high degradation temperature of the molecules (>400°C) as demonstrated in the TGA analysis (Figure D.1.8, Appendix D).

Furthermore, we performed the water contact angle measurement on the HTM films deposited on top of the perovskite substrate in order to assess the preliminary stability of the compound in the presence of moisture. The HTMs are prepared under the same doping conditions as used in the device. The water contact angle analysis of **Car[1,3]**, **Car[2,3]**, and

spiro-OMeTAD is presented in Figure D.1.17 (Appendix D). The average contact angle values of **Car[1,3]**, **Car[2,3]**, and spiro-OMeTAD are 68.5°, 69.3°, and 65.5°, respectively. Both of the carbazole-based HTMs exhibit similar contact angle values. The higher contact angle values of the carbazole-based HTMs (**Car[1,3]** and **Car[2,3]**) suggest that they are more hydrophobic in comparison with spiro-OMeTAD, which indicates enhanced stability against moisture under the operating conditions.

6.1.5 Conclusion

In summary, we present the synthesis and a systematic study of the effect of two isomeric carbazole-based hole transporting materials on the photovoltaic performance of PSCs. The position of arylamine substitution on the carbazole core had a notable impact on the optical, electrochemical, and photovoltaic performances of the **Car[1,3]** and **Car[2,3]** HTMs. The downshifted HOMO energy level and higher hole mobility and conductivity values of **Car[2,3]** resulted in a higher open-circuit potential and improved short-circuit current. Additionally, the molecular dynamics simulation reveals that **Car[2,3]** exhibits a more planar molecular orientation on top of the perovskite surface, enabling a better interaction and hole-transporting capability. Thus, we have tuned the photovoltaic performances by altering the substitution position of the carbazole core. The PSC device fabricated with **Car[2,3]** as the HTM displayed the highest power conversion efficiency of 19.23%. Importantly, the devices based on **Car[1,3]** and **Car[2,3]** demonstrated excellent devices stabilities after 1000 h of light illumination by retaining >80% of their initial PCEs. Our findings unveil the effective way to functionally tune carbazole-based HTMs for PSCs through variation in linking topology.

6.2 Stable Perovskite Solar Cells Using Molecularly Engineered Functionalized Oligothiophenes as Low-cost Hole-transporting Materials

This section is based on the published work in Small, 2021, 17, 2100783, DOI: 10.1002/smll.202100783.[380] In this work I contributed equally with Dr. V. Joseph (National Central University, Taiwan) where we conceptualized the idea and designed the experiments. Specifically, I performed the fabrication as well as the characterizations of perovskite thin films and solar cells. Dr. V. Joseph synthesized the thiophene-based HTMs. We collaborated with Dr. O.A. Syzgantseva and (Lomonosov Moscow State University, Russia) to perform the theoretical computation. The xerographic time-of-flight (XTOF) measurement were carried out in collaboration with Dr. V. Jankauskas (Vilnius University, Lithuania) and Dr. K. Rakstys (Kaunas University of Technology, Lithuania).

6.2.1 Introduction

In the normal (*n-i-p*) device configuration, *p*-type semiconducting materials, also known as hole transporting materials (HTMs), are sandwiched between perovskite and metal electrode. HTMs play a vital role in PSCs to extract and transfer the positive charges and thus achieve high efficiency.[335, 343, 381-383] They can be classified as inorganic,[384] polymeric[385] and small molecular organic HTMs.[386, 387] Among them, small molecular HTMs are superior to other counterparts owing to their structural diversity, well-defined molecular structure, precise molecular weight and reliable batch-to-batch reproducibility.[124, 388-390] To date, 2,2,7,7-tetrakis(*N*,*N*-di-*p*-methoxyphenylamine)-9,9-spirobifluorene (spiro-OMeTAD) has been widely employed as the benchmark HTM in PSC devices.[159] Unfortunately, the complicated synthesis and tedious purification of spiro-cored HTMs make it expensive.[266, 391, 392] Also, the performance of PSCs is highly dependent on the purity of spiro-OMeTAD employed which limits its large-scale applications. The poor stability of spiro-OMeTAD deteriorates the device photovoltaic performance rapidly and thereby the durability of PSCs is reduced drastically.[115, 257, 393] Therefore, the development of cost-effective HTMs possessing excellent stability, appropriate HOMO and LUMO energy levels to transport holes and block electrons respectively, is required for commercialization of perovskite solar cells.[394-398]

Donor-π-donor configured HTMs such as benzene,[399] biphenyl,[400] thiophene,[401, 402] fused thiophenes,[403-405] anthracene,[406] carbazole,[407] fluorene[408] and bifluorenylidene[409] flanked by arylamine donors are extensively studied in PSCs to replace the expensive spiro-OMeTAD. The ease of synthesis and purification of HTMs have a direct impact on cutting the cost of the device. When we consider the cost of HTMs, synthesis must have a shorter synthetic route and simple purification. Oligothiophene-based small molecules are well known for their potential applications such as organic thin film transistors, organic light-emitting diodes, organic solar

cells, and perovskite solar cells. Indeed, fused thiophene-based HTMs showed excellent performance in PSCs,[410-412] but the tedious synthetic route and high cost of synthesis restrict their applications in large scale devices. On the other hand, non-fused thiophene building blocks deserve much attention because they can be synthesized at low cost via facile synthetic pathways. Linear HTMs possessing thiophene and bithiophene as core moiety have been reported in the literature.[413-418] Interestingly, as the number of triphenylamine-arms on the core increases, the augmentation of power conversion efficiency (PCE) is observed. Since oligothiophenes are electron rich π spacer, functionalization of oligothiophenes with triarylamine would result in improved electron donating ability and thereby increased hole mobility and tuning of frontier molecular energy levels. In addition, the sulphur atom present in thiophene unit (HTM) is beneficial to enhance charge extraction through strong interaction between perovskite layer and HTM via Pb-S interaction.[419] Thus, we can manipulate charge extraction of HTM from perovskite layer to achieve high power conversion efficiency. Keeping these things in mind, we designed triarylamine substituted non-fused oligothiophenes (bithiophene, terthiophene and quaterthiophene) to realize improved charge extraction and increased hole mobility. To the best of our knowledge, low cost and facile synthesis of tetra-triarylamine substituted oligothiophenes as HTMs are scarcely studied in perovskite solar cells.

In this report, we designed and synthesized triarylamine-substituted oligothiophenes as small molecular HTMs for PSCs. The device fabricated with triphenylamine substituted bithiophene (**BT-4D**) showed the PCE of 19.34%, which is one of the best PCEs among the devices fabricated with thiophene, bithiophene-based small molecular HTMs (Table D.2.1, Appendix D). The solar cell based on **BT-4D** also showed excellent stability by maintaining 98% of its initial efficiency after continuous one sun illumination for 1186 h. In addition, we calculated the cost of synthesis for **BT-4D** and found it to be about ~$26/g (Table D.2.2, Appendix D). In contrast, the price of benchmark spiro-OMeTAD involving multistep synthesis is $92/g.[213] Further, we have demonstrated non-fused oligothiophenes as a promising building block for constructing HTMs to achieve highly efficient, stable, and cost-effective PSCs.

6.2.2 Synthesis of the Carbazole-based HTMs

The synthetic route for the target compounds is shown in Scheme 6.2.1. The intermediates 3,3',5,5'-tetrabromo-2,2'-bithiophene (**4**), 3,3'',5,5''-tetrabromo-2,2':5',2''-terthiophene (**5**) and 5,5',5'',5'''-tetrabromo-2,3':2',2'':3'',2'''-quaterthiophene (**6**) were synthesized by following the literature procedures.[420-422] The metal-catalyzed Stille coupling reactions of 4-methoxy-*N*-(4-methoxyphenyl)-*N*-(4-(tributylstannyl)phenyl)aniline (**7**) with the

bromo intermediates (**4-6**) under nitrogen atmosphere yielded the target molecules. All the final compounds are found to be soluble in common organic solvents making them accessible for solution processed device fabrication. All the final compounds are thoroughly characterized by ^{1}H NMR, ^{13}C NMR spectroscopy and HRMS analysis (Figure D.2.1–Figure D.2.9, Appendix D) and the obtained results were found to be consistent with the proposed molecular structure.

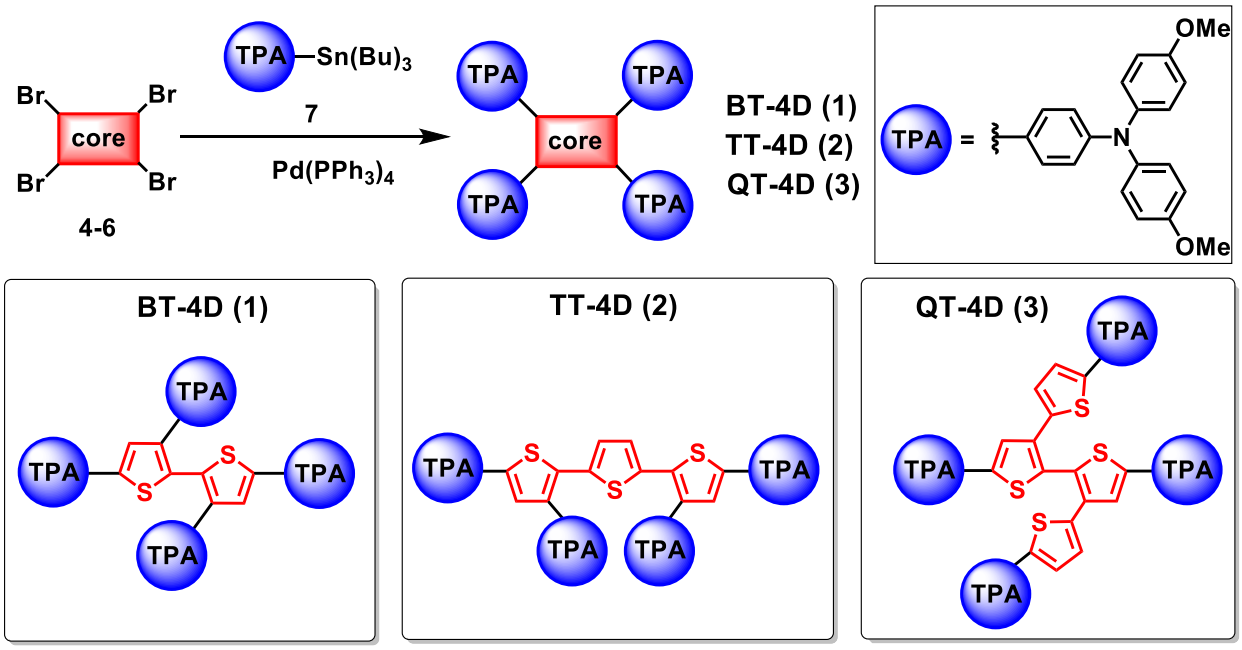

Scheme 6.2.1 Schematic synthetic route for the target compounds **BT-4D**, **TT-4D** and **QT-4D.**

6.2.3 Optical, Electrochemical, and Thermal Characteristics

The absorption spectra of the compounds recorded in the *o*-dichlorobenzene solution are displayed in Figure 6.2.1a, and the relevant data are compiled in Table 6.2.1. The absorption maximum for the compounds **BT-4D**, **TT-4D** and **QT-4D** is 366, 443, 388 nm, respectively. **QT-4D** showed a bathochromic shifted absorption maximum (22 nm) when compared to that of **BT-4D**. It arises from the elongation of the conjugated backbone exerted from an additional thiophene unit present in **QT-4D**. Further, **TT-4D** showed the longest bathochromic shift of 77 nm when compared to **BT-4D**. It is ascribed to additional thiophene unit present in central core that augments the linear conjugation.

The electrochemical properties of the compounds were studied by differential pulse voltammetry (DPV) recorded in the *o*-dichlorobenzene solution with Bu_4NPF_6 as supporting electrolyte (Table 6.2.1 and Figure D.2.10). The oxidation potential was calibrated against ferrocene internal standard. The HOMO energy level of the compounds is calculated by adding 4.44 eV to the oxidation potential. The deduced HOMO energy level was aligning well with the valence band energy level of the triple cation $(FAPbI_3)_{0.87}(MAPbBr_3)_{0.13}]_{0.92}(CsPbI_3)_{0.08}$ perovskite used in this study (-5.70 eV), which guarantees the effective hole extraction and transportation

to the metal electrode (anode).[373] The bandgap of the compounds is derived from the onset of absorption spectra. The LUMO values are obtained by the addition of HOMO and bandgap value. The estimated HOMO/LUMO values of the compounds are to be -5.22/-2.66 eV for **BT-4D**, -5.23/-2.92 eV for **TT-4D** and -5.30/-2.66 eV for **QT-4D**. All the thiophene-based molecules exhibit reversible redox peaks based on the cyclic voltammetry (CV) analysis (Figure D.2.11, Appendix D), indicating their excellent electrochemical stability.

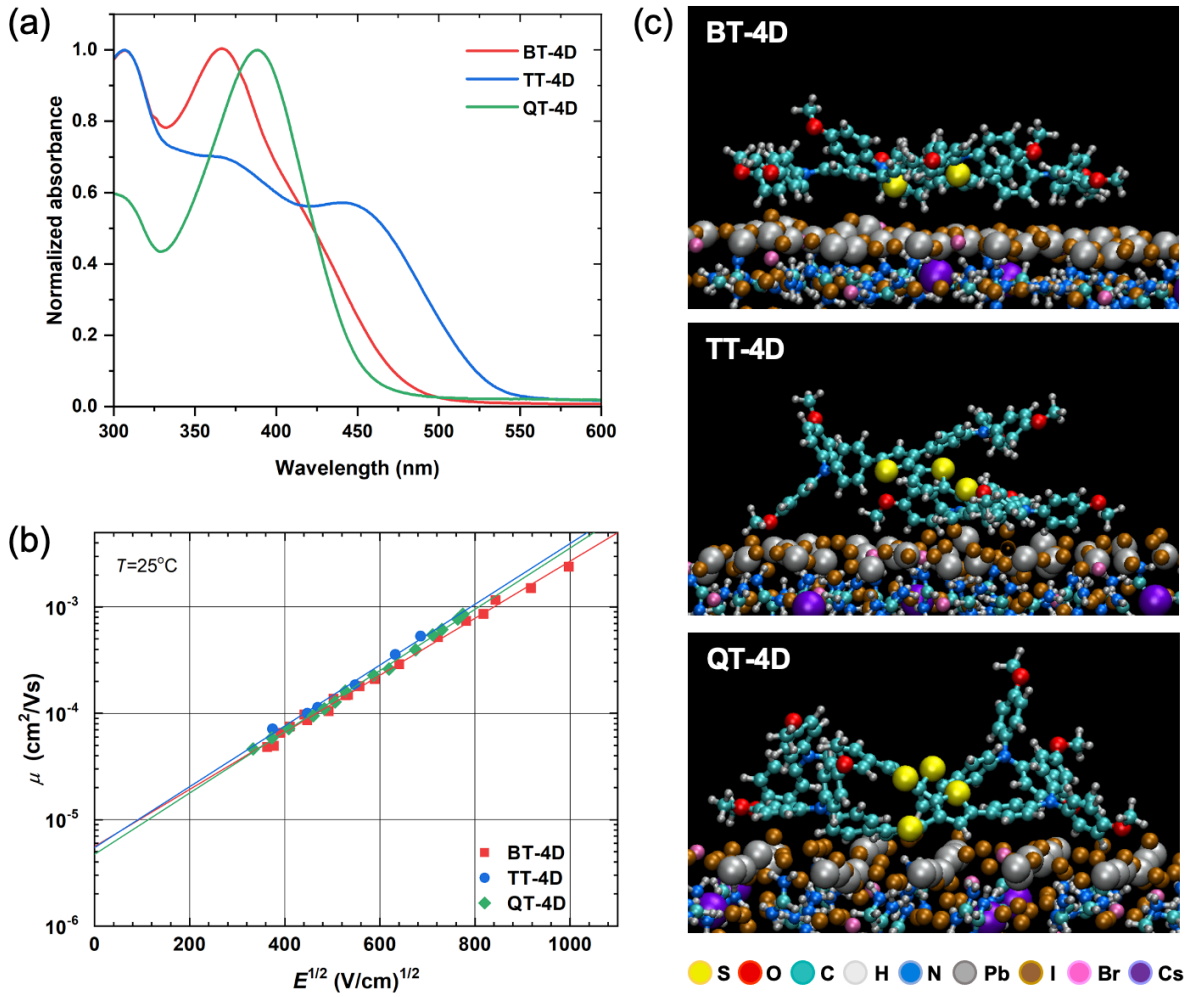

Figure 6.2.1 (a) Absorption spectra of the compounds recorded in *o*-dichlorobenzene. (b) Hole drift mobility field dependencies for **BT-4D**, **TT-4D**, and **QT-4D**. (c) Theoretical simulations of the interaction of **BT-4D**, **TT-4D**, and **QT-4D** with triple cation perovskite surface.

In order to gain deep insight into the electronic properties of the compounds, density functional theory (DFT) calculations were performed at B3LYP/6-31* level of the Gaussian 03W program. The HOMOs of the compounds are localized on the central core (BT, TT and QT) and slightly diffused over triarylamine arms, whereas, the LUMOs are primarily concentrated on central core (Figure D.2.12, Appendix D). The trend of longer wavelength absorption maximum

of the compounds matches well with that of experimental data (Table D.2.3, Appendix D). The computed HOMO/LUMO values of the compounds are -4.35/-1.27 eV for **BT-4D**, -4.35/-1.41 eV for **TT-4D** and -4.38/-1.35 eV for **QT-4D** (Figure D.2.12, Appendix D). The DPV derived HOMO of **QT-4D** is slightly downshifted as compared to those of **BT-4D** and **TT-4D**. Thus, the computed HOMO/LUMO energy level trend is consistent with that of electrochemically (DPV) derived HOMO/LUMO data (Figure D.2.10, Appendix D).

Table 6.2.1 Thermal, optical and electrochemical properties of **BT-4D**, **TT-4D** and **QT-4D**.

HTM	T_d [°C] [a]	T_m [°C] [b]	λ_{abs} **(soln)**[c] **[nm]**	**HOMO [eV]**[f]		**LUMO [eV]**[f]		ΔE_g **[eV]**[g]	λ_{onset} **(soln)**[c] **[nm]**	μ_o **[cm² V⁻¹ s⁻¹]**[h]
				DFT[d]	DPV[e]	DFT	DPV			
BT-4D	403	190	366	-4.35	-5.22	-1.27	-2.66	2.56	485	5.6×10^{-6}
TT-4D	421	125	443	-4.35	-5.23	-1.41	-2.92	2.31	537	5.0×10^{-6}
QT-4D	427	182	388	-4.38	-5.30	-1.35	-2.66	2.64	470	4.7×10^{-6}

[a]Decomposition temperature corresponding to 5% weight loss determined from TGA; [b]Melting temperature; [c]Absorption spectra measured in *o*-dichlorobenezene; [d]Calculated from density functional theory; [e]Determined from DPV in *o*-dichlorobenzene at 25 °C with reference to Fc/Fc^+ internal standard (at +0.64 V); [f]HOMO = -(4.44+0.64+E_{ox}) against NHE; [f]LUMO = HOMO + ΔE_g; [g]$\Delta E_g = 1240/\lambda_{onset}$; [h]Mobility values at zero field strength.

Thermal properties of the compounds were characterized by thermogravimetric analysis (TGA) recorded under the nitrogen atmosphere at the heating rate of 10 °C/min. All the compounds showed thermal decomposition temperature >400 °C, corresponding to a 5% weight loss (Figure D.2.13, Appendix D). We next performed the hole-mobility measurement on the thiophene-based HTMs using the xerographic time of flight (XTOF) method at room temperature (see Appendix D for details). The hole drift mobility field dependent results for **BT-4D**, **TT-4D**, and **QT-4D** are presented in Figure 6.2.1b and the hole mobility values at zero field (μ_o) and the other mobility defining parameters are summarized in Table 6.2.1 and Table D.2.4 (Appendix D), respectively. **BT-4D** yields highest hole mobility value of 5.6 x 10^{-6} cm^2 V^{-1} s^{-1} comparing to **TT-4D** (5 x 10^{-6} cm^2 V^{-1} s^{-1}) and **QT-4D** (4.7 x1 o^{-6} cm^2 V^{-1} s^{-1}).

Besides, the interaction of the thiophene-based HTMs with the perovskite surface was modeled using *ab initio* molecular dynamics. In the performed computational experiment, the HTM molecules were placed at the perovskite surface and allowed to interact with it, maintaining the temperature constant at 300K. Figure 6.2.1c shows the simulated adsorption of **BT-4D**, **TT-4D**, and **QT-4D** on top of the triple cation perovskite surface. **BT-4D** exhibited a more compact molecular structure on top of perovskite in comparison with **TT-4D** and **QT-4D**.

This is related to the fact that the increase of the thiophene content in the HTM results in the enhanced steric hindrance for the TPA moieties leading to the significant conformational distortion. Thus, the increasing number of thiophene core results in a more distorted molecular structure. In this connection, the more planar molecular orientation of **BT-4D** could allow a better intermolecular π–π stacking of the HTM on top of perovskite resulting in a better hole transfer capability which is consistent with the higher hole mobility value of **BT-4D**.[423, 424]

6.2.4 Devices Characteristics

We incorporated the thiophene-based HTMs in *n-i-p* solar cells device architecture consisting of the following layers: fluorine-doped tin oxide (FTO), compact TiO_2 (c-TiO_2), mesoporous TiO_2 (mp-TiO_2), SnO_2, perovskite, HTM, and gold electrode (Figure 6.2.2a). PSC devices are employing spiro-OMeTAD as the HTM were also fabricated having the same device configuration. The hole-transporting layers (HTLs) were prepared using solution process and the solutions were doped with Li-bis(trifluoromethanesulphonyl) imide (Li-TFSI), tris(2-(1*H*-pyrazol-1-yl)-4-*tert*-butylpyridine)cobalt(III) (FK-209), and 4-*tert*-butylpyridine (tBP) (see experimental methods, Appendix D for details).

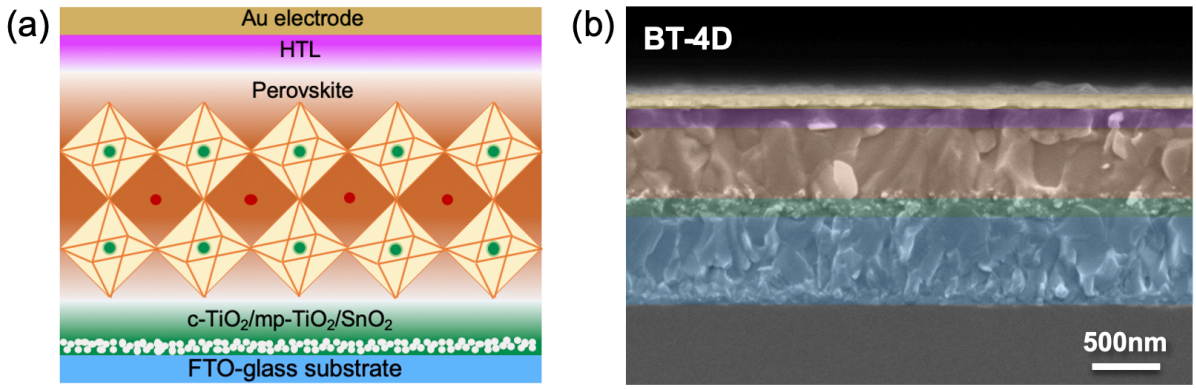

Figure 6.2.2 (a) Cartoon drawing illustrating the device configuration. (b) Cross-sectional scanning electron microscope (SEM) image of the PSC employing BT-4D as HTL. Each layer's color code in the SEM image corresponds to the layers illustrated in (a).

Scanning electron microscope (SEM) analysis was performed on the complete solar cell devices to further know how the HTLs sat on top of perovskite. The cross-sectional SEM images confirm that the deposition of **BT-4D**, **TT-4D**, and **QT-4D** layers results in the formation of ~150 nm-thick HTLs, while the deposition of spiro-OMeTAD results in the formation of ~250 nm-thick HTL (see Figure 6.2.2 and Figure D.2.14). It is worth mentioning that PSCs based on **BT-4D** and spiro-OMeTAD layers exhibit dense and uniform layers on top of perovskite. However,

PSCs based on **TT-4D** and **QT-4D** show some voids on the cross-sectional SEM images (Figure D.2.14 a and b, Appendix D), which are further confirmed by the top-view SEM images of the HTLs (Figure D.2.15, Appendix D). The voids formed in the **TT-4D** and **QT-4D** layers could be caused by the lower solubility of **TT-4D** and **QT-4D** in chlorobenzene.[425] Further, differential scanning calorimetry (DSC) analysis was carried out to ascertain morphological feature of HTMs. All the three HTMs did not show glass transition temperature (Figure D.2.16, Appendix D). DSC data reveal the crystallization peak (T_c) for **TT-4D** and **QT-4D**, despite the intensity of crystallization peak is small. It suggests that the crystallization process is slow which might eventually induce the formation of aggregates in the film state, resulting a poor film morphology. On the other hand, **BT-4D** showed the lowest intensity of crystallization peak in DSC analysis. This could suggest the amorphous nature of **BT-4D** in film state which in turn results in smooth surface. Thus, **BT-4D** show comparable morphological stability with spiro-OMeTAD which shows high glass transition temperature and thus result in good amorphous nature and morphology.[426]

Table 6.2.2 Photovoltaic parameters of the champion PSCs employing **BT-4D**, **TT-4D**, **QT-4D** as HTMs

HTM	V_{OC} (V)	J_{SC} (mA cm^{-2})	*FF*	PCE (%)
BT-4D	1.056	23.21	0.789	19.34
TT-4D	1.042	22.77	0.718	17.04
QT-4D	1.051	22.39	0.703	16.55
Spiro-OMeTAD	1.107	23.06	0.785	20.03

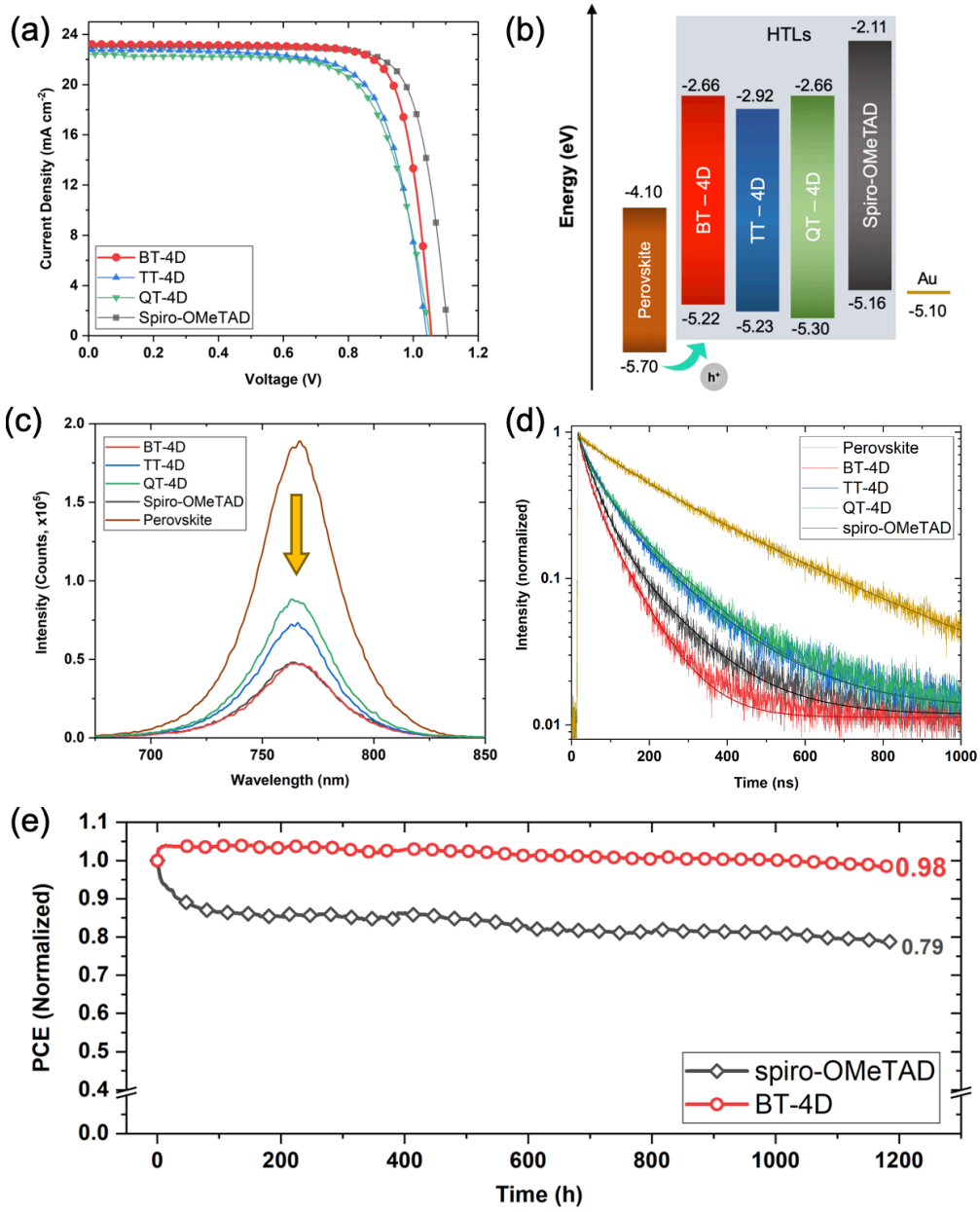

Figure 6.2.3 (a) *J-V* curves of the champion cells employing **BT-4D**, **TT-4D**, **QT-4D**, and spiro-OMeTAD as HTLs. (b) Schematic energy level diagram of **BT-4D**, **TT-4D**, and **QT-4D**. The energy levels of perovskite layer, spiro-OMeTAD, and gold electrode are included for comparison.[373] (c) Steady-state photoluminescence spectra of perovskite thin-films with **BT-4D**, **TT-4D**, **QT-4D**, and spiro-OMeTAD deposited on top upon excitation at 625 nm. (d) Transient PL (TrPL) spectra of perovskite thin-films with **BT-4D**, **TT-4D**, **QT-4D**, and spiro-OMeTAD deposited on top upon excitation at 635 nm. (e) Long-term stability test of the unencapsulated devices employing **BT-4D** and spiro-OMeTAD as HTLs under continuous 1-sun illumination and inert atmosphere for ~1186 h.

The current density-voltage (*J-V*) curves of the champion PSCs fabricated with thiophene-based molecules (**BT-4D**, **TT-4D**, and **QT-4D**) as HTLs are shown in Figure 6.2.3a and the corresponding photovoltaic parameters are summarized in Table 6.2.2. Control device based on spiro-OMeTAD as HTL is also included for the comparison. The PCEs of 19.34%, 17.04%, and 16.55% are achieved for the champion cells employing **BT-4D**, **TT-4D**, and **QT-4D**, respectively. **BT-4D** yields the highest PCE with higher open-circuit voltage (V_{OC}), short-circuit current density (J_{SC}), and fill factor (*FF*) values among the other thiophene-based HTLs. The trend in the PCEs obtained from the thiophene-based HTLs is also in agreement with the statistical value, ranging from 15.92 to 19.13% (Table D.2.5 and Figure D.2.17, Appendix D). Interestingly, the gradual increase in the thiophene core substitution causes further deterioration in device photovoltaic performance as observed in **TT-4D** and **QT-4D** (with three and four thiophene-substitution, respectively).[419, 427] In this case, *FF* is the main photovoltaic parameter leading to the lower PCE of **TT-4D** and **QT-4D** in comparison with **BT-4D**. The low *FF* values of **TT-4D** and **QT-4D** can be explained with lower conductivity (*vide infra*) and poor film formation, as observed in the SEM images (Figure D.2.15, Appendix D).[377] Moreover, a slight decrease in the V_{OC} and J_{SC} are observed for the PSCs employing **TT-4D** and **QT-4D**. The slightly lower V_{OC} of **TT-4D** and **QT-4D** might be due to the poor thin-film morphology of **TT-4D** and **QT-4D**. The reduced J_{SC} values of **TT-4D** and **QT-4D** are in a good agreement with the lower hole mobility of **TT-4D** and **QT-4D** compared to **BT-4D** (Figure 6.2.1b and Table 6.2.1). The J_{SC} values trend is also consistent with the integrated J_{SC} value from the incident photon to current conversion efficiency (IPCE) spectra (Figure D.2.18, Appendix D). Overall, the calculated J_{SC} is in a good agreement with the *J-V* curves (within 5% deviation). Note that the lower IPCE values of **TT-4D** and **QT-4D** could be correlated with reduced absorption originating from the HTMs (Figure D.2.19 and Figure D.2.20, Appendix D). It is also worth noting that the overall photovoltaic performance of **BT-4D** is on par with spiro-OMeTAD, which is considered as the state-of-the-art HTL so far. Interestingly, **BT-4D** shows statistically higher *FF* value and comparable J_{SC} value as to spiro-OMeTAD (Table D.2.5 and Figure D.2.17, Appendix D).

To explain the hysteresis behavior as reported in Figure D.2.21 (Appendix D), we performed the impedance spectra measurement. Figure D.2.22a (Appendix D) shows the capacitance of PSCs employing different HTMs as a function of frequency. The low-frequency capacitance of **BT-4D**, **TT-4D**, **QT-4D** and spiro-OMeTAD at 100 Hz were 121 nF/cm^2, 65 nF/cm^2, 138 nF/cm^2, and 107 nF/cm^2, respectively. The higher capacitance value indicates the higher ion migration.[428] The trend in the capacitance value was consistent with the hysteresis index (HI) of **BT-4D** (0.043), **QT-4D** (0.071), and spiro-OMeTAD (0.033). The hysteresis index (HI) was

calculated as HI = (($PCE_{reverse\ scan}$ – $PCE_{forward\ scan}$)/$PCE_{reverse\ scan}$).[429] It is worth mentioning that **BT-4D** demonstrates a comparable HI with spiro-OMeTAD indicating the efficiency of **BT-4D** in extracting the holes, thus, preventing the ions accumulation on the perovskite-HTL interface.[375] However, **TT-4D** exhibits the largest HI of 0.116, which is not in agreement with the trend in the capacitance value. This result suggests that the reason for large hysteresis of **TT-4D** might be not due to the ion migration. Then, we investigated the Cole-Cole plot (Figure D.2.22b) at high-frequency range to understand the carrier transportation from the perovskite to the HTMs.[430] **TT-4D** exhibits the largest semi-circle compared to the other HTMs. This demonstrates that **TT-4D** has a large parallel resistance indicating a lower carrier transportation capability from the perovskite to **TT-4D**, which may further cause the large hysteresis.

To further examine the observed trend in solar cell performance, we investigated the conductivity of **BT-4D**, **TT-4D**, **QT-4D** and spiro-OMeTAD. HTM solutions doped with FK-209, Li-TFSI and tBP were spin coated onto organic field effect transistor (OFET) substrates. Conductivity was measured by using a two-contact electrical conductivity set-up with *I–V* sweeps between -10 and +10 V. The detailed results are presented in Table D.2.6 and Figure D.2.23 (Appendix D). Doped **BT-4D** shows better lateral thin-film conductivity (4.89×10^{-4} S cm^{-1}) than that of TT-4D (3.02×10^{-4} S cm^{-1}) and QT-4D (4.83×10^{-5} S cm^{-1}). The conductivity of doped spiro-OMeTAD was determined to be $\sigma = 5.83 \times 10^{-4}$ S cm^{-1}, which is comparable value to the **BT-4D** HTM. Upon increasing the number of the thiophene unit the conductivity decreases gradually, and for the **QT-4D** conductivity value was found to be one order of magnitude lower than for **BT-4D**. These findings are in good agreement with the device performance. The higher conductivity for **BT-4D** than **TT-4D** and **QT-4D** are beneficial to the hole extraction and transport, thus can explain the higher J_{SC} and *FF*.

To gain a deeper understanding of the hole extraction efficiency of the thiophene-based HTMs, we performed steady-state photoluminescence (PL) measurement. The steady-state PL spectra of the perovskite thin-films employing **BT-4D**, **TT-4D**, **QT-4D**, and spiro-OMeTAD as HTLs were recorded upon 625 nm excitation wavelength and reported in Figure 6.2.3c. The steady-state PL spectrum of the bare perovskite layer without HTL was also measured as the reference (Figure 6.2.3c). The bare perovskite film shows an emission peak at 767 nm, which is consistent to the emission peak of $(FAPbI_3)_{0.87}(MAPbBr_3)_{0.13}]_{0.92}(CsPbI_3)_{0.08}$ triple-cation perovskite.[223] Upon the deposition of HTL on top of the pristine perovskite layer, a slight blue shifts in the emission peak are observed which could be attributed to the optical properties of the perovskite-HTL interface and also the chemical interaction between HTL/perovskite surfaces.[377] Importantly, all the perovskite thin-films with HTLs revealed a quenching in the PL

intensity. The percentage of PL quenching is summarized in Table D.2.7 (Appendix D). **BT-4D** shows the largest PL quenching of 74.27% among the other thiophene-based HTLs. The PL quenching relative to the perovskite reference film upon the deposition of HTL indicates more efficient hole extraction at the perovskite-HTL interface.[27, 377] These results demonstrated that **BT-4D** has a better hole extracting capability compared to **TT-4D** and **QT-4D**, which is also in agreement with the photovoltaic performances observed from the *J-V* characteristics. It is also worth mentioning that **BT-4D** exhibits a slightly larger PL quenching percentage in respect to spiro-OMeTAD indicating the comparable hole-extraction capability of **BT-4D**.

Additionally, we carried out the transient PL (TrPL) measurement in order to further understand the charge carrier dynamics of the perovskite thin-films employing **BT-4D**, **TT-4D**, **QT-4D**, and spiro-OMeTAD as HTLs. The same set of thin-films as used in steady-state PL measurement is examined for TrPL measurement. The TrPL spectra were recorded upon 635 nm excitation wavelength and shown in Figure 6.2.3d. The carrier lifetime of the perovskite films incorporating different HTLs was fitted according to a biexponential decay function and reported in Table D.2.8 (Appendix D). All the perovskite thin-films with the HTLs deposited on top show a reduced carrier lifetime compared to the bare perovskite film (t_1= 113.8 ns and t_2= 329.9 ns). **BT-4D** exhibits the fastest decay (t_1= 22.0 ns and t_2= 80.3 ns) among the other thiophene-based HTLs and also outperforms spiro-OMeTAD (t_1= 40.4 ns and t_2= 134.9 ns). Both faster decay and larger PL quenching of **BT-4D** strongly suggest that the hole injection from the perovskite into **BT-4D** is more efficient compared to spiro-OMeTAD.[377]

Finally, to gain more insight into the devices' stability under operating condition, we investigated the long-term stability of the devices incorporating the best performing among the series (**BT-4D**) and spiro-OMeTAD as HTLs. The stability test was carried out on the unencapsulated devices at maximum power point tracking (MPPT) under continuous one sun illumination in an inert (Ar) atmosphere for 1186 h (see experimental methods for details). The long-term stability test results are reported in Figure 6.2.3e. Devices employing **BT-4D** and spiro-OMeTAD exhibit a different degradation behavior. During the first 15 hours, the device based on **BT-4D** shows a slight increase of 4% compared to the initial PCE, followed by a slow degradation process, retaining 98% of its initial PCE after 1186 h of light exposure. On the contrary, the device based on spiro-OMeTAD exhibits a fast degradation behavior at the first 50 hours, followed by a slow degradation process, retaining 79% of its initial PCE. The fast degradation behavior of spiro-OMeTAD based device during the initial stage has been also observed in the previous reports.[222, 431] It is known that the use of dopants in the HTL negatively influences the long-term stability of PSC,[113, 115, 432] however, this study confirms that the use of

dopants in HTL does not accelerate the degradation of PSC in the case of **BT-4D** based device. These results also demonstrate the superior stability of **BT-4D** under continuous light illumination, outperforming spiro-OMeTAD, with a negligible loss of 2% from the initial PCE after 1186 h. In addition, we carried out the shelf-life stability test of the unencapsulated PSCs employing **BT-4D** and spiro-OMeTAD by keeping the devices in the ambient atmosphere (relative humidity <15%) under dark. The PSCs with **BT-4D** still demonstrates a better stability compared to spiro-OMeTAD under this testing condition (Figure D.2.24, Appendix D). The enhanced stability of **BT-4D** based PSC could be due to the planar molecular orientation of **BT-4D** when it interacts with the perovskite surface (Figure 6.2.1c). This could lead to a better stacking or packing in the perovskite-HTM which may further prevent severe degradation of the HTM layer in the devices.[222] This outstanding stability of **BT-4D** makes it as one of the most stable doped HTL among the other reported doped HTLs (Table D.2.9)[222, 392, 418, 433, 434] with comparable device photovoltaic performance to spiro-OMeTAD.

In addition, we carried out water contact angle measurements on top of HTLs to investigate the hydrophobicity of the HTLs in thin-films (Figure D.2.25). The thiophene-based HTLs demonstrated higher water contact angle in comparison with spiro-OMeTAD. Interestingly, the water droplet completely wetted spiro-OMeTAD surface after 20 s of being in contact with water, while the water droplet on top of the **BT-4D**, **TT-4D**, and **QT-4D** still maintained similar contact angle values after 20 s. These results suggest that the thiophene-based HTLs are more hydrophobic compared to spiro-OMeTAD, which is beneficial for the improved device stability against the moisture during the operation.

6.2.5 Conclusion

In summary, molecularly engineered TPA-functionalized oligothiophene small molecular HTMs have been designed, synthesized, and studied in PSCs. The inexpensive precursors are utilized to synthesize these HTMs in scalable batches through an easily accessible synthetic pathway. The PSCs employing **BT-4D** as HTL demonstrated the highest PCE of 19.34%, which is on par with spiro-OMeTAD as the reference. Hole mobility, lateral conductivity, PL, and SEM analyses showed that **BT-4D** has better hole-extraction properties and film formation compared to **TT-4D** and **QT-4D**, resulting in the best photovoltaic performance among the synthesized thiophene-based HTMs. Notably, PSCs fabricated with **BT-4D** exhibited impressive long-term stability under the continuous one sun exposure for 1186 h by retaining 98% of its initial efficiency, outperforming the spiro-OMeTAD based PSCs. These results demonstrate the

prospective advantages of arylamine terminated non-fused oliogothiophenes for efficient, stable, and low-cost HTMs in perovskite solar cells.

6.3 Conclusion

In this chapter, we have designed two classes of HTMs based on carbazole and thiophene molecules and applied them in the *n-i-p* configured PSCs. Both carbazole and thiophene-based HTMs have been synthesized using facile and low-cost synthetic steps in comparison with spiro-OMeTAD as the benchmark. In the case of the carbazole-based HTMs, the position of the TPA arms on the carbazole core will determine how the molecules are adsorbed on top of the perovskite surface. **Car[2,3]** molecule with the TPA substitutions at 2,3,6,7 positions has demonstrated more planar configuration, enabling better noncovalent interactions between the perovskite surface and denser molecular packing, which is beneficial for the hole transport. Consequently, a higher hole mobility value is achieved for **Car[2,3]**, resulting in a maximum PCE of 19.23%. On the other hand, the molecular orientation of the thiophene-based HTMs on the surface of perovskite is influenced by the number of the thiophene cores. **BT-4D** (with 2 thiophene units) exhibits a more compact molecular structure compared to **TT-4D** and **QT-4D** (with 3 and 4 thiophene units, respectively). The planar structure of **BT-4D** allows a better intermolecular π–π stacking of the HTM on top of perovskite which improves the hole extraction efficiency, leading to the maximum PCE of 19.34%. Essentially, both of the carbazole and thiophene-based HTMs have demonstrated enhanced long-term stability. PSC based on **Car[2,3]** maintained 81% of its initial PCE after 1000 h aging under continuous light illumination. Remarkably, PSC incorporating **BT-4D** showed a negligible lost by retaining 98% of its initial PCE for a longer aging time of 1186 h under constant light exposure. The improved long-term stability of the carbazole and thiophene-based HTMs could originate from the high decomposition temperature and improved hydrophobicity. This study highlights the importance of the HTM engineering in promoting the hole extraction for an efficient PSC as well as realizing a stable device performance using a low-cost material.

Chapter 7: Conclusions and Outlook

The main goals of this thesis are to improve the perovskite solar cells (PSCs) performance and stability by means of interface engineering. The fundamentals of the interfacial processes have been thoroughly investigated to provide a clear understanding on how the perovskite's interface could be tuned to boost the photovoltaic performance and long-term stability of the devices. I have chosen two different strategies to incorporate an interfacial layer at the perovskite/hole-transporting material (HTM) interface: low-dimensional perovskites and Lewis base molecule. The optical, structural, chemical, energetical, and photovoltaic analyses have been carried out to unveil the key roles of the interface in determining PSCs performance and stability. On top of that, I employed another strategy to improve the perovskite/HTM interface by directly modifying the HTM itself. The correlation between the molecular design of the HTM and the hole extracting efficiency as well as the robustness of the HTM upon the aging under the operation condition have also been carefully examined.

Chapter 2 summarizes the current state of interfacial engineering in PSCs for defect passivation and stability improvement. I have carried out a thorough literature study and analysis on the various interfacial engineering strategies. Several techniques of surface passivation ranging from PbI_2-rich perovskite composition, alkylammonium halides, Lewis acids and bases, hydrophobic organic molecules, wide bandgap materials, to low-dimensional perovskite are discussed. Interestingly, the passivating agent could be finely tuned to target a specific type of defect, inducing different passivation mechanism. Moreover, the effect of those interlayers on the device stability are compared. Based on this analysis, I found that the use of low-dimensional (2D) perovskites and Lewis bases show a great promise in improving both photovoltaic performance and long-term stability of PSCs.

Then, I introduced a 2D perovskite layer as an interlayer between 3D perovskite layer and HTM, resulting in a 2D/3D bilayer structure. The thin layer of 2D perovskite serves as both interface passivation and stability enhancer for *n-i-p* PSCs. In chapter 3, the investigation of the 2D/3D interfaces are mainly focused on the role of the 2D perovskite in preventing the degradation of the devices. Three new large organic cations were incorporated as the precursor for the 2D perovskite overlayer: 2-thiophenemethylamine iodide (2-TMAI), 3-thiophenemethylamine iodide (3-TMAI), and 2-thiopheneethylammonium iodide (2-TEAI). These thiophene-based cations were designed with different alkyl chains length and position.

When they were implemented in solar cells, I observed the enhancement of PV performance, mainly in the V_{OC} and *FF*, which could be ascribed to the interface passivation effect of 2D perovskite. Additionally, the evolution of the PV performance upon aging under dark and dry environment (RH<10%) were also observed. All the 2D/3D based PSCs showed continuous improvement in PV performance after long-term storage (18-24 weeks), while the 3D-only device showed the increase in PV performance in the first two weeks of storage followed by degradation process. Motivated by this observation, I performed structural and optical characterization to gain a better understanding on the origin of this evolution and the effect on the long-term stability. PL and XRD analyses revealed that the 2D phases transformed to higher *n* to lower *n* number upon aging. I found that the less transforming 2D perovskite phase, 2-TEAI, resulted in the most stable PSCs. On the other hand, the more transforming 2D perovskite phase, such as 2-TMAI and 3-TMAI, showed inferior long-term stability. We propose that this transformation could happen due to the mobilization of volatile cations (such as MA and FA) from the 3D perovskite layer underneath. Hence, a judicious design in the large organic layer is very crucial to block the migration of small cations, resulting in stable PSCs.

Following this finding, I am motivated to explore the impact of the thermal stress on the 2D/3D PSCs stability. Thus, I selected 2-TMAI as the representative of the thiophene cation family as the large organic cation and then I compared it with the widely used commercial cation, 2-phenylethylammonium iodide (PEAI), for synthesizing the 2D perovskite layer. The 2D/3D perovskite thin-films and devices were stressed under 50°C heat. The thin-films were characterized using in situ grazing incident wide angle X-ray scattering (GIWAXS) analysis. Both 2-TMAI 2D/3D and PEAI 2D/3D exhibited decrease in the pure 2D phase (n= 1) peak upon heating. Consistent with the observation in the previous chapter, 2-TMAI 2D/3D showed the formation of n= 2 phases during heating. On the contrary, PEAI 2D/3D perovskite did not show formation of a new phase under the thermal aging process. It is worth noting that the 3D perovskite peak stayed intact during the thermal cycle, which was confirmed by insignificant change in the PV performances of the devices employing both 2-TMAI 2D and PEAI 2D after thermal stress. From these results, I gain understanding that 2D perovskite protects the 3D perovskite from degradation regardless of the 2D perovskite phase evolution upon heating.

In chapter 4, I studied the energetic landscape of the 2D/3D interfaces and their roles in reducing the nonradiative recombination. Three cations based on the 2-thiophenemethyl ammonium halide family (2-TMAX with X: Cl, Br, I) were designed as the building block for the 2D/3D perovskite interfaces. The small difference on the halide counter ions could result in the contrasting interface energetic. The UPS depth profiling measurement reveals that the 2D/3D

interfaces formed by 2-TMAI and 2-TMABr cations exhibited a favorable valence and conduction band alignment for hole extraction and electron blocking, respectively. On the other hand, the 2-TMACl 2D/3D interface exhibited a slight uphill energy barrier. It is also worth mentioning that 2-TMAI and 2-TMABr 2D/3D perovskites showed the formation of a *p-n* junction at the interface which could improve the charge extraction and reduce the interface recombination. Remarkably, 2-TMABr 2D/3D perovskite interface has successfully reached zero interfacial voltage loss with the maximum photoluminescence quantum yield (PLQY) of 2% in the device, which is reflected in the high V_{OC} of 1.19 V and the power conversion efficiency (PCE) approaching 21%. This finding shed light on the importance of the 2D/3D interface design by manipulating the chemical composition of the large organic cation to achieve an optimal interface energetics, resulting in the elimination of the interfacial recombination and ultimately the improvement of the photovoltaic performance.

Further, the interface engineering using a Lewis base is reported in Chapter 5. I applied a new phosphine oxide derivative, tris(5-((tetrahydro-2*H*-pyran-2-yl)oxy)pentyl)phosphine oxide (THPPO), to passivate the defect on the surface of the perovskite layer, especially by targeting the undercoordinated Pb^{2+} sites. The ^{31}P NMR analyses confirmed the interaction between the lone pair of electrons in the phosphine oxide and the undercoordinated Pb^{2+}. Besides, the suppression of the defect sites was also evidenced by the decrease of Pb^{0} signal in the XPS spectra. As a result, the nonradiative recombination was successfully reduced, which was validated in the increase of the PL intensity and lifetimes. In addition, the THPPO-passivated perovskite films exhibited a positive shift in the energy level alignment compared to the pristine film, enabling a favorable hole extraction as well as electron blocking properties at the interface. Hence, the HTL-free devices have demonstrated a significant increase in PCE from 5.84% to 13.31% thanks to the passivation effect and improved energy level alignment. A similar trend has been obtained when THPPO was incorporated the complete *n-i-p* configured solar cells using spiro-OMeTAD as the HTM by boosting the device's PCE from 19.87% to 20.70%.

Based on the studies on the interface engineering above, I find that the incorporated low dimensional halide perovskites and Lewis base could effectively reduce the interfacial recombination at the perovskite/HTM interface and enhance the device lifetime. Then, I worked on the HTMs engineering topic which could be explored to further improve the hole extraction at the interface and long-term stability. Spiro-OMeTAD is commonly used as the state-of-art HTMs in PSCs. However, its instability under the operation condition along with the costly synthetic steps limit the application of PSCs from the commercialization. Thus, I have investigated two families of new HTMs in Chapter 6 for the efficient, stable, and low-cost PSCs

development. The first series of the HTMs is based on the two isomeric carbazole molecules functionalized with four triphenylamine (TPA) groups at 1,3,6,8 positions (**Car[1,3]**) and 2,3,6,7 positions (**Car[2,3]**). The molecular dynamic simulation reveals that **Car[2,3]** exhibited a more planar molecular configuration compared to **Car[1,3]** upon the interaction with the surface of the perovskite layer. The planar conformation of **Car[2,3]** allows a dense stacking of HTM molecules, enabling an efficient hole transfer process which is in accordance with the higher hole mobility of **Car[2,3]**. In combination with the favorable energetics between perovskite and HTM, **Car[2,3]** could deliver PSC with the maximum PCE of 19.23% which is comparable with the spiro-OMeTAD as the reference. Importantly, the carbazole-based HTMs could maintain $\geq$80% of their initial PCEs after keeping them under continuous light illumination for 1000 h.

The second series of the HTMs studied in Chapter 6 of this thesis is based on the thiophene molecules functionalized with four TPA arms. Similar to the carbazole-based HTMs, the thiophene-based HTMs are designed because of its versatility for organic electronic applications as well as its facile and cheap synthetic cost. The thiophene-based HTMs vary on the number of the thiophene core: bithiophene (**BT-4D**), terthiophene (**TT-4D**), and quarterthiophene (**QT-4D**). From the theoretical calculation, the increasing number of the thiophene cores distorted the molecular structure which could hamper the conformal stacking of the HTM molecules on top of the perovskite. Thus, **BT-4D** with two thiophenes exhibited a more planar molecular orientation, allowing a better intermolecular π–π stacking of the HTM on top of perovskite for the hole extraction. Consequently, the device employing **BT-4D** yielded the highest PCE of 19.34%. Notably, the long-term stability of the devices has been enhanced to a great extent by incorporating **BT-4D**. The aged device under constant light irradiation maintained 98% of the initial efficiency after 1186 h. This finding highlights the importance of the HTM engineering for stable and efficient solar cells.

To summarize, I have extensively investigated the reasons behind the improvement of photovoltaic performance and stability of PSCs by interface engineering. The judicious design of large organic cations for low dimensional perovskite will determine the robustness of the 2D/3D perovskite interface, particularly in protecting the 3D perovskite bulk from the ambient atmosphere as well as elevated temperature during operation. Moreover, careful molecular tuning of the large organic cations could give a precise control on the energetic landscape of the 2D/3D perovskite interface which is important for eliminating radiative loss due to the interfacial recombination. In addition, the use of a Lewis base has been demonstrated to effectively target the undercoordinated Pb^{2+} defect which could improve the performance of both HTL-free and standard PSCs. Besides, the performance and stability enhancement of PSCs

could be realized by molecular engineering of the HTM. Equally, the cost of the HTMs should be considered to make PSCs more feasible for large-scale applications. The integration of the main findings in this thesis by coupling the optimized interface with the optimally designed HTMs could bring the development of the PSCs to the next level. I believe that the works carried out in this thesis will give a fundamental understanding of the smart device design for achieving high performance, stable, and low-cost PSCs towards commercial application.

References

1. International Energy Agency (IEA), Electricity consumption, World 1990—2018, https://www.iea.org/data-and-statistics?country=WORLD&fuel=Energy%20consumption&indicator=TotElecCons, (accessed 22 March, 2021).
2. International Energy Agency (IEA), CO_2 Emissions from Fuel Combustion: Overview, https://www.iea.org/reports/co2-emissions-from-fuel-combustion-overview, (accessed 22 March, 2021).
3. A. Korfiati, C. Gkonos, F. Veronesi, A. Gaki, S. Grassi, R. Schenkel, S. Volkwein, M. Raubal and L. Hurni, *IJSEPM*, 2016, **9**, 17-30.
4. International Energy Agency (IEA), Renewable electricity generation by source (non-combustible), World 1990-2018 https://www.iea.org/fuels-and-technologies/renewables, (accessed 22 March, 2021).
5. D. M. Chapin, C. S. Fuller and G. L. Pearson, *J. Appl. Phys.*, 1954, **25**, 676-677.
6. National Renewable Energy Laboratory (NREL), Best Research-Cell Efficiency Chart, https://www.nrel.gov/pv/cell-efficiency.html, (accessed 22 March, 2021).
7. Fraunhofer Institute for Solar Energy Systems, Photovoltaics Report, https://www.ise.fraunhofer.de/content/dam/ise/de/documents/publications/studies/Photovoltaics-Report.pdf, (accessed 22 March, 2021).
8. S. R. Wenham and M. A. Green, *Progress in Photovoltaics: Research and Applications*, 1996, **4**, 3-33.
9. A. Smets, K. Jäger, O. Isabella, R. v. Swaaij and M. Zeman, *Solar Energy: The Physics and Engineering of Photovoltaic Conversion, Technologies and Systems*, UIT Cambridge, Cambridge, 2016.
10. A. Kojima, K. Teshima, Y. Shirai and T. Miyasaka, *J. Am. Chem. Soc.*, 2009, **131**, 6050-6051.
11. H.-S. Kim, C.-R. Lee, J.-H. Im, K.-B. Lee, T. Moehl, A. Marchioro, S.-J. Moon, R. Humphry-Baker, J.-H. Yum, J. E. Moser, M. Grätzel and N.-G. Park, *Sci. Rep.*, 2012, **2**, 591.
12. M. M. Lee, J. Teuscher, T. Miyasaka, T. N. Murakami and H. J. Snaith, *Science*, 2012, **338**, 643-647.
13. M. I. H. Ansari, A. Qurashi and M. K. Nazeeruddin, *Journal of Photochemistry and Photobiology C: Photochemistry Reviews*, 2018, **35**, 1-24.
14. P. Wang, Y. Wu, B. Cai, Q. Ma, X. Zheng and W.-H. Zhang, *Adv. Funct. Mater.*, 2019, **29**, 1807661.
15. G. Lee, M.-c. Kim, Y. W. Choi, N. Ahn, J. Jang, J. Yoon, S. M. Kim, J.-G. Lee, D. Kang, H. S. Jung and M. Choi, *Energy Environ. Sci.*, 2019, **12**, 3182-3191.
16. X. Hu, F. Li and Y. Song, *ACS Energy Lett.*, 2019, **4**, 1065-1072.
17. H. Wang, H. A. Dewi, T. M. Koh, A. Bruno, S. Mhaisalkar and N. Mathews, *ACS Applied Materials & Interfaces*, 2020, **12**, 484-493.
18. A. Roy, A. Ghosh, S. Bhandari, S. Sundaram and T. K. Mallick, *Buildings*, 2020, **10**, 129.
19. M. Batmunkh, Y. L. Zhong and H. Zhao, *Adv. Mater.*, 2020, **32**, 2000631.
20. G. Grancini and M. K. Nazeeruddin, *Nat. Rev. Mater.*, 2019, **4**, 4-22.
21. G. Kieslich, S. Sun and A. K. Cheetham, *Chemical Science*, 2014, **5**, 4712-4715.
22. J.-P. Correa-Baena, M. Saliba, T. Buonassisi, M. Grätzel, A. Abate, W. Tress and A. Hagfeldt, *Science*, 2017, **358**, 739-744.
23. H.-S. Kim, J.-W. Lee, N. Yantara, P. P. Boix, S. A. Kulkarni, S. Mhaisalkar, M. Grätzel and N.-G. Park, *Nano Lett.*, 2013, **13**, 2412-2417.
24. Q. Lin, A. Armin, R. C. R. Nagiri, P. L. Burn and P. Meredith, *Nat. Photon.*, 2015, **9**, 106-112.

25. Z. Chen, Q. Dong, Y. Liu, C. Bao, Y. Fang, Y. Lin, S. Tang, Q. Wang, X. Xiao, Y. Bai, Y. Deng and J. Huang, *Nat. Commun.*, 2017, **8**, 1890.
26. S. D. Stranks, G. E. Eperon, G. Grancini, C. Menelaou, M. J. P. Alcocer, T. Leijtens, L. M. Herz, A. Petrozza and H. J. Snaith, *Science*, 2013, **342**, 341-344.
27. G. Xing, N. Mathews, S. Sun, S. S. Lim, Y. M. Lam, M. Grätzel, S. Mhaisalkar and T. C. Sum, *Science*, 2013, **342**, 344-347.
28. G. Xing, N. Mathews, S. S. Lim, N. Yantara, X. Liu, D. Sabba, M. Grätzel, S. Mhaisalkar and T. C. Sum, *Nat. Mater.*, 2014, **13**, 476-480.
29. H. Huang, J. Raith, S. V. Kershaw, S. Kalytchuk, O. Tomanec, L. Jing, A. S. Susha, R. Zboril and A. L. Rogach, *Nat. Commun.*, 2017, **8**, 996.
30. C. Wehrenfennig, G. E. Eperon, M. B. Johnston, H. J. Snaith and L. M. Herz, *Adv. Mater.*, 2014, **26**, 1584-1589.
31. H. Oga, A. Saeki, Y. Ogomi, S. Hayase and S. Seki, *J. Am. Chem. Soc.*, 2014, **136**, 13818-13825.
32. C. S. Ponseca, T. J. Savenije, M. Abdellah, K. Zheng, A. Yartsev, T. Pascher, T. Harlang, P. Chabera, T. Pullerits, A. Stepanov, J.-P. Wolf and V. Sundström, *J. Am. Chem. Soc.*, 2014, **136**, 5189-5192.
33. H. J. Snaith, *J. Phys. Chem. Lett.*, 2013, **4**, 3623-3630.
34. B. Brunetti, C. Cavallo, A. Ciccioli, G. Gigli and A. Latini, *Sci. Rep.*, 2016, **6**, 31896.
35. T. M. Koh, K. Fu, Y. Fang, S. Chen, T. C. Sum, N. Mathews, S. G. Mhaisalkar, P. P. Boix and T. Baikie, *J. Phys. Chem. C*, 2014, **118**, 16458-16462.
36. Z. Li, M. Yang, J.-S. Park, S.-H. Wei, J. J. Berry and K. Zhu, *Chem. Mater.*, 2016, **28**, 284-292.
37. M. Saliba, T. Matsui, K. Domanski, J.-Y. Seo, A. Ummadisingu, S. M. Zakeeruddin, J.-P. Correa-Baena, W. R. Tress, A. Abate, A. Hagfeldt and M. Grätzel, *Science*, 2016, **354**, 206-209.
38. M. Saliba, T. Matsui, J.-Y. Seo, K. Domanski, J.-P. Correa-Baena, M. K. Nazeeruddin, S. M. Zakeeruddin, W. Tress, A. Abate, A. Hagfeldt and M. Grätzel, *Energy Environ. Sci.*, 2016, **9**, 1989-1997.
39. G. Grancini, C. Roldán-Carmona, I. Zimmermann, E. Mosconi, X. Lee, D. Martineau, S. Narbey, F. Oswald, F. De Angelis, M. Graetzel and M. K. Nazeeruddin, *Nat. Commun.*, 2017, **8**, 15684.
40. Y. Liu, S. Akin, A. Hinderhofer, F. T. Eickemeyer, H. Zhu, J.-Y. Seo, J. Zhang, F. Schreiber, H. Zhang, S. M. Zakeeruddin, A. Hagfeldt, M. I. Dar and M. Grätzel, *Angew. Chem. Int. Ed.*, 2020, **59**, 15688-15694.
41. Q. Jiang, Y. Zhao, X. Zhang, X. Yang, Y. Chen, Z. Chu, Q. Ye, X. Li, Z. Yin and J. You, *Nat. Photon.*, 2019, **13**, 460-466.
42. H. Kim, S.-U. Lee, D. Y. Lee, M. J. Paik, H. Na, J. Lee and S. I. Seok, *Adv. Energy Mater.*, 2019, **9**, 1902740.
43. F. Matteocci, L. Cinà, E. Lamanna, S. Cacovich, G. Divitini, P. A. Midgley, C. Ducati and A. Di Carlo, *Nano Energy*, 2016, **30**, 162-172.
44. Z. Fu, M. Xu, Y. Sheng, Z. Yan, J. Meng, C. Tong, D. Li, Z. Wan, Y. Ming, A. Mei, Y. Hu, Y. Rong and H. Han, *Adv. Funct. Mater.*, 2019, **29**, 1809129.
45. R. Cheacharoen, N. Rolston, D. Harwood, K. A. Bush, R. H. Dauskardt and M. D. McGehee, *Energy Environ. Sci.*, 2018, **11**, 144-150.
46. C. Ortiz-Cervantes, P. Carmona-Monroy and D. Solis-Ibarra, *ChemSusChem*, 2019, **12**, 1560-1575.
47. C. C. Stoumpos, D. H. Cao, D. J. Clark, J. Young, J. M. Rondinelli, J. I. Jang, J. T. Hupp and M. G. Kanatzidis, *Chem. Mater.*, 2016, **28**, 2852-2867.

48. I. Spanopoulos, I. Hadar, W. Ke, Q. Tu, M. Chen, H. Tsai, Y. He, G. Shekhawat, V. P. Dravid, M. R. Wasielewski, A. D. Mohite, C. C. Stoumpos and M. G. Kanatzidis, *J. Am. Chem. Soc.*, 2019, **141**, 5518-5534.
49. I. C. Smith, E. T. Hoke, D. Solis-Ibarra, M. D. McGehee and H. I. Karunadasa, *Angew. Chem.*, 2014, **126**, 11414-11417.
50. P. Huang, S. Kazim, M. Wang and S. Ahmad, *ACS Energy Lett.*, 2019, **4**, 2960-2974.
51. D. H. Cao, C. C. Stoumpos, O. K. Farha, J. T. Hupp and M. G. Kanatzidis, *J. Am. Chem. Soc.*, 2015, **137**, 7843-7850.
52. L. N. Quan, M. Yuan, R. Comin, O. Voznyy, E. M. Beauregard, S. Hoogland, A. Buin, A. R. Kirmani, K. Zhao, A. Amassian, D. H. Kim and E. H. Sargent, *J. Am. Chem. Soc.*, 2016, **138**, 2649-2655.
53. K. Tanaka, T. Takahashi, T. Kondo, T. Umebayashi, K. Asai and K. Ema, *Phys. Rev. B*, 2005, **71**, 045312.
54. K. Tanaka, F. Sano, T. Takahashi, T. Kondo, R. Ito and K. Ema, *Solid State Commun.*, 2002, **122**, 249-252.
55. T. Ishihara, X. Hong, J. Ding and A. V. Nurmikko, *Surface Science*, 1992, **267**, 323-326.
56. E. R. Dohner, A. Jaffe, L. R. Bradshaw and H. I. Karunadasa, *J. Am. Chem. Soc.*, 2014, **136**, 13154-13157.
57. H. Cho, S.-H. Jeong, M.-H. Park, Y.-H. Kim, C. Wolf, C.-L. Lee, J. H. Heo, A. Sadhanala, N. Myoung, S. Yoo, S. H. Im, R. H. Friend and T.-W. Lee, *Science*, 2015, **350**, 1222-1225.
58. Y. Chen, Y. Sun, J. Peng, J. Tang, K. Zheng and Z. Liang, *Adv. Mater.*, 2018, **30**, 1703487.
59. H. Tsai, W. Nie, J.-C. Blancon, C. C. Stoumpos, R. Asadpour, B. Harutyunyan, A. J. Neukirch, R. Verduzco, J. J. Crochet, S. Tretiak, L. Pedesseau, J. Even, M. A. Alam, G. Gupta, J. Lou, P. M. Ajayan, M. J. Bedzyk, M. G. Kanatzidis and A. D. Mohite, *Nature*, 2016, **536**, 312-316.
60. W. Fu, H. Liu, X. Shi, L. Zuo, X. Li and A. K.-Y. Jen, *Adv. Funct. Mater.*, 2019, **29**, 1900221.
61. H. Lai, B. Kan, T. Liu, N. Zheng, Z. Xie, T. Zhou, X. Wan, X. Zhang, Y. Liu and Y. Chen, *J. Am. Chem. Soc.*, 2018, **140**, 11639-11646.
62. H. Zheng, G. Liu, L. Zhu, J. Ye, X. Zhang, A. Alsaedi, T. Hayat, X. Pan and S. Dai, *Adv. Energy Mater.*, 2018, **8**, 1800051.
63. R. Yang, R. Li, Y. Cao, Y. Wei, Y. Miao, W. L. Tan, X. Jiao, H. Chen, L. Zhang, Q. Chen, H. Zhang, W. Zou, Y. Wang, M. Yang, C. Yi, N. Wang, F. Gao, C. R. McNeill, T. Qin, J. Wang and W. Huang, *Adv. Mater.*, 2018, **30**, 1804771.
64. S. Hubbard, in *Photovoltaic Solar Energy*, 2016, DOI: https://doi.org/10.1002/9781118927496.ch5, pp. 39-46.
65. J. Huang, Y. Yuan, Y. Shao and Y. Yan, *Nat. Rev. Mater.*, 2017, **2**, 17042.
66. Q. Dong, Y. Fang, Y. Shao, P. Mulligan, J. Qiu, L. Cao and J. Huang, *Science*, 2015, **347**, 967-970.
67. N. J. Jeon, J. H. Noh, Y. C. Kim, W. S. Yang, S. Ryu and S. I. Seok, *Nat. Mater.*, 2014, **13**, 897-903.
68. H. J. Snaith, A. Abate, J. M. Ball, G. E. Eperon, T. Leijtens, N. K. Noel, S. D. Stranks, J. T.-W. Wang, K. Wojciechowski and W. Zhang, *J. Phys. Chem. Lett.*, 2014, **5**, 1511-1515.
69. T. Liu, K. Chen, Q. Hu, R. Zhu and Q. Gong, *Adv. Energy Mater.*, 2016, **6**, 1600457.
70. D. Li, L. Chao, C. Chen, X. Ran, Y. Wang, T. Niu, S. Lv, H. Wu, Y. Xia, C. Ran, L. Song, S. Chen, Y. Chen and W. Huang, *Nano Lett.*, 2020, **20**, 5799-5806.
71. D. Bogachuk, S. Zouhair, K. Wojciechowski, B. Yang, V. Babu, L. Wagner, B. Xu, J. Lim, S. Mastroianni, H. Pettersson, A. Hagfeldt and A. Hinsch, *Energy Environ. Sci.*, 2020, **13**, 3880-3916.
72. V. K. Ravi, B. Mondal, V. V. Nawale and A. Nag, *ACS Omega*, 2020, **5**, 29631-29641.
73. A. L. Wani, A. Ara and J. A. Usmani, *Interdiscip. Toxicol.*, 2016, **8**, 55-64.

74. Directive (EU) 2020/2184 of the European Parliament and of the Council of 16 December 2020 on the quality of water intended for human consumption., https://eur-lex.europa.eu/legal-content/EN/TXT/PDF/?uri=CELEX:32020L2184&from=EN, (accessed 22 March, 2021).
75. W. Ke and M. G. Kanatzidis, *Nat. Commun.*, 2019, **10**, 965.
76. E. Jokar, C.-H. Chien, C.-M. Tsai, A. Fathi and E. W.-G. Diau, *Adv. Mater.*, 2019, **31**, 1804835.
77. E. Jokar, P.-Y. Cheng, C.-Y. Lin, S. Narra, S. Shahbazi and E. Wei-Guang Diau, *ACS Energy Lett.*, 2021, **6**, 485-492.
78. G. Schileo and G. Grancini, *J. Mater. Chem. C*, 2021, **9**, 67-76.
79. T. Krishnamoorthy, H. Ding, C. Yan, W. L. Leong, T. Baikie, Z. Zhang, M. Sherburne, S. Li, M. Asta, N. Mathews and S. G. Mhaisalkar, *J. Mater. Chem. A*, 2015, **3**, 23829-23832.
80. I. Kopacic, B. Friesenbichler, S. F. Hoefler, B. Kunert, H. Plank, T. Rath and G. Trimmel, *ACS Appl. Energy Mater.*, 2018, **1**, 343-347.
81. S. M. Jain, D. Phuyal, M. L. Davies, M. Li, B. Philippe, C. De Castro, Z. Qiu, J. Kim, T. Watson, W. C. Tsoi, O. Karis, H. Rensmo, G. Boschloo, T. Edvinsson and J. R. Durrant, *Nano Energy*, 2018, **49**, 614-624.
82. C. Momblona, H. Kanda, A. A. Sutanto, M. Mensi, C. Roldán-Carmona and M. K. Nazeeruddin, *Sci. Rep.*, 2020, **10**, 10640.
83. J. Xu, J.-B. Liu, B.-X. Liu and B. Huang, *J. Phys. Chem. Lett.*, 2017, **8**, 4391-4396.
84. F. Aslam, B.Sabir and M. Hassan, *Appl. Phys. A*, 2021, **127**, 112.
85. R. Nishikubo, H. Kanda, I. García-Benito, A. Molina-Ontoria, G. Pozzi, A. M. Asiri, M. K. Nazeeruddin and A. Saeki, *Chem. Mater.*, 2020, **32**, 6416-6424.
86. F. Jiang, D. Yang, Y. Jiang, T. Liu, X. Zhao, Y. Ming, B. Luo, F. Qin, J. Fan, H. Han, L. Zhang and Y. Zhou, *J. Am. Chem. Soc.*, 2018, **140**, 1019-1027.
87. M. Pantaler, K. T. Cho, V. I. E. Queloz, I. García Benito, C. Fettkenhauer, I. Anusca, M. K. Nazeeruddin, D. C. Lupascu and G. Grancini, *ACS Energy Lett.*, 2018, **3**, 1781-1786.
88. C. Wu, Q. Zhang, Y. Liu, W. Luo, X. Guo, Z. Huang, H. Ting, W. Sun, X. Zhong, S. Wei, S. Wang, Z. Chen and L. Xiao, *Advanced Science*, 2018, **5**, 1700759.
89. A. J. Huckaba, D. T. Sun, A. A. Sutanto, M. Mensi, Y. Zhang, W. L. Queen and M. K. Nazeeruddin, *Energy Technology*, 2020, **8**, 2000239.
90. S. Wu, Z. Li, M.-Q. Li, Y. Diao, F. Lin, T. Liu, J. Zhang, P. Tieu, W. Gao, F. Qi, X. Pan, Z. Xu, Z. Zhu and A. K. Y. Jen, *Nature Nanotechnology*, 2020, **15**, 934-940.
91. Y. Jiang, L. Qiu, E. J. Juarez-Perez, L. K. Ono, Z. Hu, Z. Liu, Z. Wu, L. Meng, Q. Wang and Y. Qi, *Nat. Energy.*, 2019, **4**, 585-593.
92. P. Holzhey and M. Saliba, *J. Mater. Chem. A*, 2018, **6**, 21794-21808.
93. M. V. Khenkin, E. A. Katz, A. Abate, G. Bardizza, J. J. Berry, C. Brabec, F. Brunetti, V. Bulović, Q. Burlingame, A. Di Carlo, R. Cheacharoen, Y.-B. Cheng, A. Colsmann, S. Cros, K. Domanski, M. Dusza, C. J. Fell, S. R. Forrest, Y. Galagan, D. Di Girolamo, M. Grätzel, A. Hagfeldt, E. von Hauff, H. Hoppe, J. Kettle, H. Köbler, M. S. Leite, S. Liu, Y.-L. Loo, J. M. Luther, C.-Q. Ma, M. Madsen, M. Manceau, M. Matheron, M. McGehee, R. Meitzner, M. K. Nazeeruddin, A. F. Nogueira, Ç. Odabaşı, A. Osherov, N.-G. Park, M. O. Reese, F. De Rossi, M. Saliba, U. S. Schubert, H. J. Snaith, S. D. Stranks, W. Tress, P. A. Troshin, V. Turkovic, S. Veenstra, I. Visoly-Fisher, A. Walsh, T. Watson, H. Xie, R. Yıldırım, S. M. Zakeeruddin, K. Zhu and M. Lira-Cantu, *Nat. Energy.*, 2020, **5**, 35-49.
94. L. Meng, J. You and Y. Yang, *Nat. Commun.*, 2018, **9**, 5265.
95. A. Uddin, M. B. Upama, H. Yi and L. Duan, *Coatings*, 2019, **9**, 65.
96. T. Leijtens, K. Bush, R. Cheacharoen, R. Beal, A. Bowring and M. D. McGehee, *J. Mater. Chem. A*, 2017, **5**, 11483-11500.
97. S. Kundu and T. L. Kelly, *EcoMat*, 2020, **2**, e12025.

98. B. Conings, J. Drijkoningen, N. Gauquelin, A. Babayigit, J. D'Haen, L. D'Olieslaeger, A. Ethirajan, J. Verbeeck, J. Manca, E. Mosconi, F. D. Angelis and H.-G. Boyen, *Adv. Energy Mater.*, 2015, **5**, 1500477.
99. G. E. Eperon, S. D. Stranks, C. Menelaou, M. B. Johnston, L. M. Herz and H. J. Snaith, *Energy Environ. Sci.*, 2014, **7**, 982-988.
100. Y. Zhang, S.-G. Kim, D.-K. Lee and N.-G. Park, *ChemSusChem*, 2018, **11**, 1813-1823.
101. E. Gutierrez-Partida, H. Hempel, S. Caicedo-Dávila, M. Raoufi, F. Peña-Camargo, M. Grischek, R. Gunder, J. Diekmann, P. Caprioglio, K. O. Brinkmann, H. Köbler, S. Albrecht, T. Riedl, A. Abate, D. Abou-Ras, T. Unold, D. Neher and M. Stolterfoht, *ACS Energy Lett.*, 2021, DOI: 10.1021/acsenergylett.0c02642, 1045-1054.
102. J. Liang, C. Wang, Y. Wang, Z. Xu, Z. Lu, Y. Ma, H. Zhu, Y. Hu, C. Xiao, X. Yi, G. Zhu, H. Lv, L. Ma, T. Chen, Z. Tie, Z. Jin and J. Liu, *J. Am. Chem. Soc.*, 2016, **138**, 15829-15832.
103. B. Li, Y. Zhang, L. Fu, T. Yu, S. Zhou, L. Zhang and L. Yin, *Nat. Commun.*, 2018, **9**, 1076.
104. N. A. N. Ouedraogo, Y. Chen, Y. Y. Xiao, Q. Meng, C. B. Han, H. Yan and Y. Zhang, *Nano Energy*, 2020, **67**, 104249.
105. A. M. A. Leguy, Y. Hu, M. Campoy-Quiles, M. I. Alonso, O. J. Weber, P. Azarhoosh, M. van Schilfgaarde, M. T. Weller, T. Bein, J. Nelson, P. Docampo and P. R. F. Barnes, *Chem. Mater.*, 2015, **27**, 3397-3407.
106. J. Yang, B. D. Siempelkamp, D. Liu and T. L. Kelly, *ACS Nano*, 2015, **9**, 1955-1963.
107. J. A. Christians, P. A. Miranda Herrera and P. V. Kamat, *J. Am. Chem. Soc.*, 2015, **137**, 1530-1538.
108. D. Li, S. A. Bretschneider, V. W. Bergmann, I. M. Hermes, J. Mars, A. Klasen, H. Lu, W. Tremel, M. Mezger, H.-J. Butt, S. A. L. Weber and R. Berger, *J. Phys. Chem. C*, 2016, **120**, 6363-6368.
109. Z. Song, N. Shrestha, S. C. Watthage, G. K. Liyanage, Z. S. Almutawah, R. H. Ahangharnejhad, A. B. Phillips, R. J. Ellingson and M. J. Heben, *J. Phys. Chem. Lett.*, 2018, **9**, 6312-6320.
110. J.-W. Lee, D.-H. Kim, H.-S. Kim, S.-W. Seo, S. M. Cho and N.-G. Park, *Adv. Energy Mater.*, 2015, **5**, 1501310.
111. Z. Wang, D. P. McMeekin, N. Sakai, S. van Reenen, K. Wojciechowski, J. B. Patel, M. B. Johnston and H. J. Snaith, *Adv. Mater.*, 2017, **29**, 1604186.
112. W. Zhang, J. Xiong, J. Li and W. A. Daoud, *ACS Applied Materials & Interfaces*, 2019, **11**, 12699-12708.
113. J. Liu, Y. Wu, C. Qin, X. Yang, T. Yasuda, A. Islam, K. Zhang, W. Peng, W. Chen and L. Han, *Energy Environ. Sci.*, 2014, **7**, 2963-2967.
114. Y. Liu, Q. Chen, H.-S. Duan, H. Zhou, Y. Yang, H. Chen, S. Luo, T.-B. Song, L. Dou, Z. Hong and Y. Yang, *J. Mater. Chem. A*, 2015, **3**, 11940-11947.
115. Z. Hawash, L. K. Ono, S. R. Raga, M. V. Lee and Y. Qi, *Chem. Mater.*, 2015, **27**, 562-569.
116. B. Salhi, Y. S. Wudil, M. K. Hossain, A. Al-Ahmed and F. A. Al-Sulaiman, *Renewable and Sustainable Energy Reviews*, 2018, **90**, 210-222.
117. S. Ito, S. Tanaka, K. Manabe and H. Nishino, *J. Phys. Chem. C*, 2014, **118**, 16995-17000.
118. T. Leijtens, G. E. Eperon, S. Pathak, A. Abate, M. M. Lee and H. J. Snaith, *Nat. Commun.*, 2013, **4**, 2885.
119. Y. Lee, S. Paek, K. T. Cho, E. Oveisi, P. Gao, S. Lee, J.-S. Park, Y. Zhang, R. Humphry-Baker, A. M. Asiri and M. K. Nazeeruddin, *J. Mater. Chem. A*, 2017, **5**, 12729-12734.
120. X. Tang, M. Brandl, B. May, I. Levchuk, Y. Hou, M. Richter, H. Chen, S. Chen, S. Kahmann, A. Osvet, F. Maier, H.-P. Steinrück, R. Hock, G. J. Matt and C. J. Brabec, *J. Mater. Chem. A*, 2016, **4**, 15896-15903.
121. R.-P. Xu, Y.-Q. Li, T.-Y. Jin, Y.-Q. Liu, Q.-Y. Bao, C. O'Carroll and J.-X. Tang, *ACS Applied Materials & Interfaces*, 2018, **10**, 6737-6746.

122. G. Abdelmageed, C. Mackeen, K. Hellier, L. Jewell, L. Seymour, M. Tingwald, F. Bridges, J. Z. Zhang and S. Carter, *Sol. Energy Mater. Sol. Cells*, 2018, **174**, 566-571.
123. J. Yang, Q. Hong, Z. Yuan, R. Xu, X. Guo, S. Xiong, X. Liu, S. Braun, Y. Li, J. Tang, C. Duan, M. Fahlman and Q. Bao, *Advanced Optical Materials*, 2018, **6**, 1800262.
124. K. Rakstys, C. Igci and M. K. Nazeeruddin, *Chemical Science*, 2019, **10**, 6748-6769.
125. W. S. Yang, J. H. Noh, N. J. Jeon, Y. C. Kim, S. Ryu, J. Seo and S. I. Seok, *Science*, 2015, **348**, 1234-1237.
126. G.-W. Kim, H. Choi, M. Kim, J. Lee, S. Y. Son and T. Park, *Adv. Energy Mater.*, 2020, **10**, 1903403.
127. T. P. I. Saragi, T. Spehr, A. Siebert, T. Fuhrmann-Lieker and J. Salbeck, *Chem. Rev.*, 2007, **107**, 1011-1065.
128. J. Salbeck, F. Weissörtel and J. Bauer, *Macromolecular Symposia*, 1998, **125**, 121-132.
129. J. Salbeck, N. Yu, J. Bauer, F. Weissörtel and H. Bestgen, *Synth. Met.*, 1997, **91**, 209-215.
130. J. P. Bastos, S. Manghooli, M. Jaysankar, J. G. Tait, W. Qiu, R. Gehlhaar, M. D. Volder, G. Uytterhoeven, J. Poortmans and U. W. Paetzold, *Appl. Phys. Lett.*, 2017, **110**, 233902.
131. M. Liu, M. B. Johnston and H. J. Snaith, *Nature*, 2013, **501**, 395-398.
132. U. W. Paetzold, W. Qiu, F. Finger, J. Poortmans and D. Cheyns, *Appl. Phys. Lett.*, 2015, **106**, 173101.
133. W. Qiu, M. Buffière, G. Brammertz, U. W. Paetzold, L. Froyen, P. Heremans and D. Cheyns, *Org. Electron.*, 2015, **26**, 30-35.
134. M. Kaltenbrunner, G. Adam, E. D. Głowacki, M. Drack, R. Schwödiauer, L. Leonat, D. H. Apaydin, H. Groiss, M. C. Scharber, M. S. White, N. S. Sariciftci and S. Bauer, *Nat. Mater.*, 2015, **14**, 1032-1039.
135. A. K. Chauhan and P. Kumar, *Journal of Materials Science: Materials in Electronics*, 2019, **30**, 9582-9592.
136. K. Domanski, J.-P. Correa-Baena, N. Mine, M. K. Nazeeruddin, A. Abate, M. Saliba, W. Tress, A. Hagfeldt and M. Grätzel, *ACS Nano*, 2016, **10**, 6306-6314.
137. Y. Deng, Q. Dong, C. Bi, Y. Yuan and J. Huang, *Adv. Energy Mater.*, 2016, **6**, 1600372.
138. Y. Kato, L. K. Ono, M. V. Lee, S. Wang, S. R. Raga and Y. Qi, *Advanced Materials Interfaces*, 2015, **2**, 1500195.
139. H. Zhang, J. Xiao, J. Shi, H. Su, Y. Luo, D. Li, H. Wu, Y.-B. Cheng and Q. Meng, *Adv. Funct. Mater.*, 2018, **28**, 1802985.
140. S. Rühle, *Solar Energy*, 2016, **130**, 139-147.
141. W. Shockley and H. J. Queisser, *J. Appl. Phys.*, 1961, **32**, 510-519.
142. H. J. Queisser, *Materials Science and Engineering: B*, 2009, **159-160**, 322-328.
143. L. Gu, D. Zhang, M. Kam, Q. Zhang, S. Poddar, Y. Fu, X. Mo and Z. Fan, *Nanoscale*, 2018, **10**, 15164-15172.
144. B. Wang, X. Xiao and T. Chen, *Nanoscale*, 2014, **6**, 12287-12297.
145. J. Y. Kim, J.-W. Lee, H. S. Jung, H. Shin and N.-G. Park, *Chem. Rev.*, 2020, **120**, 7867-7918.
146. J. Kim, S.-H. Lee, J. H. Lee and K.-H. Hong, *J. Phys. Chem. Lett.*, 2014, **5**, 1312-1317.
147. S. D. Stranks, P. K. Nayak, W. Zhang, T. Stergiopoulos and H. J. Snaith, *Angew. Chem. Int. Ed.*, 2015, **54**, 3240-3248.
148. R. S. Bonilla, B. Hoex, P. Hamer and P. R. Wilshaw, *physica status solidi (a)*, 2017, **214**, 1700293.
149. F. Gao, Y. Zhao, X. Zhang and J. You, *Adv. Energy Mater.*, 2020, **10**, 1902650.
150. J. Kim, A. Ho-Baillie and S. Huang, *Solar RRL*, 2019, **3**, 1800302.
151. A. G. Aberle, *Progress in Photovoltaics: Research and Applications*, 2000, **8**, 473-487.
152. J. Chen and N.-G. Park, *ACS Energy Lett.*, 2020, **5**, 2742-2786.
153. P. Caprioglio, M. Stolterfoht, C. M. Wolff, T. Unold, B. Rech, S. Albrecht and D. Neher, *Adv. Energy Mater.*, 2019, **9**, 1901631.

154. A. R. b. Mohd Yusoff, M. Vasilopoulou, D. G. Georgiadou, L. C. Palilis, A. Abate and M. K. Nazeeruddin, *Energy Environ. Sci.*, 2021, DOI: 10.1039/D1EE00062D.
155. T. Supasai, N. Rujisamphan, K. Ullrich, A. Chemseddine and T. Dittrich, *Appl. Phys. Lett.*, 2013, **103**, 183906.
156. L. Wang, C. McCleese, A. Kovalsky, Y. Zhao and C. Burda, *J. Am. Chem. Soc.*, 2014, **136**, 12205-12208.
157. Q. Chen, H. Zhou, T.-B. Song, S. Luo, Z. Hong, H.-S. Duan, L. Dou, Y. Liu and Y. Yang, *Nano Lett.*, 2014, **14**, 4158-4163.
158. C. Roldán-Carmona, P. Gratia, I. Zimmermann, G. Grancini, P. Gao, M. Graetzel and M. K. Nazeeruddin, *Energy Environ. Sci.*, 2015, **8**, 3550-3556.
159. D. Bi, W. Tress, M. I. Dar, P. Gao, J. Luo, C. Renevier, K. Schenk, A. Abate, F. Giordano, J.-P. Correa Baena, J.-D. Decoppet, S. M. Zakeeruddin, M. K. Nazeeruddin, M. Grätzel and A. Hagfeldt, *Science Advances*, 2016, **2**, e1501170.
160. Q. Jiang, Z. Chu, P. Wang, X. Yang, H. Liu, Y. Wang, Z. Yin, J. Wu, X. Zhang and J. You, *Adv. Mater.*, 2017, **29**, 1703852.
161. Y. Zhao, Q. Li, W. Zhou, Y. Hou, Y. Zhao, R. Fu, D. Yu, X. Liu and Q. Zhao, *Solar RRL*, 2019, **3**, 1800296.
162. D.-Y. Son, J.-W. Lee, Y. J. Choi, I.-H. Jang, S. Lee, P. J. Yoo, H. Shin, N. Ahn, M. Choi, D. Kim and N.-G. Park, *Nat. Energy.*, 2016, **1**, 16081.
163. Z. Hawash, S. R. Raga, D.-Y. Son, L. K. Ono, N.-G. Park and Y. Qi, *J. Phys. Chem. Lett.*, 2017, **8**, 3947-3953.
164. J.-W. Lee, D.-J. Seol, A.-N. Cho and N.-G. Park, *Adv. Mater.*, 2014, **26**, 4991-4998.
165. T. Zhang, M. Long, K. Yan, M. Qin, X. Lu, X. Zeng, C. M. Cheng, K. S. Wong, P. Liu, W. Xie and J. Xu, *Adv. Energy Mater.*, 2017, **7**, 1700118.
166. A. Abate, M. Saliba, D. J. Hollman, S. D. Stranks, K. Wojciechowski, R. Avolio, G. Grancini, A. Petrozza and H. J. Snaith, *Nano Lett.*, 2014, **14**, 3247-3254.
167. J. Xu, A. Buin, A. H. Ip, W. Li, O. Voznyy, R. Comin, M. Yuan, S. Jeon, Z. Ning, J. J. McDowell, P. Kanjanaboos, J.-P. Sun, X. Lan, L. N. Quan, D. H. Kim, I. G. Hill, P. Maksymovych and E. H. Sargent, *Nat. Commun.*, 2015, **6**, 7081.
168. X. Fang, J. Ding, N. Yuan, P. Sun, M. Lv, G. Ding and C. Zhu, *Phys. Chem. Chem. Phys.*, 2017, **19**, 6057-6063.
169. Y. Shao, Z. Xiao, C. Bi, Y. Yuan and J. Huang, *Nat. Commun.*, 2014, **5**, 5784.
170. P.-W. Liang, C.-C. Chueh, S. T. Williams and A. K.-Y. Jen, *Adv. Energy Mater.*, 2015, **5**, 1402321.
171. N. K. Noel, A. Abate, S. D. Stranks, E. S. Parrott, V. M. Burlakov, A. Goriely and H. J. Snaith, *ACS Nano*, 2014, **8**, 9815-9821.
172. S.-G. Kim, J. Chen, J.-Y. Seo, D.-H. Kang and N.-G. Park, *ACS Applied Materials & Interfaces*, 2018, **10**, 25372-25383.
173. L. Gao, S. Huang, L. Chen, X. Li, B. Ding, S. Huang and G. Yang, *Solar RRL*, 2018, **2**, 1800088.
174. J. Yang, S. Xiong, T. Qu, Y. Zhang, X. He, X. Guo, Q. Zhao, S. Braun, J. Chen, J. Xu, Y. Li, X. Liu, C. Duan, J. Tang, M. Fahlman and Q. Bao, *ACS Applied Materials & Interfaces*, 2019, **11**, 13491-13498.
175. B. Wang, F. Wu, S. Bi, J. Zhou, J. Wang, X. Leng, D. Zhang, R. Meng, B. Xue, C. Zong, L. Zhu, Y. Zhang and H. Zhou, *J. Mater. Chem. A*, 2019, **7**, 23895-23903.
176. D. W. deQuilettes, S. Koch, S. Burke, R. K. Paranji, A. J. Shropshire, M. E. Ziffer and D. S. Ginger, *ACS Energy Lett.*, 2016, **1**, 438-444.
177. Z. Yang, J. J. Dou, S. Kou, J. L. Dang, Y. Q. Ji, G. J. Yang, W. Q. Wu, D. B. Kuang and M. Q. Wang, *Adv. Funct. Mater.*, 2020, **30**, 1910710.
178. T. Y. Wen, S. Yang, P. F. Liu, L. J. Tang, H. W. Qiao, X. Chen, X. H. Yang, Y. Hou and H. G. Yang, *Adv. Energy Mater.*, 2018, **8**, 1703143.

179. Y. Lin, L. Shen, J. Dai, Y. Deng, Y. Wu, Y. Bai, X. Zheng, J. Wang, Y. Fang, H. Wei, W. Ma, X. C. Zeng, X. Zhan and J. Huang, *Adv. Mater.*, 2017, **29**, 1604545.
180. H. Zhang, Y. Wu, C. Shen, E. Li, C. Yan, W. Zhang, H. Tian, L. Han and W.-H. Zhu, *Adv. Energy Mater.*, 2019, **9**, 1803573.
181. S. Yang, J. Dai, Z. Yu, Y. Shao, Y. Zhou, X. Xiao, X. C. Zeng and J. Huang, *J. Am. Chem. Soc.*, 2019, **141**, 5781-5787.
182. X. Zheng, B. Chen, J. Dai, Y. Fang, Y. Bai, Y. Lin, H. Wei, Xiao C. Zeng and J. Huang, *Nat. Energy.*, 2017, **2**, 17102.
183. J. Peng, J. I. Khan, W. Liu, E. Ugur, T. Duong, Y. Wu, H. Shen, K. Wang, H. Dang, E. Aydin, X. Yang, Y. Wan, K. J. Weber, K. R. Catchpole, F. Laquai, S. De Wolf and T. P. White, *Adv. Energy Mater.*, 2018, **8**, 1801208.
184. Z. Huang, X. Hu, C. Liu, X. Meng, Z. Huang, J. Yang, X. Duan, J. Long, Z. Zhao, L. Tan, Y. Song and Y. Chen, *Adv. Funct. Mater.*, 2019, **29**, 1902629.
185. L. Zuo, H. Guo, D. W. deQuilettes, S. Jariwala, N. De Marco, S. Dong, R. DeBlock, D. S. Ginger, B. Dunn, M. Wang and Y. Yang, *Science Advances*, 2017, **3**, e1700106.
186. Q. Wang, Q. Dong, T. Li, A. Gruverman and J. Huang, *Adv. Mater.*, 2016, **28**, 6734-6739.
187. D. Koushik, W. J. H. Verhees, Y. Kuang, S. Veenstra, D. Zhang, M. A. Verheijen, M. Creatore and R. E. I. Schropp, *Energy Environ. Sci.*, 2017, **10**, 91-100.
188. Y. Bai, Y. Lin, L. Ren, X. Shi, E. Strounina, Y. Deng, Q. Wang, Y. Fang, X. Zheng, Y. Lin, Z.-G. Chen, Y. Du, L. Wang and J. Huang, *ACS Energy Lett.*, 2019, **4**, 1231-1240.
189. Q.-K. Wang, R.-B. Wang, P.-F. Shen, C. Li, Y.-Q. Li, L.-J. Liu, S. Duhm and J.-X. Tang, *Advanced Materials Interfaces*, 2015, **2**, 1400528.
190. K. T. Cho, S. Paek, G. Grancini, C. Roldán-Carmona, P. Gao, Y. Lee and M. K. Nazeeruddin, *Energy Environ. Sci.*, 2017, **10**, 621-627.
191. W. Ruan, Z. Zhang, Y. Hu, F. Bai, T. Qiu and S. Zhang, *Appl. Surf. Sci.*, 2019, **465**, 420-426.
192. B. Li, Y. Zhang, L. Zhang and L. Yin, *Adv. Mater.*, 2017, **29**, 1701221.
193. M. Cha, P. Da, J. Wang, W. Wang, Z. Chen, F. Xiu, G. Zheng and Z.-S. Wang, *J. Am. Chem. Soc.*, 2016, **138**, 8581-8587.
194. Y. Zhang, H. Yang, M. Chen, N. P. Padture, O. Chen and Y. Zhou, *Adv. Energy Mater.*, 2019, **9**, 1900243.
195. J. Zhang, D. Bai, Z. Jin, H. Bian, K. Wang, J. Sun, Q. Wang and S. Liu, *Adv. Energy Mater.*, 2018, **8**, 1703246.
196. C. Ortiz-Cervantes, P. I. Román-Román, J. Vazquez-Chavez, M. Hernández-Rodríguez and D. Solis-Ibarra, *Angew. Chem. Int. Ed.*, 2018, **57**, 13882-13886.
197. N. R. Venkatesan, J. G. Labram and M. L. Chabinyc, *ACS Energy Lett.*, 2018, **3**, 380-386.
198. K. T. Cho, G. Grancini, Y. Lee, E. Oveisi, J. Ryu, O. Almora, M. Tschumi, P. A. Schouwink, G. Seo, S. Heo, J. Park, J. Jang, S. Paek, G. Garcia-Belmonte and M. K. Nazeeruddin, *Energy Environ. Sci.*, 2018, **11**, 952-959.
199. J. J. Yoo, S. Wieghold, M. C. Sponseller, M. R. Chua, S. N. Bertram, N. T. P. Hartono, J. S. Tresback, E. C. Hansen, J.-P. Correa-Baena, V. Bulović, T. Buonassisi, S. S. Shin and M. G. Bawendi, *Energy Environ. Sci.*, 2019, **12**, 2192-2199.
200. C. Ma, C. Leng, Y. Ji, X. Wei, K. Sun, L. Tang, J. Yang, W. Luo, C. Li, Y. Deng, S. Feng, J. Shen, S. Lu, C. Du and H. Shi, *Nanoscale*, 2016, **8**, 18309-18314.
201. K. Yao, X. Wang, F. Li and L. Zhou, *Chem. Commun.*, 2015, **51**, 15430-15433.
202. J. Chen, J.-Y. Seo and N.-G. Park, *Adv. Energy Mater.*, 2018, **8**, 1702714.
203. S. Gharibzadeh, B. Abdollahi Nejand, M. Jakoby, T. Abzieher, D. Hauschild, S. Moghadamzadeh, J. A. Schwenzer, P. Brenner, R. Schmager, A. A. Haghighirad, L. Weinhardt, U. Lemmer, B. S. Richards, I. A. Howard and U. W. Paetzold, *Adv. Energy Mater.*, 2019, **9**, 1803699.

204. Q. Zhou, L. Liang, J. Hu, B. Cao, L. Yang, T. Wu, X. Li, B. Zhang and P. Gao, *Adv. Energy Mater.*, 2019, **9**, 1802595.
205. S. Paek, C. Roldán-Carmona, K. T. Cho, M. Franckevičius, H. Kim, H. Kanda, N. Drigo, K.-H. Lin, M. Pei, R. Gegevičius, H. J. Yun, H. Yang, P. A. Schouwink, C. Corminboeuf, A. M. Asiri and M. K. Nazeeruddin, *Advanced Science*, 2020, **7**, 2001014.
206. Y. Liu, S. Akin, L. Pan, R. Uchida, N. Arora, J. V. Milić, A. Hinderhofer, F. Schreiber, A. R. Uhl, S. M. Zakeeruddin, A. Hagfeldt, M. I. Dar and M. Grätzel, *Science Advances*, 2019, **5**, eaaw2543.
207. K. T. Cho, Y. Zhang, S. Orlandi, M. Cavazzini, I. Zimmermann, A. Lesch, N. Tabet, G. Pozzi, G. Grancini and M. K. Nazeeruddin, *Nano Lett.*, 2018, **18**, 5467-5474.
208. E. H. Jung, N. J. Jeon, E. Y. Park, C. S. Moon, T. J. Shin, T.-Y. Yang, J. H. Noh and J. Seo, *Nature*, 2019, **567**, 511-515.
209. M. A. Mahmud, T. Duong, Y. Yin, H. T. Pham, D. Walter, J. Peng, Y. Wu, L. Li, H. Shen, N. Wu, N. Mozaffari, G. Andersson, K. R. Catchpole, K. J. Weber and T. P. White, *Adv. Funct. Mater.*, 2020, **30**, 1907962.
210. X. Yin, Z. Song, Z. Li and W. Tang, *Energy Environ. Sci.*, 2020, **13**, 4057-4086.
211. J. Jeong, M. Kim, J. Seo, H. Lu, P. Ahlawat, A. Mishra, Y. Yang, M. A. Hope, F. T. Eickemeyer, M. Kim, Y. J. Yoon, I. W. Choi, B. P. Darwich, S. J. Choi, Y. Jo, J. H. Lee, B. Walker, S. M. Zakeeruddin, L. Emsley, U. Rothlisberger, A. Hagfeldt, D. S. Kim, M. Grätzel and J. Y. Kim, *Nature*, 2021, **592**, 381-385.
212. Y.-W. Jang, S. Lee, K. M. Yeom, K. Jeong, K. Choi, M. Choi and J. H. Noh, *Nat. Energy.*, 2021, **6**, 63-71.
213. M. L. Petrus, T. Bein, T. J. Dingemans and P. Docampo, *J. Mater. Chem. A*, 2015, **3**, 12159-12162.
214. H. J. Snaith and M. Grätzel, *Appl. Phys. Lett.*, 2006, **89**, 262114.
215. J. H. Noh, N. J. Jeon, Y. C. Choi, M. K. Nazeeruddin, M. Grätzel and S. I. Seok, *J. Mater. Chem. A*, 2013, **1**, 11842-11847.
216. E. J. Juarez-Perez, M. R. Leyden, S. Wang, L. K. Ono, Z. Hawash and Y. Qi, *Chem. Mater.*, 2016, **28**, 5702-5709.
217. T. Leijtens, T. Giovenzana, S. N. Habisreutinger, J. S. Tinkham, N. K. Noel, B. A. Kamino, G. Sadoughi, A. Sellinger and H. J. Snaith, *ACS Applied Materials & Interfaces*, 2016, **8**, 5981-5989.
218. T. H. Schloemer, J. A. Christians, J. M. Luther and A. Sellinger, *Chemical Science*, 2019, **10**, 1904-1935.
219. W. S. Yang, B.-W. Park, E. H. Jung, N. J. Jeon, Y. C. Kim, D. U. Lee, S. S. Shin, J. Seo, E. K. Kim, J. H. Noh and S. I. Seok, *Science*, 2017, **356**, 1376-1379.
220. Z. Hawash, L. K. Ono and Y. Qi, *Advanced Materials Interfaces*, 2018, **5**, 1700623.
221. H. Guo, H. Zhang, C. Shen, D. Zhang, S. Liu, Y. Wu and W.-H. Zhu, *Angew. Chem. Int. Ed.*, 2021, **60**, 2674-2679.
222. N. Drigo, C. Roldan-Carmona, M. Franckevičius, K.-H. Lin, R. Gegevičius, H. Kim, P. A. Schouwink, A. A. Sutanto, S. Olthof, M. Sohail, K. Meerholz, V. Gulbinas, C. Corminboeuf, S. Paek and M. K. Nazeeruddin, *J. Am. Chem. Soc.*, 2020, **142**, 1792-1800.
223. A. A. Sutanto, N. Drigo, V. I. E. Queloz, I. Garcia-Benito, A. R. Kirmani, L. J. Richter, P. A. Schouwink, K. T. Cho, S. Paek, M. K. Nazeeruddin and G. Grancini, *J. Mater. Chem. A*, 2020, **8**, 2343-2348.
224. https://www.nrel.gov/pv/cell-efficiency.html.
225. S. H. Turren-Cruz, A. Hagfeldt and M. Saliba, *Science*, 2018, **362**, 449-453.
226. M. Kim, S. G. Motti, R. Sorrentino and A. Petrozza, *Energy Environ. Sci.*, 2018, **11**, 2609-2619.
227. H. Peng, W. Sun, Y. Li, S. Ye, H. Rao, W. Yan, H. Zhou, Z. Bian and C. Huang, *Nano Res.*, 2016, **9**, 2960-2971.

228. N. Arora, M. I. Dar, A. Hinderhofer, N. Pellet, F. Schreiber, S. M. Zakeeruddin and M. Gratzel, *Science*, 2017, **358**, 768-771.
229. A. Agresti, S. Pescetelli, B. Taheri, A. E. Del Rio Castillo, L. Cina, F. Bonaccorso and A. Di Carlo, *ChemSusChem*, 2016, **9**, 2609-2619.
230. P. O'Keeffe, D. Catone, A. Paladini, F. Toschi, S. Turchini, L. Avaldi, F. Martelli, A. Agresti, S. Pescetelli, A. E. Del Rio Castillo, F. Bonaccorso and A. Di Carlo, *Nano Lett.*, 2019, **19**, 684-691.
231. L. Najafi, B. Taheri, B. Martín-García, S. Bellani, D. Di Girolamo, A. Agresti, R. Oropesa-Nuñez, S. Pescetelli, L. Vesce, E. Calabrò, M. Prato, A. E. Del Rio Castillo, A. Di Carlo and F. Bonaccorso, *ACS Nano*, 2018, **12**, 10736-10754.
232. I. García-Benito, C. Quarti, V. I. E. Queloz, S. Orlandi, I. Zimmermann, M. Cavazzini, A. Lesch, S. Marras, D. Beljonne, G. Pozzi, M. K. Nazeeruddin and G. Grancini, *Chem. Mater.*, 2018, **30**, 8211-8220.
233. Y. Bai, S. Xiao, C. Hu, T. Zhang, X. Meng, H. Lin, Y. Yang and S. Yang, *Adv. Energy Mater.*, 2017, **7**, 1701038.
234. T. M. Koh, V. Shanmugam, X. Guo, S. S. Lim, O. Filonik, E. M. Herzig, P. Müller-Buschbaum, V. Swamy, S. T. Chien, S. G. Mhaisalkar and N. Mathews, *J. Mater. Chem. A*, 2018, **6**, 2122-2128.
235. B. Roose, A. Ummadisingu, J.-P. Correa-Baena, M. Saliba, A. Hagfeldt, M. Graetzel, U. Steiner and A. Abate, *Nano Energy*, 2017, **39**, 24-29.
236. J. M. Azpiroz, E. Mosconi, J. Bisquert and F. De Angelis, *Energy Environ. Sci.*, 2015, **8**, 2118-2127.
237. D. Meggiolaro, E. Mosconi and F. De Angelis, *ACS Energy Lett.*, 2019, **4**, 779-785.
238. Y. Yuan and J. Huang, *Acc. Chem. Res.*, 2016, **49**, 286-293.
239. M. E. F. Bouduban, V. I. E. Queloz, V. M. Caselli, K. T. Cho, A. R. Kirmani, S. Paek, C. Roldan-Carmona, L. J. Richter, J. E. Moser, T. J. Savenije, M. K. Nazeeruddin and G. Grancini, *J. Phys. Chem. Lett.*, 2019, **10**, 5713-5720.
240. S. R. Cowan, A. Roy and A. J. Heeger, *Phys. Rev. B*, 2010, **82**, 245207.
241. Z. Liu, S. Niu and N. Wang, *J. Colloid Interface Sci.*, 2018, **509**, 171-177.
242. A. A. Sutanto, R. Szostak, N. Drigo, V. I. E. Queloz, P. E. Marchezi, J. C. Germino, H. C. N. Tolentino, M. K. Nazeeruddin, A. F. Nogueira and G. Grancini, *Nano Lett.*, 2020, **20**, 3992-3998.
243. N. Aristidou, I. Sanchez-Molina, T. Chotchuangchutchaval, M. Brown, L. Martinez, T. Rath and S. A. Haque, *Angew. Chem. Int. Ed.*, 2015, **54**, 8208-8212.
244. S.-W. Lee, S. Kim, S. Bae, K. Cho, T. Chung, L. E. Mundt, S. Lee, S. Park, H. Park, M. C. Schubert, S. W. Glunz, Y. Ko, Y. Jun, Y. Kang, H.-S. Lee and D. Kim, *Sci. Rep.*, 2016, **6**, 38150.
245. Y. Yue, N. Salim, Y. Wu, X. Yang, A. Islam, W. Chen, J. Liu, E. Bi, F. Xie, M. Cai and L. Han, *Adv. Mater.*, 2016, **28**, 10738-10743.
246. H. Back, G. Kim, J. Kim, J. Kong, T. K. Kim, H. Kang, H. Kim, J. Lee, S. Lee and K. Lee, *Energy Environ. Sci.*, 2016, **9**, 1258-1263.
247. T. M. Koh, V. Shanmugam, J. Schlipf, L. Oesinghaus, P. Müller-Buschbaum, N. Ramakrishnan, V. Swamy, N. Mathews, P. P. Boix and S. G. Mhaisalkar, *Adv. Mater.*, 2016, **28**, 3653-3661.
248. Y. Hu, J. Schlipf, M. Wussler, M. L. Petrus, W. Jaegermann, T. Bein, P. Müller-Buschbaum and P. Docampo, *ACS Nano*, 2016, **10**, 5999-6007.
249. T. Zhou, H. Lai, T. Liu, D. Lu, X. Wan, X. Zhang, Y. Liu and Y. Chen, *Adv. Mater.*, 2019, **31**, 1901242.
250. H. Min, M. Kim, S.-U. Lee, H. Kim, G. Kim, K. Choi, J. H. Lee and S. I. Seok, *Science*, 2019, **366**, 749-753.
251. B. Liu, M. Long, M. Cai, L. Ding and J. Yang, *Nano Energy*, 2019, **59**, 715-720.

252. J. Wang, S. Luo, Y. Lin, Y. Chen, Y. Deng, Z. Li, K. Meng, G. Chen, T. Huang, S. Xiao, H. Huang, C. Zhou, L. Ding, J. He, J. Huang and Y. Yuan, *Nat. Commun.*, 2020, **11**, 582.
253. B. Kim and S. I. Seok, *Energy Environ. Sci.*, 2020, **13**, 805-820.
254. C. Liu, J. Sun, W. L. Tan, J. Lu, T. R. Gengenbach, C. R. McNeill, Z. Ge, Y.-B. Cheng and U. Bach, *Nano Lett.*, 2020, **20**, 1240-1251.
255. K. Wang, Z. Li, F. Zhou, H. Wang, H. Bian, H. Zhang, Q. Wang, Z. Jin, L. Ding and S. Liu, *Adv. Energy Mater.*, 2019, **9**, 1902529.
256. X. Jia, C. Zuo, S. Tao, K. Sun, Y. Zhao, S. Yang, M. Cheng, M. Wang, Y. Yuan, J. Yang, F. Gao, G. Xing, Z. Wei, L. Zhang, H.-L. Yip, M. Liu, Q. Shen, L. Yin, L. Han, S. Liu, L. Wang, J. Luo, H. Tan, Z. Jin and L. Ding, *Science Bulletin*, 2019, **64**, 1532-1539.
257. G. Divitini, S. Cacovich, F. Matteocci, L. Cinà, A. Di Carlo and C. Ducati, *Nat. Energy.*, 2016, **1**, 15012.
258. W. Peng, J. Yin, K.-T. Ho, O. Ouellette, M. De Bastiani, B. Murali, O. El Tall, C. Shen, X. Miao, J. Pan, E. Alarousu, J.-H. He, B. S. Ooi, O. F. Mohammed, E. Sargent and O. M. Bakr, *Nano Lett.*, 2017, **17**, 4759-4767.
259. S. G. Motti, T. Crothers, R. Yang, Y. Cao, R. Li, M. B. Johnston, J. Wang and L. M. Herz, *Nano Lett.*, 2019, **19**, 3953-3960.
260. G. Grancini, S. Marras, M. Prato, C. Giannini, C. Quarti, F. De Angelis, M. De Bastiani, G. E. Eperon, H. J. Snaith, L. Manna and A. Petrozza, *J. Phys. Chem. Lett.*, 2014, **5**, 3836-3842.
261. R. F. Moral, L. G. Bonato, J. C. Germino, W. X. Coelho Oliveira, R. Kamat, J. Xu, C. J. Tassone, S. D. Stranks, M. F. Toney and A. F. Nogueira, *Chem. Mater.*, 2019, **31**, 9472-9479.
262. A. A. Sutanto, P. Caprioglio, N. Drigo, Y. J. Hofstetter, I. Garcia-Benito, V. I. E. Queloz, D. Neher, M. K. Nazeeruddin, M. Stolterfoht, Y. Vaynzof and G. Grancini, *Chem*, 2021, **7**, 1903-1916.
263. S. Shao and M. A. Loi, *Advanced Materials Interfaces*, 2020, **7**, 1901469.
264. M. Stolterfoht, M. Grischek, P. Caprioglio, C. M. Wolff, E. Gutierrez-Partida, F. Peña-Camargo, D. Rothhardt, S. Zhang, M. Raoufi, J. Wolansky, M. Abdi-Jalebi, S. D. Stranks, S. Albrecht, T. Kirchartz and D. Neher, *Adv. Mater.*, 2020, **32**, 2000080.
265. Q. Yao, Q. Xue, Z. Li, K. Zhang, T. Zhang, N. Li, S. Yang, C. J. Brabec, H.-L. Yip and Y. Cao, *Adv. Mater.*, 2020, **32**, 2000571.
266. M. Jeong, I. W. Choi, E. M. Go, Y. Cho, M. Kim, B. Lee, S. Jeong, Y. Jo, H. W. Choi, J. Lee, J.-H. Bae, S. K. Kwak, D. S. Kim and C. Yang, *Science*, 2020, **369**, 1615.
267. C. H. Ng, K. Hamada, G. Kapil, M. A. Kamarudin, Z. Wang, S. Iikubo, Q. Shen, K. Yoshino, T. Minemoto and S. Hayase, *J. Mater. Chem. A*, 2020, **8**, 2962-2968.
268. C. Zuo, A. D. Scully, W. L. Tan, F. Zheng, K. P. Ghiggino, D. Vak, H. Weerasinghe, C. R. McNeill, D. Angmo, A. S. R. Chesman and M. Gao, *Communications Materials*, 2020, **1**, 33.
269. D. Luo, R. Su, W. Zhang, Q. Gong and R. Zhu, *Nat. Rev. Mater.*, 2020, **5**, 44-60.
270. Z. Liu, L. Krückemeier, B. Krogmeier, B. Klingebiel, J. A. Márquez, S. Levcenko, S. Öz, S. Mathur, U. Rau, T. Unold and T. Kirchartz, *ACS Energy Lett.*, 2019, **4**, 110-117.
271. M. Abdi-Jalebi, Z. Andaji-Garmaroudi, S. Cacovich, C. Stavrakas, B. Philippe, J. M. Richter, M. Alsari, E. P. Booker, E. M. Hutter, A. J. Pearson, S. Lilliu, T. J. Savenije, H. Rensmo, G. Divitini, C. Ducati, R. H. Friend and S. D. Stranks, *Nature*, 2018, **555**, 497-501.
272. D. Kiermasch, L. Gil-Escrig, H. J. Bolink and K. Tvingstedt, *Joule*, 2019, **3**, 16-26.
273. V. Lami, A. Weu, J. Zhang, Y. Chen, Z. Fei, M. Heeney, R. H. Friend and Y. Vaynzof, *Joule*, 2019, **3**, 2513-2534.
274. V. Lami, Y. J. Hofstetter, J. F. Butscher and Y. Vaynzof, *Advanced Electronic Materials*, **n/a**, 2000213.

275. J. Zhang, M. H. Futscher, V. Lami, F. U. Kosasih, C. Cho, Q. Gu, A. Sadhanala, A. J. Pearson, B. Kan, G. Divitini, X. Wan, D. Credgington, N. C. Greenham, Y. Chen, C. Ducati, B. Ehrler, Y. Vaynzof, R. H. Friend and A. A. Bakulin, *Adv. Energy Mater.*, 2019, **9**, 1902145.
276. A. Wittmann, G. Schweicher, K. Broch, J. Novak, V. Lami, D. Cornil, E. R. McNellis, O. Zadvorna, D. Venkateshvaran, K. Takimiya, Y. H. Geerts, J. Cornil, Y. Vaynzof, J. Sinova, S. Watanabe and H. Sirringhaus, *Phys. Rev. Lett.*, 2020, **124**, 027204.
277. T. Zhang, M. Long, M. Qin, X. Lu, S. Chen, F. Xie, L. Gong, J. Chen, M. Chu, Q. Miao, Z. Chen, W. Xu, P. Liu, W. Xie and J.-b. Xu, *Joule*, 2018, **2**, 2706-2721.
278. L. M. Falk, K. P. Goetz, V. Lami, Q. An, P. Fassl, J. Herkel, F. Thome, A. D. Taylor, F. Paulus and Y. Vaynzof, *Energy Technology*, 2020, **8**, 1900737.
279. P. Fassl, V. Lami, A. Bausch, Z. Wang, M. T. Klug, H. J. Snaith and Y. Vaynzof, *Energy Environ. Sci.*, 2018, **11**, 3380-3391.
280. P. Cui, D. Wei, J. Ji, H. Huang, E. Jia, S. Dou, T. Wang, W. Wang and M. Li, *Nat. Energy.*, 2019, **4**, 150-159.
281. J. Diekmann, P. Caprioglio, D. Rothhardt, M. Arvind, T. Unold, T. Kirchartz, D. Neher and M. Stolterfoht, *Journal*, 2019.
282. P. Caprioglio, C. M. Wolff, O. J. Sandberg, A. Armin, B. Rech, S. Albrecht, D. Neher and M. Stolterfoht, *Adv. Energy Mater.*, 2020, **10**, 2000502.
283. M. Stolterfoht, P. Caprioglio, C. M. Wolff, J. A. Márquez, J. Nordmann, S. Zhang, D. Rothhardt, U. Hörmann, Y. Amir, A. Redinger, L. Kegelmann, F. Zu, S. Albrecht, N. Koch, T. Kirchartz, M. Saliba, T. Unold and D. Neher, *Energy Environ. Sci.*, 2019, **12**, 2778-2788.
284. M. Stolterfoht, V. M. Le Corre, M. Feuerstein, P. Caprioglio, L. J. A. Koster and D. Neher, *ACS Energy Lett.*, 2019, **4**, 2887-2892.
285. M. Stolterfoht, C. M. Wolff, J. A. Márquez, S. Zhang, C. J. Hages, D. Rothhardt, S. Albrecht, P. L. Burn, P. Meredith, T. Unold and D. Neher, *Nat. Energy.*, 2018, **3**, 847-854.
286. C. M. Wolff, P. Caprioglio, M. Stolterfoht and D. Neher, *Adv. Mater.*, 2019, **31**, 1902762.
287. Q. Wang, F. Zu, P. Caprioglio, C. M. Wolff, M. Stolterfoht, M. Li, S.-H. Turren-Cruz, N. Koch, D. Neher and A. Abate, *ACS Energy Lett.*, 2020, **5**, 2343-2348.
288. A. A. Sutanto, C. Igci, H. Kim, H. Kanda, N. Shibayama, M. Mensi, V. I. E. Queloz, C. Momblona, H. J. Yun, H. J. Bolink, A. J. Huckaba and M. K. Nazeeruddin, *ACS Appl. Energy Mater.*, 2021, **4**, 1259-1268.
289. Best Research-Cell Efficiency Chart, https://www.nrel.gov/pv/cell-efficiency.html, (accessed November 2020).
290. J.-P. Correa-Baena, W. Tress, K. Domanski, E. H. Anaraki, S.-H. Turren-Cruz, B. Roose, P. P. Boix, M. Grätzel, M. Saliba, A. Abate and A. Hagfeldt, *Energy Environ. Sci.*, 2017, **10**, 1207-1212.
291. P. Schulz, *ACS Energy Lett.*, 2018, **3**, 1287-1293.
292. H. Kanda, N. Shibayama, A. J. Huckaba, Y. Lee, S. Paek, N. Klipfel, C. Roldan-Carmona, V. I. E. Queloz, G. Grancini, Y. Zhang, M. Abuhelaiga, K. T. Cho, M. Li, M. D. Mensi, S. Kinge and M. K. Nazeeruddin, *Energy Environ. Sci.*, 2020, **13**, 1222-1230.
293. B. Chen, M. Yang, S. Priya and K. Zhu, *J. Phys. Chem. Lett.*, 2016, **7**, 905-917.
294. S. Akin, N. Arora, S. M. Zakeeruddin, M. Grätzel, R. H. Friend and M. I. Dar, *Adv. Energy Mater.*, 2020, **10**, 1903090.
295. H. Zhou, Q. Chen, G. Li, S. Luo, T.-b. Song, H.-S. Duan, Z. Hong, J. You, Y. Liu and Y. Yang, *Science*, 2014, **345**, 542-546.
296. S. Yang, Y. Wang, P. Liu, Y.-B. Cheng, H. J. Zhao and H. G. Yang, *Nat. Energy.*, 2016, **1**, 15016.
297. B. Wu, H. T. Nguyen, Z. Ku, G. Han, D. Giovanni, N. Mathews, H. J. Fan and T. C. Sum, *Adv. Energy Mater.*, 2016, **6**, 1600551.

298. G. S. Han, H. S. Chung, B. J. Kim, D. H. Kim, J. W. Lee, B. S. Swain, K. Mahmood, J. S. Yoo, N.-G. Park, J. H. Lee and H. S. Jung, *J. Mater. Chem. A*, 2015, **3**, 9160-9164.
299. Q. Hu, J. Wu, C. Jiang, T. Liu, X. Que, R. Zhu and Q. Gong, *ACS Nano*, 2014, **8**, 10161-10167.
300. F. Han, J. Luo, B. Zhao, Z. Wan, R. Wang and C. Jia, *Electrochim. Acta*, 2017, **236**, 122-130.
301. J. Zhang, Z. Hu, L. Huang, G. Yue, J. Liu, X. Lu, Z. Hu, M. Shang, L. Han and Y. Zhu, *Chem. Commun.*, 2015, **51**, 7047-7050.
302. D.-X. Yuan, X.-D. Yuan, Q.-Y. Xu, M.-F. Xu, X.-B. Shi, Z.-K. Wang and L.-S. Liao, *Phys. Chem. Chem. Phys.*, 2015, **17**, 26653-26658.
303. L.-L. Jiang, S. Cong, Y.-H. Lou, Q.-H. Yi, J.-T. Zhu, H. Ma and G.-F. Zou, *J. Mater. Chem. A*, 2016, **4**, 217-222.
304. L. Zuo, Q. Chen, N. De Marco, Y.-T. Hsieh, H. Chen, P. Sun, S.-Y. Chang, H. Zhao, S. Dong and Y. Yang, *Nano Lett.*, 2017, **17**, 269-275.
305. K. Wojciechowski, S. D. Stranks, A. Abate, G. Sadoughi, A. Sadhanala, N. Kopidakis, G. Rumbles, C.-Z. Li, R. H. Friend, A. K. Y. Jen and H. J. Snaith, *ACS Nano*, 2014, **8**, 12701-12709.
306. Z. Liu, S. Li, X. Wang, Y. Cui, Y. Qin, S. Leng, Y.-x. Xu, K. Yao and H. Huang, *Nano Energy*, 2019, **62**, 734-744.
307. M. Salado, F. J. Ramos, V. M. Manzanares, P. Gao, M. K. Nazeeruddin, P. J. Dyson and S. Ahmad, *ChemSusChem*, 2016, **9**, 2708-2714.
308. J. Chang, Z. Lin, H. Zhu, F. H. Isikgor, Q.-H. Xu, C. Zhang, Y. Hao and J. Ouyang, *J. Mater. Chem. A*, 2016, **4**, 16546-16552.
309. X. Li, M. Ibrahim Dar, C. Yi, J. Luo, M. Tschumi, S. M. Zakeeruddin, M. K. Nazeeruddin, H. Han and M. Grätzel, *Nat. Chem.*, 2015, **7**, 703-711.
310. H. Kim, M. Pei, Y. Lee, A. A. Sutanto, S. Paek, V. I. E. Queloz, A. J. Huckaba, K. T. Cho, H. J. Yun, H. Yang and M. K. Nazeeruddin, *Adv. Funct. Mater.*, 2020, **30**, 1910620.
311. G. Almeida, O. J. Ashton, L. Goldoni, D. Maggioni, U. Petralanda, N. Mishra, Q. A. Akkerman, I. Infante, H. J. Snaith and L. Manna, *J. Am. Chem. Soc.*, 2018, **140**, 14878-14886.
312. K. T. Munson, C. Grieco, E. R. Kennehan, R. J. Stewart and J. B. Asbury, *ACS Energy Lett.*, 2017, **2**, 651-658.
313. F. Palazon, D. Pérez-del-Rey, S. Marras, M. Prato, M. Sessolo, H. J. Bolink and L. Manna, *ACS Energy Lett.*, 2018, **3**, 835-839.
314. I. L. Braly, D. W. deQuilettes, L. M. Pazos-Outón, S. Burke, M. E. Ziffer, D. S. Ginger and H. W. Hillhouse, *Nat. Photon.*, 2018, **12**, 355-361.
315. F. Ambroz, W. Xu, S. Gadipelli, D. J. L. Brett, C.-T. Lin, C. Contini, M. A. McLachlan, J. R. Durrant, I. P. Parkin and T. J. Macdonald, *Part. Part. Syst. Charact.*, 2020, **37**, 1900391.
316. F. McGrath, U. V. Ghorpade and K. M. Ryan, *J. Chem. Phys.*, 2020, **152**, 174702.
317. A. Torres and L. G. C. Rego, *J. Phys. Chem. C*, 2014, **118**, 26947-26954.
318. H.-Y. Cheng, C.-S. Sun and D.-R. Hou, *J. Org. Chem.*, 2007, **72**, 2674-2677.
319. Q. Zhang, J. Dong, Q. Meng, G. Huang and S. Li, *Russ. J. Gen. Chem.*, 2018, **88**, 2388-2393.
320. K. Behm, J. B. Essner, C. L. Barnes, G. A. Baker and J. R. Walensky, *Dalton Trans.*, 2017, **46**, 10867-10875.
321. J.-A. Zhang, N.-F. Yang, L.-W. Yang, S. Wu, Y.-H. Chen and J. Zhang, *Macromol. Res.*, 2013, **21**, 641-648.
322. K.-S. Lim, D.-K. Lee, J.-W. Lee and N.-G. Park, *J. Mater. Chem. A*, 2020, **8**, 9345-9354.
323. K. Sun, Z. Hu, B. Shen, C. Lu, L. Huang, J. Zhang, J. Zhang and Y. Zhu, *ACS Appl. Energy Mater.*, 2018, **1**, 2114-2122.
324. P. Chen, Y. Bai, S. Wang, M. Lyu, J.-H. Yun and L. Wang, *Adv. Funct. Mater.*, 2018, **28**, 1706923.

325. D. H. Wang, Y. Hu, J. J. Zhao, L. L. Zeng, X. M. Tao and W. Chen, *J. Mater. Chem. A*, 2014, **2**, 17415-17420.
326. C. Rocks, V. Svrcek, P. Maguire and D. Mariotti, *J. Mater. Chem. C*, 2017, **5**, 902-916.
327. S.-S. Dong, W.-Z. Shao, L. Yang, H.-J. Ye and L. Zhen, *RSC Adv.*, 2018, **8**, 28152-28160.
328. R. Yerushalmi, J. C. Ho, Z. Fan and A. Javey, *Angew. Chem. Int. Ed.*, 2008, **47**, 4440-4442.
329. G. Biagiotti, V. Langè, C. Ligi, S. Caporali, M. Muniz-Miranda, A. Flis, K. M. Pietrusiewicz, G. Ghini, A. Brandi and S. Cicchi, *Beilstein J. Nanotechnol.*, 2017, **8**, 485-493.
330. Y. Yang, J. Wu, X. Wang, Q. Guo, X. Liu, W. Sun, Y. Wei, Y. Huang, Z. Lan, M. Huang, J. Lin, H. Chen and Z. Wei, *Adv. Mater.*, 2020, **32**, 1904347.
331. L. Wang, H. Zhou, J. Hu, B. Huang, M. Sun, B. Dong, G. Zheng, Y. Huang, Y. Chen, L. Li, Z. Xu, N. Li, Z. Liu, Q. Chen, L.-D. Sun and C.-H. Yan, *Science*, 2019, **363**, 265-270.
332. W. Zhang, S. Pathak, N. Sakai, T. Stergiopoulos, P. K. Nayak, N. K. Noel, A. A. Haghighirad, V. M. Burlakov, D. W. deQuilettes, A. Sadhanala, W. Li, L. Wang, D. S. Ginger, R. H. Friend and H. J. Snaith, *Nat. Commun.*, 2015, **6**, 10030.
333. R. Lindblad, D. Bi, B.-w. Park, J. Oscarsson, M. Gorgoi, H. Siegbahn, M. Odelius, E. M. J. Johansson and H. Rensmo, *J. Phys. Chem. Lett.*, 2014, **5**, 648-653.
334. A. A. Sutanto, V. Joseph, C. Igci, O. A. Syzgantseva, M. A. Syzgantseva, V. Jankauskas, K. Rakstys, V. I. E. Queloz, P.-Y. Huang, J.-S. Ni, S. Kinge, A. M. Asiri, M.-C. Chen and M. K. Nazeeruddin, *Chem. Mater.*, 2021, **33**, 3286-3296.
335. W. Ke, P. Priyanka, S. Vegiraju, C. C. Stoumpos, I. Spanopoulos, C. M. M. Soe, T. J. Marks, M.-C. Chen and M. G. Kanatzidis, *J. Am. Chem. Soc.*, 2018, **140**, 388-393.
336. W. Rehman, R. L. Milot, G. E. Eperon, C. Wehrenfennig, J. L. Boland, H. J. Snaith, M. B. Johnston and L. M. Herz, *Adv. Mater.*, 2015, **27**, 7938-7944.
337. T. Cao, K. Chen, Q. Chen, Y. Zhou, N. Chen and Y. Li, *ACS Applied Materials & Interfaces*, 2019, **11**, 33825-33834.
338. C. Liu, M. Cai, Y. Yang, Z. Arain, Y. Ding, X. Shi, P. Shi, S. Ma, T. Hayat, A. Alsaedi, J. Wu, S. Dai and G. Cao, *J. Mater. Chem. A*, 2019, **7**, 11086-11094.
339. P. Huang, Manju, S. Kazim, G. Sivakumar, M. Salado, R. Misra and S. Ahmad, *ACS Applied Materials & Interfaces*, 2020, **12**, 22881-22890.
340. K. Rakstys, S. Paek, A. Drevilkauskaite, H. Kanda, S. Daskeviciute, N. Shibayama, M. Daskeviciene, A. Gruodis, E. Kamarauskas, V. Jankauskas, V. Getautis and M. K. Nazeeruddin, *ACS Applied Materials & Interfaces*, 2020, **12**, 19710-19717.
341. J. Wang, H. Zhang, B. Wu, Z. Wang, Z. Sun, S. Xue, Y. Wu, A. Hagfeldt and M. Liang, *Angew. Chem. Int. Ed.*, 2019, **58**, 15721-15725.
342. X. Zhang, Z. a. Zhou, S. Ma, G. Wu, X. Liu, M. Mateen, R. Ghadari, Y. Wu, Y. Ding, M. Cai and S. Dai, *Chem. Commun.*, 2020, **56**, 3159-3162.
343. S. Vegiraju, W. Ke, P. Priyanka, J.-S. Ni, Y.-C. Wu, I. Spanopoulos, S. L. Yau, T. J. Marks, M.-C. Chen and M. G. Kanatzidis, *Adv. Funct. Mater.*, 2019, **29**, 1905393.
344. H. D. Pham, T. C.-J. Yang, S. M. Jain, G. J. Wilson and P. Sonar, *Adv. Energy Mater.*, 2020, **10**, 1903326.
345. H. D. Pham, S. M. Jain, M. Li, Z.-K. Wang, S. Manzhos, K. Feron, S. Pitchaimuthu, Z. Liu, N. Motta, J. R. Durrant and P. Sonar, *Advanced Electronic Materials*, 2020, **6**, 1900884.
346. H. D. Pham, L. Xianqiang, W. Li, S. Manzhos, A. K. K. Kyaw and P. Sonar, *Energy Environ. Sci.*, 2019, **12**, 1177-1209.
347. V. E. Madhavan, I. Zimmermann, A. A. B. Baloch, A. Manekkathodi, A. Belaidi, N. Tabet and M. K. Nazeeruddin, *ACS Appl. Energy Mater.*, 2020, **3**, 114-121.
348. G. You, Q. Zhuang, L. Wang, X. Lin, D. Zou, Z. Lin, H. Zhen, W. Zhuang and Q. Ling, *Adv. Energy Mater.*, 2020, **10**, 1903146.
349. H. D. Pham, H. Hu, K. Feron, S. Manzhos, H. Wang, Y. M. Lam and P. Sonar, *Solar RRL*, 2017, **1**, 1700105.

350. H. D. Pham, H. Hu, F.-L. Wong, C.-S. Lee, W.-C. Chen, K. Feron, S. Manzhos, H. Wang, N. Motta, Y. M. Lam and P. Sonar, *J. Mater. Chem. C*, 2018, **6**, 9017-9029.
351. J. Zhang, Q. Sun, Q. Chen, Y. Wang, Y. Zhou, B. Song, N. Yuan, J. Ding and Y. Li, *Adv. Funct. Mater.*, 2019, **29**, 1900484.
352. H. D. Pham, L. Gil-Escrig, K. Feron, S. Manzhos, S. Albrecht, H. J. Bolink and P. Sonar, *J. Mater. Chem. A*, 2019, **7**, 12507-12517.
353. N. J. Jeon, J. Lee, J. H. Noh, M. K. Nazeeruddin, M. Grätzel and S. I. Seok, *J. Am. Chem. Soc.*, 2013, **135**, 19087-19090.
354. Q.-Q. Ge, J.-Y. Shao, J. Ding, L.-Y. Deng, W.-K. Zhou, Y.-X. Chen, J.-Y. Ma, L.-J. Wan, J. Yao, J.-S. Hu and Y.-W. Zhong, *Angew. Chem. Int. Ed.*, 2018, **57**, 10959-10965.
355. M. Li, Z. Wang, M. Liang, L. Liu, X. Wang, Z. Sun and S. Xue, *J. Phys. Chem. C*, 2018, **122**, 24014-24024.
356. X. Liu, X. Shi, C. Liu, Y. Ren, Y. Wu, W. Yang, A. Alsaedi, T. Hayat, F. Kong, X. Liu, Y. Ding, J. Yao and S. Dai, *J. Phys. Chem. C*, 2018, **122**, 26337-26343.
357. M. Daskeviciene, S. Paek, A. Magomedov, K. T. Cho, M. Saliba, A. Kizeleviciute, T. Malinauskas, A. Gruodis, V. Jankauskas, E. Kamarauskas, M. K. Nazeeruddin and V. Getautis, *J. Mater. Chem. C*, 2019, **7**, 2717-2724.
358. H. D. Pham, K. Hayasake, J. Kim, T. T. Do, H. Matsui, S. Manzhos, K. Feron, S. Tokito, T. Watson, W. C. Tsoi, N. Motta, J. R. Durrant, S. M. Jain and P. Sonar, *J. Mater. Chem. C*, 2018, **6**, 3699-3708.
359. H. D. Pham, S. M. Jain, M. Li, S. Manzhos, K. Feron, S. Pitchaimuthu, Z. Liu, N. Motta, H. Wang, J. R. Durrant and P. Sonar, *J. Mater. Chem. A*, 2019, **7**, 5315-5323.
360. R. Nakar, F. J. Ramos, C. Dalinot, P. S. Marques, C. Cabanetos, P. Leriche, L. Sanguinet, M. Kobeissi, P. Blanchard, J. Faure-Vincent, F. Tran-Van, N. Berton, J. Rousset and B. Schmaltz, *J. Phys. Chem. C*, 2019, **123**, 22767-22774.
361. X. Yin, L. Guan, J. Yu, D. Zhao, C. Wang, N. Shrestha, Y. Han, Q. An, J. Zhou, B. Zhou, Y. Yu, C. R. Grice, R. A. Awni, F. Zhang, J. Wang, R. J. Ellingson, Y. Yan and W. Tang, *Nano Energy*, 2017, **40**, 163-169.
362. Z. Chen, H. Li, X. Zheng, Q. Zhang, Z. Li, Y. Hao and G. Fang, *ChemSusChem*, 2017, **10**, 3111-3117.
363. A. Magomedov, S. Paek, P. Gratia, E. Kasparavicius, M. Daskeviciene, E. Kamarauskas, A. Gruodis, V. Jankauskas, K. Kantminiene, K. T. Cho, K. Rakstys, T. Malinauskas, V. Getautis and M. K. Nazeeruddin, *Adv. Funct. Mater.*, 2018, **28**, 1704351.
364. B. Xu, E. Sheibani, P. Liu, J. Zhang, H. Tian, N. Vlachopoulos, G. Boschloo, L. Kloo, A. Hagfeldt and L. Sun, *Adv. Mater.*, 2014, **26**, 6629-6634.
365. Y. Shi, K. Hou, Y. Wang, K. Wang, H. Ren, M. Pang, F. Chen and S. Zhang, *J. Mater. Chem. A*, 2016, **4**, 5415-5422.
366. X. Li, M. Cai, Z. Zhou, K. Yun, F. Xie, Z. Lan, J. Hua and L. Han, *J. Mater. Chem. A*, 2017, **5**, 10480-10485.
367. X. Liu, S. Ma, M. Mateen, P. Shi, C. Liu, Y. Ding, M. Cai, M. Guli, M. K. Nazeeruddin and S. Dai, *Sustainable Energy & Fuels*, 2020, **4**, 1875-1882.
368. X. Liu, S. Ma, Y. Ding, J. Gao, X. Liu, J. Yao and S. Dai, *Solar RRL*, 2019, **3**, 1800337.
369. W. Li, M. Otsuka, T. Kato, Y. Wang, T. Mori and T. Michinobu, *Beilstein J. Org. Chem.*, 2016, **12**, 1401-1409.
370. W.-L. Gong, F. Zhong, M. P. Aldred, Q. Fu, T. Chen, D.-K. Huang, Y. Shen, X.-F. Qiao, D. Ma and M.-Q. Zhu, *RSC Adv.*, 2012, **2**, 10821-10828.
371. S. Kumar and Y.-T. Tao, *J. Org. Chem.*, 2015, **80**, 5066-5076.
372. L. Zhu, Y. Shan, R. Wang, D. Liu, C. Zhong, Q. Song and F. Wu, *Chemistry – A European Journal*, 2017, **23**, 4373-4379.

373. J. Urieta-Mora, I. García-Benito, I. Zimmermann, J. Aragó, J. Calbo, G. Grancini, A. Molina-Ontoria, E. Ortí, N. Martín and M. K. Nazeeruddin, *J. Mater. Chem. C*, 2019, **7**, 6656-6663.
374. H. Baig, H. Kanda, A. M. Asiri, M. K. Nazeeruddin and T. Mallick, *Sustainable Energy & Fuels*, 2020, **4**, 528-537.
375. M. Salado, J. Idigoras, L. Calio, S. Kazim, M. K. Nazeeruddin, J. A. Anta and S. Ahmad, *ACS Applied Materials & Interfaces*, 2016, **8**, 34414-34421.
376. P. Gratia, A. Magomedov, T. Malinauskas, M. Daskeviciene, A. Abate, S. Ahmad, M. Grätzel, V. Getautis and M. K. Nazeeruddin, *Angew. Chem. Int. Ed.*, 2015, **54**, 11409-11413.
377. K. Rakstys, A. Abate, M. I. Dar, P. Gao, V. Jankauskas, G. Jacopin, E. Kamarauskas, S. Kazim, S. Ahmad, M. Grätzel and M. K. Nazeeruddin, *J. Am. Chem. Soc.*, 2015, **137**, 16172-16178.
378. D. W. de Quilettes, S. M. Vorpahl, S. D. Stranks, H. Nagaoka, G. E. Eperon, M. E. Ziffer, H. J. Snaith and D. S. Ginger, *Science*, 2015, **348**, 683-686.
379. N. Berton, R. Nakar and B. Schmaltz, *Synth. Met.*, 2019, **252**, 91-106.
380. V. Joseph, A. A. Sutanto, C. Igci, O. A. Syzgantseva, V. Jankauskas, K. Rakstys, V. I. E. Queloz, H. Kanda, P. Y. Huang, J. S. Ni, S. Kinge, M. C. Chen and M. K. Nazeeruddin, *Small*, 2021, **17**, 2100783.
381. Y. Chen, X. Xu, N. Cai, S. Qian, R. Luo, Y. Huo and S.-W. Tsang, *Adv. Energy Mater.*, 2019, **9**, 1901268.
382. I. Zimmermann, S. Aghazada and M. K. Nazeeruddin, *Angew. Chem. Int. Ed.*, 2019, **58**, 1072-1076.
383. X. Liu, F. Zhang, Z. Liu, Y. Xiao, S. Wang and X. Li, *J. Mater. Chem. C*, 2017, **5**, 11429-11435.
384. J. Chen and N.-G. Park, *J. Phys. Chem. C*, 2018, **122**, 14039-14063.
385. S.-H. Peng, T.-W. Huang, G. Gollavelli and C.-S. Hsu, *J. Mater. Chem. C*, 2017, **5**, 5193-5198.
386. M. L. Petrus, K. Schutt, M. T. Sirtl, E. M. Hutter, A. C. Closs, J. M. Ball, J. C. Bijleveld, A. Petrozza, T. Bein, T. J. Dingemans, T. J. Savenije, H. Snaith and P. Docampo, *Adv. Energy Mater.*, 2018, **8**, 1801605.
387. N. Xu, A. Zheng, Y. Wei, Y. Yuan, J. Zhang, M. Lei and P. Wang, *Chemical Science*, 2020, **11**, 3418-3426.
388. M. Shasti, S. F. Völker, S. Collavini, S. Valero, F. Ruipérez, A. Mortezaali, S. M. Zakeeruddin, M. Grätzel, A. Hagfeldt and J. L. Delgado, *Org. Lett.*, 2019, **21**, 3261-3264.
389. C. Lu, M. Paramasivam, K. Park, C. H. Kim and H. K. Kim, *ACS Applied Materials & Interfaces*, 2019, **11**, 14011-14022.
390. L. Duan, Y. Chen, J. Jia, X. Zong, Z. Sun, Q. Wu and S. Xue, *ACS Appl. Energy Mater.*, 2020, **3**, 1672-1683.
391. M. Saliba, S. Orlandi, T. Matsui, S. Aghazada, M. Cavazzini, J.-P. Correa-Baena, P. Gao, R. Scopelliti, E. Mosconi, K.-H. Dahmen, F. De Angelis, A. Abate, A. Hagfeldt, G. Pozzi, M. Graetzel and M. K. Nazeeruddin, *Nat. Energy.*, 2016, **1**, 15017.
392. N. J. Jeon, H. Na, E. H. Jung, T.-Y. Yang, Y. G. Lee, G. Kim, H.-W. Shin, S. Il Seok, J. Lee and J. Seo, *Nat. Energy.*, 2018, **3**, 682-689.
393. A. K. Jena, Y. Numata, M. Ikegami and T. Miyasaka, *J. Mater. Chem. A*, 2018, **6**, 2219-2230.
394. R. Sandoval-Torrientes, I. Zimmermann, J. Calbo, J. Aragó, J. Santos, E. Ortí, N. Martín and M. K. Nazeeruddin, *J. Mater. Chem. A*, 2018, **6**, 5944-5951.
395. G. Gong, N. Zhao, D. Ni, J. Chen, Y. Shen, M. Wang and G. Tu, *J. Mater. Chem. A*, 2016, **4**, 3661-3666.
396. Y. Wang, W. Chen, L. Wang, B. Tu, T. Chen, B. Liu, K. Yang, C. W. Koh, X. Zhang, H. Sun, G. Chen, X. Feng, H. Y. Woo, A. B. Djurišić, Z. He and X. Guo, *Adv. Mater.*, 2019, **31**, 1902781.

397. J. Zhou, X. Yin, Z. Dong, A. Ali, Z. Song, N. Shrestha, S. S. Bista, Q. Bao, R. J. Ellingson, Y. Yan and W. Tang, *Angew. Chem. Int. Ed.*, 2019, **58**, 13717-13721.
398. J. Urieta-Mora, I. García-Benito, I. Zimmermann, J. Aragó, A. Molina-Ontoria, E. Ortí, N. Martín and M. K. Nazeeruddin, *J. Org. Chem.*, 2020, **85**, 224-233.
399. X. Liu, F. Kong, S. Jin, W. Chen, T. Yu, T. Hayat, A. Alsaedi, H. Wang, Z. a. Tan, J. Chen and S. Dai, *ACS Applied Materials & Interfaces*, 2017, **9**, 27657-27663.
400. B.-B. Cui, C. Zhu, S. Yang, Y. Han, N. Yang, L. Zhang, Y. Wang, Y. Jia, L. Zhao and Q. Chen, *ACS Omega*, 2018, **3**, 10791-10797.
401. Y. Wu, Z. Wang, M. Liang, H. Cheng, M. Li, L. Liu, B. Wang, J. Wu, R. Prasad Ghimire, X. Wang, Z. Sun, S. Xue and Q. Qiao, *ACS Applied Materials & Interfaces*, 2018, **10**, 17883-17895.
402. J. Wu, C. Liu, X. Deng, L. Zhang, M. Hu, J. Tang, W. Tan, Y. Tian and B. Xu, *RSC Adv.*, 2017, **7**, 45478-45483.
403. C. Shen, Y. Wu, H. Zhang, E. Li, W. Zhang, X. Xu, W. Wu, H. Tian and W.-H. Zhu, *Angew. Chem. Int. Ed.*, 2019, **58**, 3784-3789.
404. L. Zhao, L. Qiu, D. Xia, S. Liu, X. Yi, J. Fan, K. Lin, R. Fan, Y. Guo and Y. Yang, *ACS Appl. Energy Mater.*, 2019, **2**, 8173-8180.
405. J. Urieta-Mora, I. Zimmermann, J. Aragó, A. Molina-Ontoria, E. Ortí, N. Martín and M. K. Nazeeruddin, *Chem. Mater.*, 2019, **31**, 6435-6442.
406. X. Liu, F. Kong, R. Ghadari, S. Jin, T. Yu, W. Chen, G. Liu, Z. a. Tan, J. Chen and S. Dai, *Chem. Commun.*, 2017, **53**, 9558-9561.
407. X. Liu, X. Ding, Y. Ren, Y. Yang, Y. Ding, X. Liu, A. Alsaedi, T. Hayat, J. Yao and S. Dai, *J. Mater. Chem. C*, 2018, **6**, 12912-12918.
408. Y.-K. Wang, Z.-C. Yuan, G.-Z. Shi, Y.-X. Li, Q. Li, F. Hui, B.-Q. Sun, Z.-Q. Jiang and L.-S. Liao, *Adv. Funct. Mater.*, 2016, **26**, 1375-1381.
409. K. Rakstys, S. Paek, G. Grancini, P. Gao, V. Jankauskas, A. M. Asiri and M. K. Nazeeruddin, *ChemSusChem*, 2017, **10**, 3825-3832.
410. I. García-Benito, I. Zimmermann, J. Urieta-Mora, J. Aragó, A. Molina-Ontoria, E. Ortí, N. Martín and M. K. Nazeeruddin, *J. Mater. Chem. A*, 2017, **5**, 8317-8324.
411. D. E. M. Rojas, K. T. Cho, Y. Zhang, M. Urbani, N. Tabet, G. de la Torre, M. K. Nazeeruddin and T. Torres, *Adv. Energy Mater.*, 2018, **8**, 1800681.
412. W. Hu, Z. Zhang, J. Cui, W. Shen, M. Li and R. He, *Nanoscale*, 2017, **9**, 12916-12924.
413. K. Rakstys, S. Paek, M. Sohail, P. Gao, K. T. Cho, P. Gratia, Y. Lee, K. H. Dahmen and M. K. Nazeeruddin, *J. Mater. Chem. A*, 2016, **4**, 18259-18264.
414. X. Liu, F. Kong, R. Ghadari, S. Jin, W. Chen, T. Yu, T. Hayat, A. Alsaedi, F. Guo, Z. a. Tan, J. Chen and S. Dai, *Energy Technology*, 2017, **5**, 1788-1794.
415. T. Krishnamoorthy, F. Kunwu, P. P. Boix, H. Li, T. M. Koh, W. L. Leong, S. Powar, A. Grimsdale, M. Grätzel, N. Mathews and S. G. Mhaisalkar, *J. Mater. Chem. A*, 2014, **2**, 6305-6309.
416. J. Wu, C. Liu, M. Hu, X. Deng, W. Tan, Y. Tian and B. Xu, *J. Mater. Chem. A*, 2018, **6**, 13123-13132.
417. H. Li, K. Fu, P. P. Boix, L. H. Wong, A. Hagfeldt, M. Grätzel, S. G. Mhaisalkar and A. C. Grimsdale, *ChemSusChem*, 2014, **7**, 3420-3425.
418. S. Paek, I. Zimmermann, P. Gao, P. Gratia, K. Rakstys, G. Grancini, M. K. Nazeeruddin, M. A. Rub, S. A. Kosa, K. A. Alamry and A. M. Asiri, *Chemical Science*, 2016, **7**, 6068-6075.
419. Q. Wang, E. Mosconi, C. Wolff, J. Li, D. Neher, F. De Angelis, G. P. Suranna, R. Grisorio and A. Abate, *Adv. Energy Mater.*, 2019, **9**, 1900990.
420. W.-L. Yu, H. Meng, J. Pei, W. Huang, Y. Li and A. J. Heeger, *Macromolecules*, 1998, **31**, 4838-4844.
421. S. Karpe, A. Cravino, P. Frère, M. Allain, G. Mabon and J. Roncali, *Adv. Funct. Mater.*, 2007, **17**, 1163-1171.

422. A. Facchetti, M.-H. Yoon, C. L. Stern, G. R. Hutchison, M. A. Ratner and T. J. Marks, *J. Am. Chem. Soc.*, 2004, **126**, 13480-13501.
423. D. Liu, B. Kan, X. Ke, N. Zheng, Z. Xie, D. Lu and Y. Liu, *Adv. Energy Mater.*, 2018, **8**, 1801618.
424. X. Ji, T. Zhou, X. Ke, W. Wang, S. Wu, M. Zhang, D. Lu, X. Zhang and Y. Liu, *J. Mater. Chem. A*, 2020, **8**, 5163-5170.
425. W. Chi and S. K. Banerjee, *Small*, 2020, **16**, 1907531.
426. T. Malinauskas, D. Tomkute-Luksiene, R. Sens, M. Daskeviciene, R. Send, H. Wonneberger, V. Jankauskas, I. Bruder and V. Getautis, *ACS Applied Materials & Interfaces*, 2015, **7**, 11107-11116.
427. W. Budiawan, K.-W. Lai, P. Karuppuswamy, T. S. Jadhav, Y.-A. Lu, K.-C. Ho, P.-C. Wang, C.-C. Chang and C.-W. Chu, *ACS Applied Materials & Interfaces*, 2020, **12**.
428. M. H. Futscher, J. M. Lee, L. McGovern, L. A. Muscarella, T. Wang, M. I. Haider, A. Fakharuddin, L. Schmidt-Mende and B. Ehrler, *Materials Horizons*, 2019, **6**, 1497-1503.
429. S. N. Habisreutinger, N. K. Noel and H. J. Snaith, *ACS Energy Lett.*, 2018, **3**, 2472-2476.
430. Q. Wang, *Phys. Chem. Chem. Phys.*, 2018, **20**, 10114-10120.
431. C. Igci, S. Paek, K. Rakstys, H. Kanda, N. Shibayama, V. Jankauskas, C. Roldán-Carmona, H. Kim, A. M. Asiri and M. K. Nazeeruddin, *Solar RRL*, 2020, **4**, 2000173.
432. R. S. Sanchez and E. Mas-Marza, *Sol. Energy Mater. Sol. Cells*, 2016, **158**, 189-194.
433. S. Akin, M. Bauer, R. Uchida, N. Arora, G. Jacopin, Y. Liu, D. Hertel, K. Meerholz, E. Mena-Osteritz, P. Bäuerle, S. M. Zakeeruddin, M. I. Dar and M. Grätzel, *ACS Appl. Energy Mater.*, 2020, **3**, 7456-7463.
434. J. A. Christians, P. Schulz, J. S. Tinkham, T. H. Schloemer, S. P. Harvey, B. J. Tremolet de Villers, A. Sellinger, J. J. Berry and J. M. Luther, *Nat. Energy.*, 2018, **3**, 68-74.
435. M. S. de Holanda, R. Szostak, P. E. Marchezi, L. G. T. A. Duarte, J. C. Germino, T. D. Z. Atvars and A. F. Nogueira, *Solar RRL*, 2019, **3**, 1900199.
436. C. Ma, D. Shen, T.-W. Ng, M.-F. Lo and C.-S. Lee, *Adv. Mater.*, 2018, **30**, 1800710.
437. D. Thrithamarassery Gangadharan and D. Ma, *Energy Environ. Sci.*, 2019, **12**, 2860-2889.
438. P. Wurfel, *J. Phys. C: Solid State Phys.*, 1982, **15**, 3967-3985.
439. J. P. Perdew, K. Burke and M. Ernzerhof, *Phys. Rev. Lett.*, 1996, **77**, 3865-3868.
440. S. Grimme, J. Antony, S. Ehrlich and H. Krieg, *J. Chem. Phys.*, 2010, **132**, 154104.
441. J. VandeVondele and J. Hutter, *J. Chem. Phys.*, 2007, **127**, 114105.
442. S. Goedecker, M. Teter and J. Hutter, *Phys. Rev. B*, 1996, **54**, 1703-1710.
443. T. D. Kühne, M. Iannuzzi, M. D. Ben, V. V. Rybkin, P. Seewald, F. Stein, T. Laino, R. Z. Khaliullin, O. Schütt, F. Schiffmann, D. Golze, J. Wilhelm, S. Chulkov, M. H. Bani-Hashemian, V. Weber, U. Borštnik, M. Taillefumier, A. S. Jakobovits, A. Lazzaro, H. Pabst, T. Müller, R. Schade, M. Guidon, S. Andermatt, N. Holmberg, G. K. Schenter, A. Hehn, A. Bussy, F. Belleflamme, G. Tabacchi, A. Glöß, M. Lass, I. Bethune, C. J. Mundy, C. Plessl, M. Watkins, J. VandeVondele, M. Krack and J. Hutter, *J. Chem. Phys.*, 2020, **152**, 194103.
444. W. Humphrey, A. Dalke and K. Schulten, *Journal of Molecular Graphics*, 1996, **14**, 33-38.

Appendices

Appendix A: Supplementary Information to Chapter 3

A.1 Dynamical evolution of the 2D/3D interface: a hidden driver behind perovskite solar cell instability

Experimental Methods

Synthesis of thiophene-based cations

A desired concentrated aqueous solution of HI (1.1 eq) was added dropwise to a stirred 1.0 mol/L ethanol solution of the corresponding thiophenealkylamine (1.0 eq) at 0°C. The mixture was allowed to gradually reach room temperature and then it was poured into an excess of diethyl ether (Et_2O). The formed precipitate was collected and washed thoroughly with Et_2O. The salts were recrystallized from EtOH-Et_2O mixtures, providing with crystalline solids (yields ≈70 %).

Preparation of 2D/3D perovskite films and device fabrication

FTO-coated glass (Nippon sheet glass) was chemically etched using zinc powder and HCl solution, followed by cleaning using Hellmanex, water, acetone, and 2-propanol. A 30 nm thick compact TiO_2 layer as electron transporting layer was deposited by spray pyrolysis using a titanium diisopropoxide bis(acetylacetonate) solution (Sigma-Aldrich) diluted in 2-propanol (1:15 v/v) at 450 °C. On top of the compact layer, a 100 nm thick mesoporous layer of TiO_2 was deposited by spin coating TiO_2 paste (GreatCellSolar, 30NR-D) diluted in ethanol (1:8 w/v) at 5000 rpm for 20 s followed by heating at 125 °C for 10 min and sintering at 500 °C for 20 min. A thin layer of passivating tin oxide of ≈20 nm was spin-coated by using tin (IV) chloride (Acros) solution (12 µL diluted in 988 µL water) at 3000 rpm for 30 s, followed by annealing at 100 °C for 10 min and 190 °C for 1 h. The prepared substrates were treated with UV-ozone for 15 min before perovskite deposition. A 1.3 mol/L $[(FAPbI_3)_{0.87}(MAPbBr_3)_{0.13}]_{0.92}(CsPbI_3)_{0.08}$ perovskite solution with excess PbI_2 (PbI_2:FAI = 1.05:1) was prepared by mixing FAI (GreatCellSolar), MABr (GreatCellSolar), CsI (ABCR), PbI_2 (TCI), and $PbBr_2$ (TCI) in DMF and DMSO (0.78:0.22 v/v). For the 2D perovskite n=1 (R_2PbI_4, R is the corresponding thiophene alkylammonium cation), the perovskite precursor solution was prepared by dissolving thiophene alkylammonium cation and PbI_2 with the molar ratio of 2:1 in mixed solvent of DMF and DMSO (0.78:0.22 v/v). For the quasi 2D perovskite n=2 ($R_2MAPb_2I_7$), the perovskite precursor solution was prepared by dissolving thiophene alkylammonium cation, methylammonium iodide (MAI, GreatCellSolar),

and PbI_2 with the molar ratio of 2:1:2 in mixed solvent of DMF and DMSO (0.78:0.22 v/v). The prepared perovskite precursor was then spin-coated on the prepared at 2000 rpm for 12 s and 5000 rpm for 30 s. Chlorobenzene was added as an anti-solvent at 15 s before the end of spin coating process. The films were subsequently annealed at 100 °C for 60 min. After cooling down to room temperature, 0.06 mol/L of thiophene alkyl ammonium iodide cations in 2-propanol were spin-coated dynamically by adding the solution during spinning at 4000 rpm for 30 s, followed by annealing at 100 °C for 6 min. Spiro OMeTAD was used as the hole-transporting materials (HTM). The HTM layer was prepared by dissolving 78.2 mg spiro-OMeTAD (Merck) in 1 mL chlorobenzene doped with 31.28 µL of 4-tert-butylpyridine (Sigma-Aldrich), 18.57 µL of Li-bis (trifluoromethanesulphonyl) imide (Aldrich) from the stock solution (196 mg in 379 µL acetonitrile), 13.69 µL of FK 209 Co(III) TFSI (GreatCellSolar) from the stock solution (99 mg in 263 µL acetonitrile). The doped spiro-OMeTAD solution was then deposited by spin-coating at 4000 rpm for 30 s. Finally, a 70 nm-thick gold counter electrode was thermally evaporated on top of HTM layer.

Film Characterization

UV-VIS Absorption

The absorption spectra of the perovskite thin films were recorded with using an ultraviolet, visible, near-infrared spectrophotometer (PerkinElmer Lambda 950S).

Photoluminescence

Photoluminescence spectra of the perovskite thin films were measured and recorded using Fluorolog3-22 spectrofluorometer. The spectra were recorded upon excitation at 450 nm. For the 2D/3D films, the emissions were measured from both front side (2D perovskite side) and back side (3D perovskite side) of the film.

X-ray Diffraction (XRD)

XRD measurements were performed at room temperature with Bruker D8 Advance diffractometer and non-monochromated Cu radiation. For the 2D-3D films, the XRD patterns were obtained using grazing incident diffraction (GID) geometry with Bruker D8 Discover diffractometer and non-monochromated Cu radiation at the incident angle of 2.0°. In situ X-ray diffraction was performed at 50°C in ambient atmosphere and using a custom-made high-temperature cell (temperature stability +/- 1 K), in Bragg Brentano geometry, with a Bruker D8 Discover diffractometer and non-monochromated Cu radiation. The data acquisition time for

the entire pattern between 2 and 16° 2θ was approx. 15 minutes, in order to allow for comparison from PL experiments.

Scanning Electron Microscopy (SEM)

Cross-section and top surface SEM images were recorded by in-lens detector of FEI Teneo scanning electron microscope at high tension of 3 kV and 5 kV.

Grazing incidence wide angle X-ray scattering (GIWAXS) measurements

GIWAXS measurements were carried out in reflection geometry at the CMS beamline of the National Synchrotron Light Source II (NSLS II), a U.S. Department of Energy (DOE) office of the Science User Facility operated for the DOE Office of Science by Brookhaven National Laboratory. Samples were measured at a detector distance of 0.153 m using X-ray wavelength of 1.24 Å, at 0.16° angle of incidence with respect to the substrate plane. Scattering intensity was detected by a PILATUS 300K detector. Nika software package was used to sector average the 2D GIWAXS images. Data plotting was done in Igor Pro (Wavemetrics, Inc., Lake Oswego, OR, USA).

Device characterization

The current density–voltage (J–V) curves were measured under 1 sun illumination (AM 1.5G) by xenon lamp solar simulator (450 W, Oriel Sol3A, AAA class). The *J-V* measurements were carried out under ambient condition and room temperature. The light intensity was calibrated to 1 sun by using a Si reference equipped with an IR-cutoff (KG5) filter. An external voltage bias was applied and the current responses were measured at the same time using a digital source meter (Keithley 2400). An active area of 0.16 cm^2 was determined by a metal mask with aperture of 0.16 cm^2. The *J-V* curves were scanned with the rate of 50 mV s^{-1} without any preconditioning, such as light soaking or pre-biasing for a long time. For the light intensity dependent measurement, the *J-V* characteristics were obtained using a VeraSol LED solar simulator (Newport) under various light intensity. External quantum efficiency (EQE) measurement was carried out by using IQE200B (Oriel).

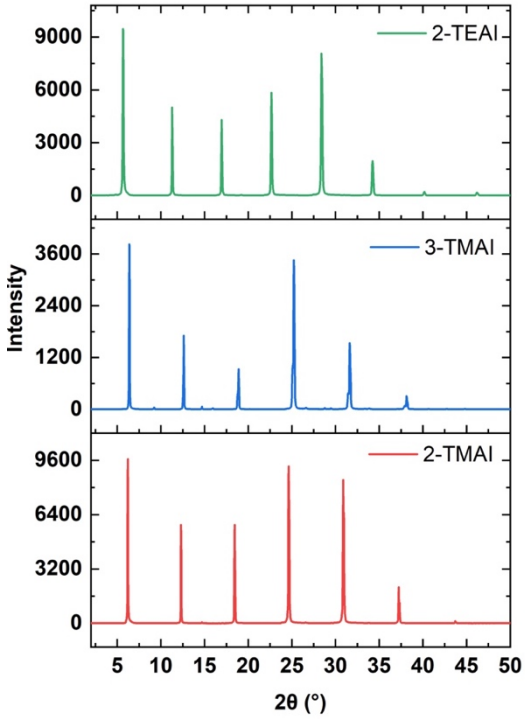

Figure A.1.1 XRD patterns of pure 2D perovskite films with *n*=1 employing 2-TMAI, 3-TMAI and 2-TEAI cations.

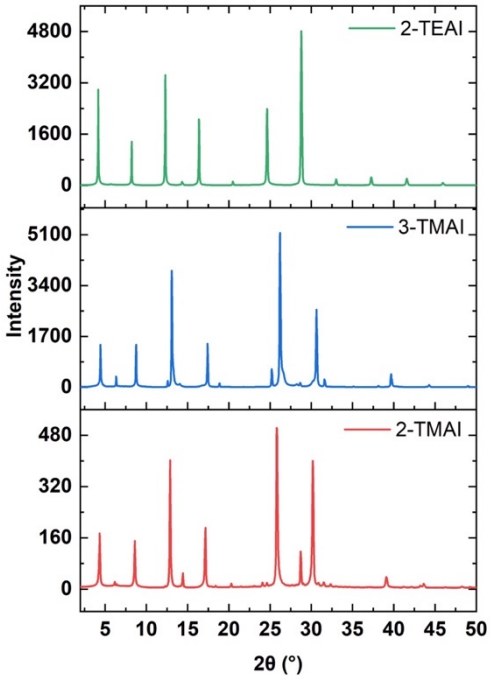

Figure A.1.2 XRD patterns of quasi-2D perovskite films with *n*=2 employing 2-TMAI, 3-TMAI and 2-TEAI cations using MA as small cation.

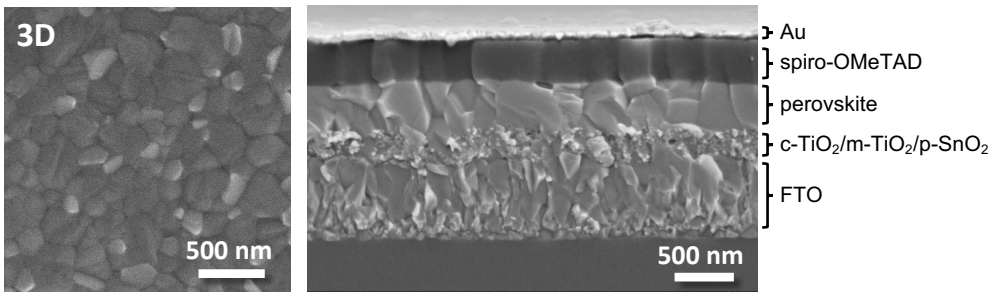

Figure A.1.3 Scanning electron microscopy images of the top view (left) of the perovskite film and cross-section (right) of the 3D control device

Table A.1.1 Optimization of the 2D layer thickness on the 3D PSCs by varying 2-TMAI concentration showed over 15 devices fabricated in the same batch.

Concentration	V_{OC} **(V)**	J_{SC} **(mA cm^{-2})**	***FF***	**PCE (%)**
0.05 M	1.07 ± 0.02	23.8 ± 0.3	0.77 ± 0.01	19.6 ± 0.4
0.06 M	1.11 ± 0.03	23.7 ± 0.2	0.76 ± 0.01	19.8 ± 0.2
0.07 M	1.07 ± 0.01	22.8 ± 0.3	0.70 ± 0.02	17.0 ± 0.2

Table A.1.2 Statistics of the photovoltaics parameters of 3D control and 2D/3D PSCs based on 2-TMAI, 3-TMAI, and 2-TEAI over 86 devices measured at their peak performance time.

	V_{OC} **(V)**	J_{SC} **(mA cm^{-2})**	***FF***	**PCE (%)**
2-TMAI	1.09 ± 0.02	23.8 ± 0.3	0.75 ± 0.01	19.3 ± 0.4
3-TMAI	1.13 ± 0.01	23.4 ± 0.1	0.76 ± 0.01	20.0 ± 0.5
2-TEAI	1.11 ± 0.00	23.2 ± 0.2	0.70 ± 0.01	18.1 ± 0.5
3D	1.09 ± 0.02	23.8 ± 0.3	0.78 ± 0.01	20.3 ± 0.5

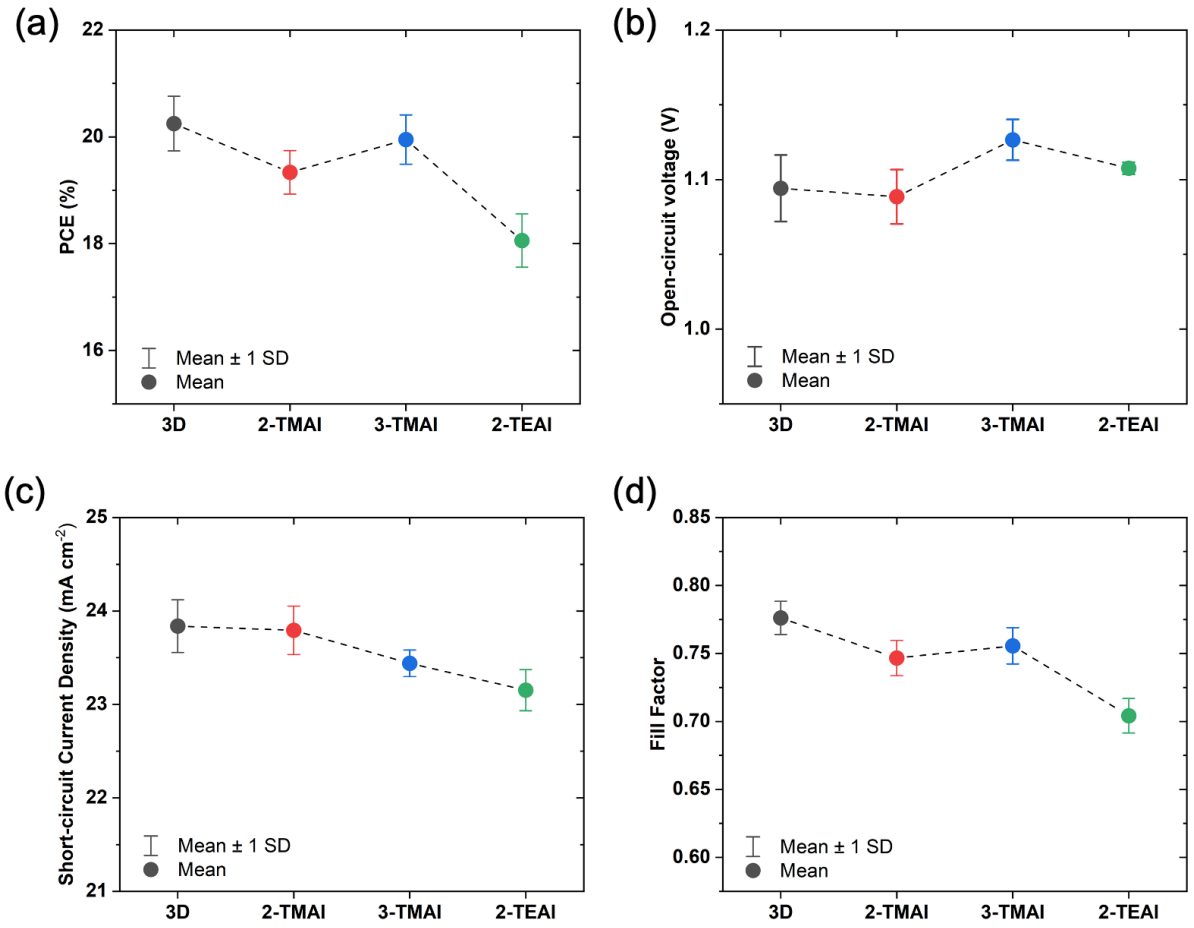

Figure A.1.4 Statistics of the photovoltaics parameters with standard deviation bars (SD) of 3D control and 2D/3D PSCs based on 2-TMAI, 3-TMAI, and 2-TEAI PSCs over 86 devices measured at their peak performance time: (a) power conversion efficiency, (b) open-circuit voltage, (c) short-circuit current density, and (d) fill factor. Color code is as in Figure 3.1.2.

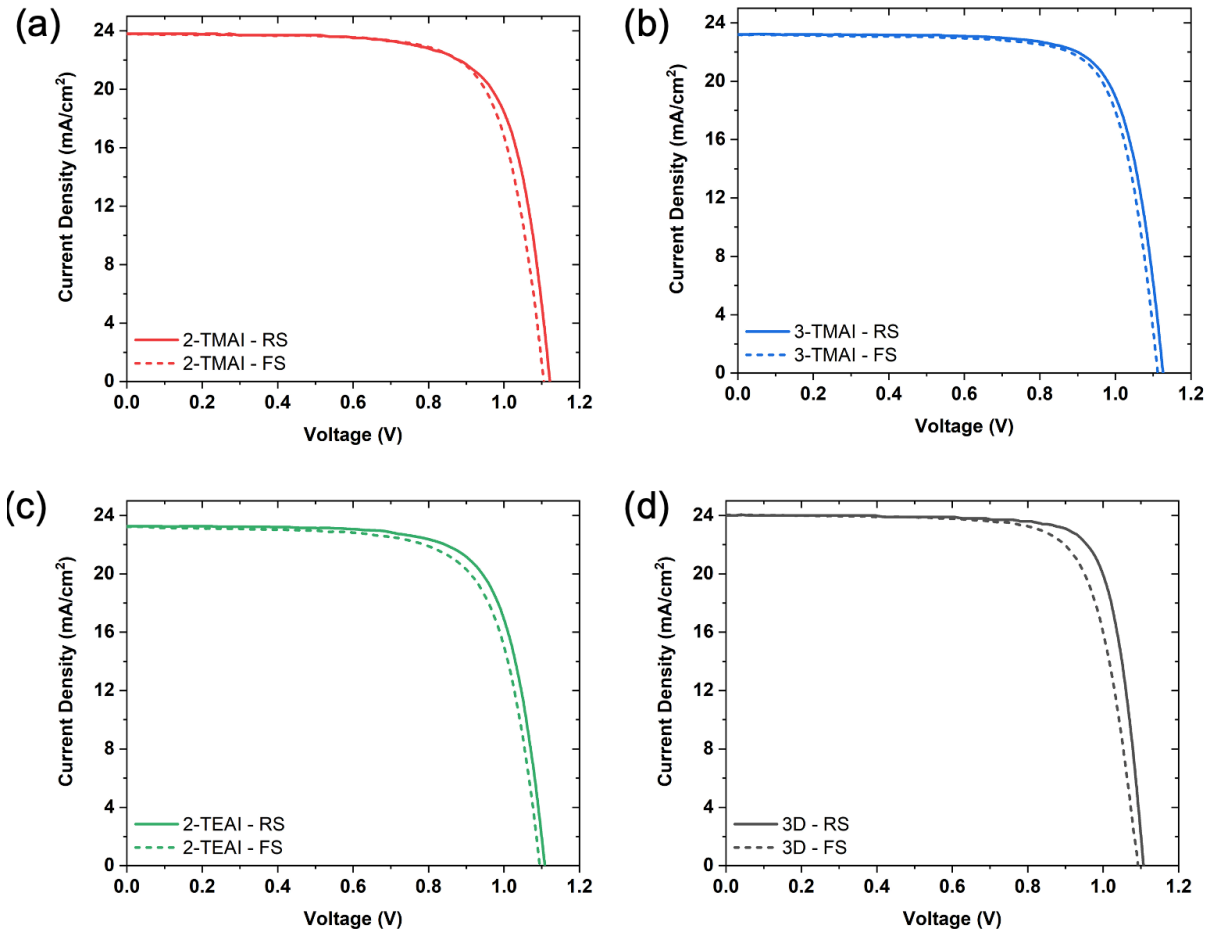

Figure A.1.5 Hysteresis measurement between reverse scan (RS) and forward scan (FS) of 2D/3D PSCs employing (a) 2-TMAI, (b) 3-TMAI, (c) 2-TEAI, and (d) 3D control measured at their peak performance time.

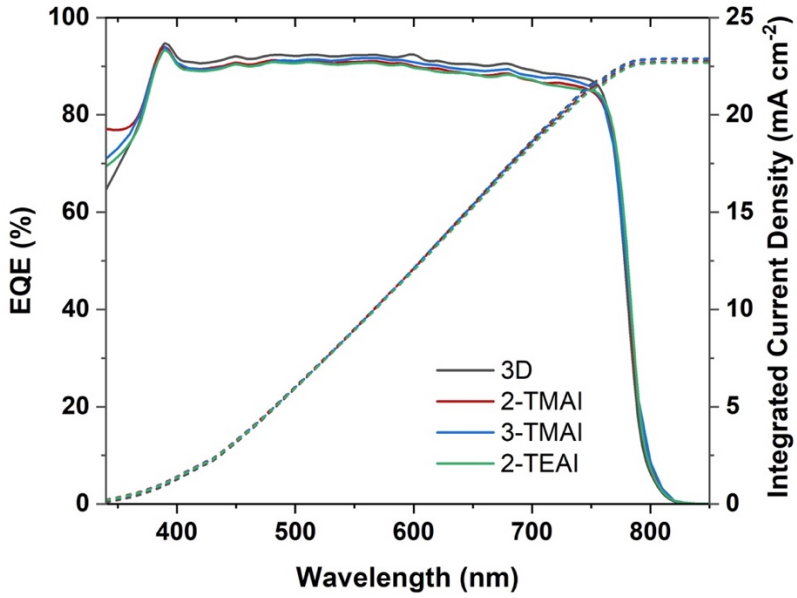

Figure A.1.6 External quantum efficiency (EQE) of 2D/3D PSCs based on 2-TMAI, 3-TMAI, 2-TEAI, and 3D control measured at their peak performance time.

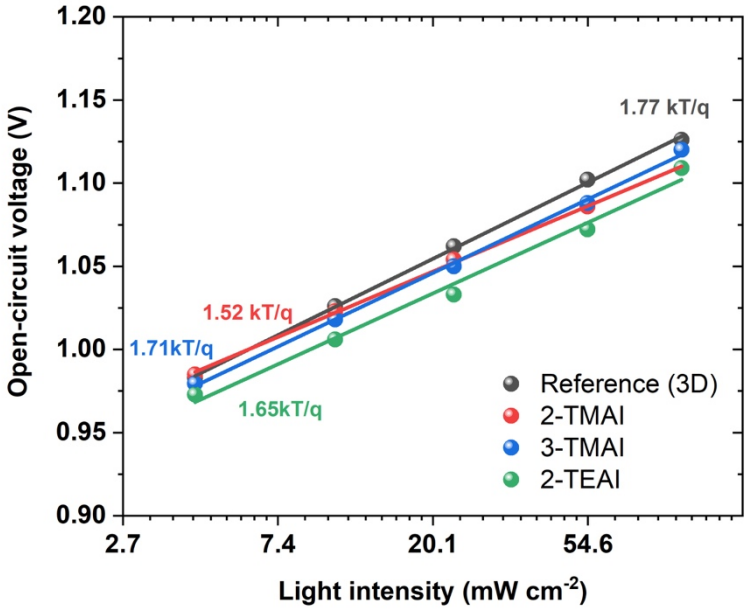

Figure A.1.7 Open-circuit voltage (V_{OC}) vs light intensity plot of 2D/3D PSC employing 2-TMAI, 3-TMAI, 2-TEAI, and 3D control on semi natural logarithmic scale.

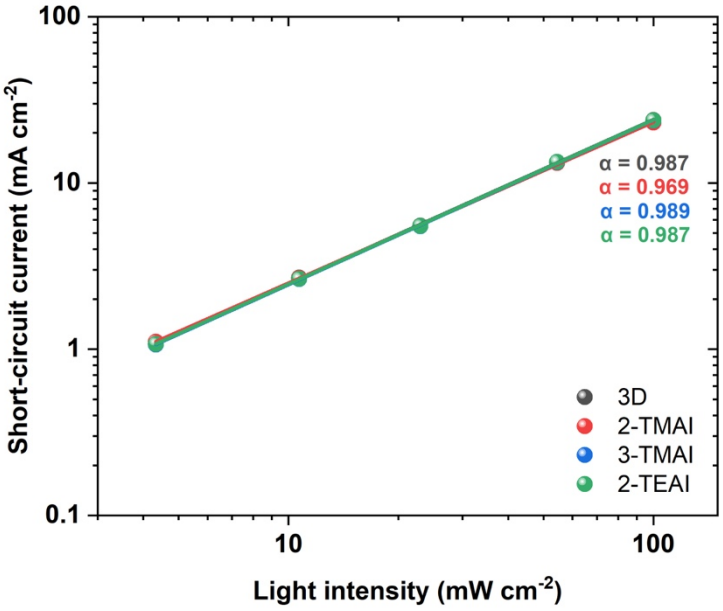

Figure A.1.8 Short-circuit current density (J_{SC}) vs light intensity plot of 2D/3D PSC employing 2-TMAI, 3-TMAI, 2-TEAI, and 3D control on double logarithmic scale.

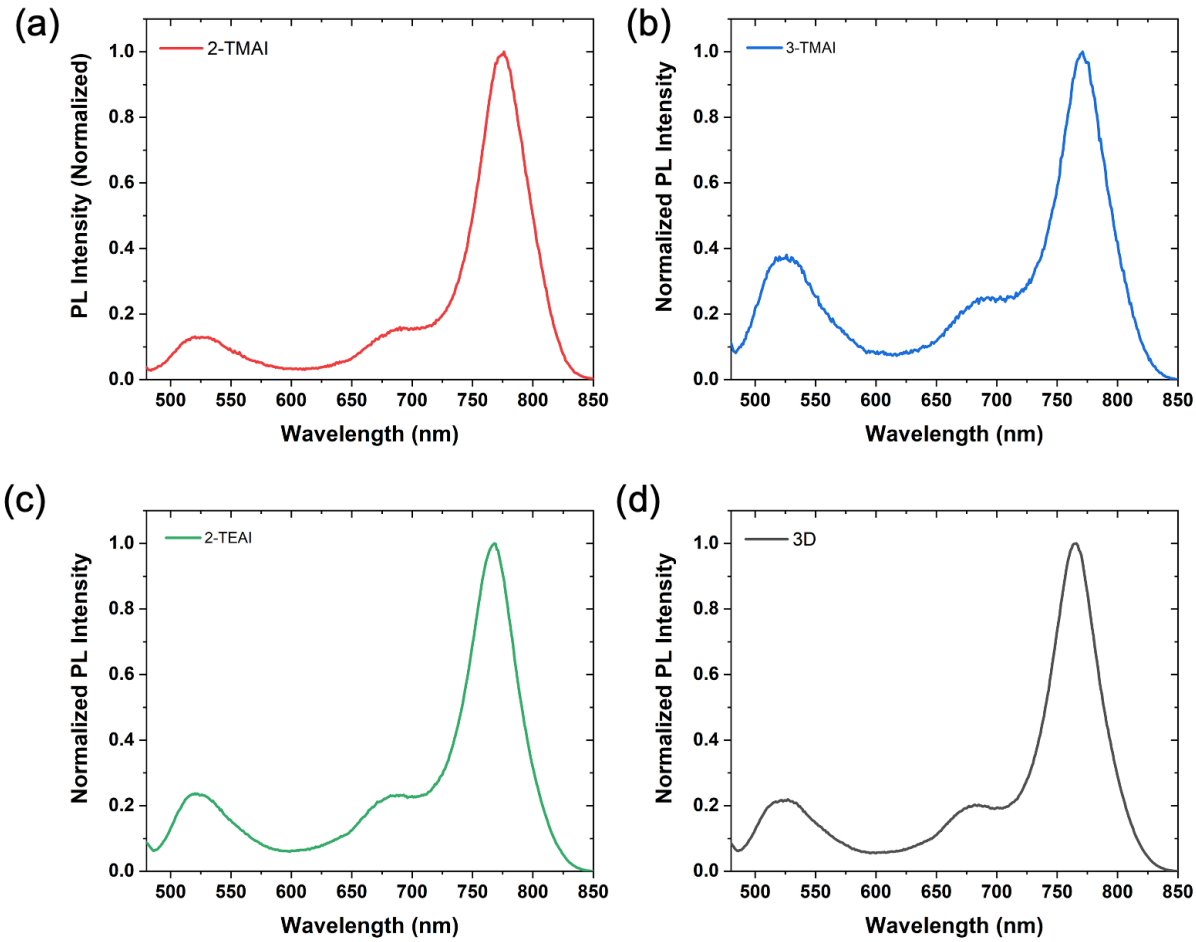

Figure A.1.9 Photoluminescence spectra of 2D/3D films employing (a) 2-TMAI, (b) 3-TMAI, (c) 2-TEAI, and (d) 3D control upon back side excitation exciting at 450 nm.

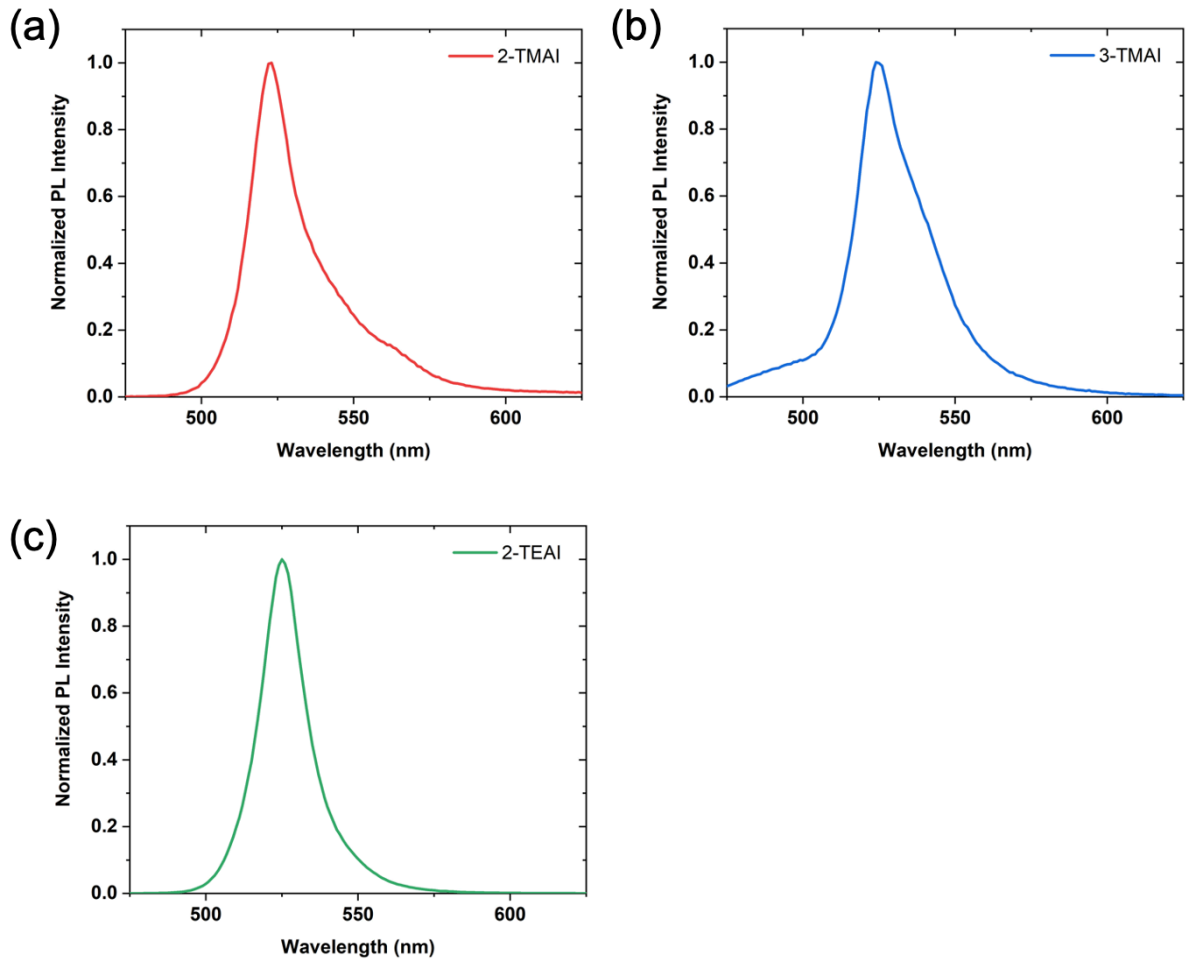

Figure A.1.10 Photoluminescence spectra of 2D perovskite films with *n*=1 employing (a) 2-TMAI, (b) 3-TMAI, and (c) 2-TEAI exciting at 450 nm.

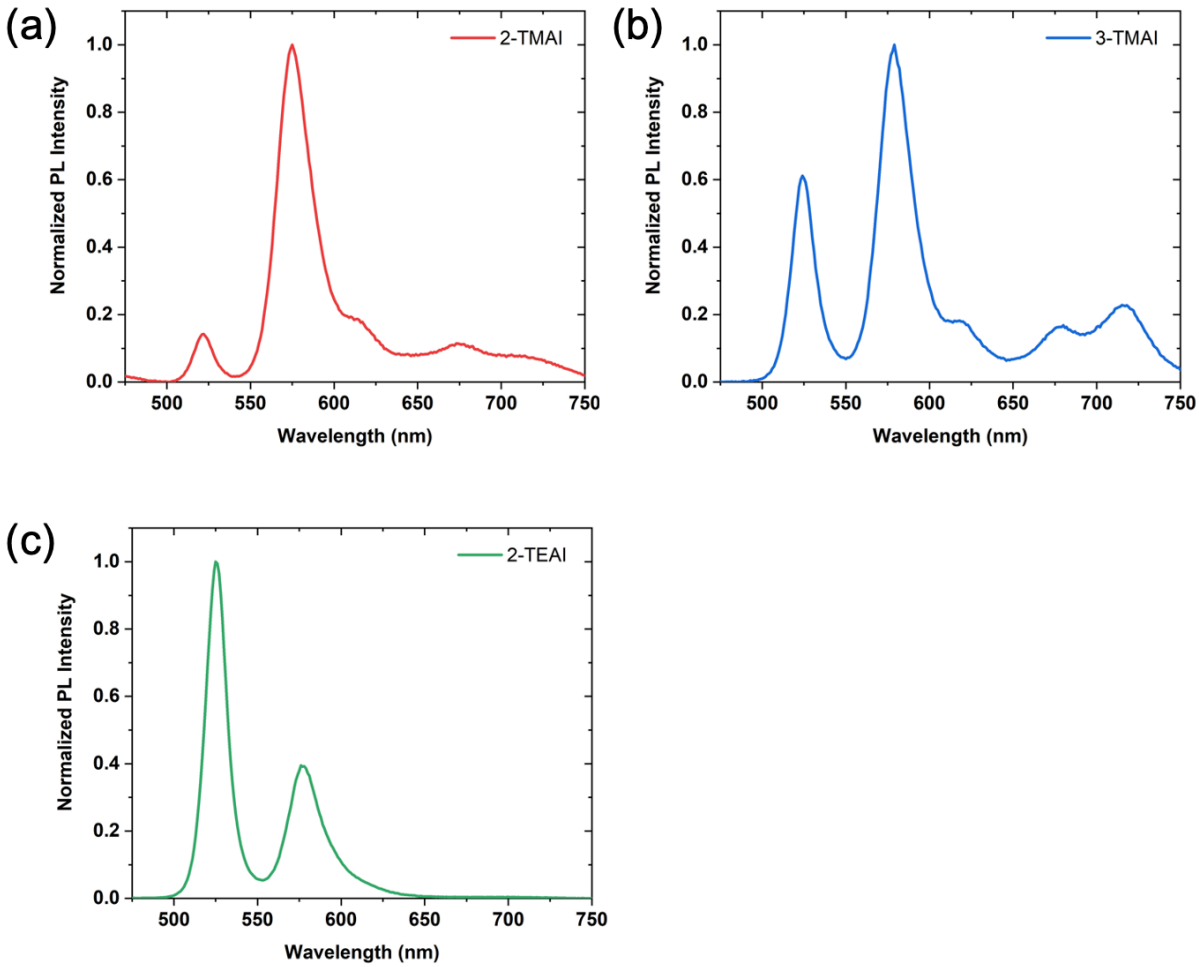

Figure A.1.11 Photoluminescence spectra of quasi-2D perovskite films with *n*=2 employing (a) 2-TMAI, (b) 3-TMAI, and (c) 2-TEAI using MA as small cation exciting at 450 nm.

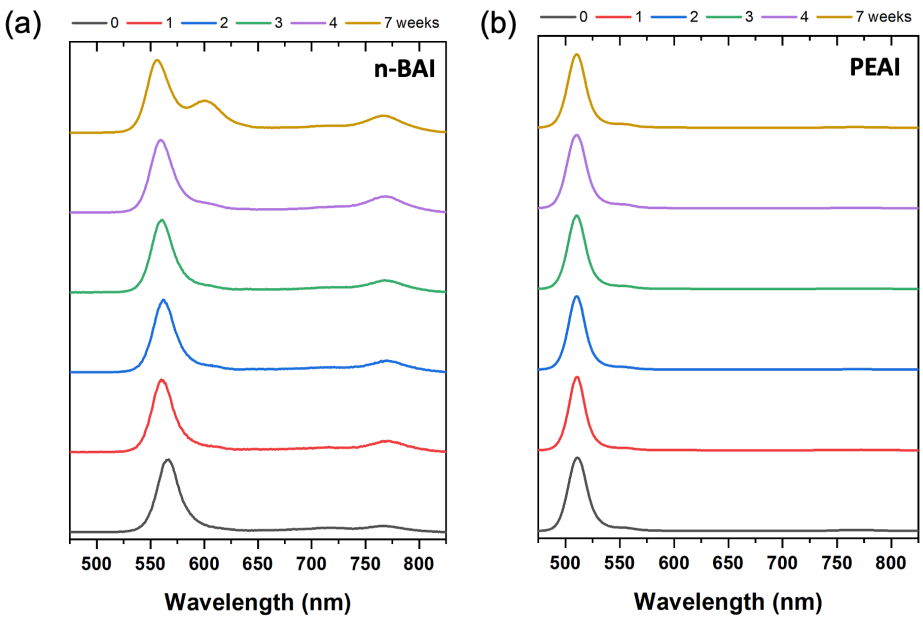

Figure A.1.12 PL spectra of 2D/3D perovskite employing n-BAI and PEAI as the large organic cations upon aging in dark and dry environment (RH <10%).

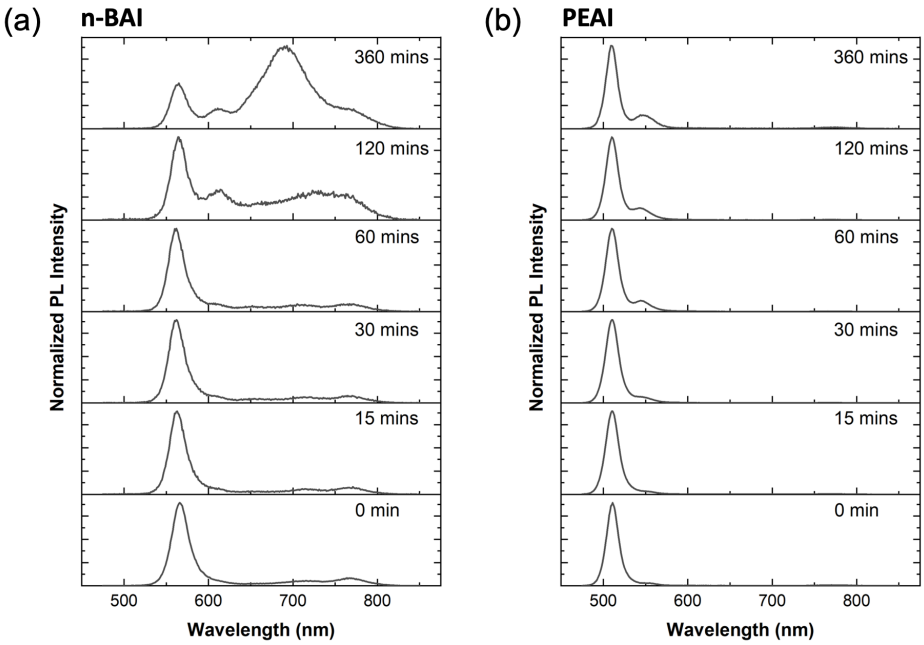

Figure A.1.13 PL spectra of 2D/3D perovskite employing n-BAI and PEAI as the large organic cations upon heating at 50°C.

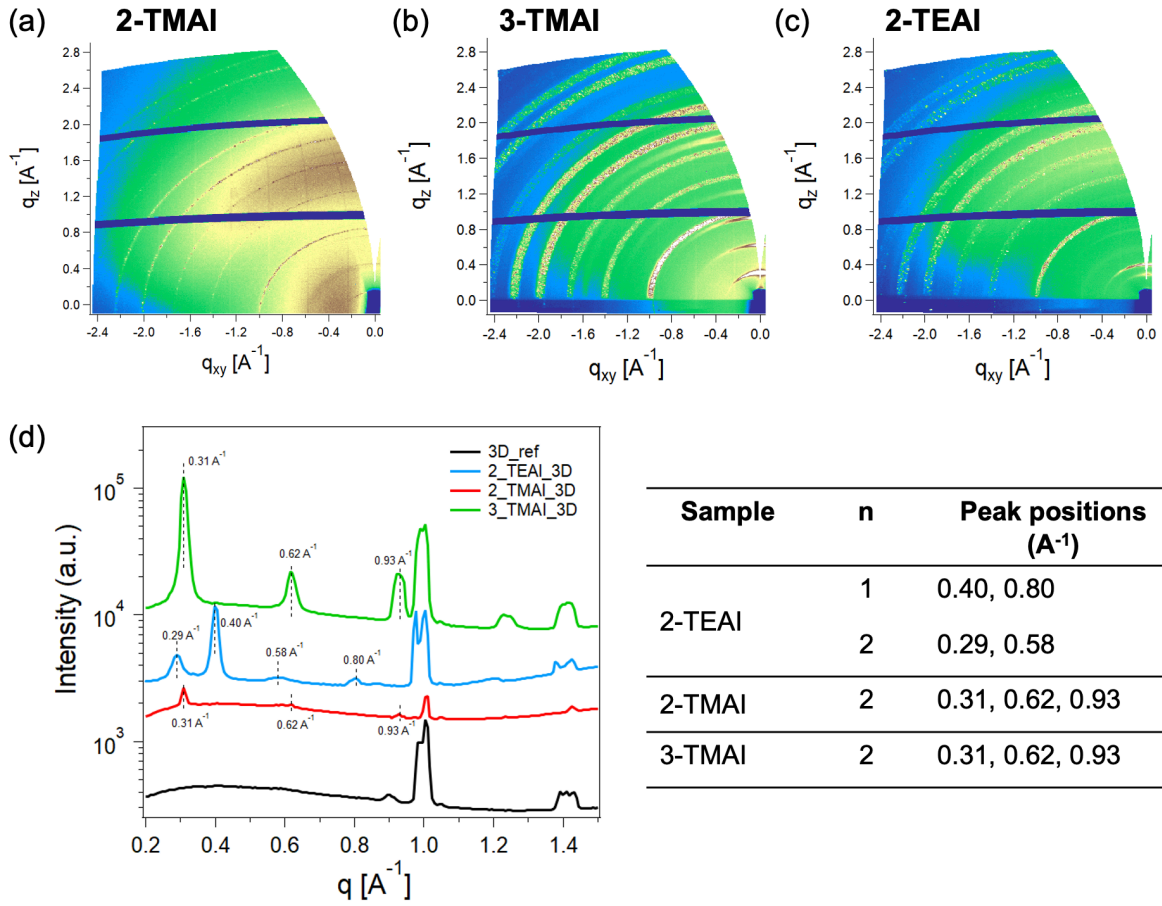

Sample	n	Peak positions (A^{-1})
2-TEAI	1	0.40, 0.80
	2	0.29, 0.58
2-TMAI	2	0.31, 0.62, 0.93
3-TMAI	2	0.31, 0.62, 0.93

Figure A.1.14 GIWAXS patterns of aged 2D/3D films employing (a) 2-TMAI, (b) 3-TMAI, and (c) 2-TEAI cations. (d) Sector average (90 to 125)° for data in (a)-(c), indicating principal features of the 2D layer. Table: Summary of the *n* number based on the GIWAXS patterns.

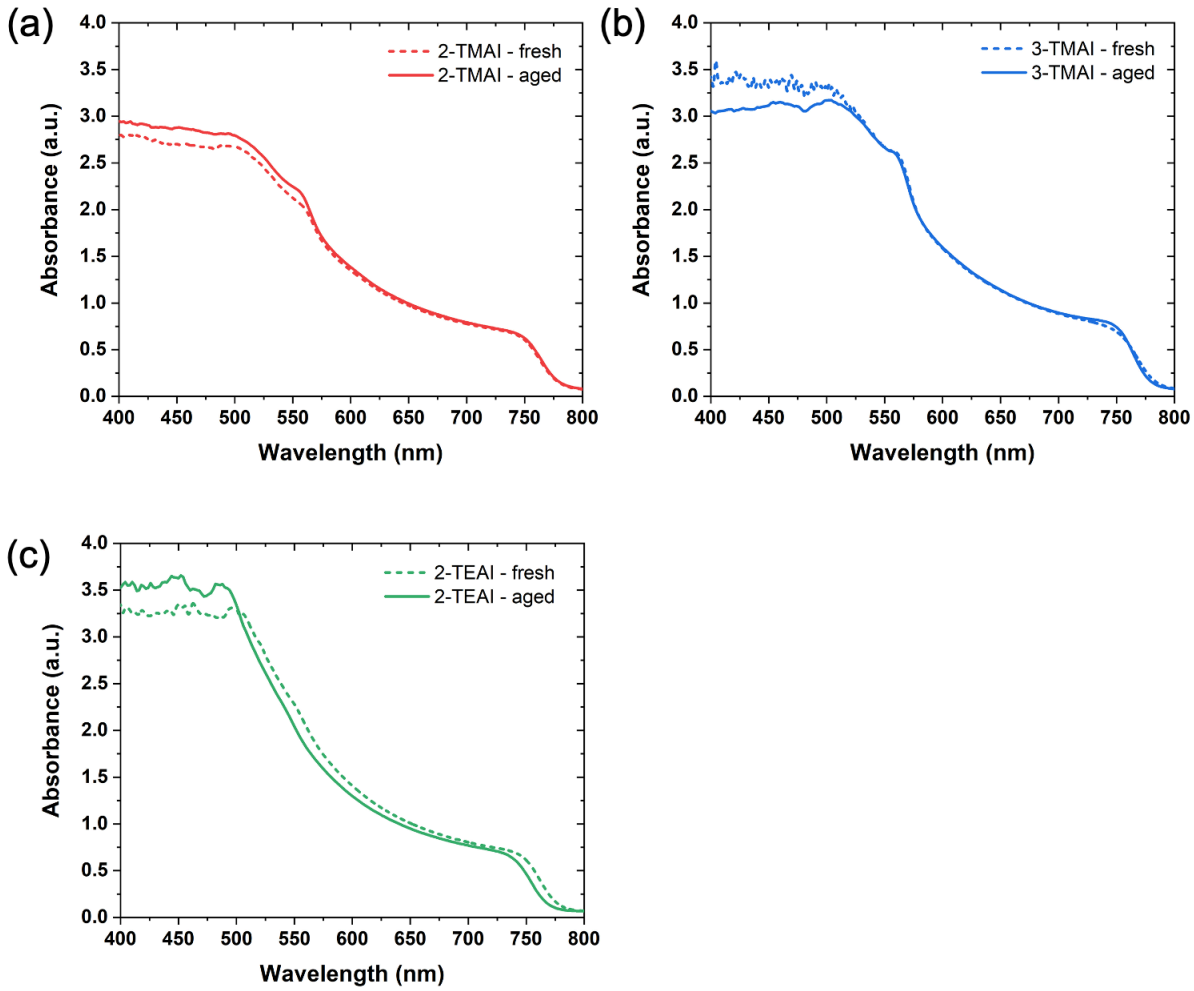

Figure A.1.15 Absorption spectra of fresh and aged (stored in the dark and dry environment for 4 months) 2D/3D films employing (a) 2-TMAI, (b) 3-TMAI, and (c) 2-TEAI cations.

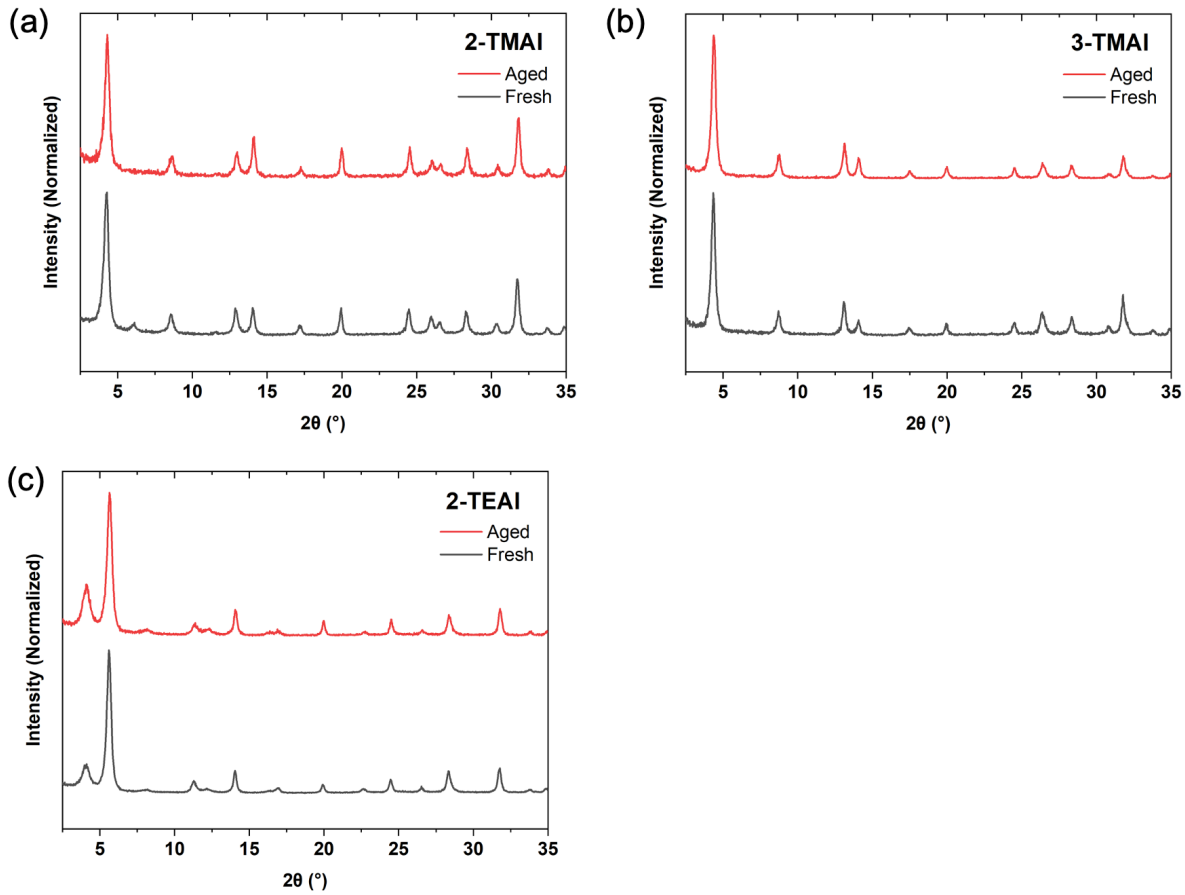

Figure A.1.16 XRD patterns of fresh and aged (stored in the dark and dry environment for 4 months) 2D/3D films employing (a) 2-TMAI, (b) 3-TMAI, and (c) 2-TEAI cations recorded at incident angle of 2°.

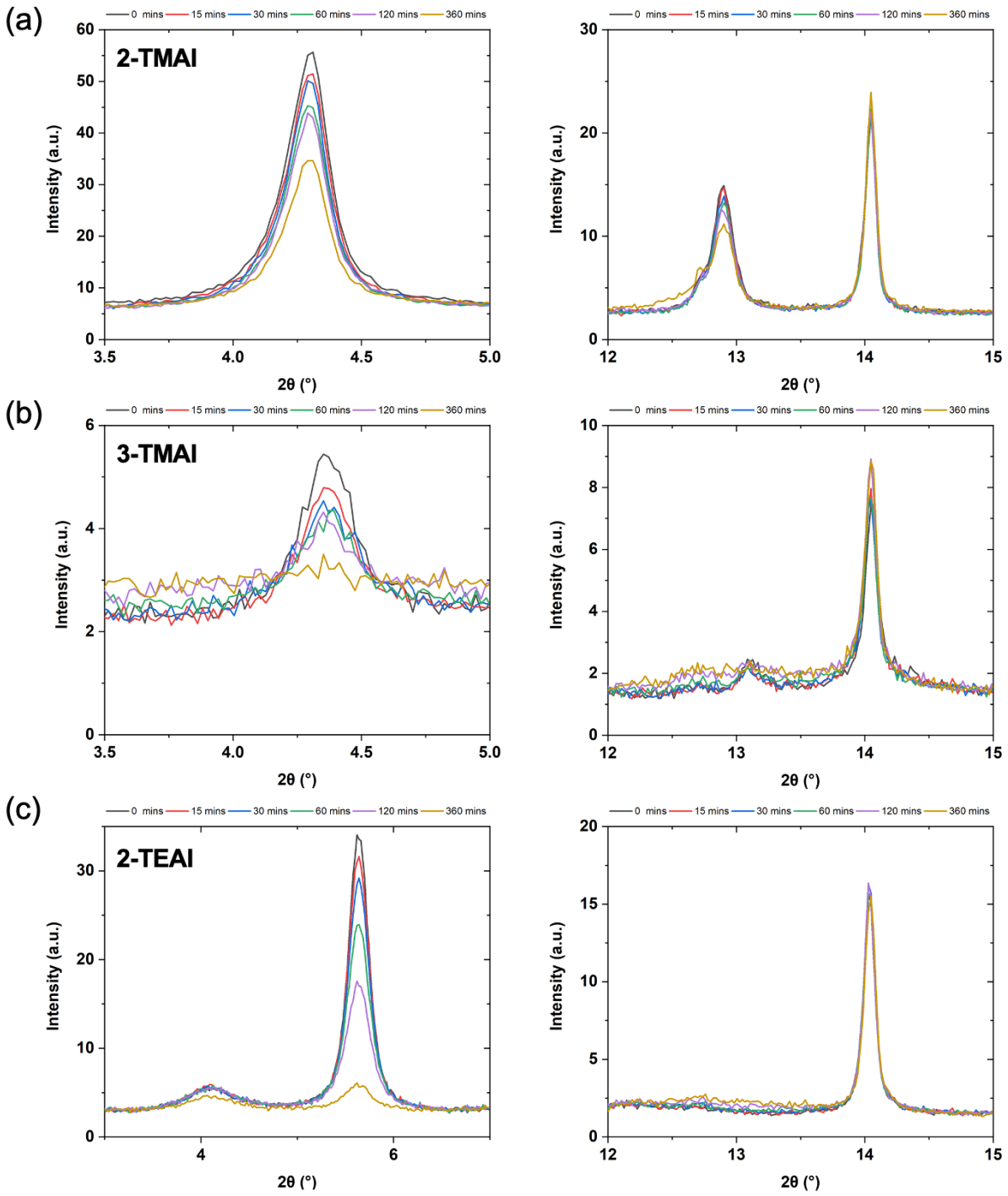

Figure A.1.17 In situ XRD measurement of 2D/3D perovskite films employing 2-TMAI, 3-TMAI, and 2-TEAI upon thermal aging at 50°C.

A.2 In situ analysis reveals the role of 2D perovskite in preventing thermal-induced degradation in 2D/3D perovskite interfaces

Experimental Methods

Synthesis of 2-thiophene methyl ammonium idodide (2-TMAI)

2-TMAI was synthesized according to the reported procedure.[223] An aqueous solution of HI (1.1 eq) was added dropwise to a stirred 1.0 mol/L ethanol solution of thiophenemethylamine (1.0 eq) at 0°C. The mixture was allowed to gradually reach room temperature and then it was poured into an excess of diethyl ether (Et_2O). The formed precipitate was collected and washed thoroughly with Et_2O. The salts were recrystallized from EtOH-Et_2O mixtures, providing with crystalline solids.

Preparation of 2D/3D perovskite films and device fabrication

FTO-coated glass (Nippon sheet glass) was chemically etched using zinc powder and HCl solution, followed by cleaning using Hellmanex, water, acetone, and 2-propanol. A 30 nm thick compact TiO_2 layer as electron transporting layer was deposited by spray pyrolysis using a titanium diisopropoxide bis(acetylacetonate) solution (Sigma-Aldrich) diluted in 2-propanol (1:15 by volume fraction) at 450 °C. On top of the compact layer, a 100 nm thick mesoporous layer of TiO_2 was deposited by spin coating TiO_2 paste (GreatCellSolar, 30NR-D) diluted in ethanol (1:6.3 by mass fraction) at 5000 rpm for 20 s followed by heating at 125 °C for 10 min and sintering at 500 °C for 20 min. A thin layer of passivating tin oxide of ≈20 nm was spin-coated by using tin (IV) chloride (Acros) solution (12 µL diluted in 988 µL water) at 3000 rpm for 30 s, followed by annealing at 100 °C for 10 min and 190 °C for 1 h. The prepared substrates were treated with UV-ozone for 15 min before perovskite deposition. A 1.3M $[(FAPbI_3)_{0.87}(MAPbBr_3)_{0.13}]_{0.92}(CsPbI_3)_{0.08}$ perovskite solution with excess PbI_2 (PbI_2:FAI = 1.05:1) was prepared by mixing FAI (GreatCellSolar), MABr (GreatCellSolar), CsI (ABCR), PbI_2 (TCI), and $PbBr_2$ (TCI) in DMF and DMSO (0.78:0.22 v/v). The prepared perovskite precursor was then spin-coated on the prepared substrates at 2000 rpm for 12 s and 5000 rpm for 30 s. Chlorobenzene was added as an anti-solvent at 15 s before the end of spin coating process. The films were subsequently annealed at 100 °C for 60 min. After cooling down to room temperature, a 100µL solution of the synthesized 2-TMAI or PEAI (GreatCellSolar) in 2-propanol (60 mM) was spin-coated dynamically by adding the solution during spinning at 4000 rpm for 30 s, followed by annealing at 100 °C for 6 min in order to form a ~60 nm thick of 2D perovskite layer

on top. For a complete device, a spiro OMeTAD layer as the hole-transporting materials (HTM) was deposited on top of the perovskite layer. 78.2 mg of spiro-OMeTAD (Merck) was dissolved in 1 mL chlorobenzene and doped with 31.28 µL of 4-tert-butylpyridine (Sigma-Aldrich), 18.57 µL of Li-bis (trifluoromethanesulphonyl) imide (Aldrich) from the stock solution (196 mg in 379 µL acetonitrile), 13.69 µL of FK 209 Co(III) TFSI (GreatCellSolar) from the stock solution (99 mg in 263 µL acetonitrile). The prepared spiro-OMeTAD solution was then spin-coated at 4000 rpm for 30 s. Finally, a 70 nm-thick gold counter electrode was thermally evaporated on top of HTM layer.

Device characterization

The current density–voltage (J–V) curves were measured under 1 sun illumination (AM 1.5G) by xenon lamp solar simulator (450 W, Oriel Sol3A, AAA class). The light intensity was calibrated to 1 sun by using a Si reference equipped with an IR-cutoff (KG5) filter. An external voltage bias was applied and the current responses were measured at the same time using a digital source meter (Keithley 2400). An active area of 0.0804 cm^2 was determined by a metal mask. The *J-V* curves were scanned with the rate of 50 mV s^{-1} without any preconditioning, such as light soaking or pre-biasing for a long time. External quantum efficiency (EQE) spectra were recorded using IQE200B (Oriel).

In situ GIWAXS

In situ GIWAXS measurements were performed at the XRD2 beamline at the Brazilian Synchrotron Light Laboratory (LNLS). The energy of the X-ray was 7 keV and the scattering signal was collected using a Pilatus 300K detector with integration time of 3s and 30s between each measurement. The incidence angle of the X-ray beam relative to the film surface was set at 3°. The modified films were measured under nitrogen atmosphere. Each GIWAXS image was azimuthally integrated to obtain 1D X-ray diffraction patterns and plotted as 2D intensity maps with respect to time (abscissa) and the 2theta (ordinate). The intensity was normalized with the storage ring current.

Photoluminescence and UV-Vis Absorption

Photoluminescence spectra of the perovskite films were measured and recorded using Fluorolog3-22 spectrofluorometer. The emission was measured upon excitation at 450 nm. The absorption spectra of the perovskite thin films were measured in an ultraviolet, visible, near-infrared spectrophotometer (PerkinElmer Lambda 950S).

Time-resolved Photoluminescence

Time-resolved photoluminescence (TrPL) decays were acquired on a time-correlated single-photon counting (TCSPC) FL900 spectrometer from Edinburgh Analytical Instruments with a Hamamatsu MCP-PMT R3809U-50, and a PicoQuant LHD-DC-440 pulsed laser diode at λ_{exc} = 440 nm (pulsewidth < 80 ps; F = 9.7 nJ cm^{-2}). The instrument response was recorded using Ludox samples. At least 1,000 counts in the peak channel were accumulated for the lifetime determination. The emission decays were analyzed using exponential functions. The films used for TrPL measurement were prepared under the same condition as GIWAXS experiment.

Table A.2.1 Photovoltaic parameters of 3D perovskite solar cells without and with heating (considering a statistic of 16 devices)

Treatment	***V_{OC}*** **(V)**	***J_{SC}*** **(mA cm^{-2})**	***FF***	**PCE (%)**
3D – Control	1.086 ± 0.008	23.42 ± 0.19	0.77 ± 0.01	19.5 ± 0.2
3D – Heated 50°C – 100 mins.	1.066 ± 0.007	22.84 ± 0.03	0.74 ± 0.01	18.1 ± 0.4

Calculation of XRD Peak Position

The interplanar distance in a 2D perovskite can be calculated by the formula:[435]

d = E + *n**T

Where, E is the length of the spacer and T the thickness of one perovskite layer and *n* the number of layers. For *n*=1 and *n*=2 we have, respectively:[435]

d (*n*=1) = E + T Equation (1)

d (*n*=2) = E + 2T Equation (2)

As E has not been reported for TMA^+ yet, we used the *n*=1 and *n*=2 synthetized perovskites to estimate d by Bragg's law and calculated E and T using the equations (1) and (2). We found T equals 0.62 nm, which is very consistent with value reported in the literature and with the size of the inorganic octahedron.[436, 437] We found that the length of the TMA spacer in the 2D perovskites is 0.82 nm consistent with the length of the benzylammonium (0.91 nm) which have similar structure. The tables 1 and 2 shows the experimental, theorical and deviation between then for *n*=1 and *n*=2 perovskites, respectively. Using these two parameters (T and E), equation 1 and Bragg' law, we estimated the XRD peak positions for *n*=3 to *n*=10 for different diffraction orders. Table A.2.4 shows the calculated values.

Table A.2.2 Experimental and calculated XRD peaks positions for *n*=1 2-TMAI 2D perovskite

XRD order peak	Experimental		Theorical	Deviation (%)
	q (nm^{-1})	d (nm)	q (nm^{-1})	
1	4.4	1.42	4.36	1.26
2	8.7	1.44	8.72	0.16
3	13.1	1.44	13.09	0.14
4	17.4	1.45	17.45	0.35
5	21.7	1.45	21.87	0.42
6	26.0	1.45	26.17	0.55

* Average d equal 1.44 nm

Table A.2.3 Experimental and calculated XRD peaks positions for *n*=2 2-TMAI 2D perovskite

XRD order peak	Experimental		Theorical	Deviation (%)
	q (nm^{-1})	d (nm)	q (nm^{-1})	
1	3.1	2.04	3.05	1.06
2	6.1	2.06	6.10	0.19
3	9.1	2.06	9.15	0.05
4	12.2	2.07	12.19	0.27
5			15.24	
6	18.2	2.07	18.29	0.42
7	21.2	2.07	21.34	0.54

* Average d equal 2.06 nm

Table A.2.4 Calculated XRD peak positions.

n	XRD order	q(nm^{-1})
3	1	2.34
3	2	4.69
3	3	7.03
3	4	9.37
3	5	11.72
4	1	1.90
4	2	3.81
4	3	5.71
4	4	7.61
4	5	9.51
5	1	1.60
5	2	3.20
5	3	4.80
5	4	6.41
5	5	8.01
6	1	1.38
6	2	2.77
6	3	4.15
6	4	5.53
6	5	6.91
7	1	1.22
7	2	2.43
7	3	3.65
7	4	4.87
7	5	6.08
8	1	1.09
8	2	2.17
8	3	3.26
8	4	4.34
8	5	5.43
9	1	0.98
9	2	1.96
9	3	2.94
9	4	3.92
9	5	4.90
9	6	5.89
9	7	6.87
10	1	0.89
10	2	1.79
10	3	2.68
10	4	3.58
10	5	4.47
10	6	5.37

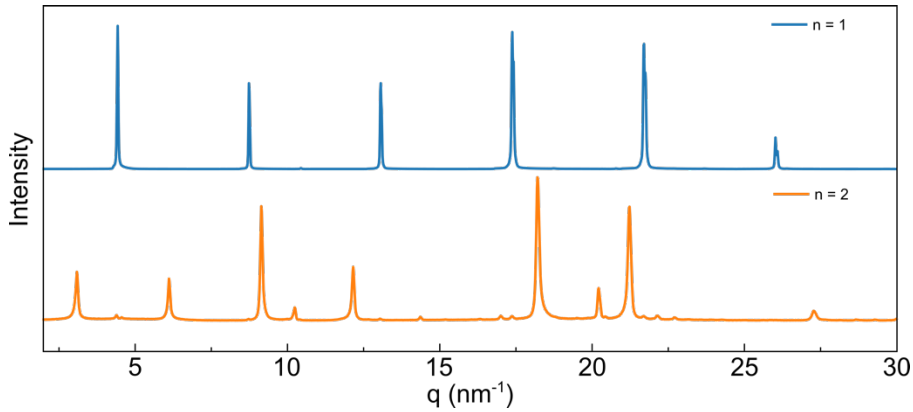

Figure A.2.1 XRD patterns of *n*=1 and *n*=2 2-TMAI 2D

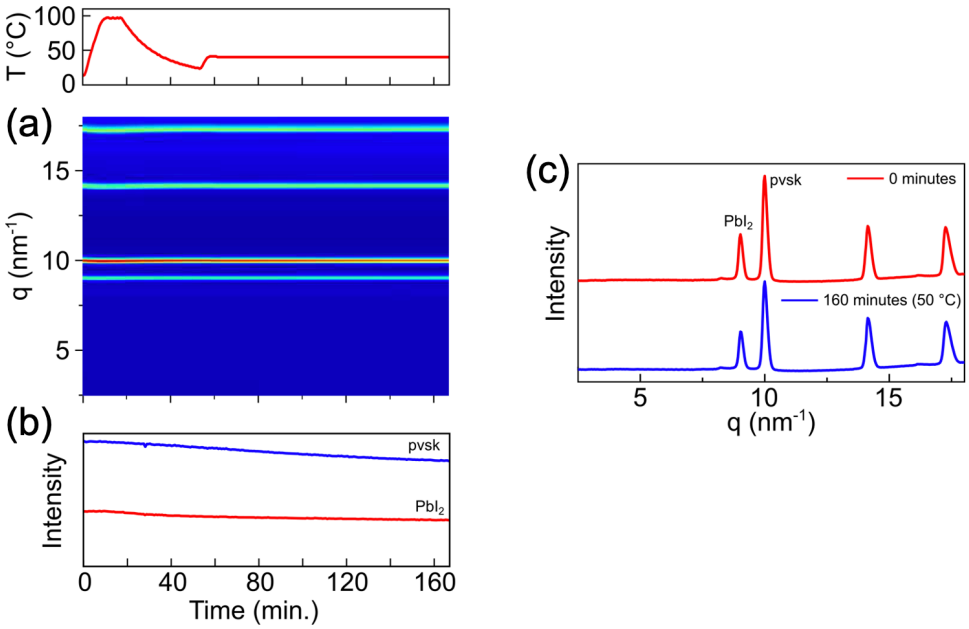

Figure A.2.2 (a) X-ray diffraction maps in function of time and temperature of pristine perovskite films, respectively, (b) respective intensity of the main peaks in function of time and (c) respective x-ray diffraction pattern in different times.

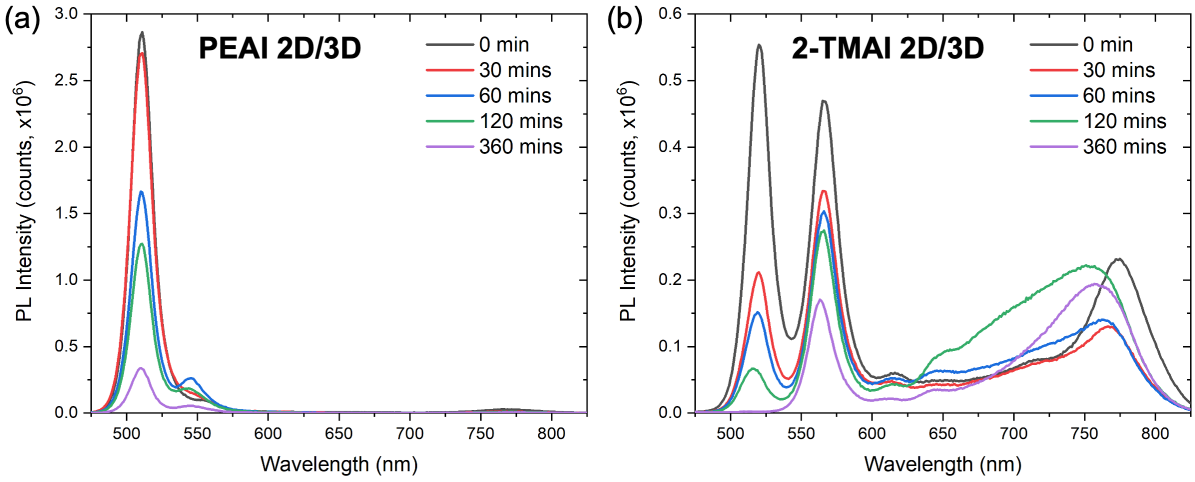

Figure A.2.3 PL spectra (not normalized) of (a) PEAI 2D/3D and (b) 2-TMAI 2D/3D under thermal aging upon excitation at 450 nm from the front side

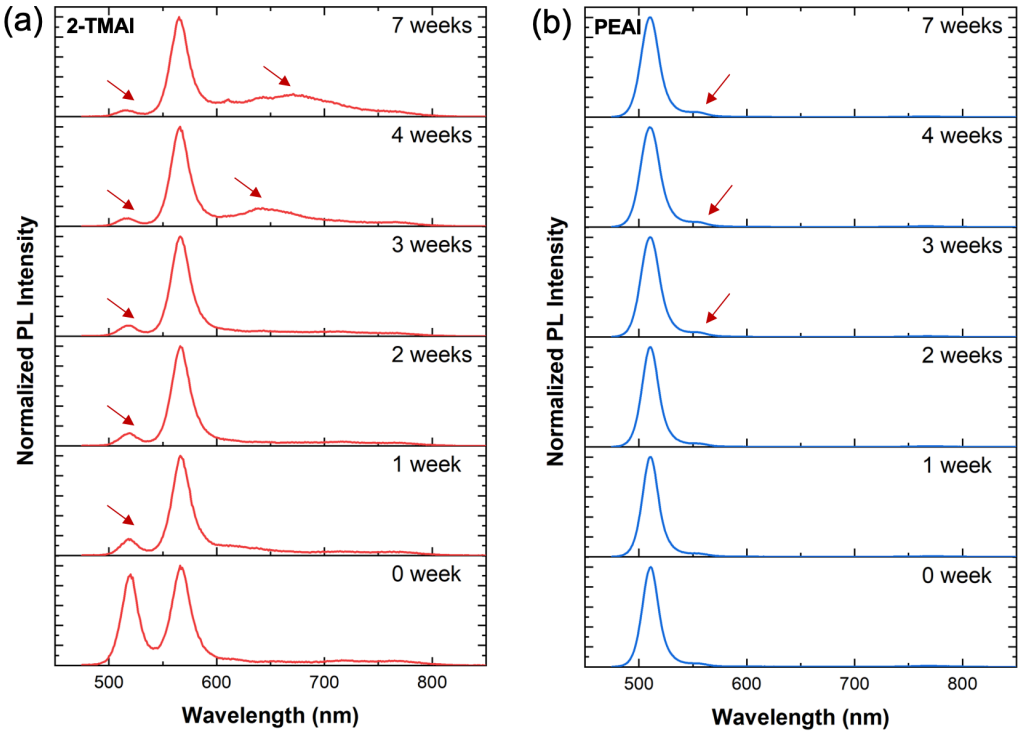

Figure A.2.4 PL spectra of 2D/3D perovskite films employing (a) 2-TMAI and (b) PEAI as the large cation upon slow aging in dark and dry environment at room temperature.

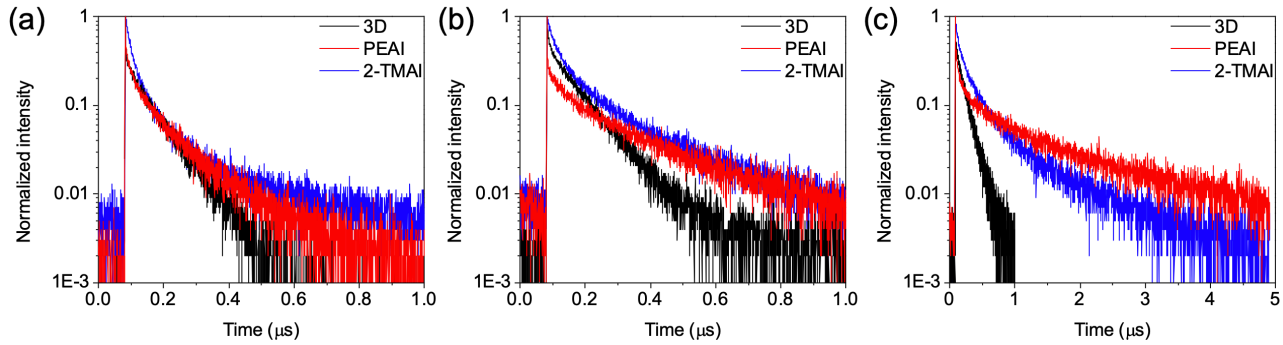

Figure A.2.5 Normalized TrPL decays (λ_{exc} = 440 nm; λ_{PL} = 780 nm) of the 3D control sample (black curves), PEAI (red curves), and 2-TMAI (blue curves) 2D/3D modified perovskite thin-films as function of the heat time at T = 50 ºC: t= 0 (a), 15 (b), and 30 min (c).

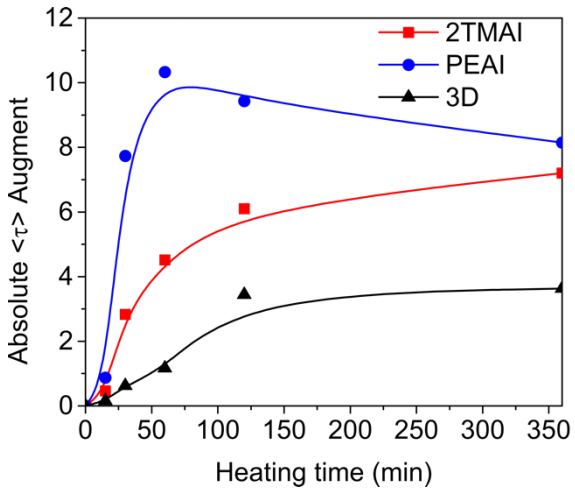

Figure A.2.6 Average augment of the charge-carrier lifetimes of the 2-TMAI (red), PEAI (blue), and 3D control (black) samples along the thermal aging treatment at 50°C.

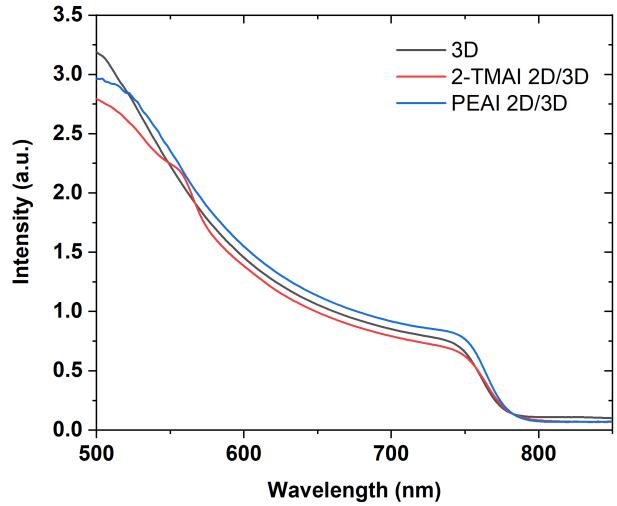

Figure A.2.7 Absorption spectra of the 3D perovskite thin-film and 2D/3D perovskite thin-films employing 2-TMAI and PEAI as the large organic cations.

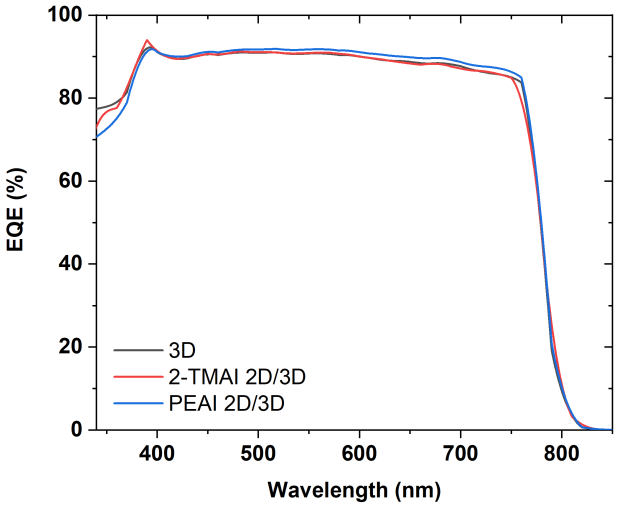

Figure A.2.8 External quantum efficiency (EQE) spectra of the 3D PSC and 2D/3D PSCs employing 2-TMAI and PEAI as the large organic cations.

Appendix B: Supplementary Information to Chapter 4

Experimental Methods

Synthesis of thiophenemethylammonium halides

A concentrated aqueous solution of an acid HX (1.1 eq, where X:Cl, Br or I) was added drop by drop to 1.0 M ethanol solution of thiophenemethylamine (1.0 eq) at 0°C under stirring. The mixture was allowed to reach room temperature gradually and then it was poured into an excess of diethyl ether (Et_2O). The precipitate was separated and washed thoroughly with Et_2O. The salts were recrystallized from ethanol (EtOH) and Et_2O mixtures, resulting in crystalline solids of the salts.

Perovskite thin-film and solar cells devices fabrication

Fluorine-doped tin oxide (FTO) substrates (Nippon Sheet Glass) were patterned by chemical etching process using zinc powder and aqueous HCl solution (3.0 M) and cleaned with the detergent (Hellmanex), water, acetone, and isopropanol subsequently. On top of the cleaned substrates, a 30-nm think of compact TiO_2 layer as electron transporting layer was spray-deposited from the titanium diisopropoxide bis(acetylacetonate) solution (Sigma-Aldrich) precursor diluted in isopropanol (1:15 by volume fraction) at 450 °C, followed by the deposition of a 100 nm thick mesoporous TiO_2 layer by spin-coating a diluted TiO_2 paste solution in ethanol (1:8 w/v) at 5000 rpm for 20 s and sintering at 500°C for 20 min. A 20 nm of tin oxide layer as a passivation layer was formed from the aqueous tin (IV) chloride solution (12 µL $SnCl_4$ for 1mL solution) by depositing the $SnCl_4$ precursor at 3000 rpm for 30 s, followed by annealing at 100°C for 10 min and 190°C for 60 min. UV-ozone treatment was carried out for 15 min before both SnO_2 layer deposition and perovskite layer deposition.

A triple-cation based 3D perovskite precursor solution (1.3 M) with the composition of $[(FAPbI_3)_{0.87}(MAPbBr_3)_{0.13}]_{0.92}(CsPbI_3)_{0.08}$ was prepared by mixing the starting materials (FAI (GreatCellSolar), MABr (GreatCellSolar), CsI (ABCR), PbI_2 (TCI), and $PbBr_2$ (TCI)) in DMF and DMSO mixture with the volume ratio of 0.78:0.22. An excess of PbI_2 by 5% towards FAI was used in the precursor solution in order to control the growth of the 2D perovskite layer. The 3D perovskite layer was deposited by spin-coating the precursor solution at 2000 rpm for 12 s and 5000 rpm for 30 s. Chlorobenzene was poured on top of the spinning substrate 15 s prior to the

end of the spin-coating process. The deposited 3D perovskite film was annealed at 100°C for 60 min. Then, the film was allowed to cool down to the room temperature and the corresponding thiophene methylammonium halide cations (60 mM in isopropanol) was deposited dynamically under 4000 rpm for 30 s. The film was then annealed at 100°C for 6 min on a hotplate. Spiro-OMeTAD (Merck) with a concentration of 60 mmol in 1 mL of chlorobenzene as hole-transporting material doped with 31.28 µL of 4-tert-butylpyridine (Sigma-Aldrich), 18.57 µL of Li-bis (trifluoromethanesulphonyl) imide (Aldrich) from the stock solution (196 mg in 379 µL acetonitrile), and 13.69 µL of FK 209 Co(III) TFSI (GreatCellSolar) from the stock solution (99 mg in 263 µL acetonitrile) was deposited by spin-coating at 4000 rpm for 30 s. Finally, a gold counter electrode (70 nm) was deposited by physical vapor deposition process under high vacuum.

Thin-films Characterizations

Photoluminescence

Steady-state photoluminescence spectra were recorded on a Fluorolog3-22 spectrofluorometer upon excitation at 450 nm. The emission was measured from both top and bottom surface of the film.

UV-Vis absorption

An ultraviolet, visible, near-infrared spectrophotometer (PerkinElmer Lambda 950s) was used to measure the absorption spectra of the perovskite thin-films.

X-ray diffraction (XRD)

XRD patterns were acquired by measuring the perovskite thin-films using Bruker D8 Advance diffractometer and non-monochromated Cu-radiation. For the 2D/3D perovskite thin films, measurements under grazing incident diffraction (GID) geometry were performed on Bruker D8 Discover diffractometer with non-monochromated Cu-radiation at the incident angle of 2° in order to obtain the XRD patterns on the surface of the films.

Scanning electron microscopy (SEM)

SEM micrographs (cross-section and surface) were recorded in the FEI Teneo scaning electron microscope using in-lens detector under the accelerating voltage of 3 kV and 5 kV.

Ultra-violet photoemission spectroscopy (UPS) depth profiling (DP)

The samples were transferred to an ultrahigh vacuum chamber (ESCALAB 250Xi), with a base pressure of $2*10^{-10}$ mbar, for UPS DP measurements. UPS measurements were performed using a double-differentially pumped He gas discharge lamp emitting He I radiation (hv=21.22 eV) with a pass energy of 2 eV and a bias of -5 V in order to ensure secondary electron onset detection. The UPS spectra are shown as a function of the binding energy with respect to the Fermi Energy. The energy edge of the valence band features is used to determine the valence band level position with respect to the Fermi level. The onset of the valence band was analysed using a linear presentation of the UPS spectra. The secondary electron onset was used to determine the vacuum level with respect to the Fermi level. The conduction bands were estimated using the optical gaps of the 2D and 3D materials. Cluster etching was performed using large Ar clusters generated by the MAGCIS Dual Beam Ion Source (Thermo Scientific) with an energy of 4000 eV.

Absolute Photoluminescence

Excitation for the PL measurements was performed with a 445 nm continuous wave laser (Insaneware) through an optical fibre into an integrating sphere. The intensity of the laser was adjusted to a 1 sun equivalent intensity by illuminating a 1 cm2 size perovskite solar cell under short-circuit and matching the current density to the J_{SC} under the sun simulator (22.0 mA cm^{-2} at 100 mW cm^{-2}, or 1.375×10^{21} photons m^{-2} s^{-1}). A second optical fiber was used from the output of the integrating sphere to an Andor SR393i-B spectrometer equipped with a silicon charge-coupled device camera (DU420A-BR-DD, iDus). The system was calibrated by using a calibrated halogen lamp with specified spectral irradiance, which was shone into to integrating sphere. A spectral correction factor was established to match the spectral output of the detector to the calibrated spectral irradiance of the lamp. The spectral photon density was obtained from the corrected detector signal (spectral irradiance) by division through the photon energy (hf) and the photon numbers of the excitation and emission obtained from numerical integration using Matlab. In a last step, three fluorescent test samples with high specified PLQY (≈70%) supplied from Hamamatsu Photonics were measured where the specified value could be accurately reproduced within a small relative error of less than 5%

All PL measurements were performed on complete cells, prepared fresh, and immediately encapsulated in a glovebox under N_2 atmosphere. The PL of the samples was readily recorded after mounting the sample and after an exposure of 1 s at each laser intensity subsequently, the incident laser was blocked by a shutter and the filter wheel position adjusted while the sample

was kept in dark conditions avoiding any effects induced by constant illumination. The cell was illuminated through the glass/ITO side. It was noted that all absolute PL measurements were performed on films with the same HTL, ETL, and perovskite thicknesses as used in the operational solar cells.

Photovoltaic characterization

The current density–voltage (J–V) curves were measured under 1 sun illumination (AM 1.5G) in the ambient atmosphere and temperature using xenon lamp solar simulator (450 W, Oriel, AAA class). The light intensity was calibrated to 1 sun by using a Si reference equipped with an IR-cutoff (KG5) filter (Oriel 91150V). The current responses were measured using a digital source meter (Keithley 2400) by applying an external voltage bias. A metal mask with aperture of 0.16 cm^2 was used during the measurement in order to determine the active area. The *J-V* curves were scanned with the rate of 50 mV/s. No pre-biasing was applied prior to the measurements. External quantum efficiency (EQE) measurement was carried out by using IQE200B (Oriel).

Quantification of the QFLS in partial cell stacks

To calculate the quasi-Fermi level splitting, we can use the Shockley-Queisser equation which links the radiative recombination density of free charges (J_{rad}) with the chemical potential per free electron-hole pair (μ) or the quasi-Fermi level splitting (QFLS) in the active material.[141, 438]

$$J_{\mathrm{rad}} = J_{0,\mathrm{rad}} \exp\left(\mu/k_{\mathrm{B}}T\right) \qquad \text{(eq. 1)}$$

Here, $J_{0,\mathrm{rad}}$ is the radiative thermal recombination current density in the dark, k_{B} the Boltzmann constant and T the temperature. We note that equation 2 is a simplification of Würfel's generalized Planck law which is only valid for a QFLS that is a few $k_{\mathrm{B}}T$ smaller that the bandgap $\mu < E_{\mathrm{G}} - 3k_{\mathrm{B}}T$. If radiative recombination comes only from free charges, the radiative recombination current is identical to the photoluminescene yield times the elementary charge, that is $J_{\mathrm{rad}} = \phi_{\mathrm{PL}} \cdot e$. Moreover, we can define the photoluminescence quantum yield (PLQY) as the ratio of radiative to total recombination ($J_{\mathrm{R,tot}}$), where the latter is identical to the generation current density (J_{G}) under open-circuit conditions (V_{OC}):

$$\mathrm{PLQY} = \frac{J_{\mathrm{rad}}}{J_{\mathrm{R,tot}}} = \frac{J_{\mathrm{rad}}}{J_{\mathrm{G}}} \qquad \text{(eq. 2)}$$

Therefore, we can relate the QFLS to the measured PLQY in the following way

$$\mu = k_B T \ln (\mathrm{PLQY} * \frac{J_G}{J_{0,rad}}) \quad \text{(eq. 3)}$$

We also note that equations 2 and 4 are only valid if the spectral dependence of J_{rad} is identical to $J_{0,rad}$, meaning recombination goes through the same channels regardless of the QFLS.
In order to quantify the intensity dependence of the QFLS, we consider the following points. Firstly, equation 4 shows that the QFLS depends on the temperature. We note that we have measured the temperature on the samples during the illumination at various light intensities using an infrared sensor. Even at an intensity of 5 equivalent suns, which is the upper limit for the results shown in the main text, we observe a negligible temperature increase on the sample (~1°C). We attribute this to the fast dissipation of heat from the rather small illumination spot area (1 cm^2) during the measurement.

Secondly, the parameters J_G and $J_{0,rad}$ were obtained in the following way: The generation current density J_G was approximated with the short-circuit current density of the complete solar cell. Similarly, the $J_{0,rad}$ was estimated by integrating the overlap of the external quantum efficiency of the device (EQE) with the black body spectrum ϕ_{BB} at 300 K over the energy.

$$J_{0,rad} = \int \mathrm{EQE}\, \phi_{BB}\, d\epsilon \quad \text{(eq. 4)}$$

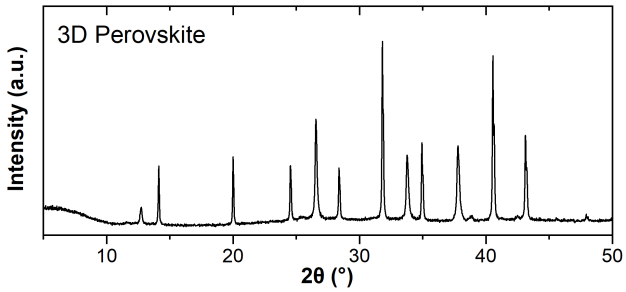

Figure B.1 XRD patterns of 3D perovskite films as the control.

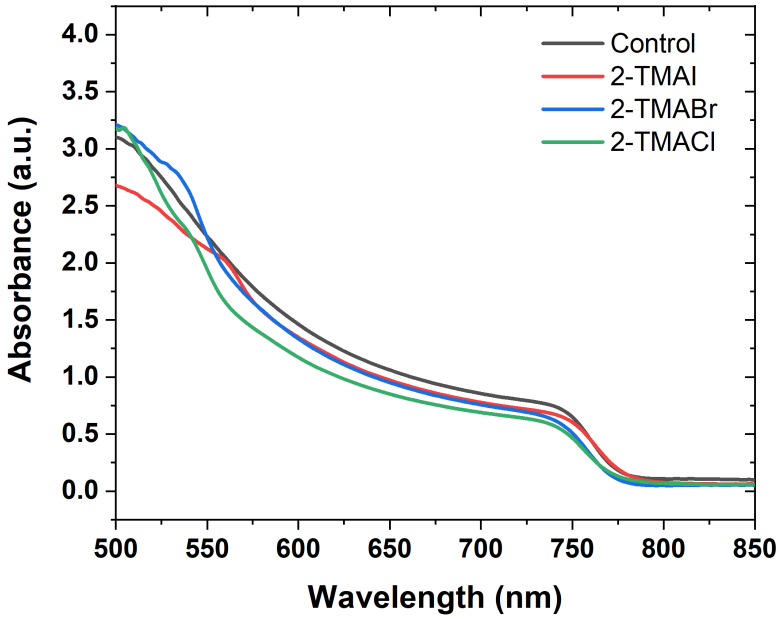

Figure B.2 UV-Vis absorption spectra of 2D/3D perovskite thin films based on 2-TMAI, 2-TMABr, and 2-TMACl, and 3D control.

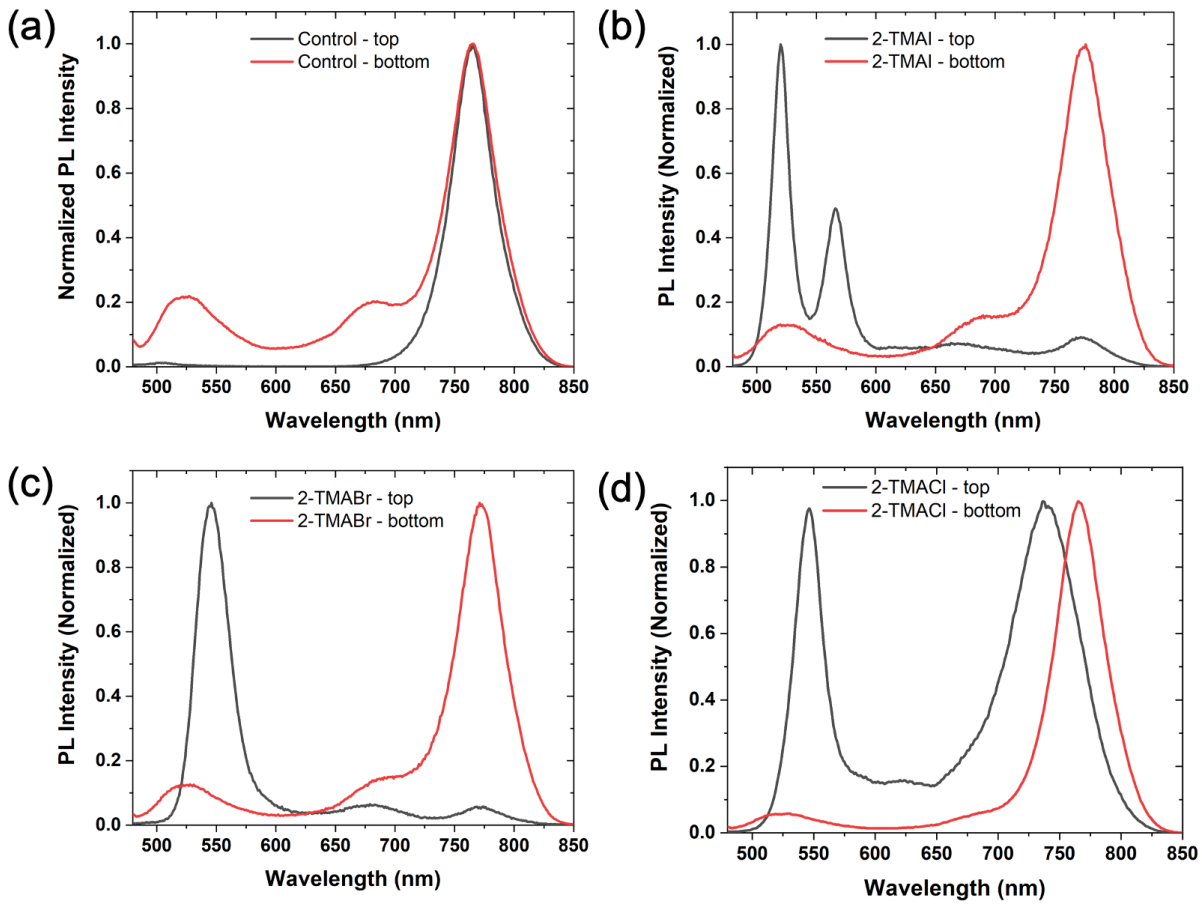

Figure B.3 Photoluminescence spectra of (a) the 3D control film and 2D/3D films employing (b) 2-TMAI, (c) 2-TMABr, and (d) 2-TMACl upon top (2D perovskite side) and bottom side (3D perovskite side) excitation exciting at 450 nm.

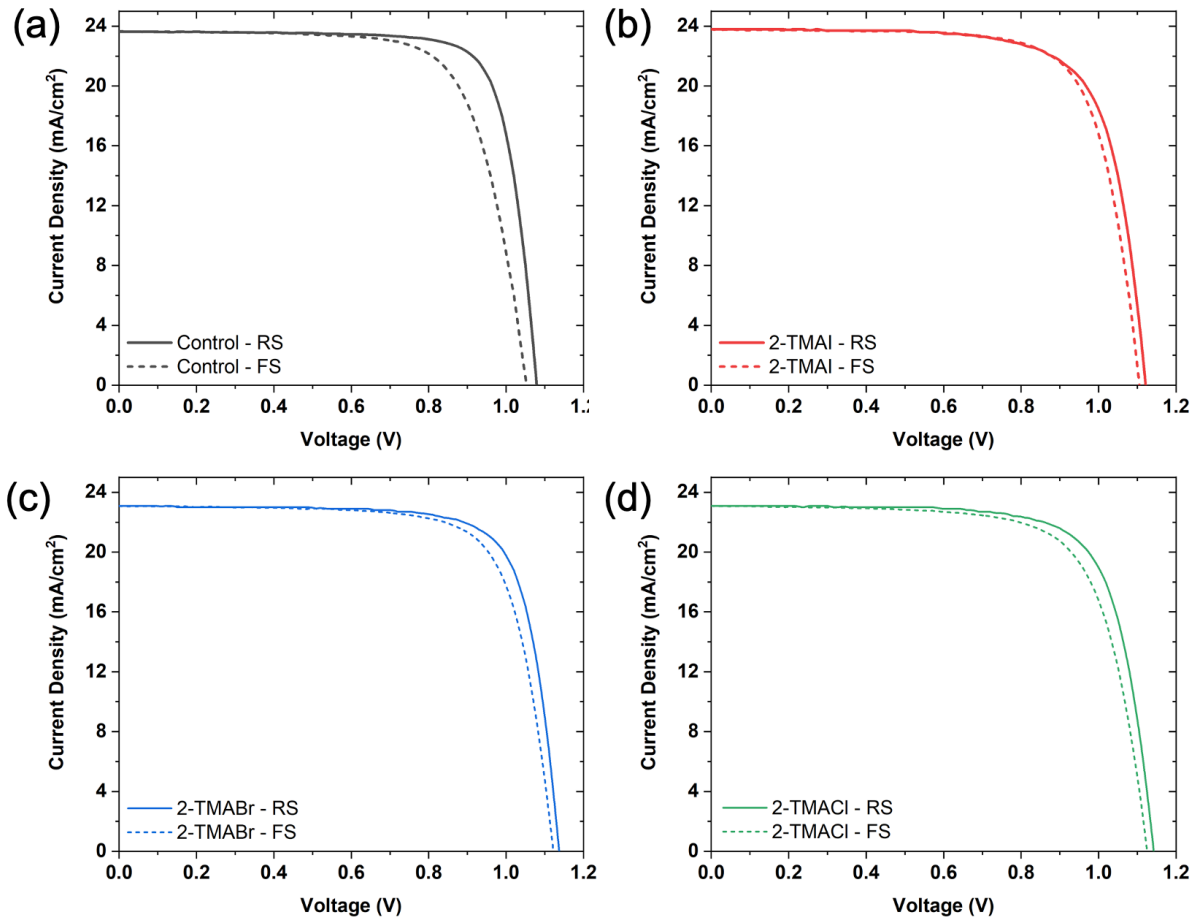

Figure B.4 Hysteresis measurement between reverse scan (RS) and forward scan (FS) of (a) the 3D control device and 2D/3D PSCs employing (b) 2-TMAI, (c) 2-TMABr, and (d) 2-TMAI.

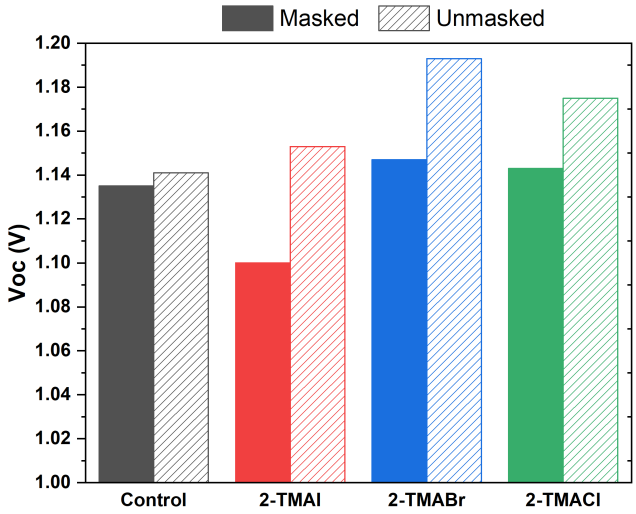

Figure B.5 Comparison of the V_{OC} measurements with and without metal mask of the 3D control PSC and 2D/3D PSCs employing 2-TMAI, 2-TMABr, and 2-TMACl cations.

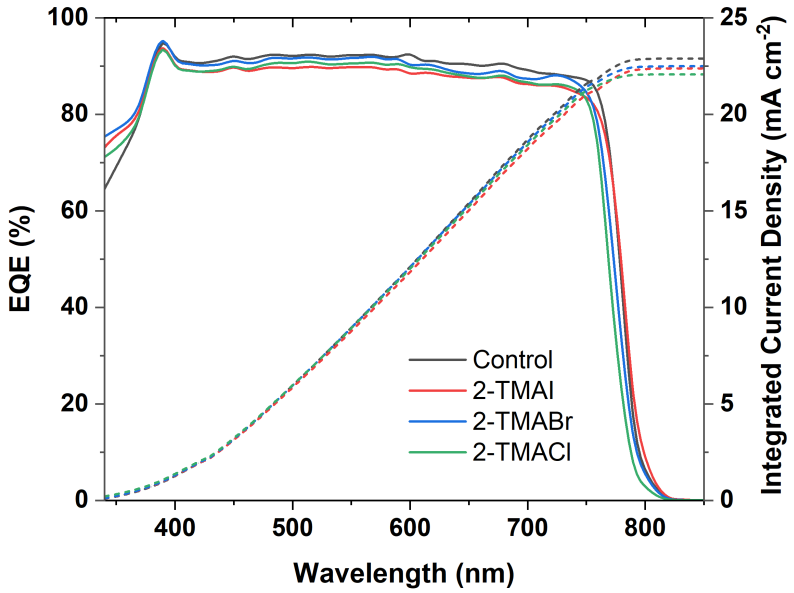

Figure B.6 External quantum efficiency (EQE) of 2D/3D PSCs based on 2-TMAI, 2-TMABr, and 2-TMACl, and 3D control.

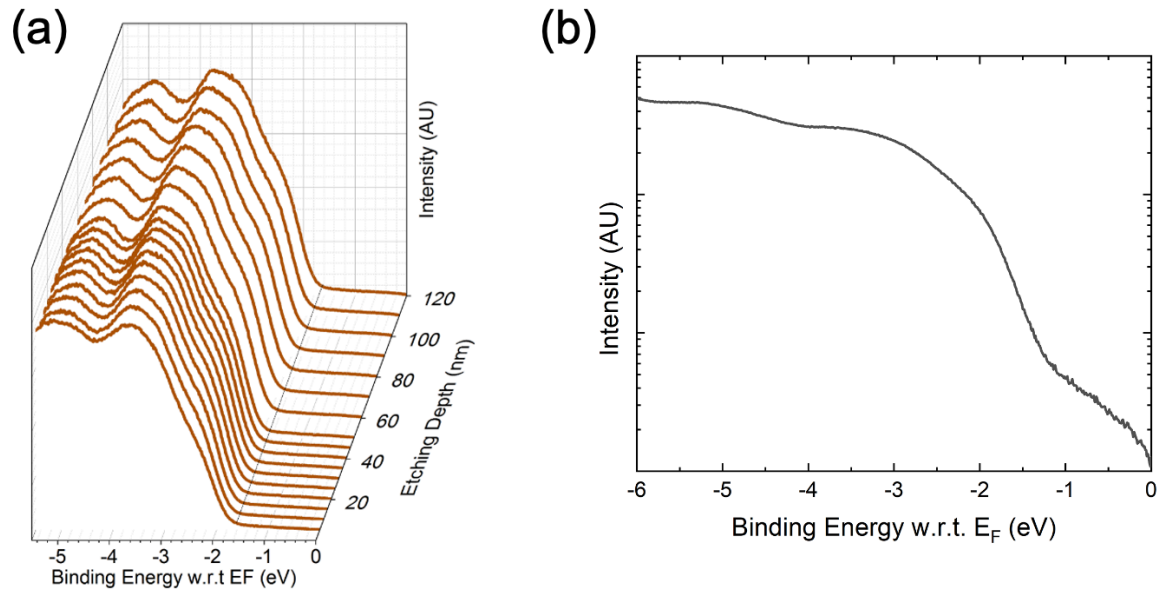

Figure B.7 UPS spectra of reference 3D sample (a) etched under identical conditions with the 2D/3D perovskite films and (b) without etching.

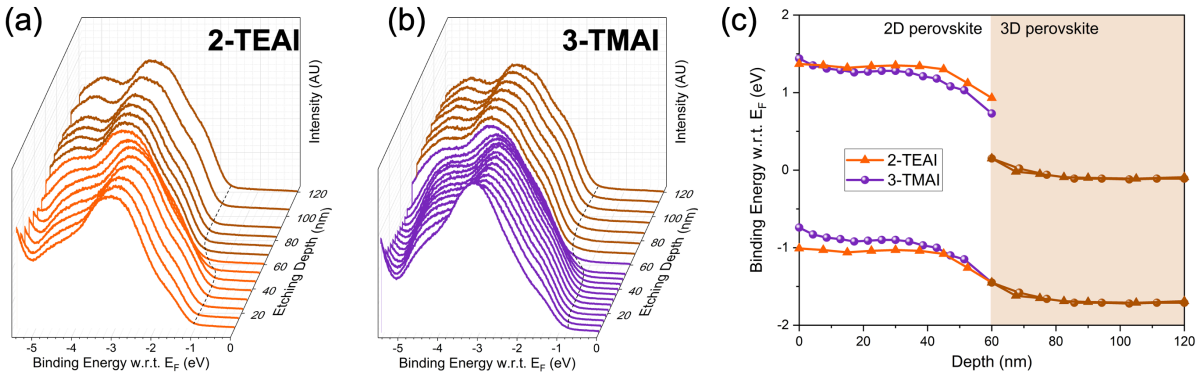

Figure B.8 UPS depth measurement of (a) 2-TEAI and (b) 3-TMAI-based 2D/3D perovskite interface. Measured UPS spectra of 2-TEAI and 3-TMAI 2D/3D perovskite. (c) The corresponding energetic level diagrams of 3-TMAI and 2-TEAI with the 3D perovskite layer.

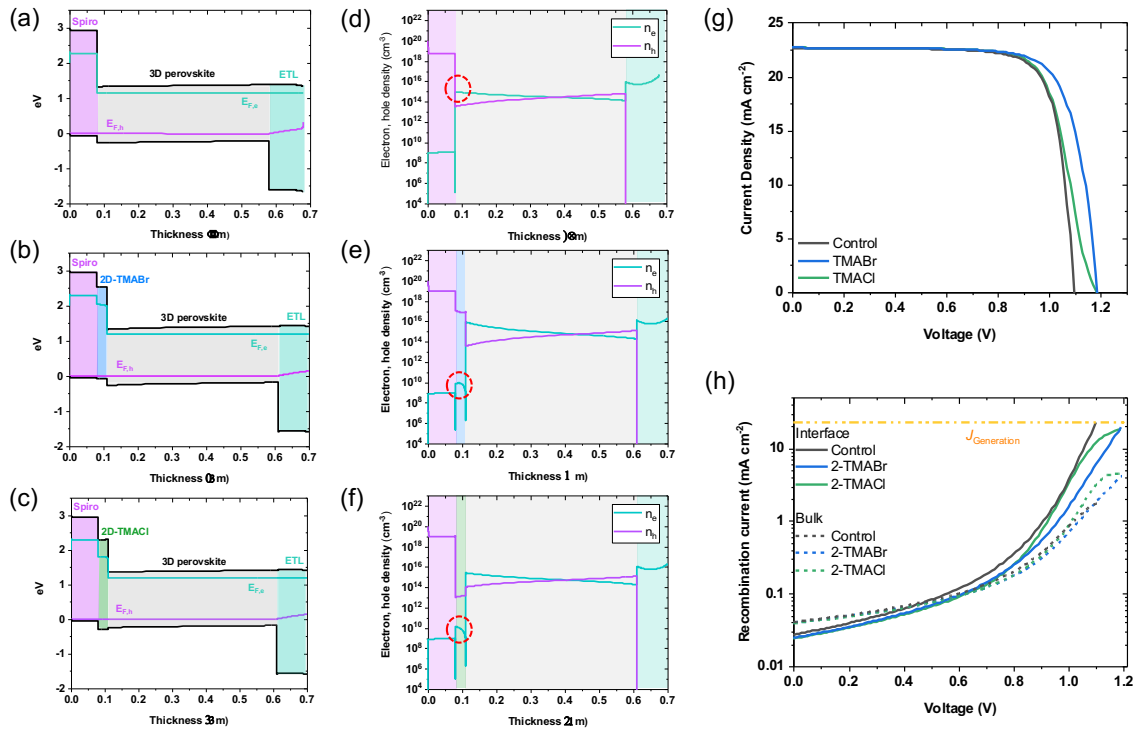

Figure B.9 Drift-diffusion simulation for different system investigate in this work. (a) Simulated band structure of the 3D perovskite device as the control, (b) the 2D/3D system implementing 2-TMABr as cation, and (c) the 2D/3D system implementing 2-TMACl. Notably, in the image, the thickness of the transport layer is artificially reduced compared to the true simulation values, in order to better visualize the perovskite interfaces. (d)-(f) Electron and hole density in the different layers of the device for the corresponding three systems in (a)-(c). (g),(h) Drift diffusion simulation *J-V* for the system depicted in (a)-(c).

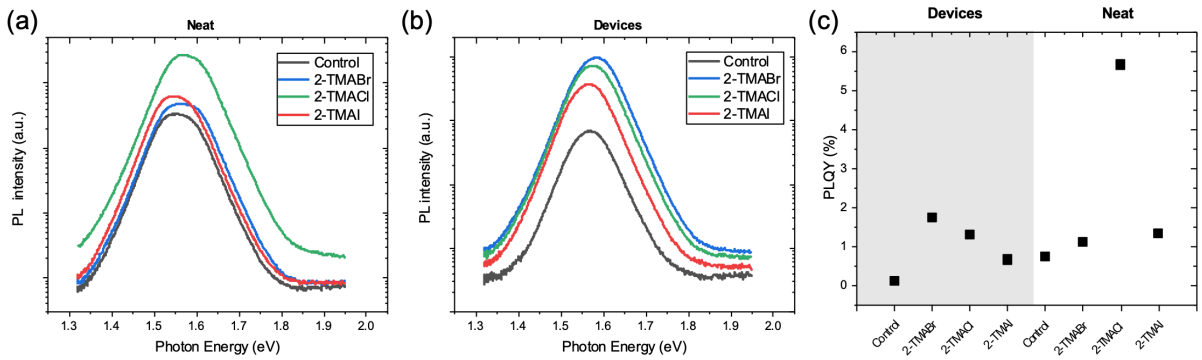

Figure B.10 Photoluminescence quantum yield (PLQY) analysis of the neat perovskite materials and solar cells. (a) PL spectra of neat perovskite materials. (b) PL spectra of perovskite solar cells devices. (c) PLQY of neat perovskite materials and solar cells devices.

Table B.1 Statistics of the photovoltaics parameters of 3D control and 2D/3D PSCs based on 2-TMAI, 2-TMABr, and 2-TMACl over 74 devices.

	V_{OC} (V)	J_{SC} (mA cm^{-2})	*FF*	PCE (%)
2-TMAI	1.09 ± 0.01	23.9 ± 0.3	0.75 ± 0.01	19.5 ± 0.2
2-TMABr	1.13 ± 0.02	23.1 ± 0.2	0.76 ± 0.01	19.9 ± 0.4
2-TMACl	1.14 ± 0.01	23.0 ± 0.2	0.73 ± 0.02	19.1 ± 0.5
Control	1.09 ± 0.02	23.8 ± 0.2	0.77 ± 0.02	19.9 ± 0.5

Table B.2 Photovoltaics parameters of 3D control and 2D/3D PSCs based on 2-TMAI, 2-TMABr, and 2-TMACl upon the hysteresis scan.

Treatment	Scan direction	V_{OC} (V)	J_{SC} (mA cm^{-2})	*FF*	PCE (%)	Hysteresis Index
2-TMAI	Reverse	1.122	23.79	0.735	19.62	0.009
	Forward	1.105	23.79	0.739	19.44	
2-TMABr	Reverse	1.137	23.09	0.767	20.15	0.043
	Forward	1.122	23.08	0.744	19.28	
2-TMACl	Reverse	1.142	23.07	0.746	19.67	0.051
	Forward	1.125	23.09	0.719	18.67	
Control	Reverse	1.079	23.65	0.787	20.08	0.108
	Forward	1.053	23.63	0.720	17.91	

Appendix C: Supplementary Information to Chapter 5

Experimental Methods

Synthetic details

Materials

All commercially available reagents were purchased from Sigma-Aldrich, Across, Tokyo Chemical Industry Co., Ltd. (TCI), and Merck and were used without further purification, unless otherwise noted. All reactions were performed under N_2. Thin- layer chromatography (TLC) was conducted with pre-coated TLC-sheets ALUGRAM® SIL G/UV254 and visualized with UV. Flash column chromatography was performed using Silicycle P60, 40-63 µm (230-400 mesh). ^{1}H and ^{13}C NMR spectra were recorded with 400 MHz Bruker NMR spectrometer and are reported in ppm using solvents as an internal standard ($CDCl_3$ at 7.26 ppm and 77.16 ppm, for ^{1}H and ^{13}C NMR spectra respectively). Data reported as: s = singlet, d = doublet, t = triplet, m = multiplet, dd = doublet of doublets, ddd = doublet of doublet of doublets, br = broad signal, coupling constant(s) in Hz; integration. Thermogravimetric analysis (TGA) data were collected using TGA 4000 from PerkinElmer. MS were recorded on 6530 Accurate-Mass Q-TOF LC/MS (Agilent Technologies) using electrospray ionization (ESI) and atmospheric pressure photoionization (APPI) techniques or Axima-CFR plus (Shimadzu) using matrix-assisted laser desorption/ionization (MALDI) technique.

General synthetic scheme

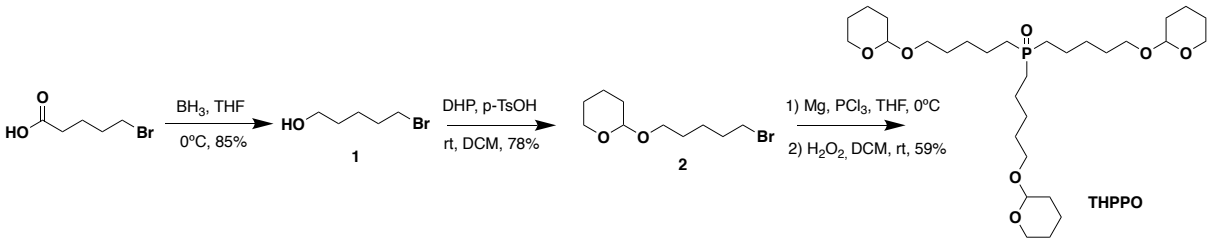

Scheme C.1 Synthetic route for tris(5-((tetrahydro-2*H*-pyran-2-yl)oxy)pentyl)phosphine oxide, **THPPO**.

Synthetic methods and procedures

5-bromopentan-1-ol; **1**. To a solution of 5-bromopentanoic acid (2 g, 11.0 mmol) in THF (15 mL) borane tetrahydrofuran complex solution (1 M, 13 mL, 13 mmol) was added at 0 °C under inert atmosphere. The mixture was stirred at rt for 3 h. Then, water/THF mixture (1:1, 20 mL) were added to the resulting mixture to quench reaction. The aqueous layer was extracted with diethyl ether (20 mL x 3), then combined organic layers were concentrated to give 1.57 g (9.38 mmol, 85 %) 5-bromopentan-1-ol **1** as a pale liquid. ^{1}H NMR (400 MHz, $CDCl_3$, δ): 3.66 (t, J = 6.4 Hz, 2H), 3.43 (t, J = 6.7 Hz, 2H), 1.95 – 1.86 (m, 2H), 1.64 – 1.49 (m, 4H, -CH_2). ^{13}C NMR (100 MHz, $CDCl_3$, δ): 62.55, 33.74, 32.51, 31.77, 23.45. HRMS (ESI) m/z: [M^+] calcd for $C_5H_{11}OBr$, 166.00, found, 165.99.

2-((5-bromopentyl)oxy)tetrahydro-2H-pyran; **2**. A solution of the 5-bromopentan-1-ol **1** (1.2 g, 7.18 mmol), 3,4-dihydro-2*H*-pyran (1.0 mL, 10.9 mmol) and p-toluenesulfonic acid mono hydrate (13.6 mg, 0.07 mmol) in dichloromethane (10 mL) was stirred at rt for 3 h. After addition of diethyl ether (12 mL), washed with saturated $NaHCO_3$(*aq*) (15 mL) and brine solution (15 mL). The combined organic layers were dried with Na_2SO_4, filtered and concentrated under reduced pressure. The resulting residue was purified by silica gel column chromatography (1:9 EtOAc:hexane) to yield **2** (1.4 g, 5.60 mmol, 78 %) as a colorless oil. ^{1}H NMR (400 MHz, $CDCl_3$, δ): 4.59 (dd, J = 4.6, 2.7 Hz, 1H), 3.91 – 3.85 (m, 1H), 3.77 (dt, J = 9.7, 6.5 Hz, 1H), 3.55 – 3.49 (m, 1H), 3.48 – 3.38 (m, 3H), 1.96 – 1.49 (m, 12H). ^{13}C NMR (100 MHz, $CDCl_3$, δ): 98.93, 67.24, 62.40, 33.76, 32.64, 30.76, 28.90, 25.49, 25.01, 19.69. HRMS (ESI) m/z: [M^+] calcd for $C_{10}H_{19}BrO_2$, 250.05, found, 250.06.

tris(5-((tetrahydro-2H-pyran-2-yl)oxy)pentyl)phosphine oxide; **THPPO**. Magnesium (0.19 g, 7.94 mmol) and dry THF (4 mL) were placed under inert atmosphere and 0.5 mL a solution of the total amount of 2-((5-bromopentyl)oxy)tetrahydro-2*H*-pyran **2** (1.2 g, 4.78 mmol) in THF (4 mL) were added followed by few drops of 1,2-dibromoethane. The mixture was cooled to 0 °C and remaining portion of the 2-((5-bromopentyl)oxy)tetrahydro-2*H*-pyran was added dropwise. The reaction mixture was stirred at rt for 2 h, then, it was cooled to 0 °C and a solution of PCl_3 (0.08 mL, 0.96 mmol) in THF (1 mL) was added over 10 min. After the mixture was stirred at rt overnight, saturated aqueous NH_4Cl (2 mL) was added. The solvent was removed under reduced pressure. The crude product was dissolved in dichloromethane (10 mL) and H_2O_2 (0.2 mL, 30% (w/w) in H_2O) was added. The solution was stirred for 1h, and 10 mL of water was added. Then, the phases extracted with DCM and sat. $NaCO_3$ solution. The solvent was removed in vacuo and

the residue was purified by silica gel column chromatography (1:9 MeOH:DCM) to yield to yield **THPPO** as a yellow oil (1.58 g, 59% yield). ^{1}H NMR (400 MHz, $CDCl_3$, δ): 4.57 (t, J = 3.7 Hz, 3H), 3.87 (ddd, J = 10.9, 7.3, 3.4 Hz, 3H), 3.76 (dt, J = 9.6, 6.6 Hz, 3H), 3.51 (ddd, J = 10.7, 5.7, 3.3 Hz, 3H), 3.40 (dt, J = 9.6, 6.3 Hz, 3H), 1.88 – 1.79 (m, 3H), 1.76 – 1.45 (m, 39H). ^{13}C NMR (100 MHz, $CDCl_3$, δ): 98.98, 67.25, 62.49, 30.77, 29.34, 27.92, 27.56, 25.47, 21.64, 19.75. ^{31}P NMR (300 MHz, $CDCl_3$, δ): 46.76. HRMS (ESI) m/z: $[M+Na]^+$ calcd for $C_{30}H_{57}O_7P$, 583.37, found, 583.38.

Perovskite thin-films and solar cells fabrication

Fluorine-doped tin oxide coated glass (FTO, Nippon Sheet Glass) was used as the conducting electrode. Prior to each use, FTO glass was patterned by chemical etching using Zn powder and aqueous HCl solution (3.0 M), then it was cleaned with detergent (Helmanex), deionized water, acetone, and isopropanol in an ultrasonic bath. A 30 nm-thick compact-TiO_2 layer was used as the electron transporting material and deposited on top of FTO glass via spray pyrolysis of titanium diisopropoxide bis(acetylacetonate) (Sigma Aldrich, diluted to 1:15 v/v in isopropanol) at 450°C. A 100 nm-thick mesoporous TiO_2 layer was then deposited by spin coating the ethanolic solution (1:8 v/v) of TiO_2 paste (GreatCellSolar, 30NR-D) at 5000 rpm for 20 s, followed by heating at 10 min and sintering at 500 °C for 20 min. A 20 nm-thick passivating tin oxide was spin coated on top of mesoporous TiO_2 layer by dissolving tin (IV) chloride (Acros) solution (12 µL in 988 µL water) at 3000 rpm for 30 s, followed by annealing at 100 °C for 10 min and 190 °C for 1 h. UV-ozone treatment was carried out for 15 minutes before perovskite layer deposition. A triple cation-based perovskite precursor solution $[(FAPbI_3)_{0.87}(MAPbBr_3)_{0.13}]_{0.92}(CsPbI_3)_{0.08}$ with a concentration of 1.3 M was prepared by mixing FAI (GreatCellSolar), MABr (GreatCellSolar), CsI (ABCR), PbI_2 (TCI), and $PbBr_2$ (TCI) in DMF and DMSO (0.78:0.22 v/v). An excess concentration of PbI_2 was used in the precursor solution (PbI_2:FAI= 1.05:1). The perovskite solution was then deposited on top of the prepared substrates at 2000 rpm for 12 s and 5000 rpm for 30 s. Chlorobenzene was dropped at 15 s before the end of the spin coating process. Perovskite film was annealed inside the glovebox for 60 minutes. A various concentration of THPPO solution (0.005, 0.010, 0.020, and 0.030 M) in chlorobenzene was deposited on top of the perovskite films at 4000 rpm for 30 s. For the HTL-based device, 2,2′,7,7′-tetrakis-(*N*,*N*-di-p-methoxyphenyl-amine)-9,9′-spirobifluorene (spiro-OMeTAD) is incorporated as the HTL. spiro-OMeTAD (Merck) with the concentration of 0.06 M was dissolved chlorobenzene. For 1 mL solution, it is doped with 18.57 µL of Li-bis (trifluoromethanesulphonyl) imide (Aldrich) from the stock solution (196 mg in 379 µL acetonitrile), 13.69 µL of FK 209 Co(III) TFSI (GreatCellSolar) from the stock solution (99 mg in

263 µL acetonitrile), and 31.28 µL of 4-*tert*-butylpyridine (Sigma-Aldrich). For a complete PSC device, a 70 nm-thick gold counter electrode was deposited by physical vapor deposition under high vacuum condition.

Device characterization

The current density-voltage (*J-V*) characteristics were measured under xenon lamp solar simulator (450 W, Oriel Sol3A, AAA class). The light intensity was calibrated to 1 sun illumination by using a Si reference equipped with an IR-cutoff (KG5) filter. The *J-V* curves then recorded with a digital source meter (Keithley 2400) by applying an external voltage bias and measuring the current response. The active area was defined by using a black metal mask with the aperture of 0.16 cm^2. The *J-V* curves were scanned under the rate of 50 mV/s without any preconditioning. External quantum efficiency (EQE) spectra were recorded using IQE200B (Oriel). Long-term stability test was carried out under continuous 1 sun illumination and maximum power point (MPP) tracking with LED lamps in an inert (Ar) atmosphere without any encapsulation.

Thin-films characterization

UV-VIS absorption

The absorption spectra of the thin films were measured using an ultraviolet, visible, near-infrared spectrophotometer (PerkinElmer Lambda 950S).

Photoluminescence

Steady-state photoluminescence spectra of the perovskite thin films were measured using Fluorolog3-22 spectrofluorometer by exciting the films at 550 nm. Transient photoluminescence spectra were measured and recorded by a time-correlated single photon counting system (Nanofinder 30) at the excitation wavelength of 480 nm. The detection wavelength was set on 763-770 nm.

X-ray Diffraction (XRD)

XRD measurements were performed on Bruker D8 Advance diffractometer and non-monochromated Cu Kα radiation at the ambient atmosphere and temperature.

Scanning Electron Microscopy (SEM)

Cross-section and top surface SEM images were recorded by in-lens detector of FEI Teneo scanning electron microscope at the accelerating voltage of 3 kV and 5 kV.

Grazing incidence wide angle X-ray scattering (GIWAXS) measurements

GIWAXS measurements were performed at SPring-8 on beamline BL19B2. The X-ray irradiation with an energy of 12.39 keV (λ = 1 Å) was used on the sample at a fixed incident angle on the order of 0.12° through a Huber diffractometer. A two-dimensional image detector (Pilatus 300K) were used to record the 2D- GIWAXS patterns.

Ultraviolet photoelectron spectroscopy (UPS) measurements

The ultraviolet photoelectron spectroscopy (UPS) were measured using He-I source ($h\nu$ = 21.22 eV) (AXIS Nova, Kratos Analytical Ltd., UK) in order to determine the valence band energy and Fermi-level. Gold (Au) which is in electrical contact with the sample is used as a reference for the Fermi-level of the samples.

X-ray photoelectron spectroscopy (XPS)

The X-ray photoelectron spectroscopy (XPS) measurements were performed using VersaProbe II (Physical Electronics Inc) with a monochromator and Al-Kα source of 1486.6 eV. The spectrum was referenced using the C-C bound component of the adventitious carbon

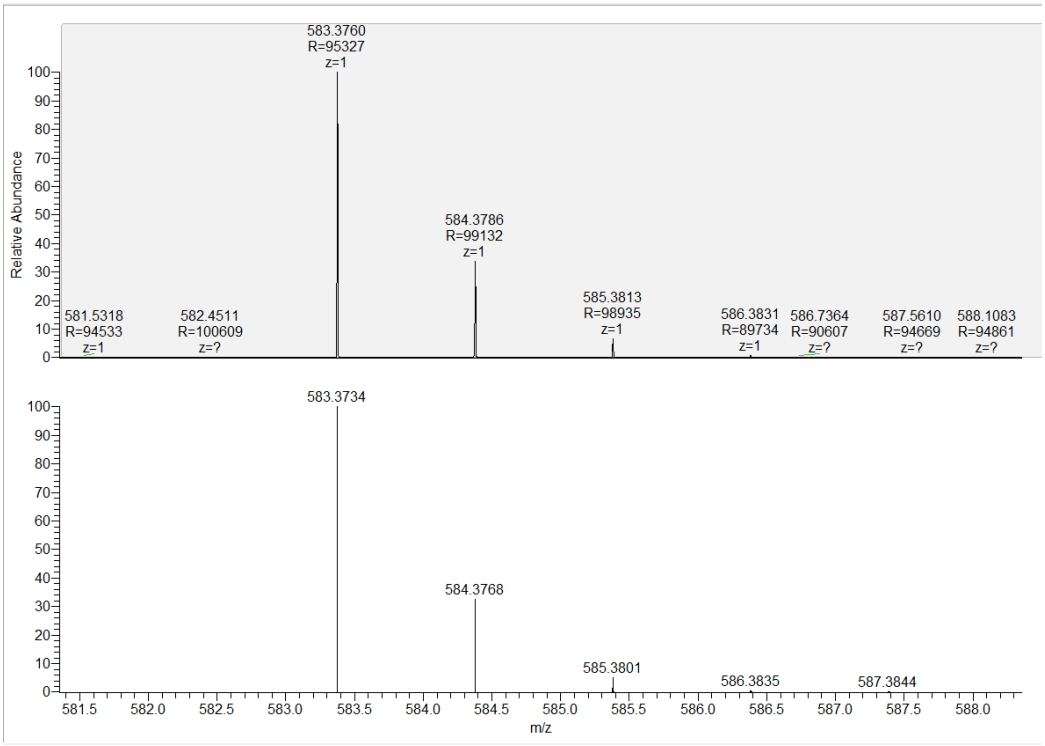

Figure C.1 ESI-QTOF-MS spectra in wide and narrow mass ranges of **THPPO**.

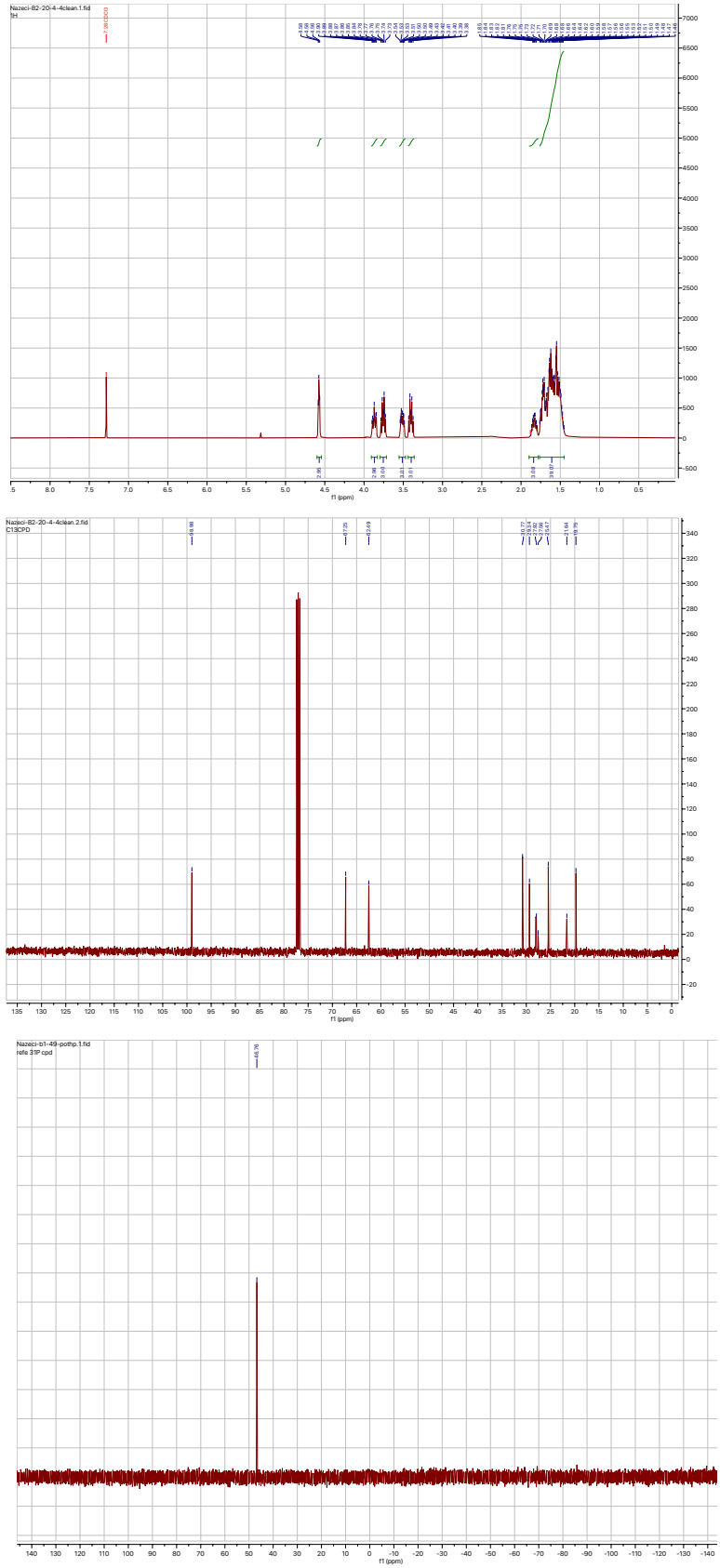

Figure C.2 ^{1}H, ^{13}C and ^{31}P NMR ($CDCl_3$) spectrum of **THPPO**.

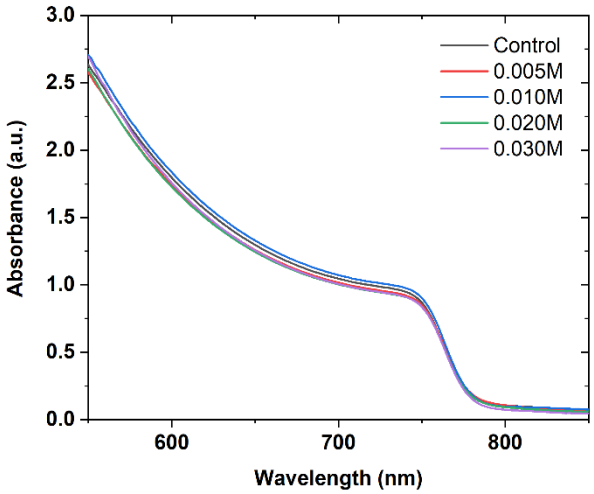

Figure C.3 Absorption spectra of control and **THPPO**-treated perovskite thin films.

Table C.1 Bi-exponential decay function, $y = y_0 + A_1 e^{-x/t_1} + A_2 e^{-x/t_2}$ fitted PL lifetime curves of perovskite films.

THPPO Concentration (M)	**t_1 (ns)**	**t_2 (ns)**
Control	12.6	96.4
0.005	18.0	146.3
0.010	19.6	184.6
0.020	19.4	193.4
0.030	19.9	192.3

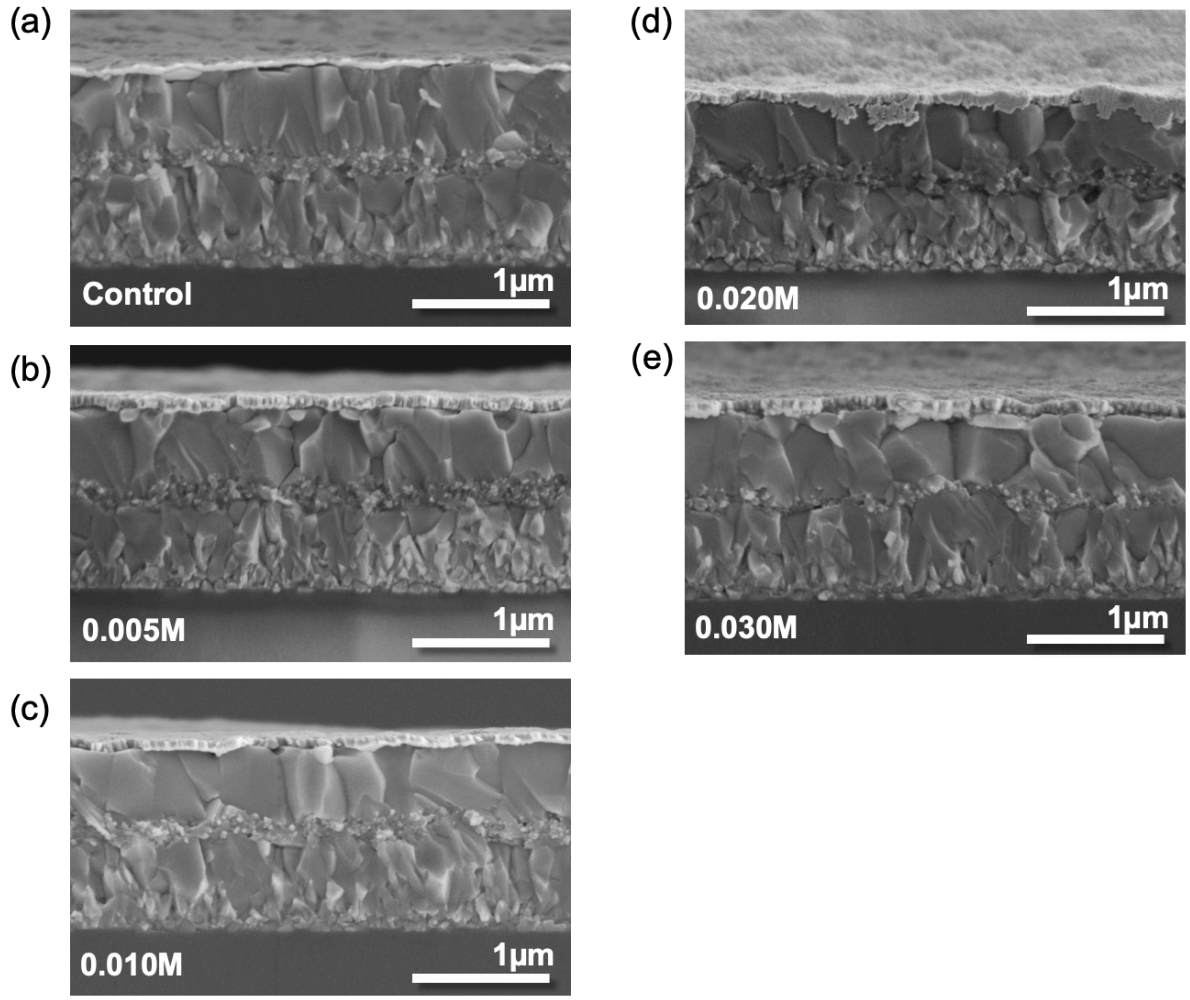

Figure C.4 Cross-sectional SEM images of control device and HTL-free devices employing **THPPO** with various concentrations (FTO/compact TiO_2/mesoporous TiO_2/passivated SnO_2/perovskite/THPPO/Au)

Table C.2 Quantitative analysis of Pb 4f spectra presenting the ratio of Pb^0 in perovskite films with various concentrations of **THPPO**.

THPPO Concentration (M)	**Ratio of Pb^0 out of the total Pb (%]**
Control	10.16
0.005	5.75
0.010	5.75
0.020	6.34
0.030	6.50

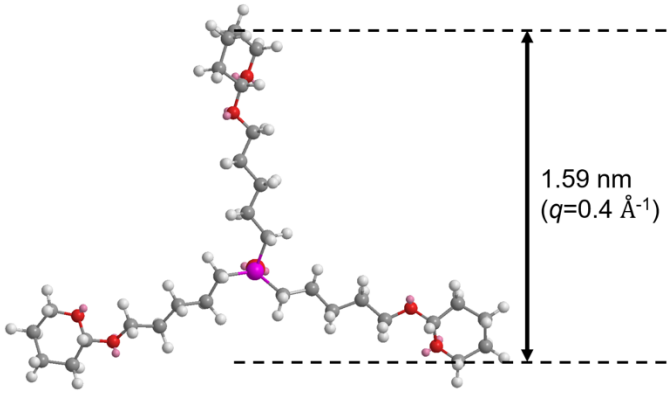

Figure C.5 Molecular modeling of **THPPO** by molecular mechanics force field (MM2, Chem3D) method with the condition of molecular dynamics at 2.0 fs step interval and heating/cooling rate of 1.0 Kcal/atom/ps at 300 K.

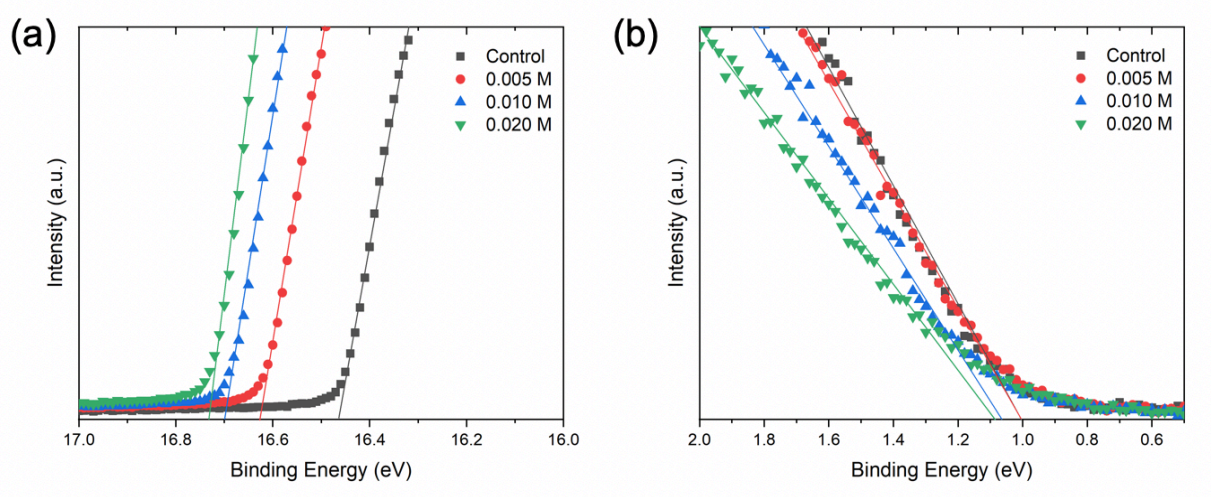

Figure C.6 Ultraviolet photoelectron spectroscopy (UPS) spectra of control perovskite film and **THPPO** passivated perovskite films showing (a) secondary cut-off and (b) onset.

Table C.3 PV parameters of the champions cells of PSCs employing **THPPO** as a passivation layer with various conditions.

THPPO Concentration (M)	***VOC*** **(V)**	***JSC*** **(mA cm^{-2})**	***FF***	**PCE (%)**
Control	0.610	22.53	0.425	5.84
0.005	0.804	23.01	0.585	10.83
0.010	0.866	23.32	0.659	13.31
0.020	0.847	22.86	0.562	10.87
0.030	0.764	22.35	0.478	8.16

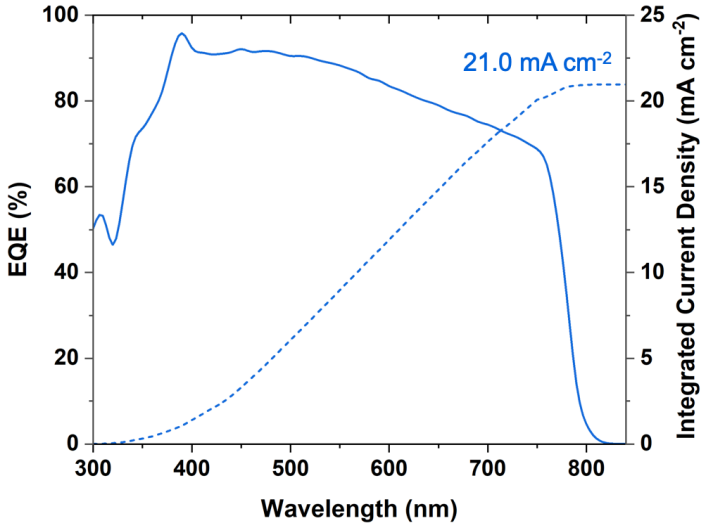

Figure C.7 EQE spectrum and the integrated J_{SC} of the **THPPO**-passivated HTL-free PSC.

Table C.4 Average values of PV parameters of 96 PSCs according to various conditions of **THPPO**.

THPPO Concentration (M)	V_{OC} **(V)**	J_{SC} **(mA cm^{-2})**	***FF***	**PCE (%)**
Control	0.64 ± 0.08	22.3 ± 0.3	0.31 ± 0.05	4.4 ± 0.9
0.005	0.80 ± 0.02	23.0 ± 0.1	0.55 ± 0.04	10.1 ± 0.7
0.010	0.84 ± 0.02	23.1 ± 0.1	0.62 ± 0.02	12.0 ± 0.4
0.020	0.81 ± 0.05	22.8 ± 0.2	0.49 ± 0.04	9.0 ± 1.0
0.030	0.80 ± 0.03	21.6 ± 1.1	0.37 ± 0.06	6.4 ± 1.2

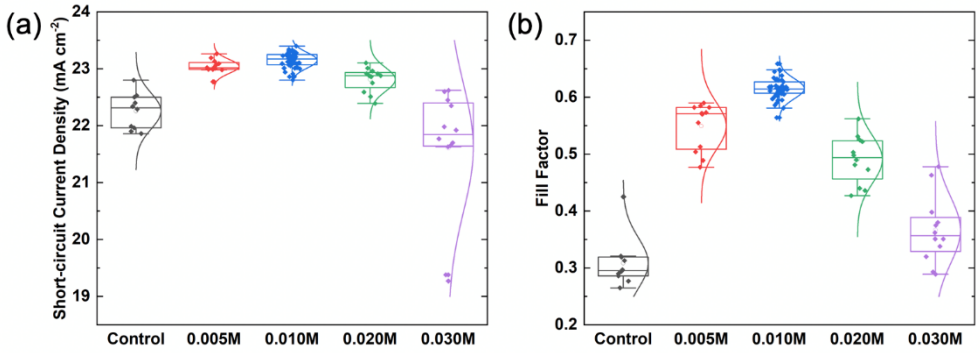

Figure C.8 Statistics of (a) short-circuit current density and (b) fill factor of HTL-free devices.

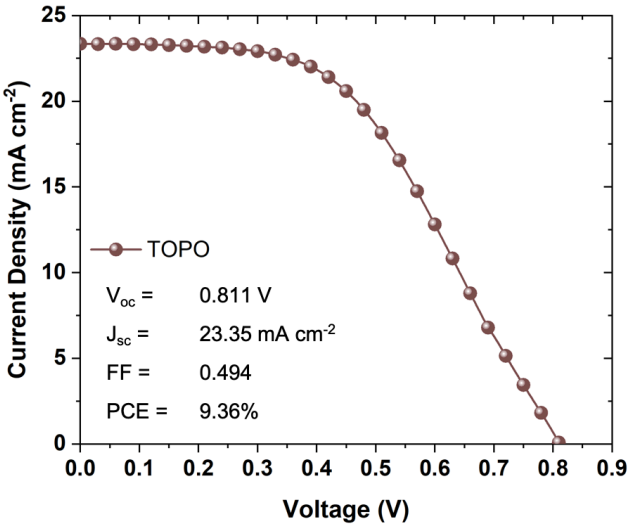

Figure C.9 *J-V* curve of the best performing HTL-free PSC using 0.010 M of trioctylphosphine oxide (TOPO) as a passivating agent.

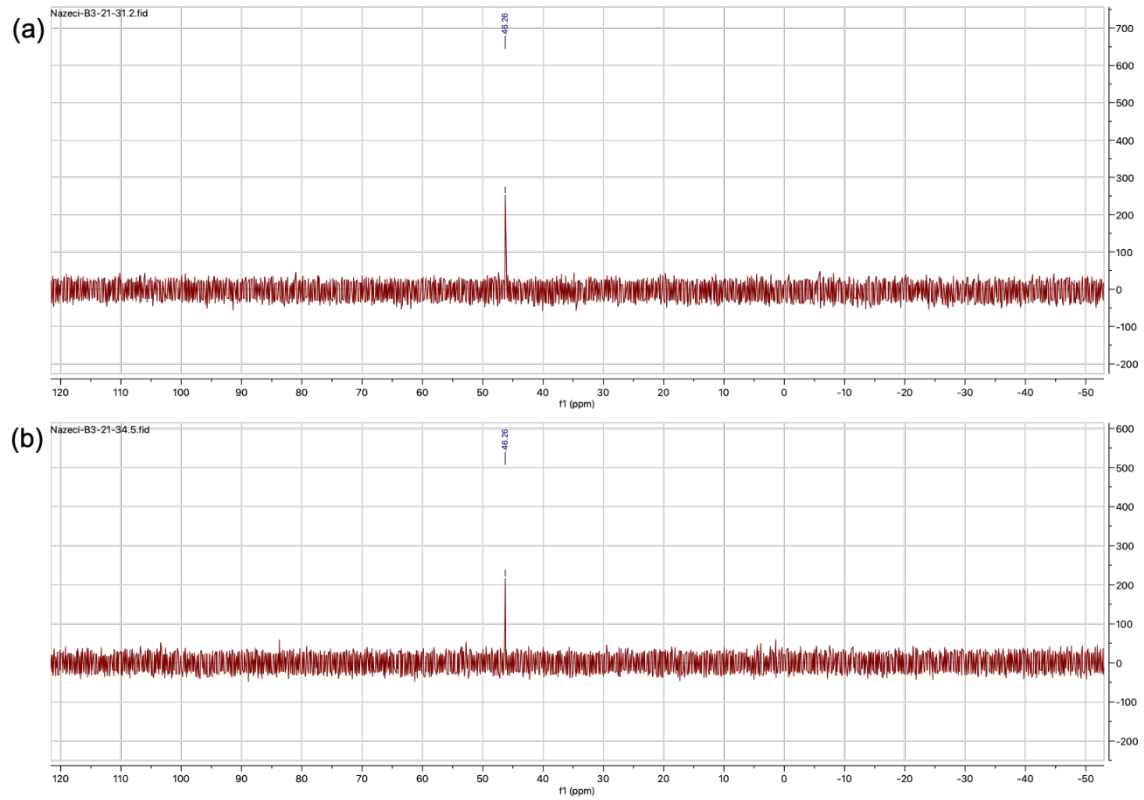

Figure C.10 ^{31}P NMR spectra of 0.030M THPPO-treated perovskite films dissolved in DMSO-d6 (a) without chlorobenzene washing and (b) with chlorobenzene washing.

We performed ^{31}P NMR spectroscopy to see the effect of chlorobenzene solvent on the THPPO layer during the deposition of spiro-OMeTAD on top of it by spin coating. Two perovskite films with 0.030M THPPO were prepared and one of them was washed with chlorobenzene by spin coating at 4000 rpm for 30 s, but the other was not washed as a control film. For the measurement, the films were dissolved in DMSO-d_6. ^{31}P NMR spectra of both specimens clearly showed a phosphorus peak at the same position (46.27 and 46.26 ppm) confirming that the passivation agent, THPPO can still remain on the perovskite film despite the deposition of spiro-OMeTAD. The presence of THPPO might be attributed to the formation of Lewis adduct, $PbI_2 \cdot$ THPPO based on a dative bond that may render it insoluble by chlorobenzene.

Table C.5 Average values of PV parameters of PSCs employing spiro-OMeTAD as an HTL.

THPPO Concentration (M)	***V*$_{OC}$ (V)**	***J*$_{SC}$ (mA cm^{-2})**	***FF***	**PCE (%)**
Control	1.059 ± 0.005	23.8 ± 0.2	0.781 ± 0.007	19.7 ± 0.2
0.010	1.106 ± 0.002	24.1 ± 0.1	0.768 ± 0.008	20.5 ± 0.2

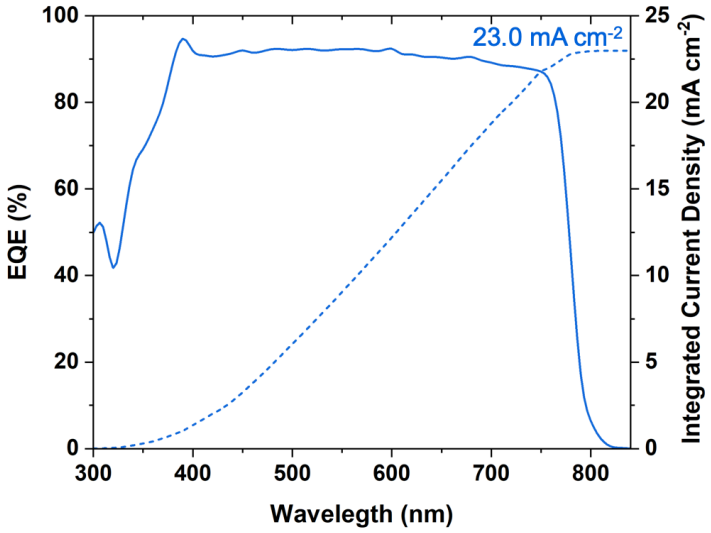

Figure C.11 EQE spectrum and the integrated J_{SC} of the **THPPO**-passivated PSC with HTL.

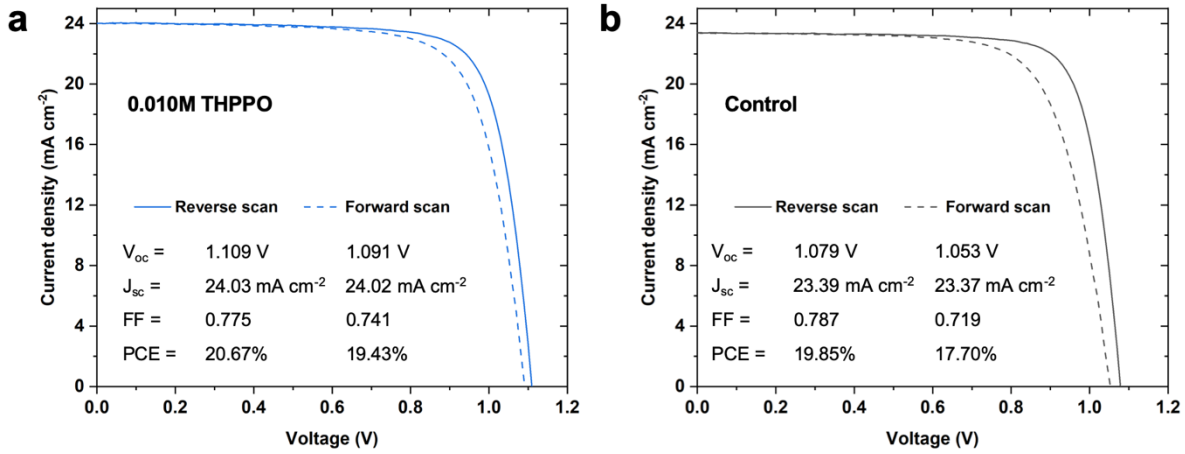

Figure C.12 *J-V* hysteresis characteristics of (a) HTL-based PSCs with 0.010M THPPO passivation and (b) control device.

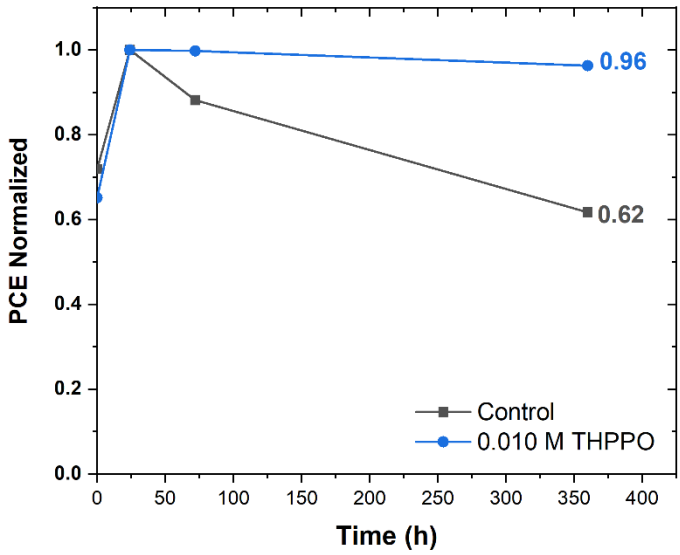

Figure C.13 Stability measurement of HTL-free devices without THPPO and with 0.010 M THPPO for 360 h. The devices have been stored under dark with relative humidity (RH) below 10%.

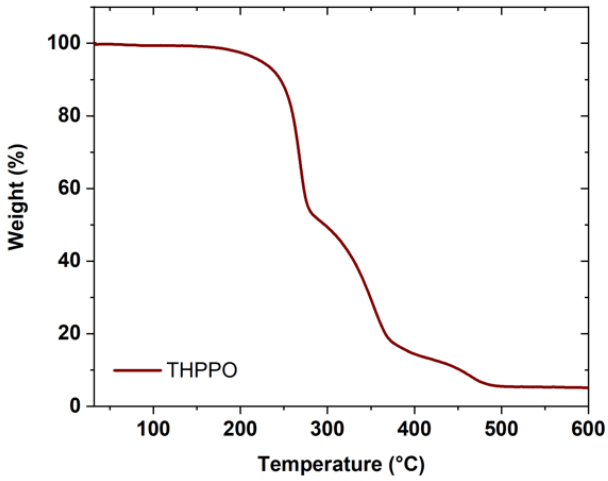

Figure C.14 Thermogravimetric analysis (TGA) of **THPPO**. The high decomposition temperature (T_d) of 251 °C was determined at the 5 % weight loss of THPPO.

Appendix D: Supplementary Information to Chapter 6

D.1 Isomeric carbazole-based hole-transporting materials: Role of linkage position on the photovoltaic performance of perovskite solar cells

Experimental Methods

Materials and characterization

All the chemical reagents were procured from commercial sources and used as received without any further purification. Solvents for reactions were distilled under nitrogen atmosphere by conventional distillation method using sodium/benzophenone, and halogenated solvents were distilled using calcium hydride as drying agent. Silica gel (230 mesh size) was used as stationary phase for column chromatography. ^{1}H NMR and ^{13}C NMR were recorded on a Bruker instrument at 500 MHz and 125 MHz respectively. Deuterated acetone (Acetone-d_6) and chloroform ($CDCl_3$) were used as solvent and the chemical shifts were calibrated using the residual peak (Acetone-d_6 at δ 2.05 and $CDCl_3$ at δ 7.26) for ^{1}H and (Acetone-d_6 at δ 206.26 and $CDCl_3$ at δ 77.0) for ^{13}C NMR spectra respectively. UV-Vis absorption spectra were recorded at room temperature in a quartz cuvette using JASCO V-600 UV-Vis spectrophotometer. Thermogravimetric analysis (TGA) was carried out using a Perkin Elmer TGA-7 instrument under nitrogen as a carrier gas. Differential pulse voltammetry experiments were performed using a CHI621C Electrochemical Analyzer (CH Instruments) with a conventional three-electrode system (a platinum disk working electrode, an auxiliary platinum wire electrode, and a non-aqueous Ag reference electrode) and supporting electrolyte of 0.1 M tetrabutylammonium hexafluorophosphate ($TBAPF_6$) in *o*-dichlorobenzene solution. All electrochemical potentials were calibrated against Fc/Fc^{+} internal standard (at 0.64 V).

Synthesis of **Car[1,3]** (1)

A mixture of 1,3,6,8-tetrabromo-9-butyl-9*H*-carbazole **4** (0.1 g, 0.19 mmol), 4-methoxy-*N*-(4-methoxyphenyl)-*N*-(4-(tributylstannyl)phenyl)aniline **5** (0.50 g, 0.84 mmol), $Pd(PPh_3)_4$ (88 mg, 0.076 mmol) and toluene (30 mL) was refluxed under nitrogen atmosphere for 24 h. After completion of reaction, the reaction mixture was allowed to room temperature and quenched by addition of water. The organic compound was extracted using dichloromethane and washed with brine solution. The combined organic layer was dried over sodium sulfate and

concentrated to get crude sample which then purified by column chromatography. Eluent: Hexane/ethyl acetate (3:1). Pale yellow solid. Yield 0.12 g (44%). ^{1}H NMR (500 MHz, $CDCl_3$): 8.27 (s, 2 H), 7.57 (d, *J* = 5.2 Hz, 4 H), 7.49 (s, 2 H), 7.34 (d, *J* = 8.5 Hz, 4 H), 7.11-7.00 (m, 16 H), 6.86 (d, *J* = 2.5 Hz, 8 H), 6.85 (d, *J* = 2.1 Hz, 16 H), 3.81 (s, 24 H), 3.73 (t, *J* = 13.3 Hz, 2 H), 1.85-1.64 (m, 4 H), 0.93 (t, *J* = 7.3 Hz, 3 H). ^{13}C NMR (125 MHz, $CDCl_3$): 155.85, 155.63, 147.91, 147.40, 141.23, 141.02, 138.99, 134.11, 132.72, 132.41, 130.01, 127.60, 126.99, 126.47, 126.21, 121.52, 120.21, 116.42, 114.73, 114.65, 55.48, 45.19, 31.90, 19.54, 13.36. HRMS (*m*/*z*, FAB$^+$): calcd for $C_{96}H_{85}N_5O_8$ 1435.6398, found 1435.6393.

Synthesis of **Car[2,3]** (2)

It was prepared from a mixture of 2,3,6,7-tetrabromo-9-butyl-9*H*-carbazole **3** (0.1 g, 0.19 mmol), 4-methoxy-*N*-(4-methoxyphenyl)-*N*-(4-(tributylstannyl)phenyl)aniline **5** (0.50 g, 0.84 mmol), $Pd(PPh_3)_4$ (88 mg, 0.076 mmol) and toluene (30 mL) by following the procedure described for **Car[1,3]**. Eluent: Hexane/Ethyl acetate (3:1). Pale Yellow solid. Yield 0.14 g (51%). ^{1}H NMR (500 MHz, Acetone-d_6): 8.20 (s, 2 H), 7.56 (s, 2 H), 7.11-7.07 (m, 8 H), 7.05-7.02 (m, 16 H), 6.97-6.87 (m, 16 H), 6.81 (d, *J* = 8.0Hz, 8 H), 4.54 (t, *J* = 7.2 Hz, 2 H), 3.79 (s, 12 H), 3.78 (s, 12 H), 1.95-1.93 (m, 2 H), 1.49 (m, 2 H), 0.95 (t, *J* = 7.5 Hz, 3 H).). ^{13}C NMR (125 MHz, Acetone-d_6): 157.07, 156.92, 148.20, 147.77, 142.23, 142.07, 141.61, 139.74, 136.57, 136.36, 133.22, 132.02, 127.28, 127.09, 122.96, 122.81, 121.56, 121.20, 115.75, 111.15, 55.90, 43.62, 32.21, 21.27, 14.44. HRMS (*m*/*z*, FAB$^+$): calcd for $C_{96}H_{85}N_5O_8$ 1435.6398, found 1435.6393.

Perovskite thin-films and solar cells fabrication

Fluorine-doped tin oxide (FTO) glass substrates (TEC-9, Nippon Sheet Glass) were used as transparent conducting electrodes. Prior to use, FTO substrates were laser-patterned and washed sonically in detergent (Helmanex), deionized water, acetone, and isopropanol (IPA) for 15 min in each solvent. The cleaned FTO substrates were treated with UV-Ozone for 20 min before TiO_2 layer deposition. A 30 nm-thick compact TiO_2 layer was then deposited on top of the cleaned substrates by spray pyrolysis at 450°C from the diluted titanium diisopropoxide bis(acetylacetonate) solution (Sigma Aldrich) in isopropanol (1:15 v/v). After cooling down to room temperature, a 100 nm-thick mesoporous TiO_2 layer was deposited by spin-coating TiO_2 paste (GreatCellSolar, 30NR-D, diluted in ethanol at 1:8 w/v ratio) at 5000 rpm for 20 s. The mesoporous TiO_2 layer was then annealed at 100°C for 10 min and 500°C for 20 min. A 20 nm-thick SnO_2 layer was spin-coated at 3000 rpm for 30 s from the aqueous $SnCl_4$ precursor (Acros, 12 µL in 988 µL water), followed by annealing at 100°C for 10 min and 190°C for 60 min. The

substrates were treated with UV-Ozone for 20 min prior to the deposition of SnO_2 and perovskite layer. Perovskite precursor was prepared by mixing of FAI (GreatCellSolar), MABr (GreatCellSolar), CsI (ABCR), PbI_2 (TCI), and $PbBr_2$ (TCI) in DMF and DMSO (0.78:0.22 v/v), resulting in 1.3 M triple cation perovskite solution with the composition of $[(FAPbI_3)_{0.87}(MAPbBr_3)_{0.13}]_{0.92}(CsPbI_3)_{0.08}$. An excess PbI_2 of 5% in respect to FAI (PbI_2:FAI = 1.05:1) was used in the precursor solution. To form the perovskite layer, 40µL of perovskite precursor was spin-coated at 2000 rpm for 12 s and 5000 rpm for 30 s. 125µL ethyl acetate as anti-solvent was dispensed 15 s before the end of spin-coating process. The deposited perovskite film was then annealed at 100°C for 60 min. The hole-transporting layer (HTL) was deposited by spin-coating the hole-transporting materials (HTMs) solutions on top of perovskite layer at 4000 rpm for 30s. For spiro-OMeTAD based PSCs, 60 mM solution of 2,2′,7,7′-tetrakis-(*N,N*-di-*p*-methoxyphenyl-amine)-9,9′-spirobifluorene (spiro-OMeTAD, Merck) was prepared in chlorobenzene and doped using Li-bis (trifluoromethanesulphonyl) imide (Li-TFSI, Aldrich), FK-209 Co(III) TFSI (GreatCellSolar), and 4-*tert*-butylpyridine (tBP, Sigma-Aldrich). The dopant ratio used was Li-TFSI:tBP:FK209 = 0.5:3.3:0.055 (mol/mol spiro-OMeTAD). For the carbazole-based HTMs (**Car[1,3]** and **Car[2,3]**), a 36 mM HTM solution was prepared in chlorobenzene with the dopant ratio of 0.5:3.3:0.03 (Li-TFSI:tBP:FK209 in mol/mol HTM). Finally, a gold electrode with the thickness of 70 nm was deposited on top of HTM by physical vapor deposition process.

Photovoltaic characterization

Current density-voltage (*J-V*) characteristics were obtained by scanning the current response of the solar cells at the applied bias under 1-sun AM1.5G illumination generated by xenon lamp solar simulator (450 W, Oriel Sol3A, AAA class) with the scan rate of 50 mV/s. The current response was recorded with a Keithley 2400 source meter. Prior to each use, the light intensity was calibrated by using Si reference with an IR-cutoff (KG5) filter. The active area was defined by using a black metal mask with the aperture of 16 mm^2. The incident photon to current conversion efficiency (IPCE) spectra were recorded using IQE200B (Oriel). Long-term stability tests under continuous light exposure were performed under 1-sun illumination generated by LED lamps and an inert (N_2) atmosphere without any encapsulation. The PSCs were tracked at their maximum power point (MPP) for the stability measurement.

Photoluminescence (PL)

PL spectra of the perovskite thin-films were acquired using Fluorolog, Horiba Jobin Yvon fluorescence spectrometer upon excitation at 625 nm for the steady-state PL measurement and 635 nm for the transient PL measurement.

Scanning electron miscroscopy (SEM)

The top-view and cross-section images were obtained using FEI Teneo scanning electron microscope. The measurements were performed under the accelerating voltage of 2-3kV. In lens detector was used to acquire the cross-section and top-view images.

Hole-drift mobility

Drift mobility measurement of **Car[1,3]** and **Car[2,3]** were carried out using the xerographic time-of-flight (XTOF) technique. Samples are prepared under drop casting technique on Al coated glass plates using THF as solvent, sample thickness was 2.0–2.3 μm. The corona charging used to create electric field in the HTM layer. Charge carriers were generated at the layer surface by illumination with pulses of nitrogen laser (pulse duration was 1 ns, wavelength 337 nm). The small charge transients were measured with the wide frequency band electrometer and Tektronix DPO 4032 oscilloscope. The transit time was determined by the kink on the curve of the transient in linear scale for **Car[2,3]** (Gaussian charge transport). For **Car[1,3]**, transit time was find in double logarithmic plot (dispersive charge transport). The drift mobility was calculated by the formula $\mu=d^2/U_0t_t$, where d is the layer thickness, U_0 – the surface potential, t_t – transit time.

Computational details

The interactions between perovskite surface and the hole transporting materials were modelled within the Density Functional Theory (DFT), applying Perdew-Burke-Ernzerhof (PBE)[439] density functional, based on generalized gradient approximation (GGA), along with Grimme's dispersion correction.[440] DZVP-MOLOPT atomic basis set[441] was used to describe the wavefunction, charge density was expanded in plane wave basis set with 600 Ry cutoff, while the core region was treated using Goedecker-Teter-Hutter pseudopotentials.[442] The number of valence electrons for Cs, I/Br, O, N, Pb/C and H was 9, 7, 6, 5, 4 and 1, respectively. The Brillouin zone was sampled at the Γ-point. All calculations have been performed using CP2K code.[443] The visualization of structures is accomplished using VMD program.[444] To model the interactions of **Car[1,3]** and **Car[2,3]** hole-transporting materials (HTM) with perovskite a molecule of each

was placed on top of perovskite surface. Using the obtained structures, the Born-Oppenheimer Molecular Dynamics was performed for about 3 ps with a time step of 1 fs at the constant temperature of 300K, maintained applying velocity rescaling algorithm, to allow the molecules freely interact with perovskite surface.

Lateral conductivity

Conductivity measurement of carbazole-based HTMs and spiro-OMeTAD were carried out using the organic field-effect transistor (OFET) configuration with two-contact electrical conductivity set-up. The OFET substrates were purchased from Fraunhofer IPMS. The substrates were prepared first washing with acetone and ethanol then with 20 min oxygen plasma cleaning. Carbazole-based HTMs and spiro-OMeTAD were deposited from a chlorobenzene solution (36 mM and 60 mM, respectively) chemically doped with FK-209, Li-TFSI, *t*-BP as additives by spin-coating (at 4000 rpm for 30 s). Conductivity measurements were carried out on the 2.5 µm channel by sweeping from -10 to 10 V (source-drain voltage) at a scan rate of 1 V s^{-1} with a Keithley 2612A. The data were recorded with KickStart software program. The channel width and height are 10 mm and 40 nm, respectively, and the gate capacity is 15nF. The conductivity was calculated from linear fit of the current-voltage measurement and Ohm's law.

Water contact angle

Water contact angle on the top of thin layers of carbazole-based HTMs was measured using the KRUSS DSA100 optical contact angle instrument. Measurements were conducted using the sessile drop program with 0.5 mm needle size. Drops of water at a rate of 0.01 mL/min and a volume of 12 µL were created. Substrates were prepared by spin coating 36 mM HTM solutions onto FTO layers. The image was recorded 1 second after the interaction of the water drop with the HTM layer.

Table D.1.1 Estimated cost for the synthesis of **Car[2,3]**/1g from our synthetic routes.

Chemical	Vendor	Amount		Price ($)	Amount required		Price ($)
		g	mL		g	mL	
2,7-dibromo-9*H*-carbazole	Local	100		310	0.5		1.55
4-bromoaniline	Alfa Aesar	1000		259	2.3		0.6
4-iodoanisole	Local	500		348	8.0		5.6
n-BuLi	Sigma		800	142		5.0	0.89
$Sn(Bu)_3Cl$	Alfa Aesar	1000		283	2.6		0.74
$Pd(PPh_3)_4$	Acros Organics	100		1317	0.64		8.43
Other solvents and reagents							~9.5
Total							~27.3

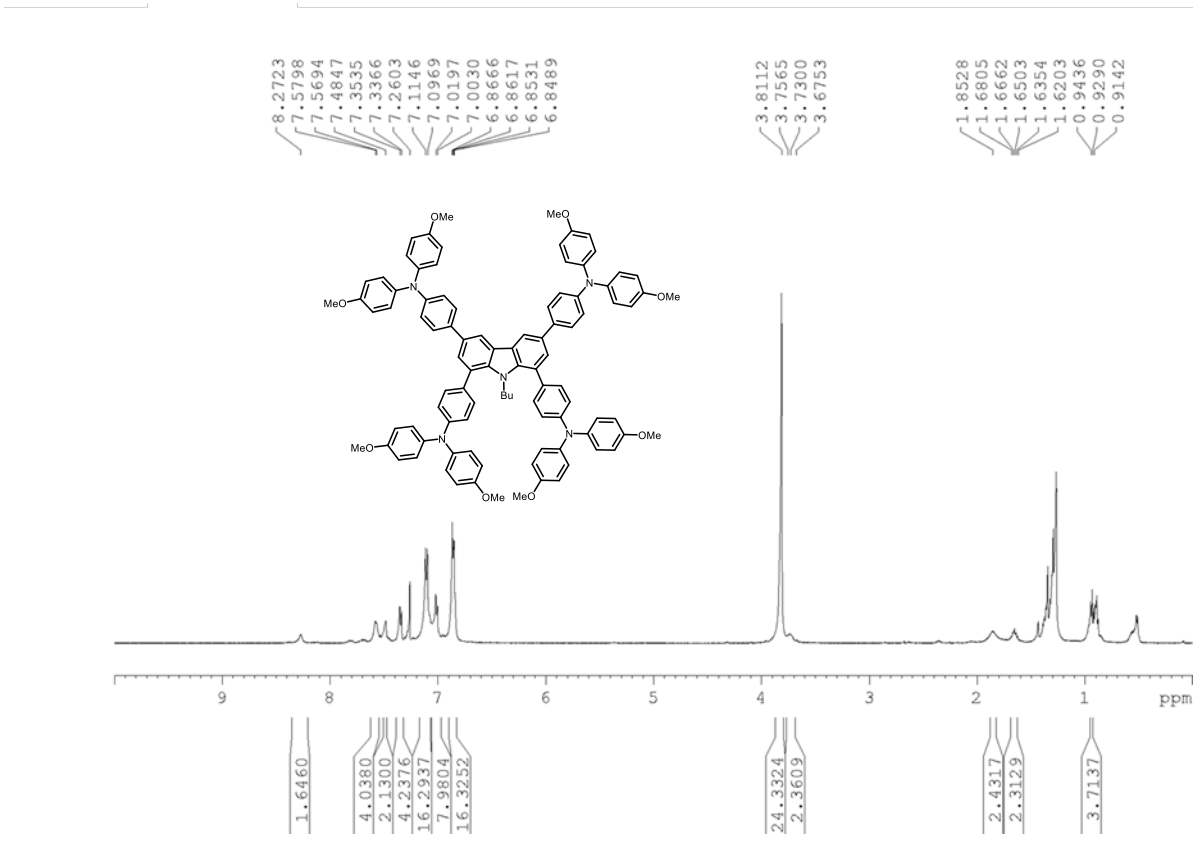

Figure D.1.1 ^1H NMR spectrum of **Car[1,3]** recorded in $CDCl_3$.

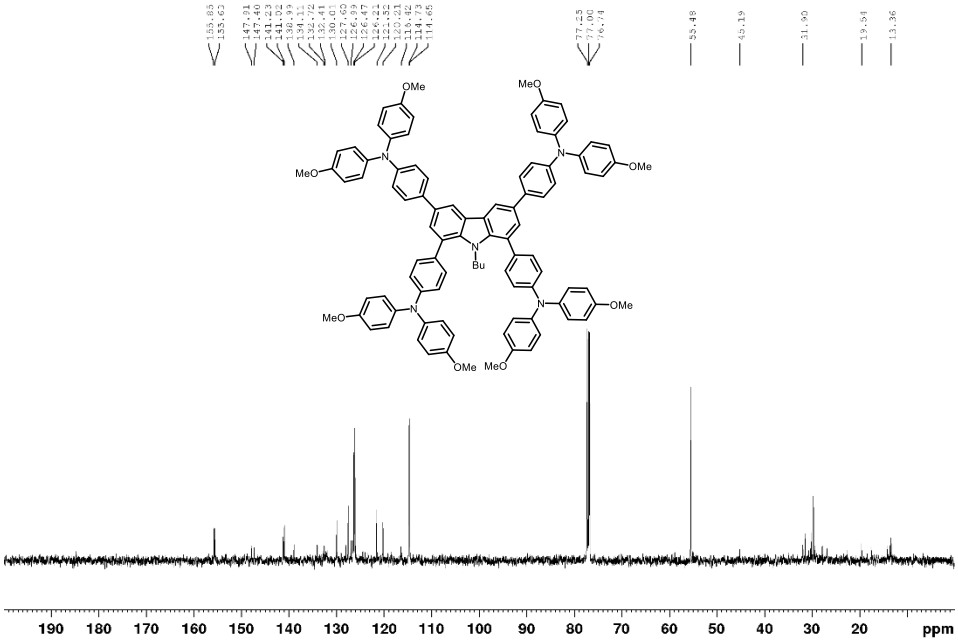

Figure D.1.2 ^{13}C NMR spectrum of **Car[1,3]** recorded in $CDCl_3$.

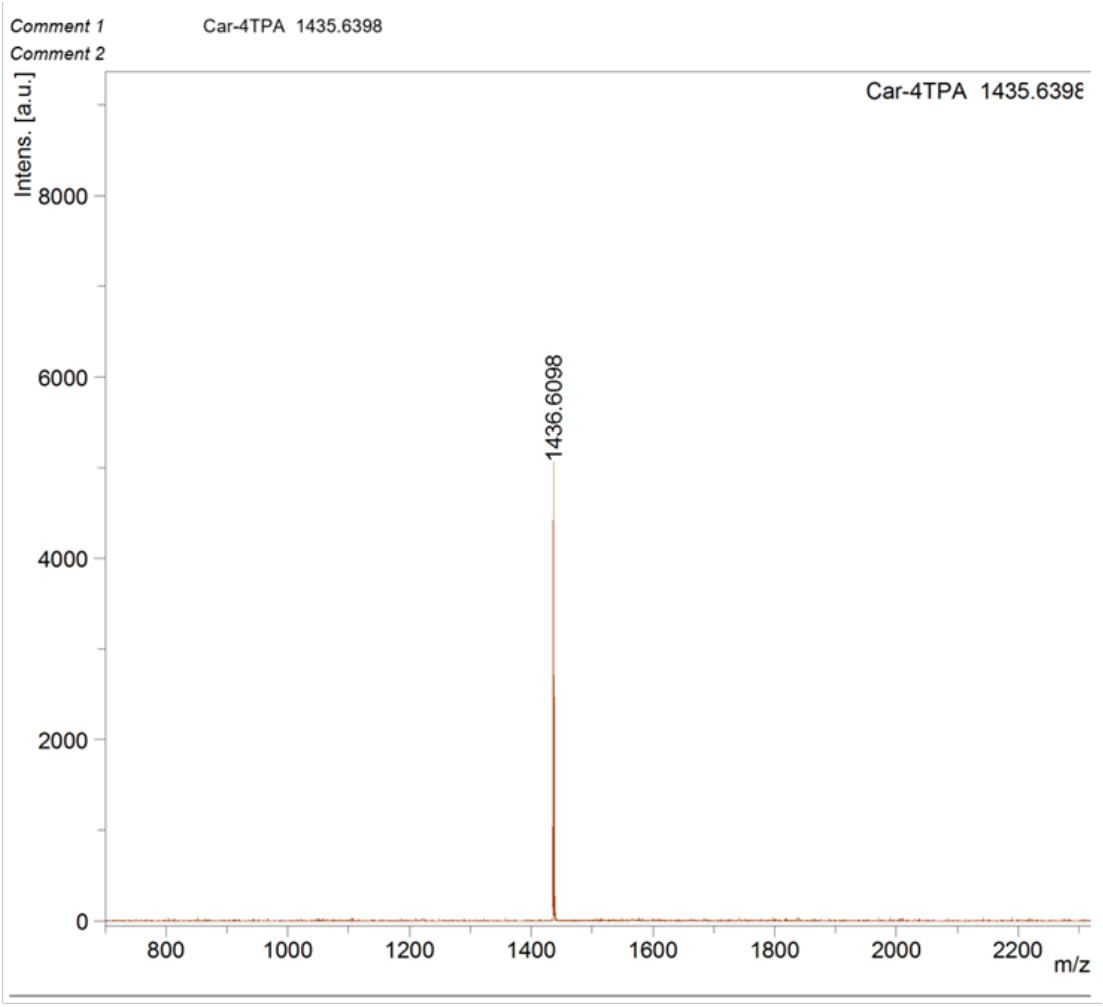

Experimental Data

Formula	Mass	Error	mSigma	DblEq	N rule	Electron Configuration
C 96 H 85 N 5 O 8	1,435.6393	2.5537	32.8114	57.00	ok	odd

Figure D.1.3 HRMS spectrum of **Car[1,3]**.

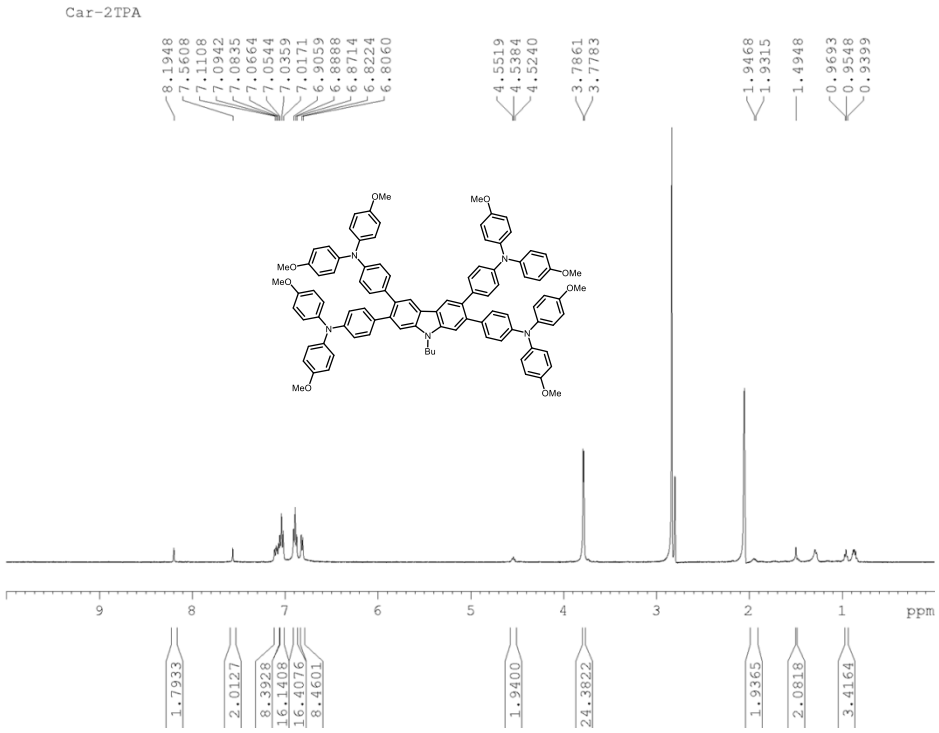

Figure D.1.4 ^{1}H NMR spectrum of **Car[2,3]** recorded in Acetone-d_6.

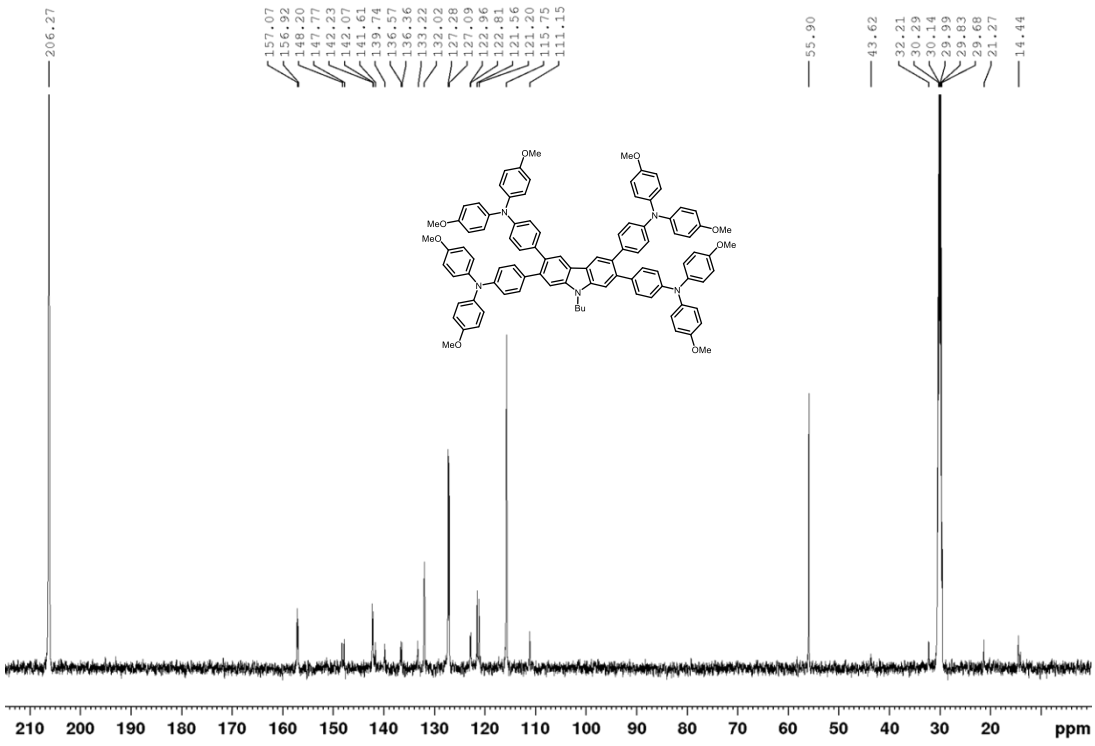

Figure D.1.5 ^{13}C NMR spectrum of **Car[2,3]** recorded in Acetone-d_6.

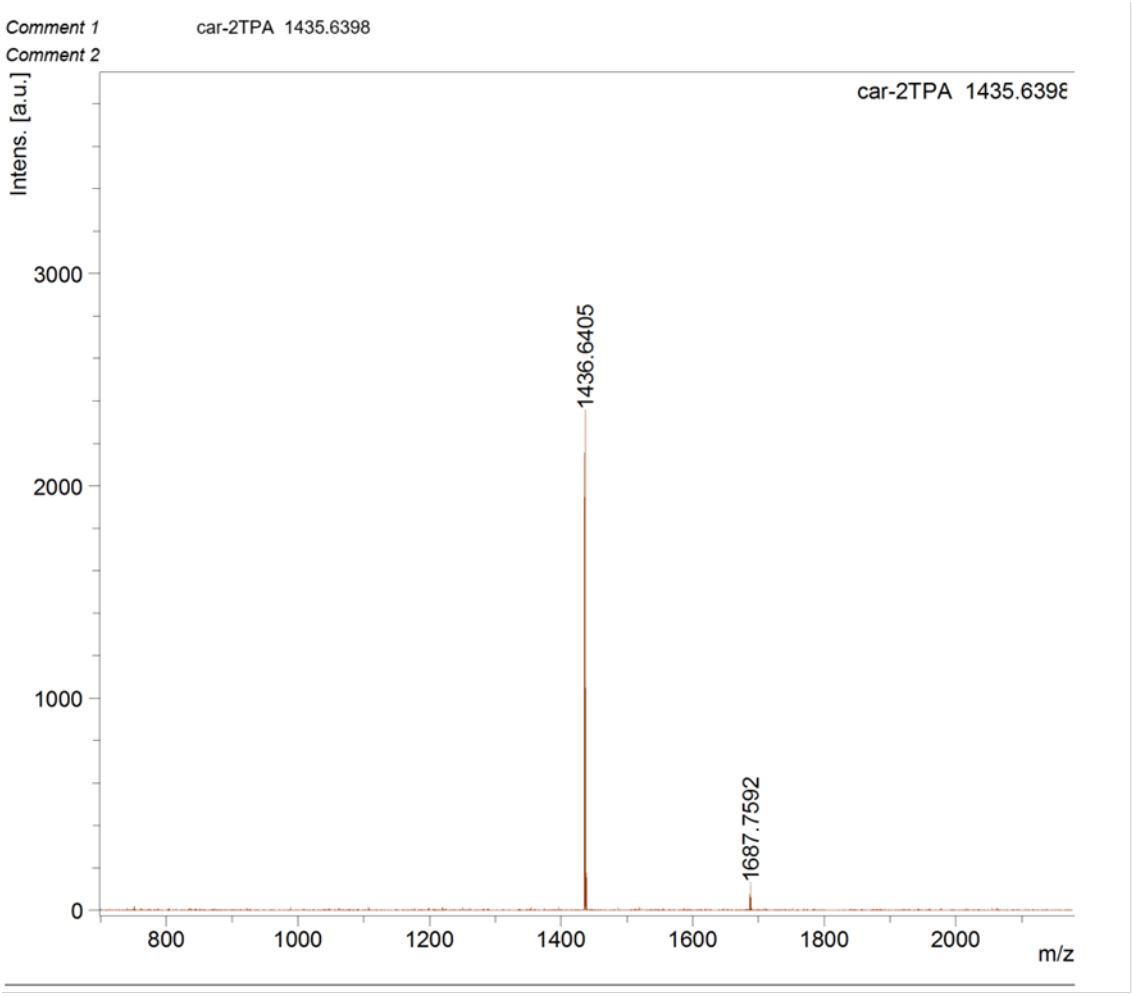

Experimental Data

Formula	Mass	Error	mSigma	DblEq	N rule	Electron Configuration
C 96 H 85 N 5 O 8	1,435.6393	2.5537	32.8114	57.00	ok	odd

Figure D.1.6 HRMS spectrum of **Car[2,3]**.

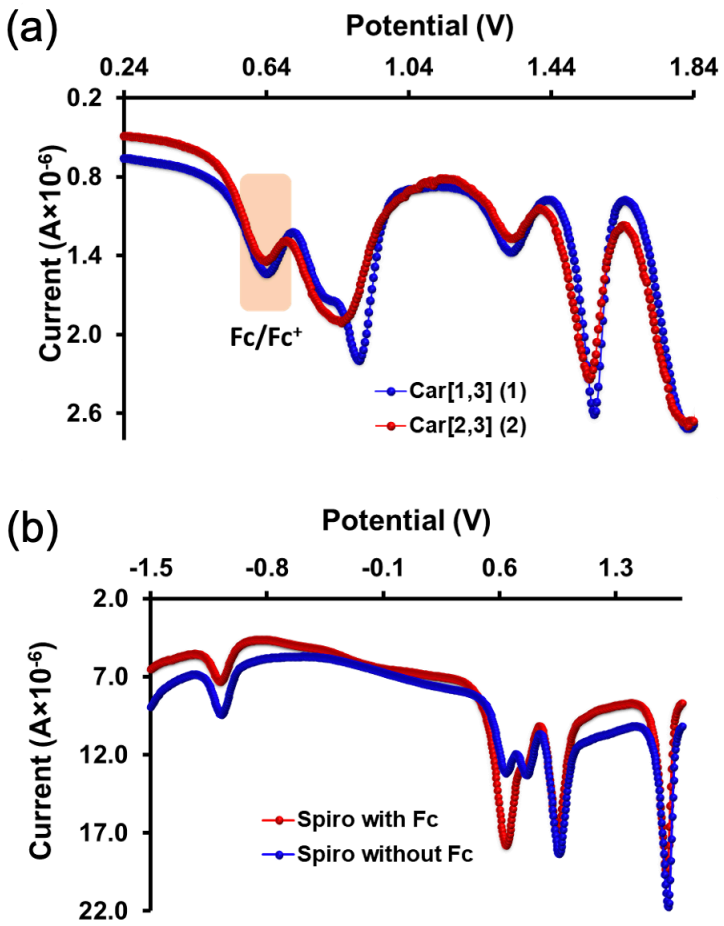

Figure D.1.7 Differential pulse voltammograms (DPV) of (a) the carbazole compounds and (b) spiro-OMeTAD recorded in *o*-$C_6H_4Cl_2$ with addition of ferrocene as internal standard, which the oxidation potential was calibrated at -5.08 eV. The HOMO of spiro-OMeTAD is calculated as HOMO = -(4.44+0.64+0.08) = -5.16 eV.

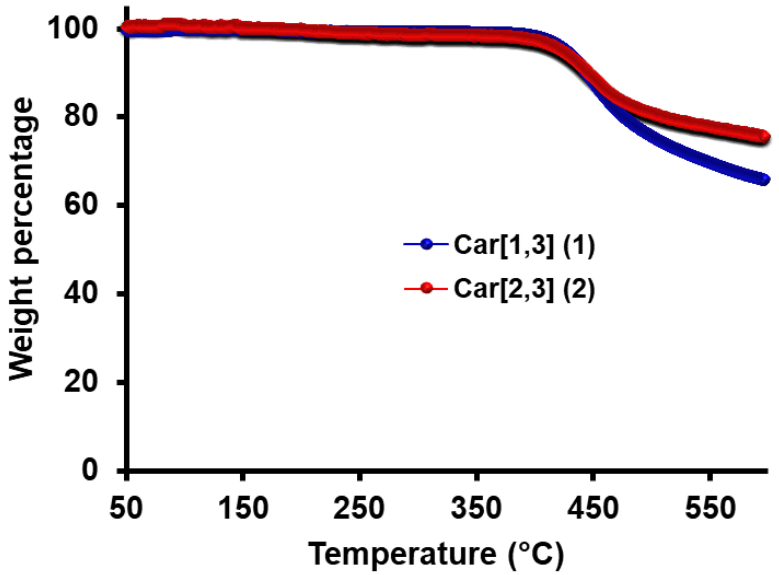

Figure D.1.8 TGA curves for **Car**[**1,3**] and **Car**[**2,3**].

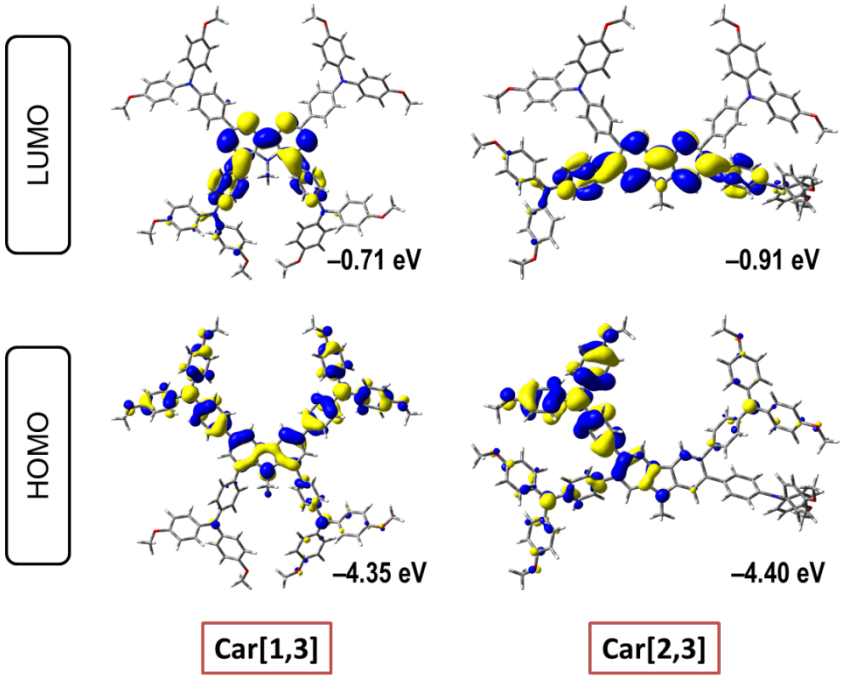

Figure D.1.9 Optimized geometry of frontier molecular orbital diagrams for the model compounds.

Table D.1.2 Predicted vertical excitation obtained by B3LYP/6-31G* method.

Compound	Transition state	Configuration	E_g (eV)	λ_{max} (nm)	f
Car[1,3]	S1	H→ L (94%)	3.23	384	0.14
	S2	H→ L+1 (82%)	3.36	370	0.98
	S3	H-1→ L (87%)	3.40	365	0.03
Car[2,3]	S1	H→ L (93%)	3.10	400	0.25
	S2	H-1→ L (91%)	3.14	395	0.29
	S3	H-3→ L (10%) H-2 → L (84%)	3.31	375	0.46

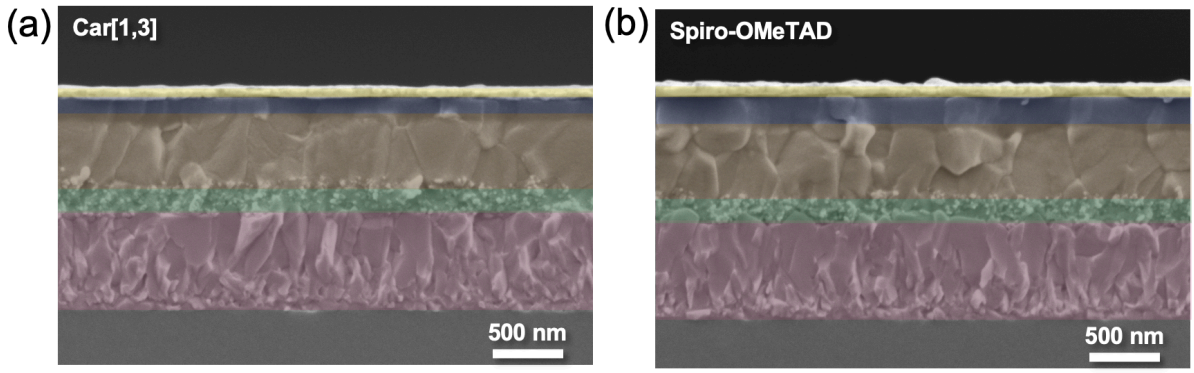

Figure D.1.10 Cross-section scanning electron microscope (SEM) images of PSCs employing (a) **Car[1,3]** and (b) spiro-OMeTAD as HTMs.

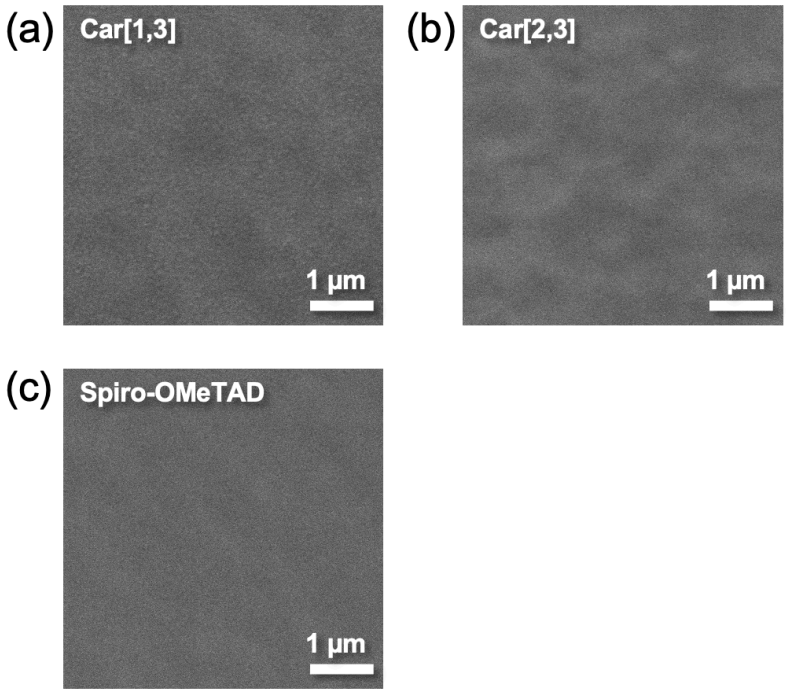

Figure D.1.11 Top-view SEM images of PSCs employing (a) **Car[1,3]**, (b) **Car[2,3]** and (c) spiro-OMeTAD as HTMs.

Table D.1.3 Photovoltaic parameters statistics of PSCs incorporating **Car[1,3]**, **Car[2,3]**, and spiro-OMeTAD as HTMs over 30 devices.

HTM	V_{OC} **(V)**	J_{SC} **(mA cm^{-2})**	***FF***	**PCE (%)**
Car [1,3]	1.032 ± 0.004	22.89 ± 0.02	0.674 ± 0.025	15.9 ± 0.6
Car [2,3]	1.062 ± 0.013	22.93 ± 0.08	0.769 ± 0.008	18.7 ± 0.4
Spiro-OMeTAD	1.106 ± 0.008	22.97 ± 0.08	0.779 ± 0.012	19.8 ± 0.3

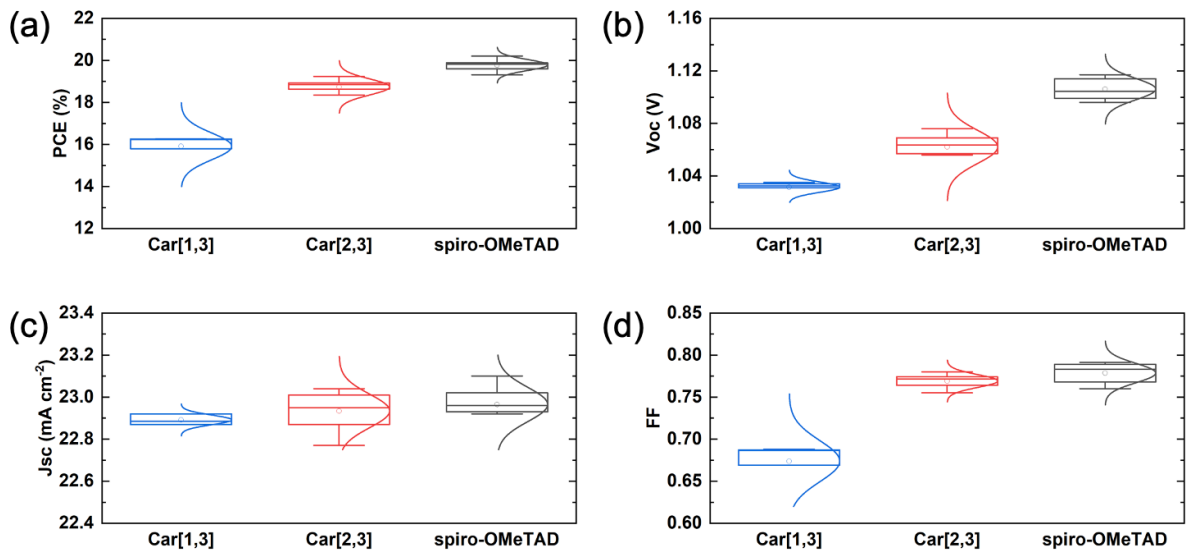

Figure D.1.12 Statistics of the photovoltaics parameters of PSCs fabricated with **Car[1,3]**, **Car[2,3]**, and spiro-OMeTAD as HTMs over 30 devices: (a) PCE, (b) V_{OC}, (c) J_{SC}, and (d) *FF*.

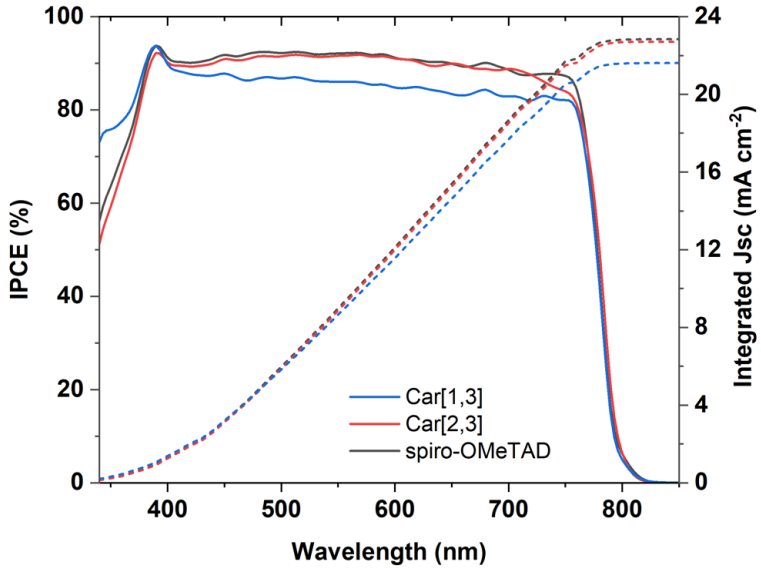

Figure D.1.13 Incident photon to electron conversion efficiency (IPCE) spectra and integrated short-circuit current density of PSCs employing **Car[1,3]**, **Car[2,3]** and spiro-OMeTAD as HTMs.

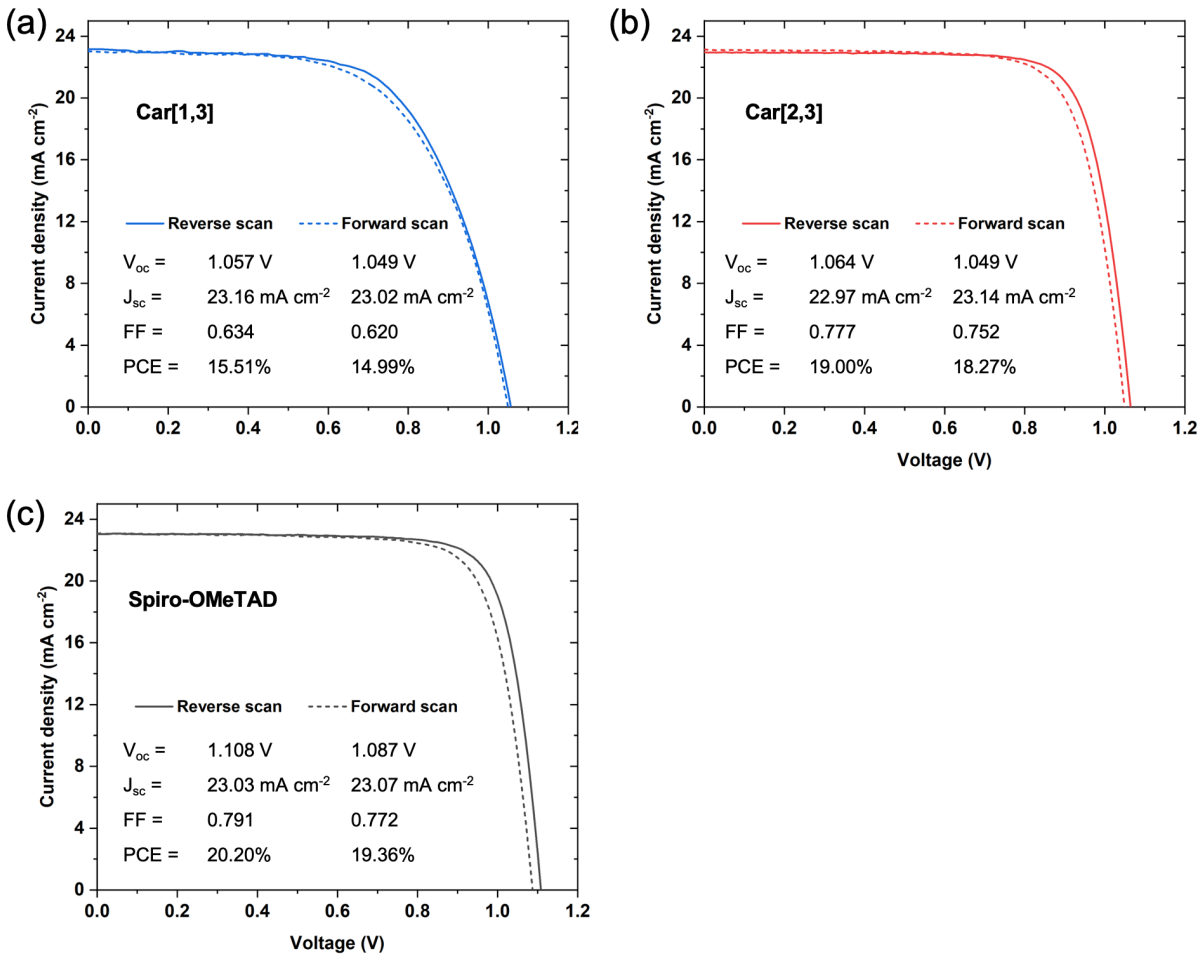

Figure D.1.14 *J-V* curves showing the hysteresis behavior of PSCs employing (a) **Car[1,3]**, (b) **Car[2,3]**, and (c) spiro-OMeTAD upon reverse and forward scan.

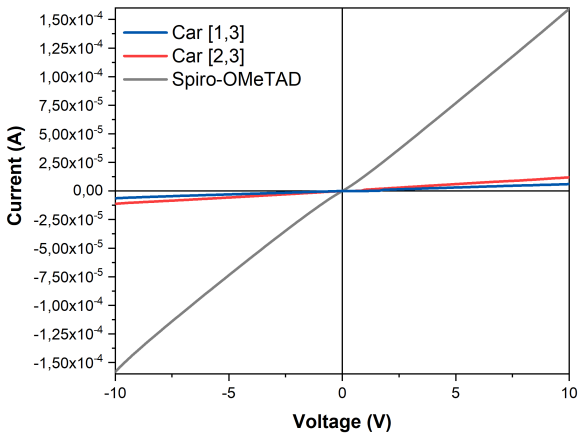

Figure D.1.15 The conductivity of **Car[1,3]**, **Car[2,3]** and spiro-OMeTAD measured on OFET substrates.

Table D.1.4 Conductivities of the **Car[1,3]** and **Car[2,3]** HTMs and the reference spiro-OMeTAD.

HTMs	**σ (S cm^{-1})**
Car[1,3]	3.79 x 10^{-5}
Car[2,3]	7.22 x 10^{-5}
spiro-OMeTAD	9.65 x 10^{-4}

Table D.1.5 PL intensity quenching of perovskite thin-films employing various HTLs in respect to the bare perovskite layer as a reference

HTL	**PL Quenching (%)**
Car[1,3]	32.1
Car[2,3]	91.5
Spiro-OMeTAD	76.7

Table D.1.6 Fitting parameters of TrPL spectra according to the stretched exponential function of $y = a\, e^{-\frac{t}{\tau_c}^{\beta}} + y_0$, where τ_c is the characteristic lifetime of the exponential and, β is the distribution factor. The stretched exponential can be interpreted as a sum of exponential function with a distribution stretched exponential β. We can derive a averaged lifetime from $<\tau> = \frac{\tau_c}{\beta}\Gamma\left(\frac{1}{\beta}\right)$, where Γ is the gamma function.

HTMs	a	τ_c **(ns)**	β	y_0	$<\tau>$ **(ns)**
Perovskite	0.99	430.32	0.68	0.00	559.94
Car[1,3]	2.00	22.17	0.40	0.03	74.00
Car[2,3]	2.00	17.38	0.59	0.02	26.96
Spiro-OMeTAD	2.00	22.54	0.78	0.01	26.05

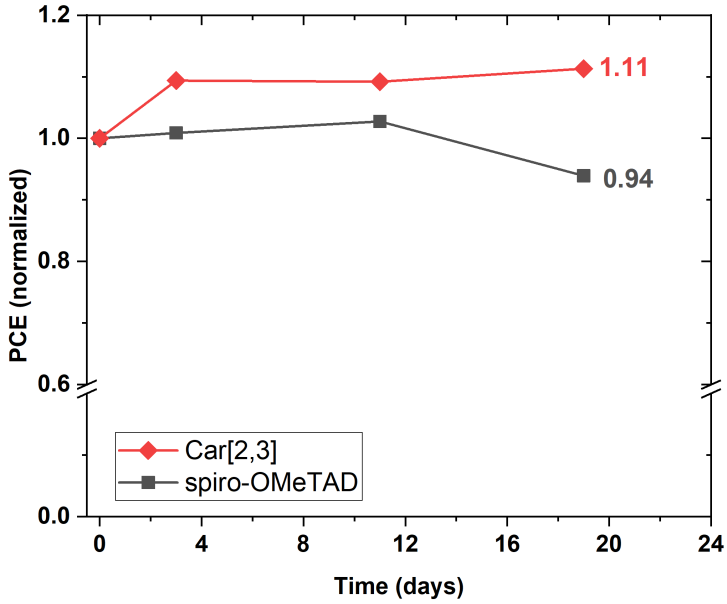

Figure D.1.16 Stability test of the unencapsulated devices employing **Car[2,3]** and spiro-OMeTAD under ambient atmosphere (relative humidity <15%) in dark condition.

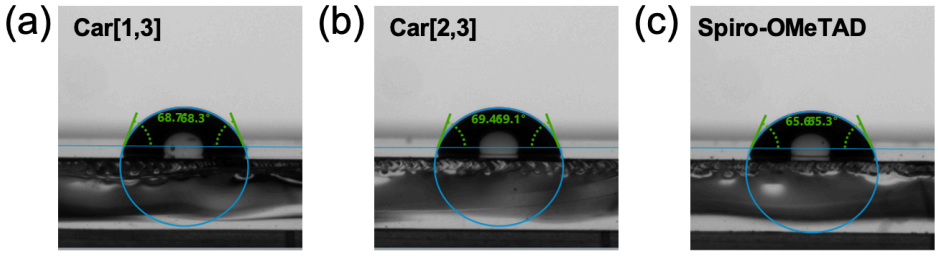

Figure D.1.17 Water contact angle measurement on top of (a) **Car[1,3]**, (b) **Car[2,3]** and (c) spiro-OMeTAD films.

D.2 Stable Perovskite Solar Cells Using Molecularly Engineered Functionalized Oligothiophenes as Low-cost Hole-transporting Materials

Experimental Methods

Materials and characterization

All the chemical reagents were procured from commercial sources and used as received without any further purification. Solvents for reactions were distilled under nitrogen atmosphere by conventional distillation method using sodium/benzophenone, and halogenated solvents were distilled using calcium hydride as drying agent. Silica gel (230 mesh size) was used as stationary phase for column chromatography. ^{1}H NMR and ^{13}C NMR were recorded on a Bruker instrument at 500 MHz and 125 MHz respectively. Deuterated acetone (Acetone-d_6) was used as solvent and the chemical shifts were calibrated using the residual peak of Acetone-d_6 at δ 2.05 for ^{1}H and δ 206.26 for ^{13}C NMR spectra respectively. UV-Vis absorption spectra were recorded at room temperature in a quartz cuvette using JASCO V-600 UV-Vis spectrophotometer. Thermogravimetric analysis (TGA) was performed using a Perkin Elmer TGA-7 instrument under nitrogen as a carrier gas and the reported decomposition temperatures indicate the temperature corresponding to 5% weight loss. Differential pulse voltammetry experiments were performed using a CHI621C Electrochemical Analyzer (CH Instruments) with a conventional three-electrode system (a platinum disk working electrode, an auxiliary platinum wire electrode, and a non-aqueous Ag reference electrode) and supporting electrolyte of 0.1 M tetrabutylammonium hexafluorophosphate ($TBAPF_6$) in *o*-dichlorobenzene solution. All electrochemical potentials were calibrated against Fc/Fc^{+} internal standard (at 0.64 V).

Synthesis

4,4',4'',4'''-([2,2'-bithiophene]-3,3',5,5'-tetrayl)tetrakis(N,N-bis(4-methoxyphenyl)aniline) BT-4D (1)

A mixture of 3,3',5,5'-tetrabromo-2,2'-bithiophene **4** (0.1 g, 0.21 mmol), 4-methoxy-*N*-(4-methoxyphenyl)-*N*-(4-(tributylstannyl)phenyl)aniline **7** (0.55 g, 0.92 mmol), $Pd(PPh_3)_4$ (97 mg, 0.084 mmol) and toluene (30 mL) was refluxed under nitrogen atmosphere for 24 h. After completion of reaction, the reaction mixture was allowed to room temperature and quenched by addition of water. The organic compound was extracted using dichloromethane and washed with brine solution. The combined organic layer was dried over sodium sulfate and concentrated to get crude sample which then purified by column chromatography. Eluent: Hexanes/Ethyl acetate (3:2). Yellow solid. Yield 0.14 g (48%). ^{1}H NMR (500 MHz, Acetone-d_6):

7.48 (d, *J* = 8.5 Hz, 4 H), 7.33 (s, 2 H), 7.07 (d, *J* = 8.5 Hz, 8 H), 7.03 (d, *J* = 8.5 Hz, 4 H), 6.97 (d, *J* = 9.0 Hz, 8 H), 6.91 (d, *J* = 9.0 Hz, 8 H), 6.86-6.81 (m, 12 H), 6.70 (d, *J* = 8.0 Hz, 4 H), 3.79 (s, 12 H), 3.74 (s, 12 H). ^{13}C NMR (125 MHz, Acetone-d_6): 157.56, 157.06, 149.75, 148.61, 144.96, 142.41, 141.92, 141.47, 129.82, 127.96, 127.25, 127.17, 124.87, 121.54, 120.94, 115.90, 115.73, 55.93. HRMS (*m*/*z*, FAB$^+$): calcd for $C_{88}H_{74}N_4O_8S_2$ 1378.4948, found 1378.4943.

4,4′,4″,4‴-([2,2′:5′,2″-terthiophene]-3,3″,5,5″-tetrayl)tetrakis(N,N-bis(4-methoxyphenyl)aniline) TT-4D (2)

It was prepared from a mixture of 3,3'',5,5''-tetrabromo-2,2':5',2''-terthiophene **5** (0.1 g, 0.18 mmol), 4-methoxy-*N*-(4-methoxyphenyl)-*N*-(4-(tributylstannyl)phenyl)aniline **7** (0.53 g, 0.90 mmol), $Pd(PPh_3)_4$ (83 mg, 0.07 mmol) and toluene (30 mL) by following the procedure described for BT-4D. Eluent: Hexanes/Ethyl acetate (3:2). Yellow solid. Yield 0.14 g (54%). ^{1}H NMR (500 MHz, Acetone-d_6): 7.51 (d, *J* = 8.5 Hz, 4 H), 7.26 (s, 2 H), 7.21 (d, *J* = 8.5 Hz, 4 H), 7.09 (d, *J* = 8.5 Hz, 8 H), 7.04 (d, *J* = 9.0 Hz, 8 H), 6.94-6.91 (m, 10 H), 6.87-6.83 (m, 16 H), 3.79 (s, 12 H), 3.73 (s, 12 H). ^{13}C NMR (125 MHz, Acetone-d_6): 157.69, 157.38, 149.89, 149.63, 143.28, 141.76, 141.43, 137.12, 130.97, 129.08, 128.12, 127.77, 127.23, 126.90, 126.33, 121.11, 120.78, 115.96, 55.98. HRMS (*m*/*z*, FAB$^+$): calcd for $C_{92}H_{76}N_4O_8S_3$ 1460.4825, found 1460.4820.

4,4′,4″,4‴-([2,3′:2′,2″:3″,2‴-quaterthiophene]-5,5′,5″,5‴-tetrayl)tetrakis(N,N-bis(4-methoxyphenyl)aniline) QT-4D (3)

It was prepared from a mixture of 5,5',5'',5'''-tetrabromo-2,3':2',2'':3'',2'''-quaterthiophene **6** (0.1 g, 0.15 mmol), 4-methoxy-*N*-(4-methoxyphenyl)-*N*-(4-(tributylstannyl)phenyl)aniline **7** (0.39 g, 0.66 mmol), $Pd(PPh_3)_4$ (69 mg, 0.06 mmol) and toluene (30 mL) by following the procedure described for BT-4D. Eluent: Hexanes/Ethyl acetate (3:2). Yellow solid. Yield 0.12 g (52%). ^{1}H NMR (500 MHz, Acetone-d_6): 7.77 (s, 2 H), 7.58 (d, *J* = 8.5Hz, 4 H), 7.30 (d, *J* = 8.5 Hz, 4 H), 7.26 (d, *J* = 4.0 Hz, 2 H), 7.12-7.04 (m, 10 H), 7.03-7.02 (m, 8 H), 6.95-6.94 (m, 8 H), 6.91-6.87 (m, 12 H), 6.76 (d, *J* = 9.0 Hz, 4 H), 3.82 (s, 12 H), 3.79 (s, 12 H). ^{13}C NMR (125 MHz, Acetone-d_6): 157.63, 157.43, 150.12, 149.42, 148.39, 147.10, 145.39, 141.49, 141.36, 138.38, 136.83, 128.07, 127.82, 127.68, 127.42, 127.15, 122.84, 122.62, 121.02, 120.75, 115.91, 115.83, 55.94. HRMS (*m*/*z*, FAB$^+$): calcd for $C_{96}H_{78}N_4O_8S_4$ 1542.4702, found 1542.4697.

Thin-films and device fabrication

Fluorine-doped tin oxide (FTO) substrate was patterned by laser etching and cleaned with detergent (Helmanex), deionized water, acetone, and isopropanol (IPA) in an ultrasonic bath for 15 min in each solvent. A 30 nm-thick electron-transporting layer (ETL) was deposited on top of cleaned FTO substrate by spraying titanium diisopropoxide bis(acetylacetonate) solution

(Sigma Aldrich) diluted in isopropanol (1:15 v/v) at 450 °C. A 100 nm-thick mesoporous titanium dioxide (mp-TiO_2) layer was spin-coated by diluting TiO_2 paste (GreatCellSolar, 30NR-D) in ethanol (1:8 w/v) at 5000 rpm for 20 s. The layer was then heated at 100 °C for 10 min, followed by thermal sintering at 500 °C for 20 min. A 20 nm-thick tin oxide (SnO_2) was then deposited by spin-coating aqueous $SnCl_4$ solution (Acros, 12 µL in 988 µL water) at 3000 rpm for 30 s and heated at 100 °C for 10 min followed annealing at 190 °C for 1 h. A 1.3 M triple cation-based perovskite solution with the composition of $[(FAPbI_3)_{0.87}(MAPbBr_3)_{0.13}]_{0.92}(CsPbI_3)_{0.08}$ was prepared by mixing the corresponding salts (FAI (GreatCellSolar), MABr (GreatCellSolar), CsI (ABCR), PbI_2 (TCI), and $PbBr_2$ (TCI)) in DMF and DMSO (0.78:0.22 v/v). A 5% excess PbI_2 (PbI_2:FAI = 1.05:1) was used in the precursor solution. To deposit the perovskite layer, the prepared perovskite solution was spin-coated at 2000 rpm for 12 s and 5000 rpm for 30 s. Ethyl acetate was used as an anti-solvent and dropped at 15 s before the spin coating finished. The hole-transporting layer (HTL) was deposited by spin-coating the corresponding hole-transporting materials (HTMs) solutions at 4000 rpm for 30s. A 60 mM solution of 2,2′,7,7′-tetrakis-(*N*,*N*-di-*p*-methoxyphenyl-amine)-9,9′-spirobifluorene (spiro-OMeTAD, Merck) was prepared in chlorobenzene and doped using Li-bis (trifluoromethanesulphonyl) imide (Li-TFSI, Aldrich), FK-209 Co(III) TFSI (GreatCellSolar), and 4-tert-butylpyridine (tBP, Sigma-Aldrich) with the ratio of Li-TFSI:tBP:FK209 = 0.5:3.3:0.055 (mol/mol spiro-OMeTAD). For the thiophene-based HTMs (**BT-4D**, **TT-4D**, and **QT-4D**), a 36 mM solution was prepared in chlorobenzene and doped with Li-TFSI:tBP:FK209 = 0.5:3.3:0.03 (mol/mol HTM). Finally, a 70 nm-thick gold counter electrode was deposited using physical vapor deposition under high vacuum.

Thin-films characterization

Photoluminescence (PL)

PL spectra of the thin-films were recorded using Fluorolog, Horiba Jobin Yvon fluorescence spectrometer upon excitation at 625 nm for the steady-state PL measurement and 635 nm for the transient PL measurement.

Lateral conductivity measurement

Conductivity measurement of **BT-4D**, **TT-4D**, **QT-4D** and spiro-OMeTAD were carried out using the organic field-effect transistor (OFET) configuration with two-contact electrical conductivity set-up. The OFET substrates were purchased from Fraunhofer IPMS. The substrates were prepared first with acetone and ethanol washing then 20 min. oxygen plasma

cleaning. **BT-4D**, **TT-4D**, **QT-4D** HTMs and spiro-OMeTAD solutions were doped with FK-209, Li-TFSI, *t*-BP in a chlorobenzene solution (36 mM) and were deposited on the substrates by spin-coating (at 4000 rpm for 30 s). Conductivity measurements were carried out with gold electrodes on the 2.5 μm channel by sweeping from -10 to 10 V (source-drain voltage) at a scan rate of 1 V s^{-1} with a Keithley 2612A. The data were recorded with KickStart software program. The channel width and height are 10 mm, and 40 nm, respectively, and the gate capacity is 15nF. The conductivity was calculated from linear fit of the current-voltage measurement and Ohm's law.

Solar cells characterization

Current density-Voltage (*J-V*) characteristics were measured under 1-sun AM 1.5G illumination generated by xenon lamp solar simulator (450 W, Oriel Sol3A, AAA class). The light intensity was calibrated using a Si reference equipped with an IR-cutoff (KG5) filter prior to the measurement. The active area of 0.16 cm^2 was defined by a black metal mask with the aperture of 4x4 mm. The *J-V* curves were scanned under the scan rate of 50 mV/s with 2 s pre-illumination time. During the *J-V* scan, an external voltage bias was applied and the current response was recorded with a digital source meter (Keithley 2400). The incident photon to current conversion efficiency (IPCE) of the solar cells devices was measured IQE200B (Oriel). Long-term stability test was performed on the PSCs without any encapsulation at room temperature. The stability measurement set up from Candlelight Instrument was used. The devices were placed inside a testing chamber which was conditioned under an inert atmosphere by using Argon gas. The testing chamber was equipped with the LED light source which gave continuous illumination of 1-sun intensity (100mW/cm^2). The devices were connected into a source meter and the photovoltaics parameters are recorded continuously under maximum power point (MPP) tracking.

Computational experiment

Interaction of HTMs with perovskite was modelled within the Density Functional Theory (DFT) performing Born-Oppenheimer molecular dynamics simulations, as implemented in CP2K code,[443] employing Perdew-Burke-Ernzerhof (PBE)[439] density functional with Grimme's dispersion correction,[440] DZVP-MOLOPT atomic basis sets,[441] auxiliary plane wave basis set with 600 Ry cutoff and Goedecker-Teter-Hutter pseudopotentials.[442] The molecules were placed on top of the perovskite surface and allowed to freely interact with it, maintaining the temperature constant at 300K applying velocity rescaling algorithm.

Impedance spectroscopy

Impedance spectra were measured by SP-200 (BioLogic Science Instruments) in the dark at 0 V of applied bias voltage and AC perturbation of 20 mV.

Table D.2.1 Previous reports on the thiophene/bithiophene-based HTM with triphenylamine substitution

Molecules Name	**Core**	**Substitution**	**Dopants**	**PCE (%)**	**References**
BT-4D	Bithiophene	Triphenylamine substitution on 3,3',5,5'-position of 2,2'-bithiophene	tBP/Li-TFSI/Co-TFSI (FK-209)	19.34%	This work
KTM3	Bithiophene	Triphenylamine substitution on 2,2',5,5'-position of 3,3'-bithiophene	tBP/Li-TFSI/Co-TFSI (FK-269)	11.4%	[415]
H111	Thiophene	Triphenylamine substitution on 2,3,4,5-position of thiophene	tBP/Li-TFSI/Co-TFSI (FK-102)	15.4%	[417]
H112	Bithiophene	Triphenylamine substitution on 4,4',5,5'-position of 2,2'-bithiophene	tBP/Li-TFSI/Co-TFSI (FK-102)	15.2%	[417]
H-3,4	Thiophene	Triphenylamine substitution on 3,4-position of thiophene	Li-TFSI/TBP/Co-TFSI (FK102)	9.05%	[414]
H-2,5	Thiophene	Triphenylamine substitution on 2,5-position of thiophene	Li-TFSI/TBP/Co-TFSI (FK102)	15.13%	[414]
PEH-3	Bithiophene	Triphenylamine substitution on 5,5'-position of 2,2'-bithiophene	tBP/Li-TFSI/ Co-TFSI (FK209)	12.56%	[418]

Table D.2.2 Estimated cost for the synthesis of **BT-4D**/1g from our synthetic routes.

Chemical	Vendor	Amount		Price ($)	Amount required		Price ($)
		g	mL		g	mL	
Bithiophene	Molbase	1000		426	0.3		0.13
Bromine	Alfa Aesar	5000		483	1.6		0.16
4-bromoaniline	Alfa Aesar	1000		259	2.5		0.65
4-iodoanisole	Local	500		348	8.8		6.12
n-BuLi	Sigma		800	142	5.5		0.98
$Sn(Bu)_3Cl$	Alfa Aesar	1000		283	2.9		0.82
$Pd(PPh_3)_4$	Acros Organics	100		1317	0.7		9.22
Other solvents and reagents							8.1
Total							~26.2

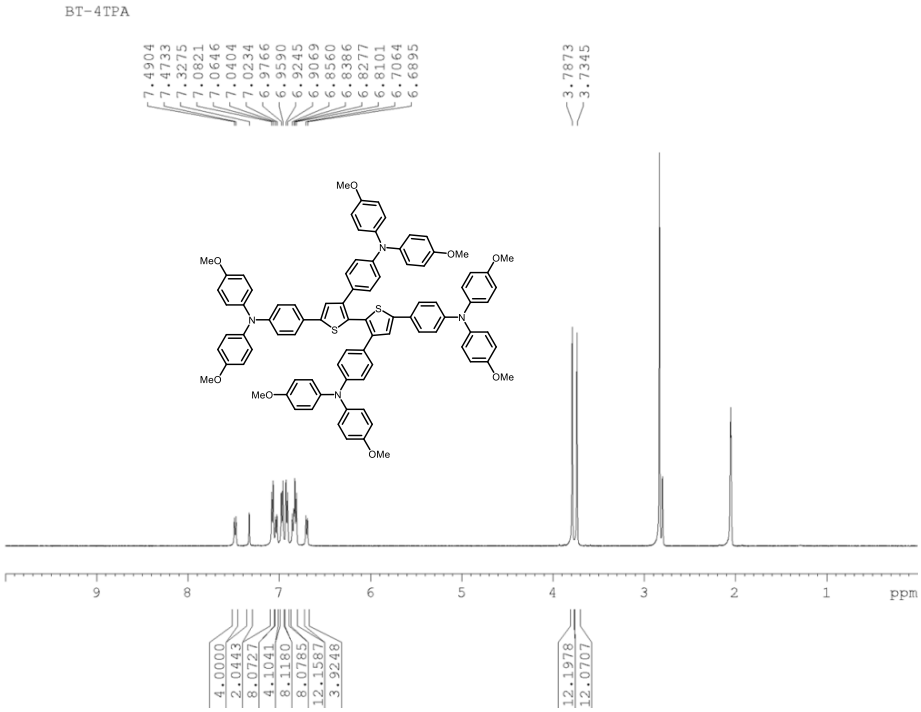

Figure D.2.1 ^{1}H NMR spectrum of **BT-4D** recorded in Acetone-d_6.

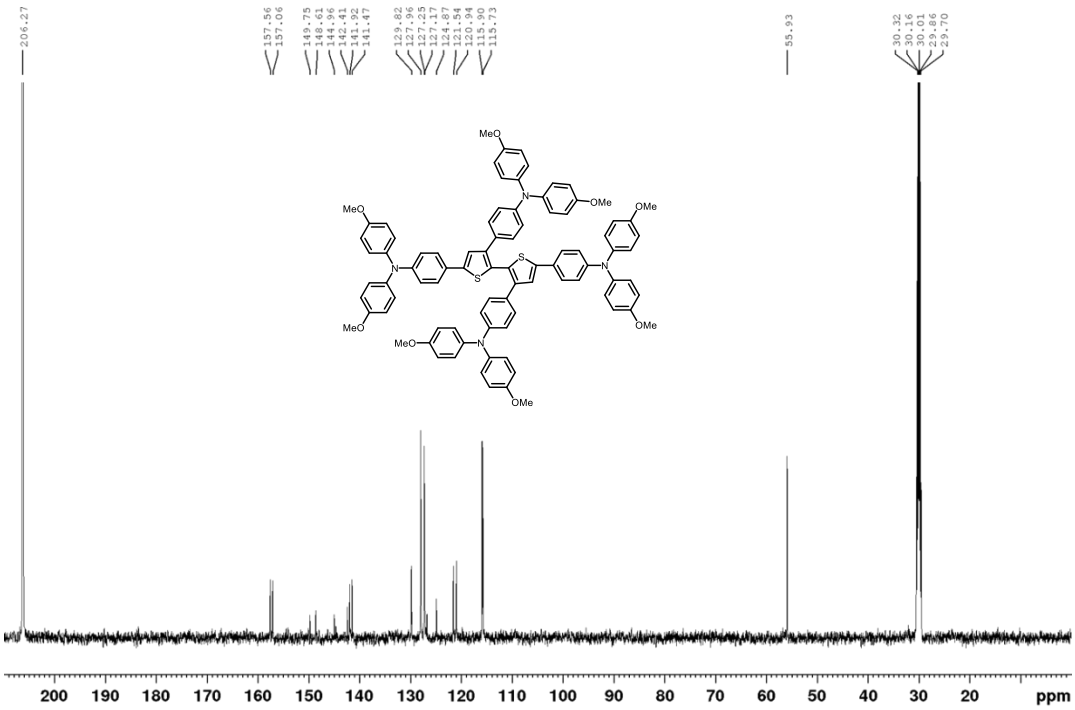

Figure D.2.2 ^{13}C NMR spectrum of **BT-4D** recorded in Acetone-d_6.

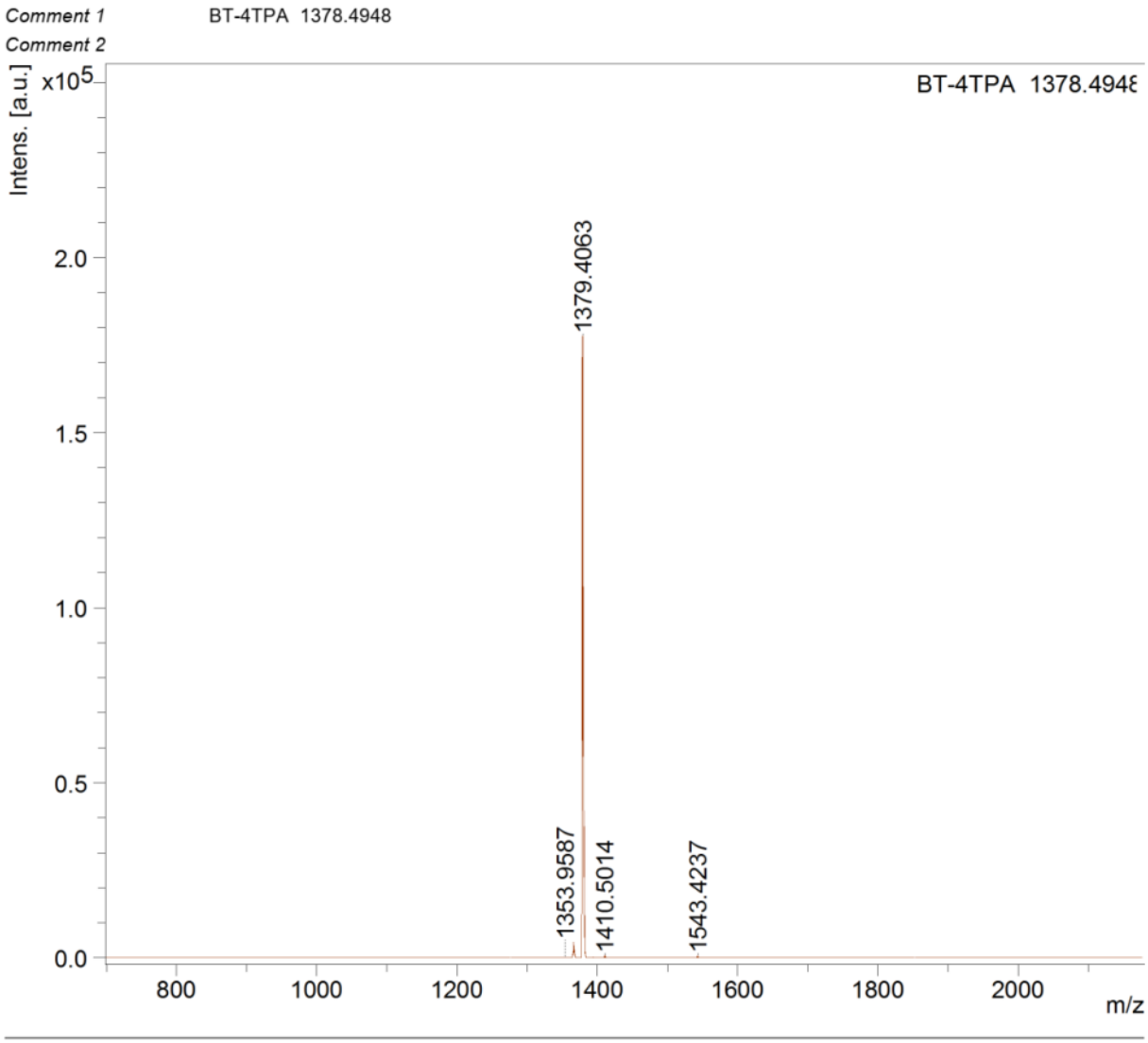

Experimental Data

Formula	Mass	Error	mSigma	DblEq	N rule	Electron Configuration
C 88 H 74 N 4 O 8 S 2	1,378.4943	2.3169	20.6154	54.00	ok	odd

Figure D.2.3 HRMS spectrum of **BT-4D**.

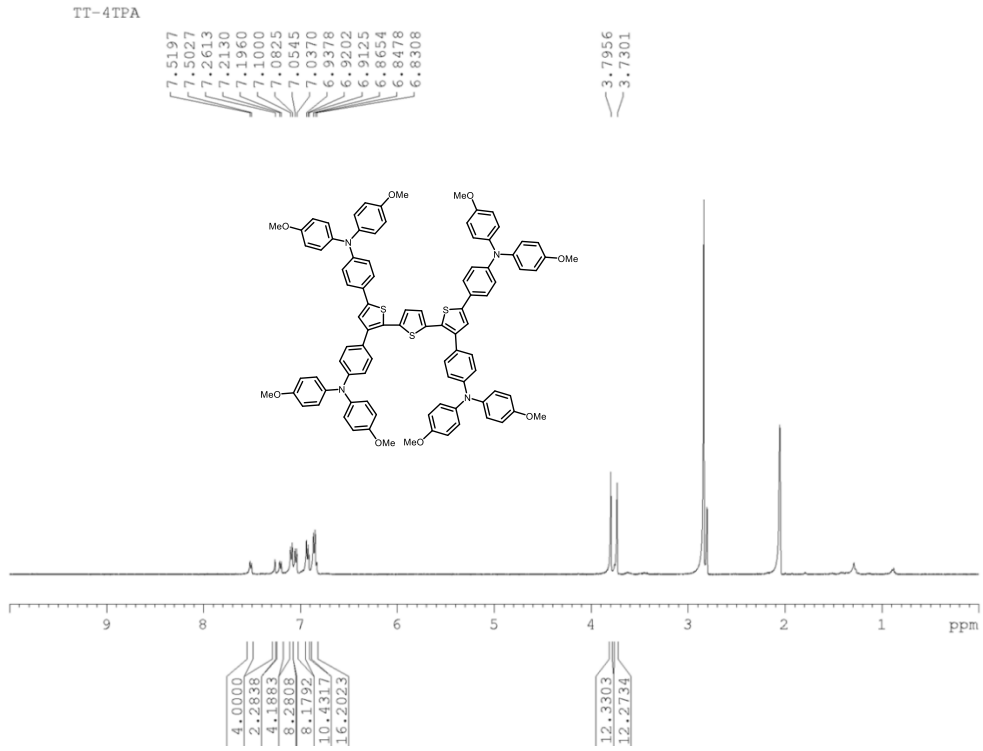

Figure D.2.4 ^{1}H NMR spectrum of **TT-4D** recorded in Acetone-d_6.

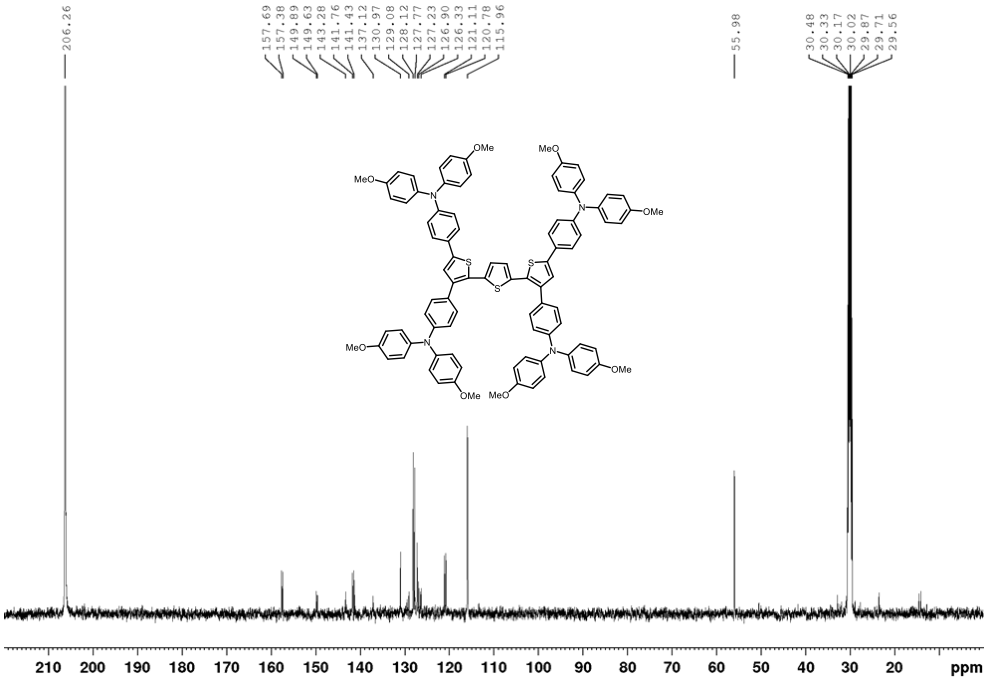

Figure D.2.5 ^{13}C NMR spectrum of **TT-4D** recorded in Acetone-d_6.

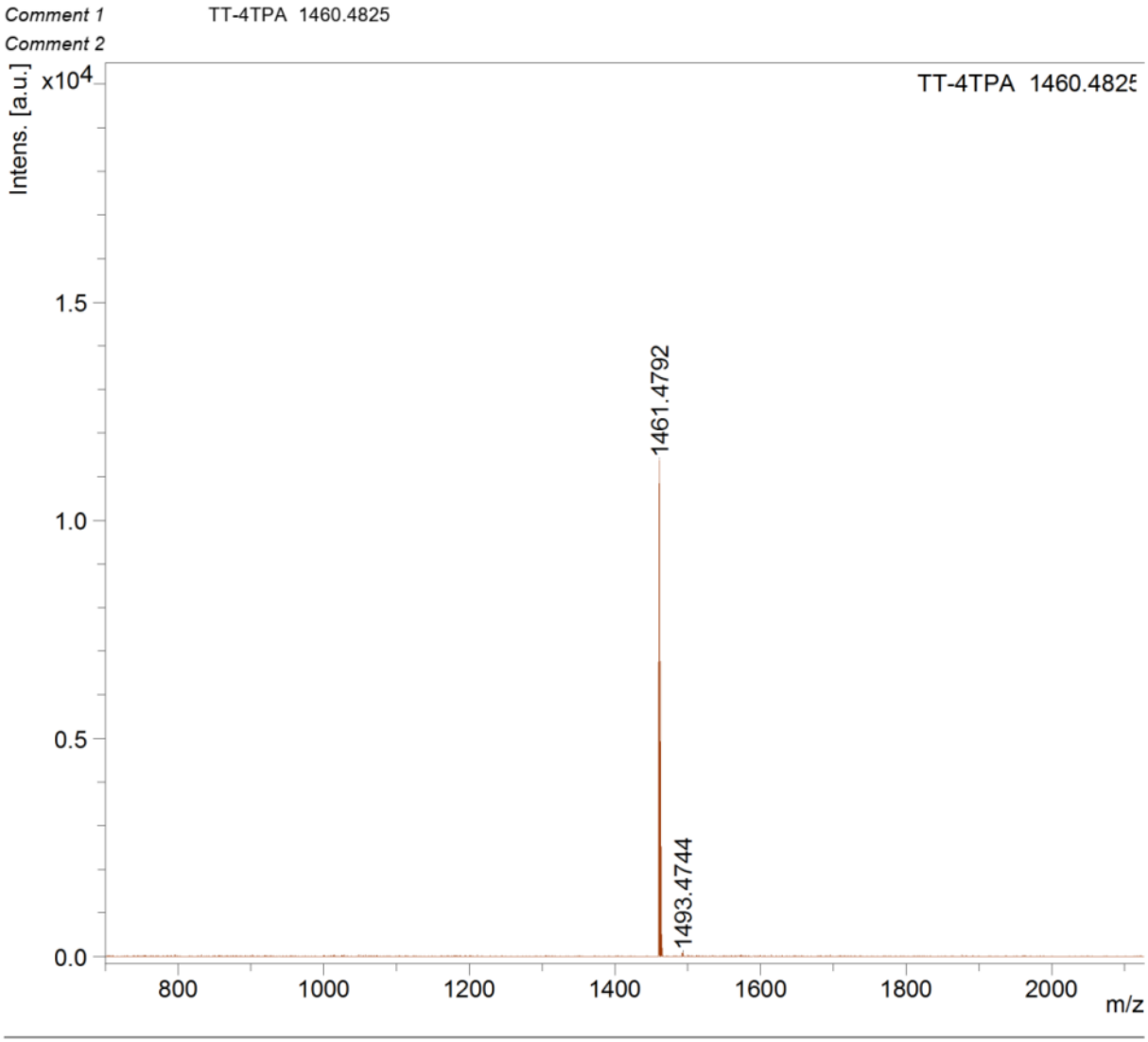

Experimental Data

Formula	Mass	Error	mSigma	DblEq	N rule	Electron Configuration
C 92 H 76 N 4 O 8 S 3	1,460.4820	2.1773	59.3982	57.00	ok	odd

Figure D.2.6 HRMS spectrum of **TT-4D**.

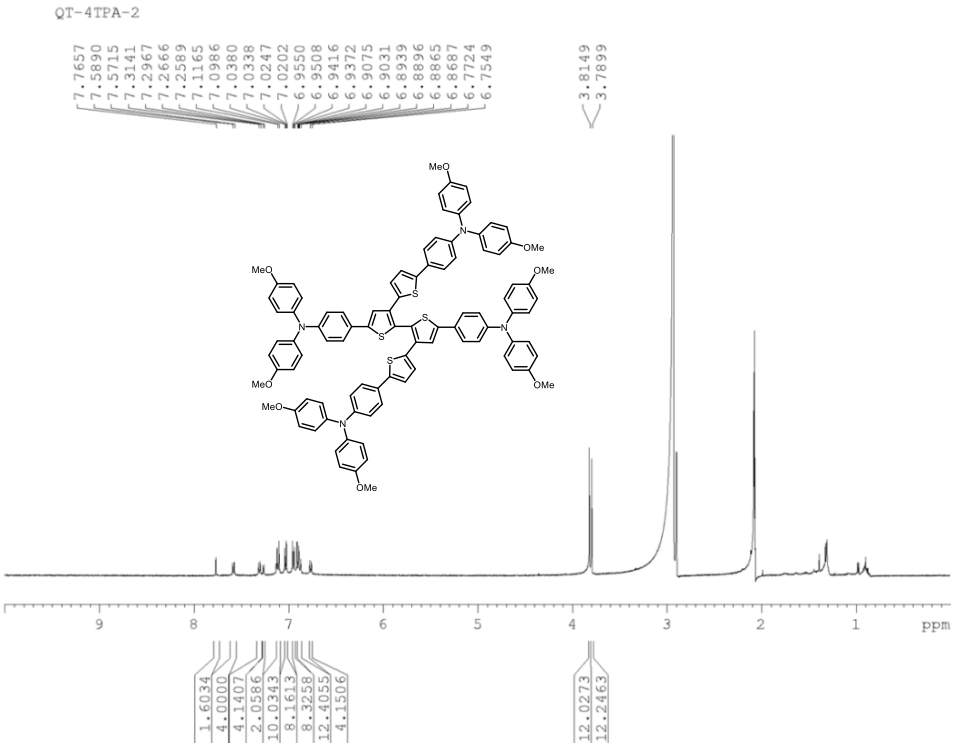

Figure D.2.7 ^{1}H NMR spectrum of **QT-4D** recorded in Acetone-d_6.

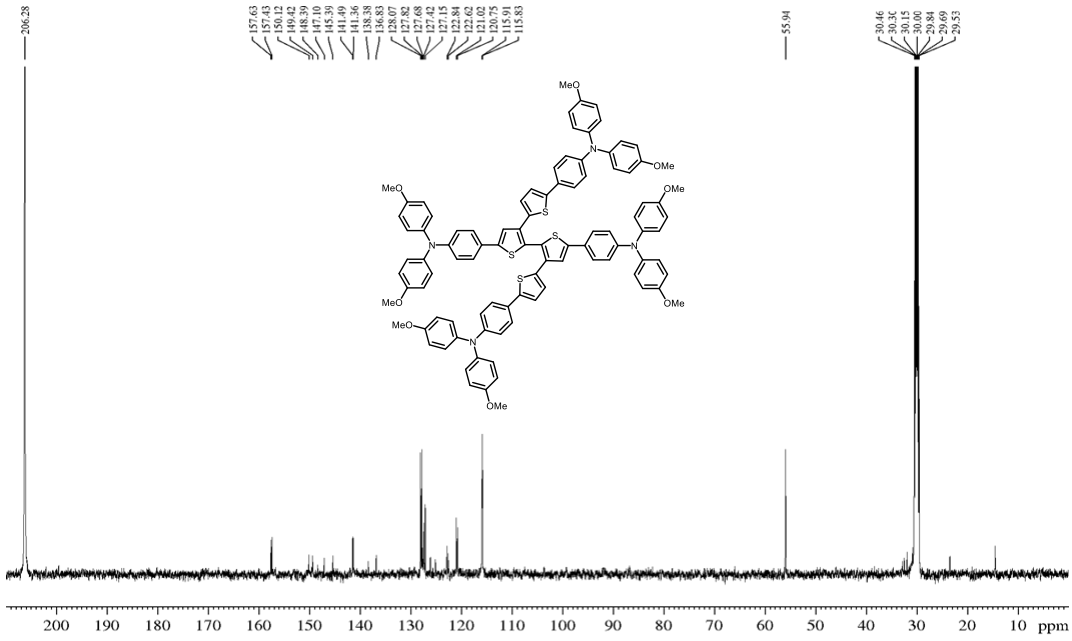

Figure D.2.8 ^{13}C NMR spectrum of **QT-4D** recorded in Acetone-d_6.

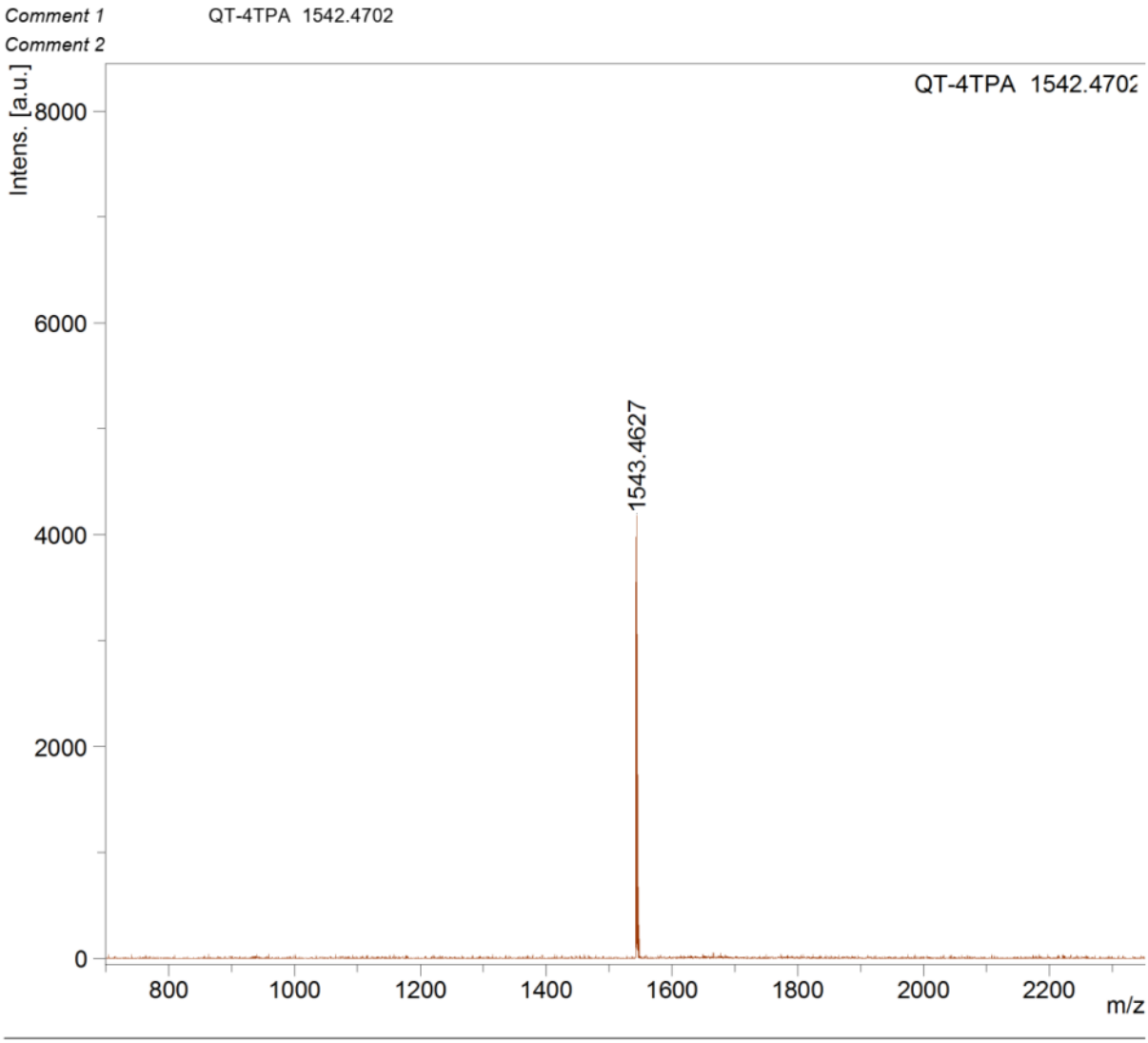

Experimental Data

Formula	Mass	Error	mSigma	DblEq	N rule	Electron Configuration
C 96 H 78 N 4 O 8 S 4	1,542.4697	2.1400	19.8908	60.00	ok	odd

Figure D.2.9 HRMS spectrum of **QT-4D**.

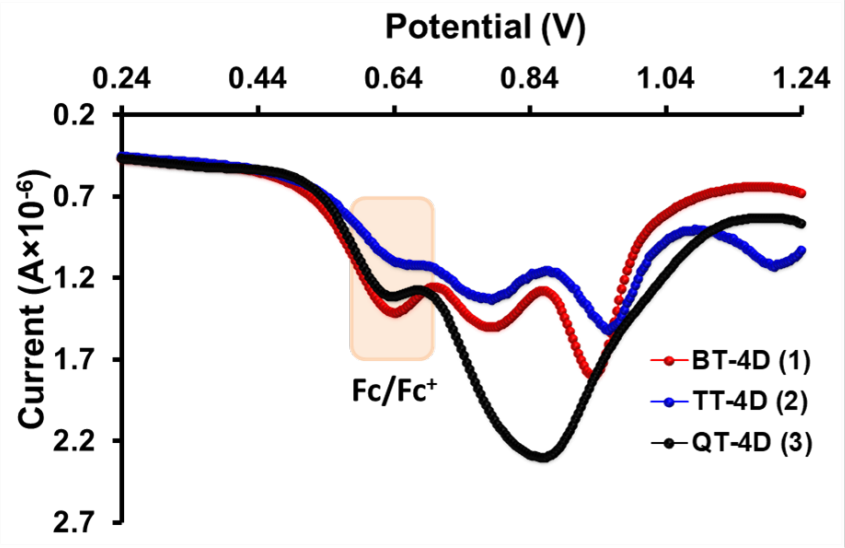

Figure D.2.10 Differential pulse voltammograms (DPV) of the compounds recorded in *o*-$C_6H_4Cl_2$ with addition of ferrocene as internal standard, which the oxidation potential was calibrated at -5.08 eV.

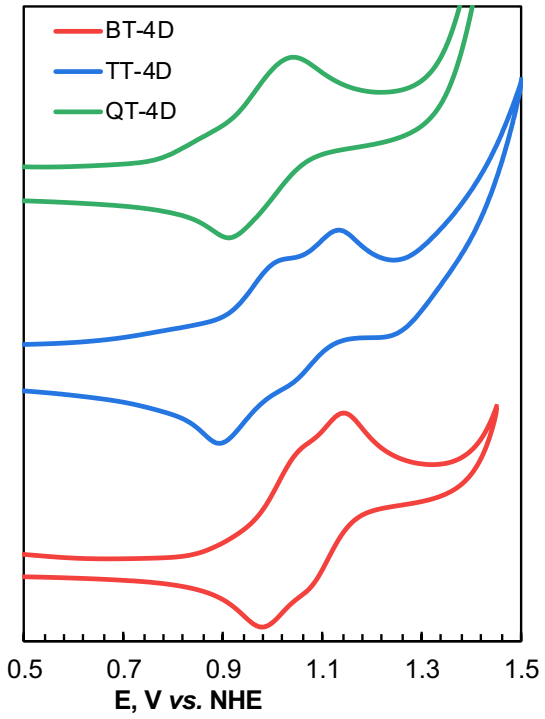

Figure D.2.11 Cyclic voltammograms (CV) of the compounds in tetrahydrofuran (THF)

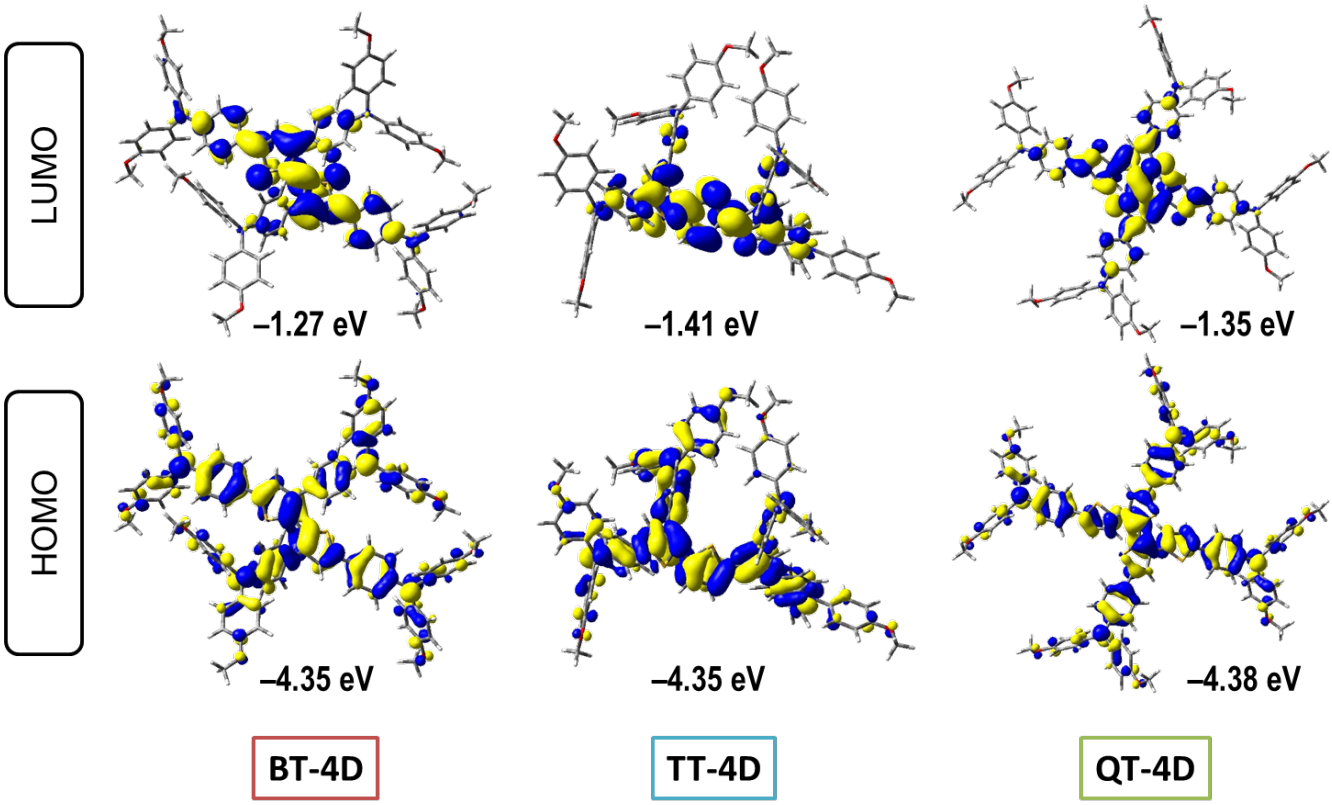

Figure D.2.12 Optimized geometry of frontier molecular orbital diagram for the model compounds.

Table D.2.3 Predicted vertical excitation obtained by B3LYP/6-31G* method

Compound	Transition state	Configuration	E_g (eV)	λ_{max} (nm)	f
BT-4D	S1	H→ L (98%)	2.65	468	0.56
	S2	H-1→ L (92%)	2.87	431	0.09
	S3	H-2→ L (94%)	2.94	422	0.62
TT-4D	S1	H→ L (97%)	2.50	495	0.78
	S2	H-1→ L (88%)	2.73	453	0.33
	S3	H-3→ L (82%)	2.82	440	0.41
		H-2 → L (16%)			
QT-4D	S1	H → L (97%)	2.62	473	0.69
	S2	H-1 → L (89%)	2.83	437	0.14
	S3	H-2 → L (96%)	2.88	430	0.77

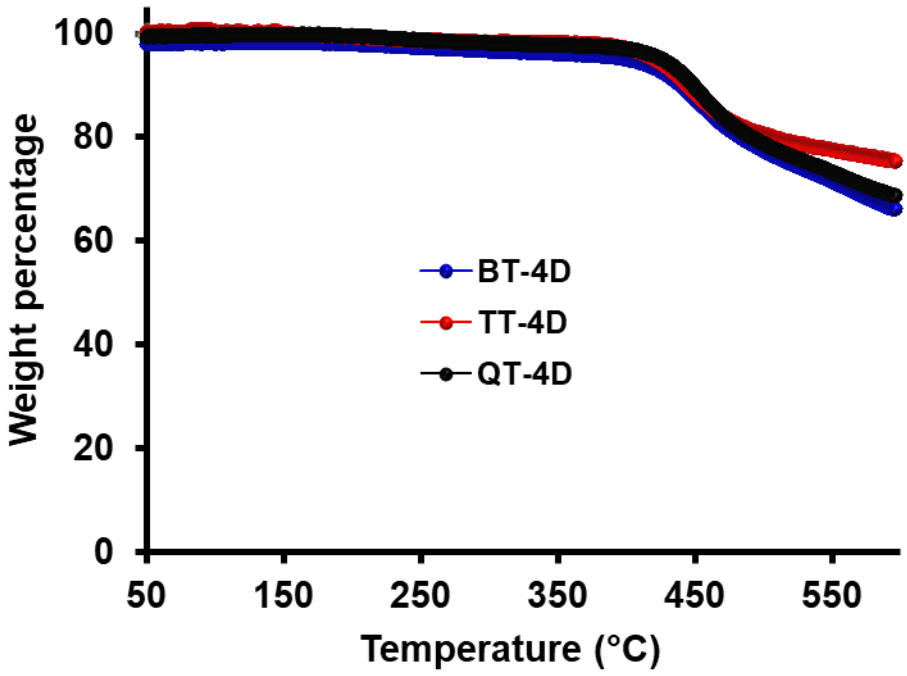

Figure D.2.13 Thermogravimetric analysis (TGA) curves of the compounds.

Drift mobility measurements

The xerographic time-of-flight (XTOF) technique was used to characterize charge transport in the films of thiophene series hole transporting materials (HTM). Samples are prepared under drop casting technique on Al coated glass plates using THF as solvent. Samples thickness were 1.9 μm for **BT-4D**, and 1.8 μm for **QT-4D**. Only for **TT-4D** sample doctor blade method was used due strong layer unevenness when used drop casting technique and sample thickness was about 1 μm. The corona charging was used to create electric field in the HTM layer. Charge carriers were generated at the layer surface by illuminating with pulses of nitrogen laser (pulse duration was 1 ns, wavelength 337 nm). The layer surface potential decrease as a result of pulse illumination was about 3 % of initial potential and so was ensured small charge mode in XTOF measurement. The capacitance probe deposited over the sample and connected to the wide frequency band electrometer measured the speed of the surface potential decrease dU/dt, which is equivalent to a current in widely known TOF technique. The transit time t_t was determined by the kink on the curve of the dU/dt transient in linear scale for **BT-4D**. These materials are characterized by Gaussian charge transport. For **QT-4D** and **TT-4D** transit time was found in double logarithmic plot and are characterized by dispersive charge transport. The drift mobility was calculated by the formula $\mu = d^2/U_0 t_t$, where d is the layer thickness and U_0 is the surface potential at the moment of illumination. The hole mobility results are shown in standard plot for organic compounds (Fig. 1b). In all the cases investigated, the mobility μ is approximated by the formula $\mu = \mu_0 \exp(\alpha\sqrt{E})$, where μ_0 is the zero-field mobility, α is field dependence parameter, and E is electric field strength. The mobility defining parameters μ_0 and α values as well as the mobility value at the 6.4×10^5 V/cm field strength are given in Table D.2.4.

Table D.2.4 Hole mobility data

HTM	μ_0 ($cm^2\ V^{-1}\ s^{-1}$)	μ ($cm^2/V{\cdot}s$)	α $(cm/V)^{0.5}$
BT-4D	5.6×10^{-6}	0.8×10^{-3}	0.0062
TT-4D	5.0×10^{-6}	1.0×10^{-3}	0.0066
QT-4D	4.7×10^{-6}	0.9×10^{-3}	0.0066

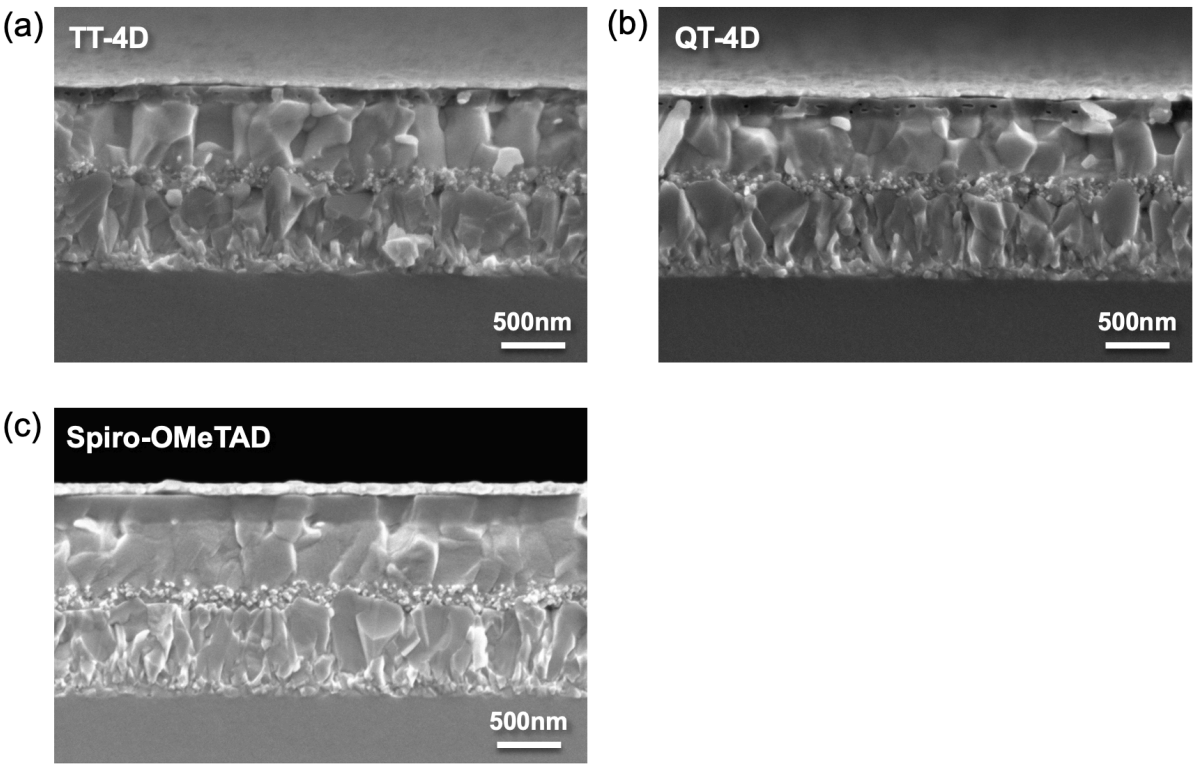

Figure D.2.14 Cross-section SEM images of complete perovskite solar cells employing (a) **TT-4D**, (b) **QT-4D**, and (c) spiro-OMeTAD as HTLs.

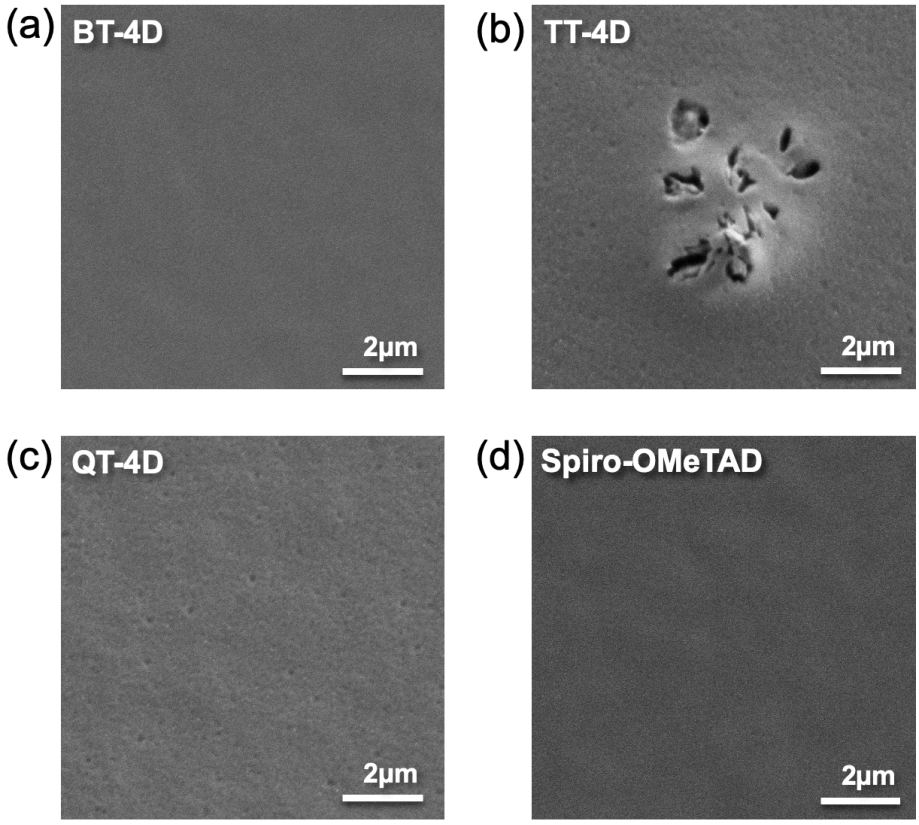

Figure D.2.15 Top-view SEM images of (a) **BT-4D**, (b) **TT-4D**, (c) **QT-4D**, and (d) spiro-OMeTAD deposited on top of perovskite layer.

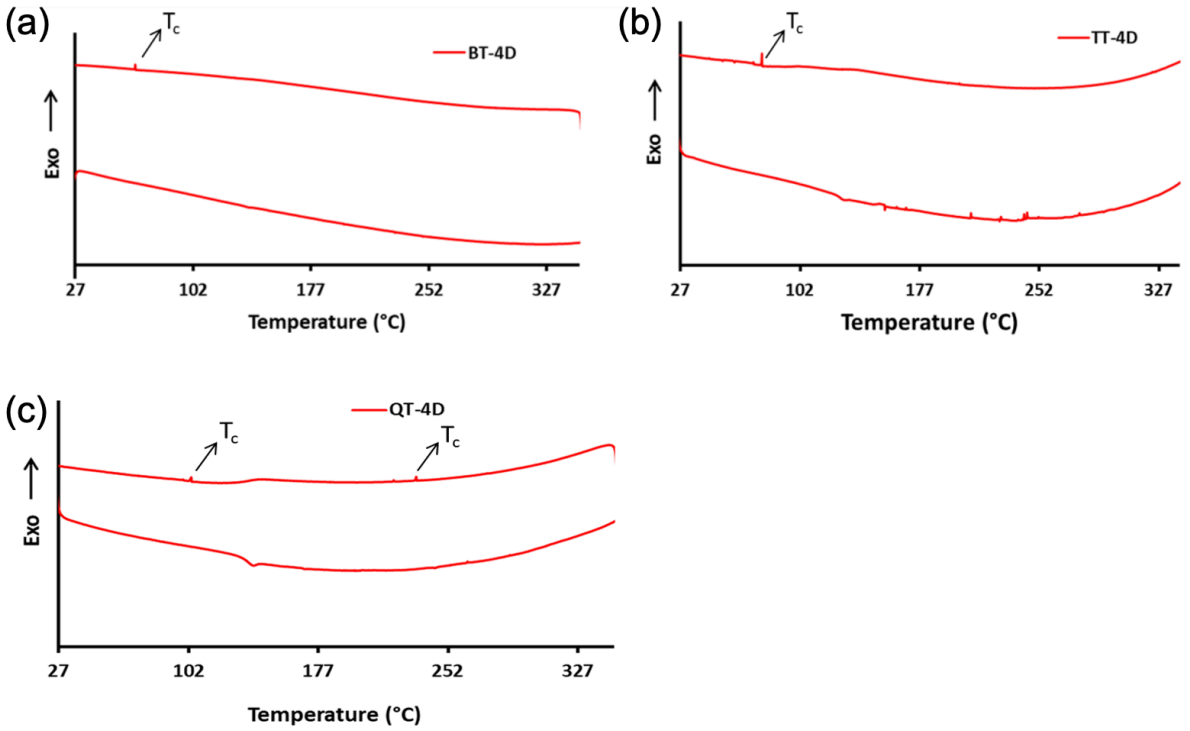

Figure D.2.16 Differential scanning calorimetry (DSC) analysis of (a) **BT-4D**, (b) **TT-4D**, and (c) **QT-4D**.

Table D.2.5 Photovoltaic parameters statistics of PSCs employing **BT-4D**, **TT-4D**, **QT-4D** as HTMs over 32 devices

HTM	V_{OC} (V)	J_{SC} (mA cm^{-2})	*FF*	PCE (%)
BT-4D	1.050 ± 0.005	23.06 ± 0.08	0.790 ± 0.005	19.13 ± 0.14
TT-4D	1.043 ± 0.002	22.63 ± 0.08	0.681 ± 0.022	16.08 ± 0.55
QT-4D	1.040 ± 0.011	22.55 ± 0.25	0.679 ± 0.023	15.92 ± 0.56
Spiro-OMeTAD	1.113 ± 0.011	23.08 ± 0.10	0.770 ± 0.012	19.78 ± 0.18

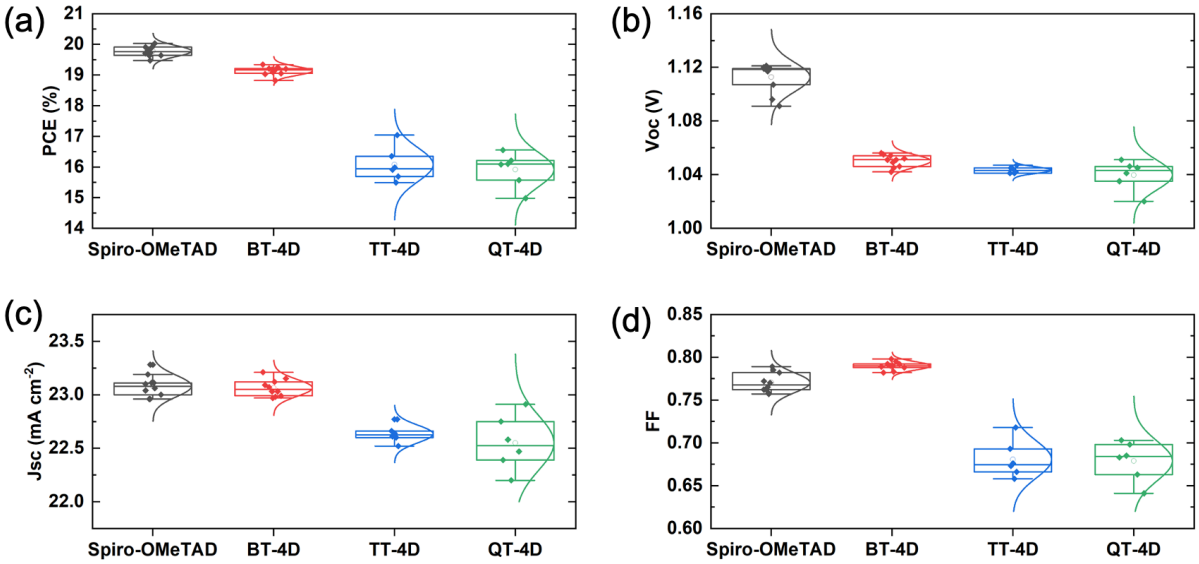

Figure D.2.17 Statistics of (a) PCE, (b)V_{OC}, (c) J_{SC}, and (d) *FF* of PSCs employing **BT-4D**, **TT-4D**, **QT-4D**, and spiro-OMeTAD as HTLs over 32 devices.

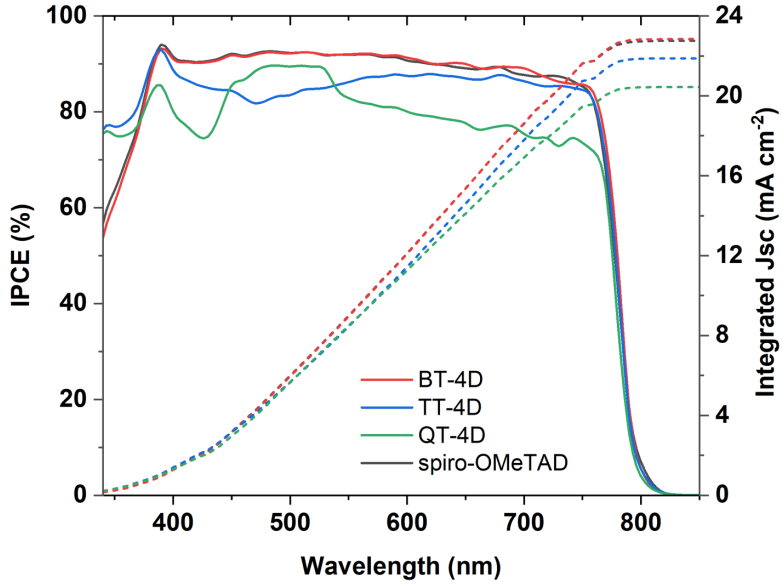

Figure D.2.18 IPCE spectra and the integrated current density of PSCs employing (a) **BT-4D**, (b) **TT-4D**, (c) **QT-4D**, and (d) spiro-OMeTAD as HTLs.

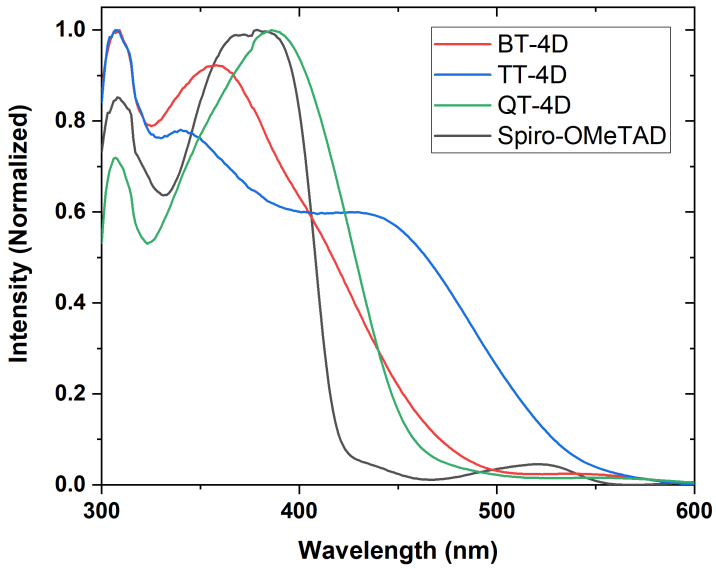

Figure D.2.19 Thin-film absorption spectra of **BT-4D**, **TT-4D**, **QT-4D**, and spiro-OMeTAD.

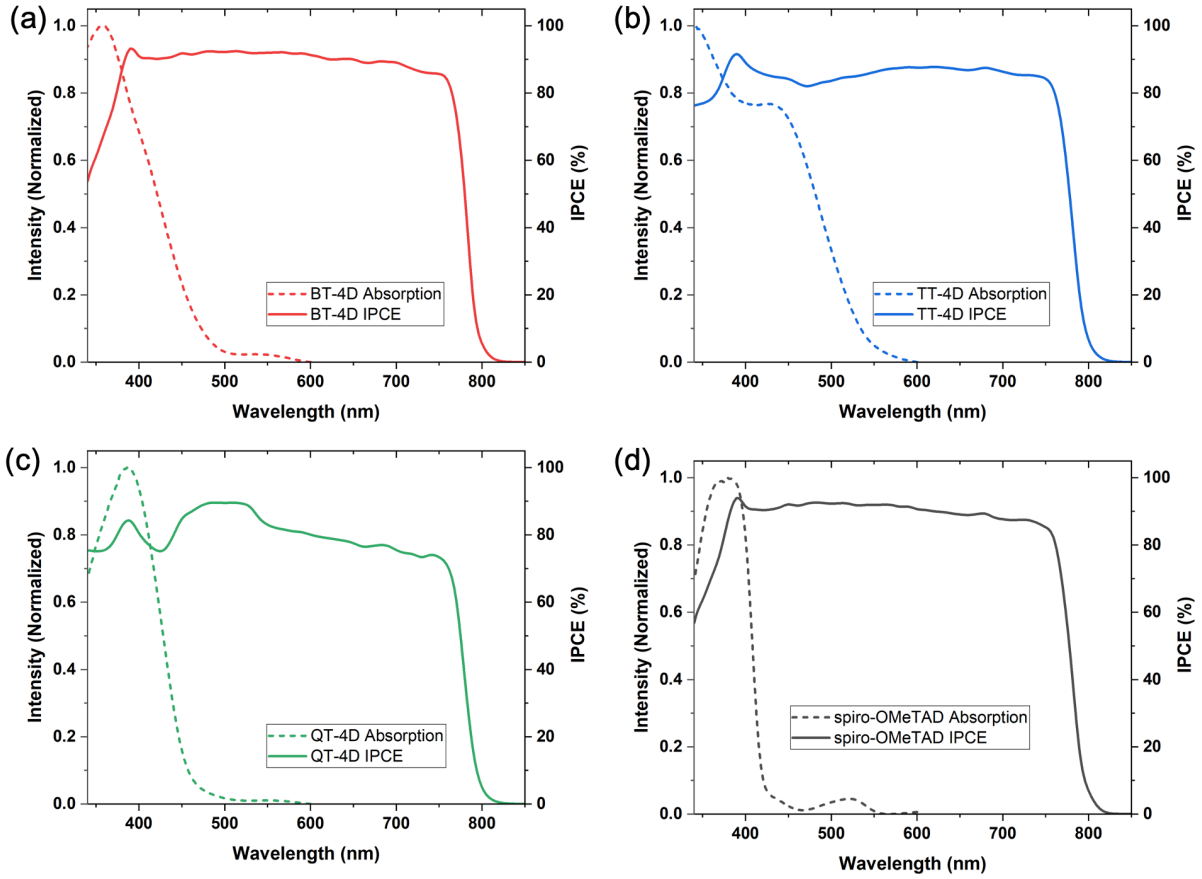

Figure D.2.20 IPCE and thin-film absorption spectra of (a) **BT-4D**, (b) **TT-4D**, (c) **QT-4D**, and (d) spiro-OMeTAD.

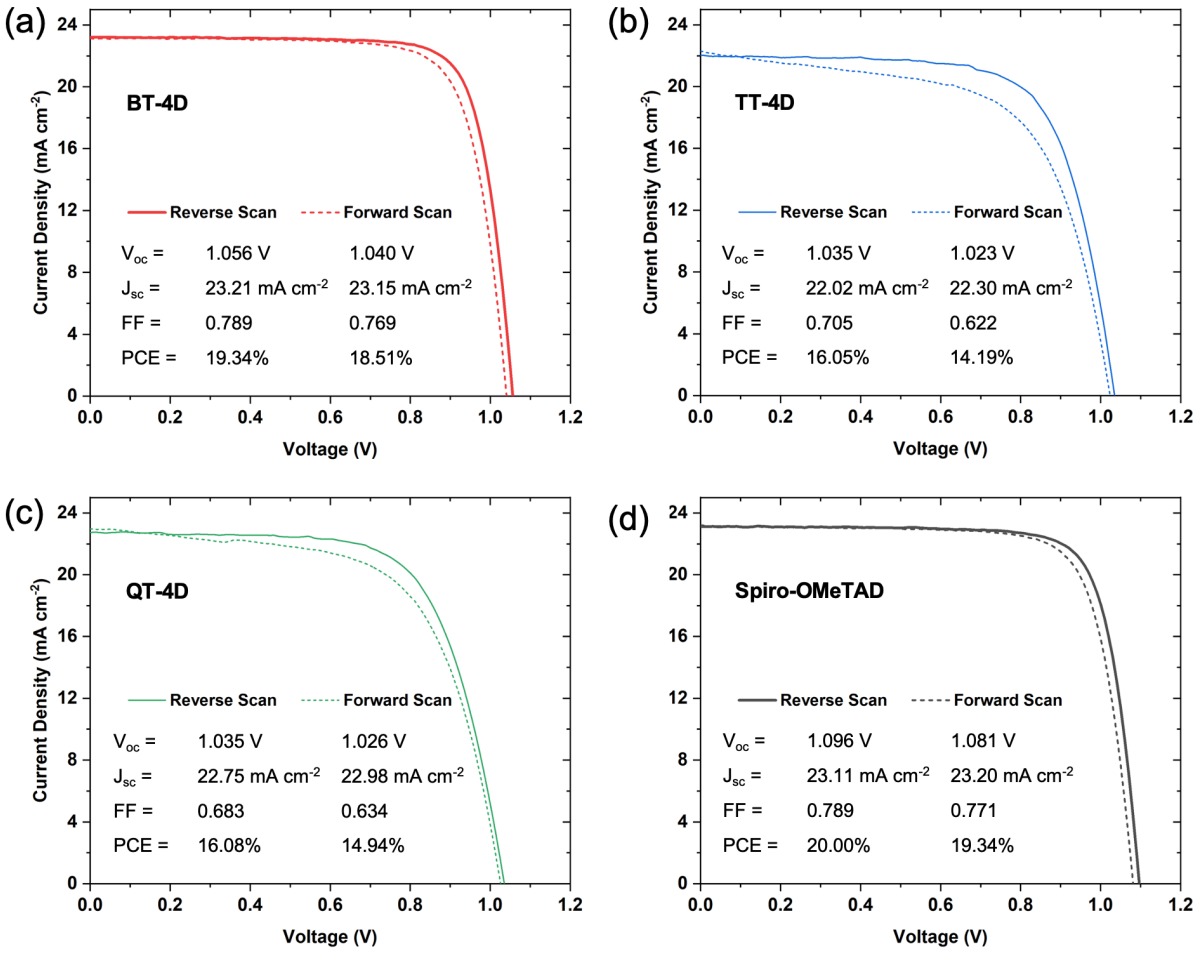

Figure D.2.21 Hysteresis measurement of PSCs employing (a) **BT-4D**, (b) **TT-4D**, (c) **QT-4D**, and (d) spiro-OMeTAD as HTLs. The hysteresis was measured by scanning the *J-V* curve in both reverse and forward direction.

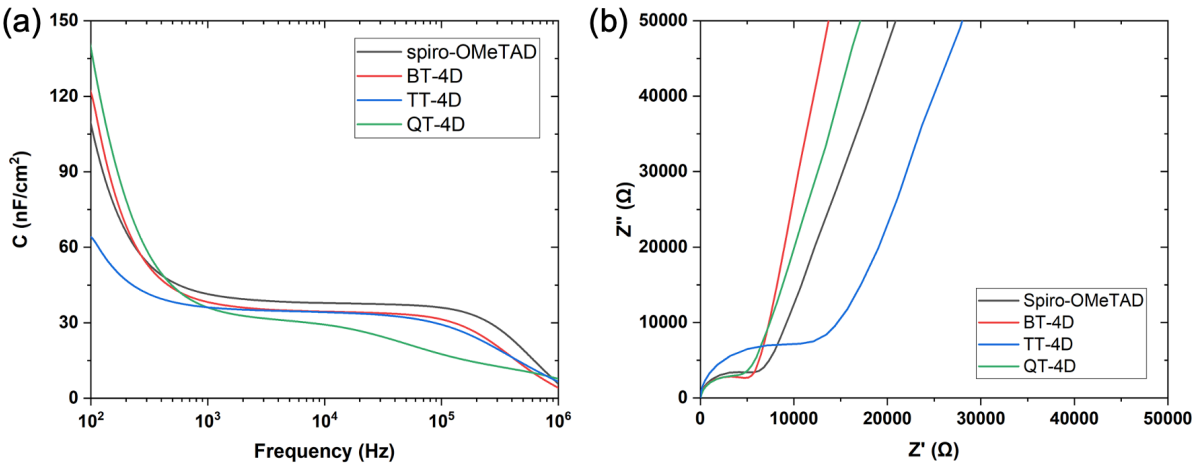

Figure D.2.22 Impedance spectra for (a) capacitance vs frequency and (b) Cole-Cole plot with different HTM.

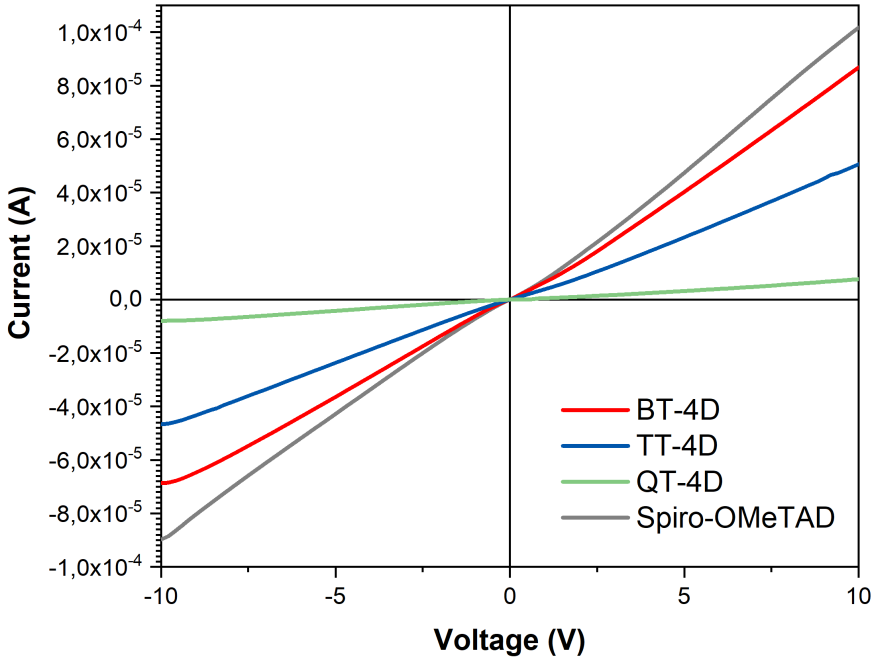

Figure D.2.23 The conductivity of **BT-4D**, **TT-4D**, **QT-4D** and spiro-OMeTAD measured on OFET substrates.

Table D.2.6 Conductivities of the **BT-4D**, **TT-4D**, **QT-4D** HTMs and the reference spiro-OMeTAD.

HTM	**σ (S cm^{-1})**
BT-4D	4.89 x 10^{-4}
TT-4D	3.02 x 10^{-4}
QT-4D	4.83 x 10^{-5}
spiro-OMeTAD	5.83 x 10^{-4}

Table D.2.7 PL Quenching of perovskite thin-films employing different HTMs in respect to the bare perovskite layer as a reference

HTM	**PL Quenching (%)**
BT-4D	74.27
TT-4D	62.23
QT-4D	54.00
Spiro-OMeTAD	73.32

Table D.2.8 Fitting parameters of TrPL spectra based on biexponential decay function of $y = y_0 + A_1 e^{-x/t_1} + A_2 e^{-x/t_2}$

HTM	x_0	y_0	A_1	A_2	t_1 (ns)	t_2 (ns)
Perovskite	0.005	0.66	0.29	0.71	113.8	329.9
BT-4D	0.006	1.27	0.89	0.62	22.0	80.3
TT-4D	0.007	1.52	0.72	0.42	50.1	167.3
QT-4D	0.007	0.92	0.63	0.55	36.5	157.5
Spiro-OMeTAD	0.006	0.97	1.00	0.32	40.4	134.9

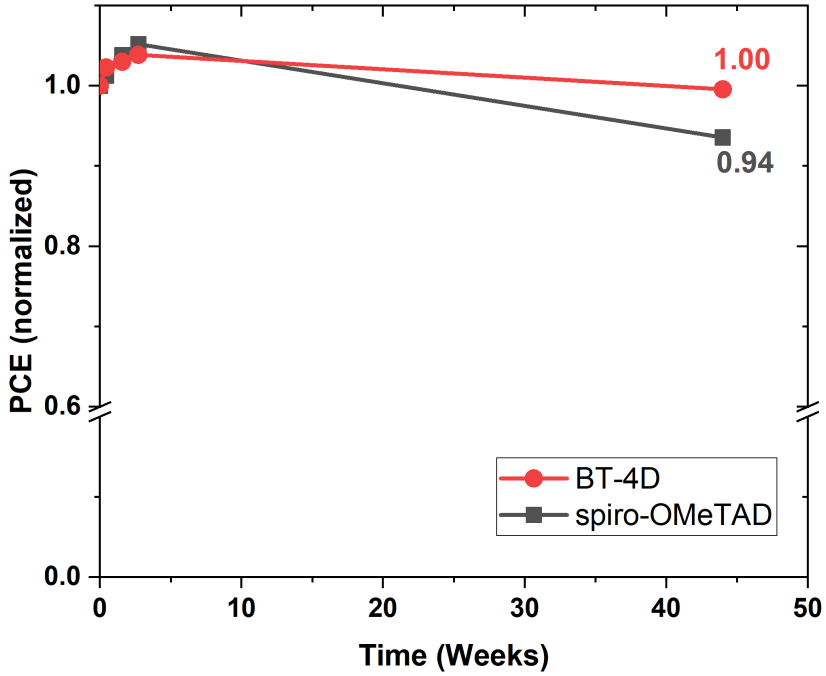

Figure D.2.24 Shelf-life stability of unencapsulated PSCs employing **BT-4D** and spiro-OMeTAD as HTMs stored under dark and ambient atmosphere (relative humidity <15%).

Table D.2.9 Comparison of stable doped-HTMs under light illumination as reported in the literature

Molecules Name	Dopants	Aging Condition	PCE Stability	References
BT-4D	tBP/Li-TFSI/Co-TFSI (FK-209)	Unencapsulated, 1-sun continuous illumination, inert (Ar) atmosphere, room temperature	98% after 1186h	This work
MeSBA-DMPA	tBP/Li-TFSI/Co-TFSI (FK-209)	Unencapsulated, 1-sun continuous illumination, inert (Ar) atmosphere, room temperature	88% after 1000h	[222]
DM	tBP/Li-TFSI	Encapsulated, 1-sun continuous illumination, room temperature	92.6% after 310h	[392]
HTM-1	tBP/Li-TFSI	Unencapsulated, 1-sun continuous illumination, inert (Ar) atmosphere, room temperature	90%, after 400h	[433]
EH44	tBP	Unencapsulated, 1-sun continuous illumination, ambient air condition	94% after 1000h	[434]
PEH-9	tBP/Li-TFSI/Co-TFSI (FK209)	Encapsulated, under ambient condition	93% after 400h	[418]

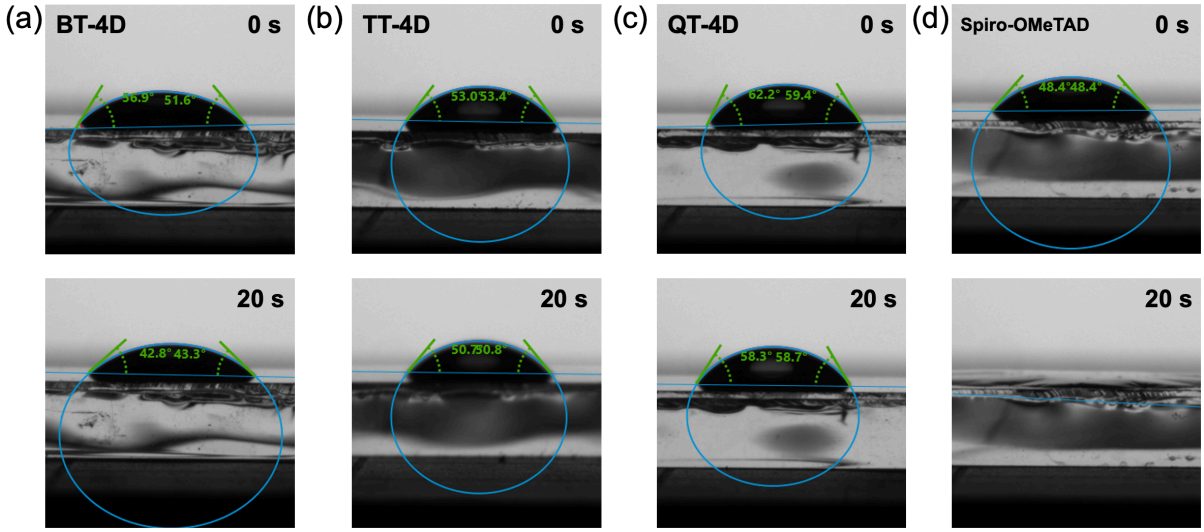

Figure D.2.25 Water contact angle characterization performed on (a) **BT-4D**, (b) **TT-4D**, (c) **QT-4D**, and (d) spiro-OMeTAD thin-films deposited on top of FTO substrates. Top images show the initial contact angle and bottom images shows the evolution of the contact angle after 20 s.

Curriculum Vitae

Albertus Adrian Sutanto

albertus.sutanto@epfl.ch
https://www.linkedin.com/in/albertus-adrian-sutanto/
http://bit.ly/sutanto_gs

Education

03/2018 – 08/2021	**École Polytechnique Fédérale de Lausanne (EPFL), Switzerland** *PhD in Chemistry and Chemical Engineering* Research interest: design of advanced hybrid perovskite materials for photovoltaic application and interfacial engineering of perovskite solar cells to improve device performances and stability. Supervisor: Prof. Mohammad Khaja Nazeeruddin
03/2014 – 08/2015	**National Taiwan University of Science and Technology (NTUST), Taiwan** *M.Sc. in Chemical Engineering (double degree program)* **Diponegoro University (UNDIP), Indonesia** *M.Eng. in Chemical Engineering*
08/2010 – 02/2014	**Diponegoro University (UNDIP), Indonesia** *B.Eng. in Chemical Engineeering*

Publications

1. N. Klipfel, A. O. Alvarez, H. Kanda, **A. A. Sutanto**, C. Igci, C. Roldán-Carmona, C. Momblona, F. Fabregat-Santiago, M. K. Nazeeruddin. C_{60} thin films in perovskite solar cells: efficient or limiting charge transport layer. *Manuscript under review*.
2. N. Klipfel, H. Kanda, **A. A. Sutanto**, M. Mensi, C. Igci, K. Leifer, S. Kinge, C. Roldán-Carmona, C. Momblona, P. J. Dyson, M. K. Nazeeruddin. Bis(trifluoromethanesulfonyl)imide ion as self-passivating agent in co-evaporated *p-i-n* perovskite solar cells. *Manuscript under review*.
3. C. Igci, H. Kanda, S.-M. Yoo, **A. A. Sutanto**, O. Syzgantseva, M. Syzgantseva, V. Jankauskas, K. Rakstys, H. Kim, A. Abdullah, M. K. Nazeeruddin. Highly Planar Benzodipyrrole-based Hole Transporting Materials with Passivation Effect for Efficient Perovskite Solar Cells. *Manuscript under review.*
4. A. S. R. Bati, **A. A. Sutanto**, M. Hao, M. Batmunkh, Y. Yamauchi, L. Wang, Y. Wang, M. K. Nazeeruddin, J. G. Shapter. Cesium-Doped $Ti_3C_2T_x$ MXene for Efficient and Thermally Stable Perovskite Solar Cells. *Manuscript under review, preprint is available on* https://dx.doi.org/10.2139/ssrn.3891059.
5. D. Vaitukaityte, C. Momblona, K. Rakstys, **A. A. Sutanto**, B. Ding, V. Jankauskas, A. Gruodis, T. Malinauskas, A. Asiri, P. J. Dyson, V. Getautis, M. K. Nazeeruddin. Cut from the same cloth: enamine-derived spirobifluorenes as stable hole transporters for perovskite solar cells. Chem. Mater. 2021, 33, 15, 6059–6067, https://doi.org/10.1021/acs.chemmater.1c01486.
6. P. Caprioglio, D. S. Cruz, S. Caicedo-Dávila, F. Zu, **A. A. Sutanto**, F. Peña-Camargo, L. Kegelmann, D. Meggiolaro, L. Gregori, C. M. Wolff, B. Stiller, L. Perdigón-Toro, H. Kobler, B. Li, E. Gutierrez-Partida, I. Lauermann, A. Abate, N. Koch, F. De Angelis, B. Rech, G. Grancini, D. Abou-Ras, M. K. Nazzeruddin, M. Stolterfoht, S. Albrecht, M. Antonietti, D. Neher. Bi-functional Interfaces by Poly-Ionic Liquid Treatment in Efficient *pin* and *nip* Perovskite Solar Cells. Energy Environ. Sci. 2021, 14, 4508-4522, https://doi.org/10.1039/D1EE00869B.

7. V. Joseph,† **A. A. Sutanto**,† C. Igci, O. A. Syzgantseva, V. Jankauskas, K. Rakstys, V. I. E. Queloz, P.-Y. Huang, J.-S. Ni, S. Kinge, M.-C Chen, M. K. Nazeeruddin. Stable Perovskite Solar Cells Using Molecularly Engineered Functionalized Oligothiophene as Low-Cost Hole-Transporting Materials. Small, 2021, 2100783. https://doi.org/10.1002/smll.202100783. (†Equal contribution)
8. **A. A. Sutanto**, P. Caprioglio, N. Drigo, Y. J. Hofstetter, I. Garcia-Benito, V. I. E. Queloz, D. Neher, M. K. Nazeeruddin, M. Stolterfoht, Y. Vaynzof, G. Grancini. 2D/3D Perovskite Engineering Eliminates Interfacial Recombination Losses in Hybrid Perovskite Solar Cells. Chem, 2021, *article in press*, https://doi.org/10.1016/j.chempr.2021.04.002.
9. **A. A. Sutanto**,† V. Joseph,† C. Igci, O. A. Syzgantseva, M. A. Syzgantseva, V. Jankauskas, K. Rakstys, V. I. E. Queloz, P.-Y. Huang, J.-S. Ni, S. Kinge, A. M. Asiri, M.-C Chen, M. K. Nazeeruddin. Isomeric carbazole-based hole-transporting materials: Role of linkage position on the photovoltaic performance of perovskite solar cells. Chem. Mater. 2021, 33, 9, 3286–3296, https://doi.org/10.1021/acs.chemmater.1c00335. (†Equal contribution)
10. V. Romano, L. Najafi, **A. A. Sutanto**, G. Schileo, V. I. E. Queloz, S. Bellani, M. Prato, S. Marras, M. K. Nazeeruddin, G. D'Angelo, F. Bonaccorso, G. Grancini. Two-Step Thermal Annealing: An Effective Route for 15% Efficient Quasi-2D Perovskite Solar Cells. ChemPlusChem, 2021, 86, https://doi.org/10.1002/cplu.202000777.
11. H. Kanda, O. J. Usiobo, C. Momblona, M. Abuhelaiqa, **A. A. Sutanto**, C. Igci, X.-X. Gao, J.-N Audinot, T. Wirtz, M. K. Nazeeruddin. Light Stability Enhancement of Perovskite Solar Cells Using *1H,1H,2H,2H*-Perfluorooctyltriethoxysilane Passivation. Sol. RRL 2021, 5, 2000650, https://doi.org/10.1002/solr.202000650.
12. S. Daskeviciute, C. Momblona, K. Rakstys, **A. A. Sutanto**, M. Daskeviciene, V. Jankauskas, A. Gruodis, G. Bubniene, V. Getautis, M. K. Nazeeruddin. Fluorene-based enamines as low-cost and dopant-free hole transporting materials for high performance and stable perovskite solar cells. J. Mater. Chem. A 2021, 9, 301-309, https://doi.org/10.1039/D0TA08452B.
13. **A. A. Sutanto**,† C. Igci,† H. Kim, H. Kanda, N. Shibayama, M. Mensi, V. I. E. Queloz, C. Momblona, H. J. Yun, H. J. Bolink, A. J. Huckaba, M. K. Nazeeruddin. Phosphine Oxide Derivative as a Passivating Agent to Enhance the Performance of Perovskite Solar Cell. ACS Appl. Energy Mater. 2021, 4, 2, 1259–1268, https://doi.org/10.1021/acsaem.0c02472. (†Equal contribution)
14. **A. A. Sutanto**, R. Szostak, N. Drigo, V. I. E. Queloz, P. E. Marchezi, J. C. Germino, H. C. N. Tolentino, M. K. Nazeeruddin, A. F. Nogueira, G. Grancini. In Situ Analysis Reveals the Role of 2D Perovskite in Preventing Thermal-Induced Degradation in 2D/3D Perovskite Interfaces. Nano Lett. 2020, 20, 5, 3992–3998, https://doi.org/10.1021/acs.nanolett.0c01271.
15. **A. A. Sutanto**, N. Drigo, V. I. E. Queloz, I. Garcia-Benito, A. R. Kirmani, L. J. Richter, P. A. Schouwink, K. T. Cho, S. Paek, M. K. Nazeeruddin, G. Grancini. Dynamical Evolution of the 2D/3D Interface: A Hidden Driver behind Perovskite Solar Cell Instability. J. Mater. Chem. A 2020, 8, 2343-2348, https://doi.org/10.1039/C9TA12489F.
16. A. J. Huckaba, D. T. Sun, **A. A. Sutanto**, Y. Zhang, M. Mensi, W. L. Queen, M. K. Nazeeruddin. Lead Sequestration from Perovskite Solar Cells Using a Polymer-MOF Composite. Energy Technol. 2020, 8, 2000239, https://doi.org/10.1002/ente.202000239.
17. H. Kanda, N. Shibayama, M. Abuhelaiqa, S. Paek, R. Kaneko, N. Klipfel, **A. A. Sutanto**, C. Roldán-Carmona, A.J. Huckaba, H. Kim, C. Momblona, A. M. Asiri, M. K. Nazeeruddin. Gradient band structure: high performance perovskite solar cells using Poly(bisphenol A anhydride-co-1,3-phenylenediamine). J. Mater. Chem. A 2020, 8, 17113-17119, https://doi.org/10.1039/D0TA05496H.
18. C. Momblona, H. Kanda, **A. A. Sutanto**, A.Todinova, M. Creatore, C. Roldán-Carmona, M. K. Nazeeruddin. Co-evaporation as an optimal technique towards compact methylammonium bismuth iodide layers. Sci. Rep. 2020, 10, 10640, https://doi.org/10.1038/s41598-020-67606-1.
19. H. Kim, M. Pei, Y. Lee, **A. A. Sutanto**, S. Paek, V. I. E. Queloz, A. J. Huckaba, K. T. Cho, H. J. Yun, H. Yang, M. K. Nazeeruddin. Self-Crystallized Multifunctional 2-Dimensional Perovskite for Efficient and Stable Perovskite Solar Cells. Adv. Funct. Mater. 2020, 30, 1910620, https://doi.org/10.1002/adfm.201910620.
20. N. A. Drigo, C. Roldán-Carmona, M. Franckevicius, K.-H. Lin, R. Gegevivius, H. Kim, P.A. Schouwink, **A. A. Sutanto**, S. Olthof, M.Sohail, K. Meerholz, V. Gulbinas, C. Corminboeuf, S. Paek, M. K. Nazeeruddin. Doped but stable: spirobisacridine hole transporting materials for

hysteresis-free and stable perovskite solar cells. J. Am. Chem. Soc. 2020, 142, 4, 1792-1800, https://doi.org/10.1021/jacs.9b07166.

21. **A. A. Sutanto**, V. I. E. Queloz, I. Garcia-Benito, K. Laasonen, B. Smit, M. K. Nazeeruddin, O. A. Syzgantseva, and G. Grancini. Pushing the limit of Cs incorporation into $FAPbBr_3$ perovskite to enhance solar cells performances. APL Materials 2019, 7 (4), 04110, https://doi.org/10.1063/1.5087246.
22. S. M. Mane†, **A. A. Sutanto**†, C.-F. Cheng, M.-Y. Xie, C.-I. Chen, M. Leonardus, S.-C. Yeh, E. W.-G. Diau, C.-T. Chen, C.-H. Hung. Oxasmaragdyrins as New and Efficient Hole-Transporting Materials for High-Performance Perovskite Solar Cells. ACS Appl. Mater. Interfaces, 2017, 9, 37, 31950-31958, https://doi.org/10.1021/acsami.7b09803. (†Equal contribution)
23. **A. A. Sutanto**, H. Lan, C.-F. Cheng, S. B. Mane, H.-P. Wu, M. Leonardus, M.-Y. Xie, S.-C. Yeh, C.-W. Tseng, C.-T. Chen, E. W.-G. Diau, C.-H. Hung. Solvent-assisted crystallization via a delayed-annealing approach for highly efficient hybrid mesoscopic/planar perovskite solar cells. Sol. Energy Mater. Sol. Cells., 2017, 172, 270-276, https://doi.org/10.1016/j.solmat.2017.07.043.
24. S. M. Mane, C-F. Cheng, **A. A. Sutanto**, A. Datta, A. Dutta, C.-H. Hung. D-A-π-A organic dyes for dye-sensitized solar cells: Effect of π-bridge length between two acceptors on photovoltaic properties. Tetrahedron, 2015, 71, 7977-7984, https://doi.org/10.1016/j.tet.2015.08.068.

Patents

1. Triphenylamine Functionalized Oligothiophenes: Stable and Low-Cost Hole-Transporting Materials for High Performance Perovskite Solar Cells. 2020. European Patent Filed.
2. Perovskite Solar Cell Provided with an Adsorbent Material for Adsorbing Toxic Materials. 2019. European Patent Filed.

Conferences

1. Materials Research Society (MRS) Fall Meeting 2019. Boston, 1 – 6 December 2019. Oral presentation: “Stable and Efficient Perovskite Solar Cells by Thiophene-based 2D Perovskite Functionalization”.
2. Perovskite Solar Cells and Optoelectronics (PSCO) 2019. Lausanne, 30 September – 2 October 2019. Poster presentation: “Compositional Engineering of $FAPbBr_3$ Perovskite by Cs incorporation to Enhance Solar Cells Performances”.